(NASA-CR-188995) NUMERICAL SIMULATION OF
THE REACTIVE FLOW IN ADVANCED (HSR)
COMBUSTORS USING KIVA-2 Final Report, 1 Feb.
1990 - 31 Aug. 1991 (Maine Univ.) 113 p
CSCL 21E G3/07

N92-11014

Unclas
0048375

NUMERICAL SIMULATION OF THE REACTIVE FLOW IN ADVANCED (HSR) COMBUSTORS USING KIVA-II

Nicholas S. Winowich
University of Maine
Orono, Maine

Final Report for
NASA Lewis Research Center
Grant No. NAG 3-1115
Period 2/1/90 - 8/31/91

ABSTRACT

Recently much work has been done with the goal of establishing ultra-low emission aircraft gas turbine combustors. A significant portion of this effort is the development of three-dimensional computational combustor models. The KIVA-II computer code which is based on the ICEd-ALE numerical scheme is one of the codes selected by NASA to achieve these goals.

This report involves a simulation of jet injection through slanted slots within the Rich-burn/Quick-quench/Lean-burn (RQL) baseline experimental rig. The RQL combustor distinguishes three regions of combustion. This work specifically focuses on modeling the quick-quench mixer region in which secondary injection air is introduced radially through 12 equally spaced slots around the mixer circumference.

Steady state solutions are achieved with modifications to the KIVA-II program. Work currently underway will evaluate thermal mixing as a function of injection air velocity and angle of inclination of the slots.

Table of Contents

PAGE

ABSTRACT ii

TABLE OF CONTENTS iii

LIST OF FIGURES v

NOMENCLATURE ix

CHAPTER I INTRODUCTION 1
- I.1 Motivation 1
- I.2 Literature Survey 4
- I.3 Current Study 6

CHAPTER II PROGRAM DEVELOPMENT 9
- II.1 Program Description 9
- II.2 Governing Equations 10
- II.3 Mesh Generation 13
- II.4 Outlet Boundary Modifications 18
- II.5 Turbulent Kinetic Energy Soln. 20

CHAPTER III PROCEDURE 42
- III.1 Initialization of Run Conditions 42
- III.2 Inflow/Outflow Boundaries 43
- III.3 Initial Problem Conditions 44
- III.4 Jet Development 45
- III.5 Steady State Determination 46

CHAPTER IV 45° SLANTED SLOT RAPID MIXER RESULTS 47
- IV.1 Initial Setup 47
- IV.2 Bulk Swirl Profile 47
- IV.3 Higher Momentum Flux Ratios 49
- IV.4 Numerical Accuracy 50
- IV.5 Lean Zone Length Effects 51
- IV.6 Bulk Temperature Profile 51
- IV.7 Swirl Number Profile 52

CHAPTER V 30° SLANTED SLOT RESULTS 128
V.1 30° Slanted Slot Geometry 128
V.2 Jet Description 128
V.3 Swirl Profile 129
V.4 tke Averaging with the 30° Slanted Slot 129

CHAPTER VI CONCLUSIONS AND RECOMMENDATIONS 154
VI.1 Conclusions and Flowfield Evaluation 154
VI.2 Future Work 155

LIST OF REFERENCES 162

APPENDIX A CASED GEOMETRY REVIEW 163

APPENDIX B HISTORY PLOTS 166

APPENDIX C PUBLICATIONS 192

LIST OF FIGURES

Figure No.	Description	Page
1-1	RQL Combustor Experimental Rig	8
2-1a	45° Slanted Slot Dimensions	23
2-1b	RQL Combustor Dimensions	24
2-2	Vertex/Cell Flagging Scheme Used to Create the 45° Slanted Slot	25

28,101 Cell 45° Slanted Slot Partially Blocked Mesh, J^* = 20, No tke Centerline Averaging

Figure No.	Description	Page
2-3	Pressure History Plot	26
2-4	Velocity History Plot	27
2-5	Temperature History Plot	28
2-6	Normal Velocity j=9	29
2-7	Pressure j=9	30
2-8	Temperature k=25	31
2-9	Pressure k=25	32
2-10	Velocity k=25	33
2-11	Velocity j=9	34
2-12	Zone Plot	35
2-13	Zone Plot	36

39,627 Cell 45° Slanted Slot Open Ended Mesh, J^*=25, Utilizing Centerline tke Averaging

Figure No.	Description	Page
2-14	Velocity j=9	37
2-15	Normal Velocity j=9	38
2-16	Temperature j=9	39
2-17	Pressure j=9	40
2-18	tke j=9	41
4-1	Zone Plot	55
4-2	Zone Plot	56
4-3	Zone Plot	57
4-4	Zone Plot	58

SWIRL PROFILE DEVELOPMENT AND DISPERSION @ J^*=5

Figure No.	Description	Page
4-5	Velocity k=42	59
4-6	Velocity k=47	60
4-7	Velocity k=55	61
4-8	Velocity k=65	62
4-9	Velocity k=75	63
4-10	Velocity k=85	64
4-11	Velocity k=95	65
4-12	Temperature k=42	66

Fig. No. Description Page

4-13 Temperature k=47 67
4-14 Temperature k=55 68
4-15 Temperature k=65 69
4-16 Temperature k=75 70
4-17 Temperature k=85 71
4-18 Temperature k=95 72
4-19 Normal Velocity j=9 73
4-20 Temperature j=9 74

MOMENTUM FLUX RATIO VARIATION

4-21 J*=5 Velocity k=25 75
4-22 40 76
4-23 120 77
4-24 J*=5 Temperature k=25 78
4-25 40 79
4-26 120 80
4-27 J*=5 tke k=25 81
4-28 40 82
4-29 120 83
4-30 J*=5 Velocity j=9 84
4-31 40 85
4-32 120 86
4-33 J*=5 Pressure j=9 87
4-34 40 88
4-35 120 89
4-36 J*=5 Temperature j=9 90
4-37 40 91
4-38 120 92
4-39 J*=5 tke j=9 93
4-40 40 94
4-41 120 95
4-42 J*=5 Normal Velocity j=9 96
4-43 40 97
4-44 120 98
4-45 J*=5 Velocity k=40 99
4-46 40 100
4-47 120 101
4-48 J*=5 Velocity k=55 102
4-49 40 103
4-50 120 104

28,101 CELL 45° SLANTED SLOT COARSE MESH, J*=25 UTILIZING CENTERLINE TKE AVERAGING

4-51 Velocity k=28 105
4-52 Velocity j=9 106
4-53 tke j=9 107
4-54 Normal Velocity j=9 108
4-55 Pressure j=9 109
4-56 Temperature k=28 110

39,627 Cell 45° Slanted Slot Mesh, $J^*=25$

Fig. No. Description Page

4-57 Velocity k=25 111
4-58 Velocity j=9 112
4-59 tke j=9 113
4-60 Normal Velocity j=9 114
4-61 Pressure j=9 115
4-62 Temperature k=25 116

COARSE 45° SLANTED SLOT MESH

4-63 Zone Plot 117

FIGURES COMPARING THE 39,627 CELL 45° SLANTED SLOT MESH WITH A TRUNCATED LEAN ZONE (TLZ) VERSION OF THE SAME GRID, $J^* = 60$

4-64 Velocity, TLZ j=9 118
4-65 Velocity j=9 119
4-66 Temperature, TLZ k=25 120
4-67 Temperature k=25 121
4-68 Pressure, TLZ j=9 122
4-69 Pressure j=9 123
4-70 Normal Velocity, TLZ j=9 124
4-71 Normal Velocity j=9 125

4-72 45° Slot Bulk Temperature Profiles 126
4-73 45° Slot Swirl Number Profiles 127

30° SLANTED SLOT MESH UTILIZING CENTERLINE tke AVERAGING

5-1 Zone Plot 131
5-2 Zone Plot 132
5-3 Zone Plot 133

VARIATION OF MOMENTUM FLUX RATIO

5-4 $J^*=5$ Temperature k=25 134
5-5 40 135
5-6 120 136
5-7 $J^*=5$ Velocity k=25 137
5-8 40 138
5-9 120 139
5-10 $J^*=5$ Velocity k=40 140
5-11 40 141
5-12 120 142
5-13 $J^*=5$ Velocity k=55 143
5-14 40 144
5-15 120 145
5-16 $J^*=5$ Pressure j=9 146
5-17 40 147

Fig. No. Description Page

5-18 $J^{*}=120$ Pressure j=9 148
5-19 $J^{*}=5$ Normal Velocity j=9 149
5-20 40 150
5-21 120 151

5-22 30° Slot Swirl Number Profiles 152
5-23 30° Slot Bulk Temperature Profiles 153

45° SLANTED SLOT MESH, NO tke AVERAGING, INCREASED CONVERGENCE CRITERIA WITH THE PRESSURE AND VELOCITY SOLUTIONS

6-1 Bulk Temperature Profile 157
6-2 Velocity j=9 158
6-3 Pressure j=9 159
6-4 Normal Velocity j=9 160
6-5 tke j=9 161

History plots shown on figures B-1 to B-24 within appendix B are categorized on page 167.

Note: Contour Plots ... The cotour plotting subroutine divides the quantity in consideration (temperature, pressure, etc.) into 11 contour levels. Low contour value (l) and high contour value (h) on figure headings are values of the 2nd and 10th contour levels respectively. Min and max values listed in fig. headings are the extreme minimum and maximum levels across the area of consideration of the respective quantity.

NOMENCLATURE

DR^* = jet-to-mainstream density ratio.
= Tm/Tj

i,j,k = grid coordinates
- i - plane coordinates ranging between the centerline and outer radius, in the radial direction.
- j - plane coordinates ranging between the azimuthal boundaries of the sector mesh,in the azimuthal direction respectively.
- k - plane coordinates ranging from the base of the mesh to the outlet, in the axial direction.

J^* = jet-to-mainstream momentum flux ratio.
= [(Vj)(Vj)(RHOj)] / [(Vm)(Vm)(RHOm)]

NX = the number of cells in the radial dircetion, with NXP = NX + 1.

NY = the number of cells in the azimuthal direction, with NYP = NY + 1.

R^* = jet-to-mainstream velocity ratio.
= (Vj/Vm)

RHOj = jet density (g/cubic cm).

RHOm = mainstream density (g/cubic cm).

Tj = jet temperature (°K).

Tm = mainstream temperature (°K).

U,V,W = cartesian velocity components (cm/sec), W denoting the axial component.

Vj = jet inflow velocity (cm/sec).

Vm = mainstream inflow velocity (cm/sec).

Win = axial velocity applied at k = 1 plane.

X,Y,Z = cartesian coordinates, with Z indicating downstream distance from k = 1 plane.

CHAPTER I

INTRODUCTION

I. 1. Motivation

Much of the research currently underway with gas turbine combustion is in the development of ultra-low emission aircraft gas turbine combustors, to ensure no significant ozone depletion due to emissions from future civil transport aircraft. Several designs are being investigated to meet this goal. One design is the Lean/ Premixed-Prevaporized (LPP) combustor. This combustor avoids droplet combustion and operates with a low fuel/air ratio in the primary zone to achieve low flame temperature with resulting low NOx emissions. Another gas turbine combustor design that shows promise is the Rich-burn/ Quick-quench/ Lean-burn (RQL) combustor. The RQL baseline combustor utilizes slanted slot injection orifices in the quench region. Research with an experimental prototype of the RQL combustor is currently underway at the NASA Lewis Research Center in Cleveland, Ohio. The baseline combustor attempts to separate combustion into three distinct burn zones (rich, intermediate, lean). In the quench region, which is the intermediate combustion zone, air is injected into the combustion products as they leave the rich burn region. The injected air is at ambient temperature and is directed radially inward from slanted slots located along the cylindrical combustor wall.

With the development of civil transport aircraft traveling at Mach 3.0-5.0 stringent emissions controls are becoming increasingly important. The new civil transport aircraft will cruise high in the stratosphere where emissions may easily interact with ozone. Ozone depletion occurs by the following reaction with nitrogen oxide [1]:

$$(1) \quad NO + O_3 \rightarrow NO_2 + O_2$$

$$(2) \quad NO_2 + O \rightarrow NO + O_2$$

Equation (1) shows destruction of ozone (O_3) and the second equation represents reconstitution of nitrogen oxide. Lefebvre [1] breaks down nitrogen oxide sources into three different categories:

1. Thermal NO
2. Prompt NO
3. NO contained within the fuel

Nitrogen oxide is generated in high temperature regions of the combustor and is most prominent above 1800° Kelvin. Prompt NO occurs directly within the flame front and is a result of interaction among intermediate species during the combustion process. Fuel NO is generated from organic nitrogen contained within its molecular structure. Thermal NO is the source of NO that both the LPP Combustor and the RQL Combustor are designed to minimize by maintaining well controlled low flame temperatures during the combustion process. Thermal NO is a direct result of the extended

Zeldovich chain mechanism expressed by the following equations:

$$(1)\quad O + N_2 \leftrightarrow N + NO$$

$$(2)\quad O + NO \leftrightarrow O_2 + N$$

$$(3)\quad N + OH \leftrightarrow H + NO$$

The RQL Combustor maintains low flame temperature with a high equivalence ratio (ER) in the rich zone. The combustor has a design ER of 1.6. The RQL combustor also reduces the production of NO from nitrogen in the fuel since higher equivalence ratios and lower flame temperatures both minimize this conversion rate.

Combustion products leaving the rich zone of the RQL Combustor enter a converging region separating the rich and mixing regions. The mixing region is equipped with twelve injection orifices that inject the secondary combustion air to complete the combustion process. An experimentally verified, bulk swirl velocity is predicted to develop downstream of the slanted slots. The combustion process is enhanced in this region by both an additional supply of oxygen and highly turbulent mixing that exists due to the jet-mainstream interaction. The mixture travels through a radial expansion as it flows into the lean zone. Figure (1-1) shows a schematic of the RQL experimental facility. Many choices exist for the size and shape of the injection orifices in the mixing region, as well as the choice of a single or double row of orifices.

I.2. Literature Survey

The mixing region of the combustor is in essence an example of turbulent jet mixing in a confined crossflow. Many papers are available that describe penetration of a circular jet into an open crossflow. However, only a few discuss jet penetration into a confined crossflow. Opposed jet injection into a confined crossflow has several specific applications in currently operating gas turbine combustors, such as air injected into the dilution zone to shape outlet temperature profiles from the combustor. Another example of this type of flow exists with some combustors in the primary zone immediately downstream of the injector. Air is injected normal to the axial flow inducing a recirculation zone. The recirculation zone entrains unburned combustion products aiding in the control of the combustion reaction rate and soot formation [1]. The RQL's mixing section introduces a new application for opposed jet injection within the gas turbine combustor.

Previous work describing the velocity and temperature profiles of a circular jet into an open cross stream has been done by Keffer & Baines [2] and Ramsey and Goldstein [3]. More work describing near field measurements of the jet trajectory, temperature and velocity profiles was conducted by Moussa et al. [4]. This work was limited to a circular jet. Prediction of the distortion of a circular jet into a kidney shaped profile was made possible by Adler & Baron [5] with an involved application of integral methods. A finite difference scheme utilizing a two equation turbulence model was used by Patankar et al. [6] to verify the experiments of Kefer & Baines and Ramsey & Goldstein.

Experiments conducted by Kamotani & Greber [7] produced velocity and temperature measurements for a single jet injected into a confined cross stream. Jones & McGuirk used a finite difference scheme with a two equation turbulence model to reproduce the experimental observations of Kamotani & Greber.

Holdeman has conducted considerable theoretical and experimental work to investigate the confined crossflow jet injection problem. Holdeman has made several important observations of jet mixing within a confined crossflow [8,9]. These are some of the important conclusions of his work that pertain directly to the RQL Combustor:

1. Mixing improves with increasing downstream distance from the jets.
2. Momentum flux ratio (J^*) is the most significant flow field variable.
3. Variation of the density ratio at a specified momentum flux ratio yields minimal variation of the flow field.
4. Smaller momentum flux ratios require a greater downstream distance for equivalent mixing.
5. Flow area convergence improves the quality of mixing.

Holdeman's numerical work was done with an interactive computer code written in Basic, which was developed to aid in modeling dilution zone air injection, which is used to shape the outlet temperature profile of gas turbine combustors [9]. His experimental work includes work with many orifice geometries, including 45 degree slots of the type found in the RQL baseline geometry. Holdeman found 45 degree slots, in a rectangular duct, produce lower mixing quality and less penetration into the mainstream of a confined cross-flow compared to equivalent area streamlined slots or circular orifices [10].

I.3. Current Study

The objective of the current research is to determine orifice geometries and operating conditions for optimum mixing in the quick-quench region. Experimental work done by the UTRC with the RQL prototype, shown in figure (1-1), evaluated three momentum flux ratios at a constant density ratio with three different 45 degree slot geometries having varying slot length and width. This work utilized planar digital imaging with an oil aerosol marking the jet. The study concluded optimum mixing occurred at the intermediate momentum flux ratio (J^*) of 17.8. The flowfield in the vicinity of the mixing region of the RQL combustor is very complex. Vortices are found to exist between the jets near the slot inlet. For parallel slots, two vortices of equal size but counter rotating exist between the slots. However, for a 45 degree slanted slot one clockwise rotating vortex is dominant in size, while the other is virtually nonexistent. As jet velocity increases, radial jet penetration and axial penetration of the swirling flow into the lean zone both increase. The swirling profile may be a significant contributor to the quality of mixing if optimum mixing in the experimental apparatus occurred at $J^* = 17.8$ and not the higher momentum flux ratio of 78.0. This conclusion is based upon the dispersion of oil droplets and not thermal mixing.

An analysis of the jet-to-mainstream interaction for this mixer requires a three-dimensional numerical model. KIVA-II with its well established ICEd-ALE finite volume numerical scheme is employed to investigate the flow field. KIVA-II uses the standard $k-\varepsilon$ turbulence model. The thermal mixing performance will be determined from the predicted temperature and velocity fields for specified orifice geometry and operating conditions.

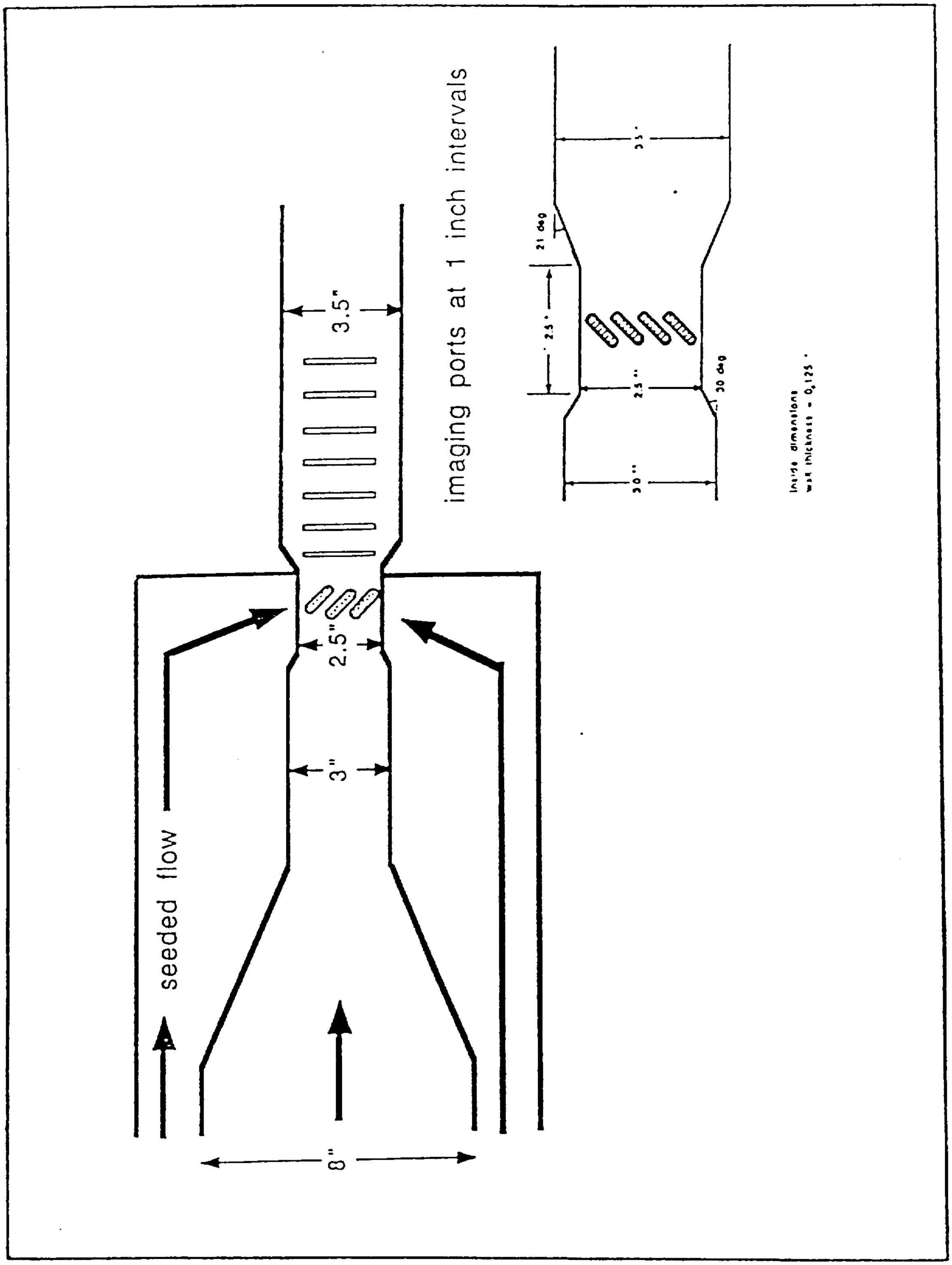
imaging ports at 1 inch intervals
3.5"
2.5"
3"
8"
seeded flow
3.5"
21 deg
2.5"
2.5"
30 deg
3.0"
inside dimensions
wall thickness = 0.125"

Figure 1-1

CHAPTER II

PROGRAM DEVELOPEMENT

II.1. Program Description

All rapid mixer geometry nonreactive flow mixing calculations were conducted with KIVA-II, a reactive flow code developed at Los Alamos National Laboratory. This code is capable of solving transient, two- and three-dimensional, chemically reactive fluid flows with sprays. KIVA-II solves the unsteady equations of motion for a turbulent, chemically reactive mixture of ideal gases, coupled with equations for a single component vaporizing fuel spray. The code resolves spatial differences by subdividing the computational region into small hexahedrons. Coordinates of the hexahedron cell corners (vertices) are calculated as functions of time, which allows for a Lagrangian, Eulerian, or combined description of the flow. A major advantage of the KIVA-II code is its ability to use nonorthogonal cells. Nonorthogonal cells are required in the converging and diverging regions of the baseline geometry. The ICE method, which is used by KIVA-II, utilizes an implicit solution for pressure. This allows larger time steps than purely explicit differencing of the pressure gradient terms.

Each time step of the solution may involve both a Lagrangian and a Eulerian rezone phase. Vertices move with the fluid in the Lagrangian phase, and then are repositioned to user specified positions during the rezone phase. After repositioning the vertices, the flowfield is interpolated onto the new computational mesh. Explicit methods are used to calculate convection in the rezone phase.

KIVA-II uses the k-ε turbulence model modified to include volumetric expansion effects and spray-turbulence interactions. Boundary layer drag and wall heat transfer are calculated with a modified turbulent law-of-the-wall model.

II.2. Governing Equations

KIVA-II is capable of solving both laminar and turbulent flows. For turbulent flows transport coefficients are derived from turbulent diffusivity. The governing equations solved by the code are as follows:

<u>Mass Conservation Equation</u>

$$\frac{\partial \rho_m}{\partial t} + \vec{\nabla}\cdot(\rho_m \vec{u}) = \vec{\nabla}\cdot\vec{J}_m + \dot{\rho}_m^c$$

for the mth species, where ρ_m is the mass density of species m, $\vec{u}$ is the fluid velocity, $\vec{J}_m$ is the diffusive mass flux of species m, and $\dot{\rho}_m^c$ is the rate of change of due to chemical reaction. The diffusive mass flux is given by Fick's Law:

$$J_m = \rho D \vec{\nabla} Y_m$$

where ρ is the total mass density and Y_m is the species mass fraction. The mass diffusivity D, which is assumed to be the same for all species, is determined using the Schmidt number Sc, (assumed constant):

$$D = \frac{\mu}{\rho Sc}$$

where μ is viscosity.

$$\frac{\partial p}{\partial t} + \vec{\nabla}\cdot(\rho\vec{u}) = 0$$

Momentum Cohservation Equation

$$\frac{\partial(\rho\vec{u})}{\partial t} + \vec{\nabla}\cdot(\rho\vec{u}\vec{u}) = -\vec{\nabla}p - \vec{\nabla}\frac{2}{3}\rho k + \vec{\nabla}\cdot\underset{\sim}{\sigma}$$

where p is the fluid pressure, and k is the specific turbulent kinetic energy. The viscous stress tensor is Newtonian and is expressed as:

$$\underset{\sim}{\sigma} = \mu[\vec{\nabla}\vec{u} + (\vec{\nabla}\vec{u})^{T}] + \lambda\vec{\nabla}\cdot\vec{u}\underset{\sim}{U}$$

where μ and λ are the shear and bulk viscosity coefficients, $\underset{\sim}{U}$ is the unit dyadic tensor, and superscript T denotes the transpose. The viscosity coefficients are given by:

$$\mu = \mu_{air} + c_{\mu}\rho\,\frac{k^2}{\varepsilon}$$

and

$$\lambda = -\frac{2}{3}\mu$$

where ε is the specific turbulent kinetic energy dissipation rate and c_{μ} is an empirical turbulence constant equalling 0.09. A Sutherland formula is used for the molecular viscosity of air with A_1 and A_2 constant:

$$\mu_{air} = \frac{A_1 T^{3/2}}{T + A_2}$$

Energy Conservation Equation

$$\frac{\partial(\rho I)}{\partial t} + \vec{\nabla}\cdot(\rho\vec{u}I) = -p\vec{\nabla}\cdot\vec{u} - \vec{\nabla}\cdot\vec{q} + \rho\varepsilon + Q^c$$

where I is the specific internal energy and Q^c is a source term due to chemical heat release. The total heat flux $\vec{q}$, is gained by summing the effects of heat conduction and enthalpy transport by mass diffusion:

$$\vec{q} = \vec{q}_c + \vec{q}_d = -K\vec{\nabla}T - \sum_m h_m \vec{J}_m$$

where K is the thermal conductivity, T is the fluid temperature, and h_m is the species specific enthalpy. The thermal conductivity is determined using the Prandtl number Pr (assumed constant).

$$K = \frac{\mu c_p}{Pr}$$

where c_p is the specific heat at constant pressure.

Turbulence Equations

$$\frac{\partial\rho k}{\partial t} + \vec{\nabla}\cdot(\rho\vec{u}k) + \frac{2}{3}\rho k\vec{\nabla}\cdot\vec{u} = \underset{\sim}{\sigma}:\vec{\nabla}\vec{u} + \vec{\nabla}\cdot\left[\frac{\mu}{Pr_k}\vec{\nabla}k\right] - \rho\varepsilon$$

$$\frac{\partial\rho\varepsilon}{\partial t} + \vec{\nabla}\cdot(\rho\vec{u}\varepsilon) + \left[\frac{2}{3}c_{\varepsilon_1} + c_{\varepsilon_3}\right]\rho\varepsilon\vec{\nabla}\cdot\vec{u} =$$
$$\vec{\nabla}\cdot\left[\frac{\mu}{Pr_\varepsilon}\vec{\nabla}\varepsilon\right] + \frac{\varepsilon}{k}\left[c_{\varepsilon_1}\underset{\sim}{\sigma}:\vec{\nabla}\vec{u} - c_{\varepsilon_2}\rho\varepsilon\right]$$

where c_{ε_1} , c_{ε_2} , c_{ε_3} , Pr_k , and Pr_ε are empirical constants having the following values:

$c_{\varepsilon_1} = 1.44$ $c_{\varepsilon_2} = 1.92$ $c_{\varepsilon_3} = -1.0$

$Pr_k = 1.0$ $Pr_\varepsilon = 1.3$

Equations of state assume ideal gas relationships. The following are the equations of state used by KIVA-II.

$$p = R_o T \Sigma(\rho_m / W_m)$$

$$I(T) = \Sigma(\rho_m / \rho) I_m(T)$$

$$c_p(T) = \Sigma(\rho_m / \rho) c_{pm}(T)$$

$$h_m(T) = I_m(T) + R_o T / W_m$$

R_o - the universal gas constant
W_m - molecular weight of species m
$I_m(T)$ - specific internal energy of species m
$c_{pm}(T)$ - specific heat at constant pressure of species m
$h_m(T)$ - enthalpy of species m
ρ_m - density of species m

II.3. Mesh Generation

KIVA-II was originally set up to allow for inflow along the bottom (k=1) boundary, and outflow along the right (i=nxp) and top (k=nzp) boundaries. To incorporate a slanted slot for secondary air injection into the mixing section the code was modified to allow inflow along a portion of the right boundary. To model the 45 degree slanted slot, k and j planes were spaced so looking at the right face of the cylindrical mesh along the i = nxp plane a line connecting the vertices could be drawn 45 degrees from the horizontal. Figure (2-1a) shows a schematic description of an actual 45 degree slot, its dimensions and important program variables used in generation of the mesh within a preprocessor. Figure (2-1b) shows dimensions of the baseline mixer from k=1 to 60.

For ns equally spaced slots, the flowfield will be periodic in 2(π)/ns degree intervals. Therefore, an important capability of KIVA-II used for this work is its ability to model only a portion of the full cylindrical geometry for problems with cyclic symmetry. The grid used to model the slanted slot geometry comprised only a 30 degree sector of the full 360 degree geometry. This reduces the number of computational cells required in each case by a factor of 12 in comparison with a full 360 degree grid.

The z and theta spacing of the k and j planes respectively are selected so that diagonal rows of vertices lie along the desired slot angle. The theta increment is defined as an angle and is referred to as thdiv below. The slot is divided up into 15 increments with respect to the j direction.

$$\text{THDIV} = \frac{L_s \sin\alpha_s + W_s}{R_m(ny)}$$

L_s - length of slot

W_s - slot width

α_s - slot angle

R_m - mixer radius

With the theta increment selected the z increment is determined via trigonometry and is defined here as DZDIV.

$$\text{DZDIV} = \frac{\text{THDIV} \cdot R_m}{\tan\alpha_s}$$

With this type of mesh development the arc length of the modeled slot in the azimuthal direction corresponds exactly to the true 45 degree slot, but a slight discrepancy with the axial length of the actual and modeled slot exists. Vertex velocities are set to the jet velocity in groups of five in a k-plane and as the k-plane number is advanced (moving axially down the mixing zone) the starting vertex of the inflow group is staggered with respect to the j direction as shown in figure (2-2). The complete slanted slot encompasses 11 k-planes in the axial direction. Total axial length of the modelled slot is calculated below:

$$\text{Axial length} = (11)(0.20259\ \text{cm}) = 2.228\ \text{cm}$$

The true length of a 45 degree slot is:

$$\text{True length} = (1.25\ \text{in})(2.54)(\sin 45) = 2.245\ \text{cm}$$

The percent error in our modeled axial length is:

$$\%\ \text{difference} = \frac{2.245\ \text{cm} - 2.228\ \text{cm}}{2.245\ \text{cm}}(100)$$

$$= 0.7570\ \% \quad \text{or less than } 1\ \%$$

Two types of velocity boundary conditions must be specified in KIVA-II. These are velocities specified at verticies and velocities specified at the cell-face centers. The latter are associated with the calculation of fluxing volumes used with the convective terms in the governing equations. In subroutine BCFC the dot product of left cell face area vector and face centered velocity is calculated (ual(i4)). Multiplying the ual(i4) quantity for cells lying along the slot edge by 2/3, since these cells only have 3 of 4 vertices set with the inflow velocity, reduces the flux passing through the cell face to 50% of that of cell faces lying fully within the slot. The following equations further describe the relationship described above:

$$\vec{u}_f = \frac{1}{4}\,(\vec{u}_{v1} + \vec{u}_{v2} + \vec{u}_{v3} + \vec{u}_{v4})$$

At a cell face along the slot edge:

$$\vec{u}_f = \frac{1}{4}\,(0 + \vec{u}_j + \vec{u}_j + \vec{u}_j) = \frac{3}{4}\,\vec{u}_j$$

For a cell face completely within the slot:

$$\delta V = \vec{u}_f \cdot \vec{A}_1 \Delta t$$

For a cell face along the slot edge:

$$\delta V = (\tfrac{2}{3})(\tfrac{3}{4}\,\vec{u}_j) \cdot \vec{A}_1 \Delta t = \frac{1}{2}\,\vec{u}_j \cdot \vec{A}_1 \Delta t$$

$\vec{u}_f$ - face centered velocity.

$\vec{u}_{vi}$ - face vertex velocities (i=1,4).

$\vec{u}_j$ - jet velocity.

$\vec{A}_1$ - cell left face area vector.

Δt - time step.

δV - volume fluxed through the left cell face in a given cycle.

The section of subroutine BCFC performing this function is listed below.

```
 vf4 = abs(  rtinf(j  ,k  ))                                         QQM11220
 vf3 = aos(  rtinf(j+1,k  ))                                         QQM11230
 vf7 = aos(  rtinf(j+1,k+1))                                         QQM11240
 vf8 = abs(  rtinf(j  ,k+1))                                         QQM11250
 flxfac=vf3+vf4+vf7+vf8                                              QQM11260
 ualnxp=0.25*((u(13)*vf3+u(14)*vf4+u(17)*vf7+u(18)*vf8)*alx(14)      QQM11270
&          + (v(13)*vf3+v(14)*vf4+v(17)*vf7+v(18)*vf8)*aly(i4)       QQM11280
&          + (w(13)*vf3+w(14)*vf4+w(17)*vf7+w(18)*vf8)*alz(14))      QQM11290
 flxfac=cvmgt(2./3.,flxfac/4., flxfac.eq.3. )                        QQM11300
 ual(14)=cvmgt(flxfac*ualnxp, ual(14), i.eq.nxp .and. rtcelf.ne.0.)QQM11310
```

The computing mesh for a 30 degree slot geometry is similar to that for the 45 degree slanted slot with a few exceptions. The method used to generate the slanted slot meshes yields optimum results with a slot at 45 degrees from the horizontal, which had an axial length error of less than 1 percent. The number of divisions with respect to the azimuthal and axial direction determines the error between actual and modeled slot measurements. An error in either the axial or azimuthal direction of 8% was found to exist with most combinations. With this in mind the number of divisions within the 30 degree slot was picked to remain the same as the number used with the 45 degree slot. The 30 degree slot's THDIV and DZDIV components are calculated below.

$$\text{THDIV} = \frac{(1.25\ \text{in})(2.54)(\sin 30) + (0.3125\ \text{in})(2.54)}{(2.5\ \text{in})(2.54)(15\ \text{div})}$$

$$= 0.025\ \text{rad}(\ 180/3.14159\ ) = 1.43239\ \text{degrees}$$

$$\text{DZDIV} = \frac{(0.025\text{rad})(2.5\ \text{in})(2.54)}{\tan 30}$$

$$= 0.27496\ \text{cm}$$

$$\text{Modeled axial length} = (11)(0.27496) = 3.0245\ \text{cm}$$

$$\text{Actual Axial Length} = (\cos 30)(1.25")(2.54) = 2.7496\ \text{cm}$$

$$\%\ \text{Difference} = \frac{3.0245\text{cm} - 2.7496\text{cm}}{2.7496\text{cm}}(100) = 9.9\%$$

Another difference in grid geometry between the two cases investigated is that 5 additional cells in the azimuthal direction were added to the 30° slot geometry. This was necessary since the slot itself encompassed only 21.48 degrees and the sector mesh encompasses 30 degrees. This increase in cells yielded a mesh of 51,282 cells in comparison with the 39,627 cell, 45 degree baseline mesh.

II.4. Outlet Boundary Modifications

The actual experimental rapid mixer test rig shown in figure (1-1) is equipped with a 6 ft lean zone. Since the flowfield becomes fully developed before the actual outflow port, a shorter computational lean zone length is used which also reduces execution run time. A 44.2 in lean zone was selected for the open end mesh. This long length ensured the bulk swirling profile dissipated prior to reaching the outflow boundary.

Early in the transient of the nonreacting runs using the pressure outlet boundary conditions provided in the KIVA-II code flow reversal occurred on the outflow boundary. Once this flow reversal occurred, air at ambient temperature would enter the mesh. This phenomenon would greatly increase the required cpu time to reach steady state. Several options are available to prevent this flow reversal from occurring, two of which are presented with this work. By deactivating some of the exit plane cells, the outflow port is modified such that flow reversal is prevented. With a 18x16x86, 45 degree slanted slot mesh the first 6 cells in the i direction were left open and the remaining 12 were blocked out. Results from this approach are presented to compare with a solution obtained by modifying the ouflow boundary conditions to prevent the flow reversal. This in effect leaves an open orifice in the center of a cylindrical blockage. This left a 2.857 cm open radius within the 8.89 cm radius lean zone. Figures (2-12) and (2-13) show the region of interest (mixing section) of the grid. This mesh used a shorter lean zone of only 24.149 in than the open end mesh. History plots showing arrival of steady state with this partially blocked off mesh at $J^{*} = 20$, are shown in figs. (2-3),(2-4), and (2-5). Figures (2-3), (2-4) and (2-5) have cgs units. The partial blockage causes a 5% pressure increase throughout the mesh accompanied by a 5% decrease in the axial flow speed, when compared to results of a completely open end calculation. Results from the open end mesh are discussed in chapter 4. Figures (2-6),(2-7),(2-8),(2-9),(2-10), and (2-11) show the results of the partially blocked grid run. Qualitatively comparing the jet flow field characteristics with the open end mesh, the results compare well. A vortex occurring directly to the right, with respect to axial flow direction, (CCW) of the slanted slot can be seen in figure (2-10). Secondly the low pressure region occurring directly downstream of the slot near the outer wall is also noted shown in figure (2-7). A disadvantage of the partially blocked end grid is a greatly increased run time. The pressure increase as steady state is approached requires roughly 3 times more runtime than a similar run with an open end grid. Average time steps from the J^* = 20 blocked grid are compared with the J^* = 25 open end grid below.

(blocked) average dt = 0.1439s/9820cyc = 1.465e-05 s/cyc

(open) average dt = 0.1067s/4693cyc = 2.273e-05 s/cyc

The blocked mesh has a lower time step due to high shear stress at the partial blockage on the outflow boundary.

To allow use of the open end grid while preventing any flow reversal along the outflow boundary required modifications to the outflow boundary conditions. Within subroutine BC a condition was set that would zero the velocity of any vertices with a negative value along the nzp plane, occurring only during the false transient. Also, in subroutine BCFC the face velocity would be set to zero along the nzp plane if the negative values occurred indicating flow reversal. Together these two modifications prevented flow reversal from occurring at any point during the transient. Steady state could be reached with 3000 to 4000 time steps typically.

II.5. Turbulent Kinetic Energy Solution

Another numerical anomaly experienced with KIVA-II during the nonreactive mixer runs was the formation of a localized tke high spot along the axis directly opposite the slanted slot. Knowing that with this geometry the turbulence should be at a maximum in the vicinity of the jet (slanted slot) [11] the localized high spot along the centerline was a numerical problem. The localized turbulent kinetic energy high spot is a result of insufficient accuracy with the convergence criteria with the velocity and pressure solutions.

The localized high spot would form almost immediately at the beginning of the transient and its magnitude was on the order of 100 times that of other surrounding cells. Once the localized high spot formed it would slowly migrate down the length of the mesh and not advect across the outflow boundary. The partially blocked end grid was able to pass the tke high spot out of the mesh. The quicker running simpler open end grid was unable to pass it through. The high spot trapped at the outflow would increase the amplitude of pressure oscillations and iterations for tke and turbulence dissipation. One run in which the localized high spot had formed at the outflow boundary and drove up the number of iterations for the turbulence solution was stopped at cycle 2749. Figures (2-14),(2-15),(2-16),(2-17), and (2-18) show plots from a run with high localized tke at the outlet centerline. Figure (2-14) of the velocity field looks well developed. The normal velocity plot in figure (2-15) also is well developed and can be compared with normal velocity plots from chapter 4 as well as the previous section of this chapter. Figures (2-17) and (2-18) reveal the localized tke high spot clearly. The tke high spot was always accompanied with a low pressure disturbance at the same location. Excerpts from file 12, and file 59 listing the iterations per cycle from a run with no tke anomaly nearing steady state and the 2749 cycle with the turbulence problem are listed below.

Localized TKE along the outlet centerline....

```
 ncyc=  2700 ca=   0.0 t= 1.3002E-01 dt= 4.3866E-05 gr=1.388 dcpuodt= 6.7358E+
05
      c8h18= 0.0000E+00 pm= 0.0000E+00 avp= 1.0136E+07 perr= 3.4771E-03 grow
      iters: y=  0 v=  8 t= 15 p= 10 k= 76 e= 73 big=  2 nfluxs= 7 pgs= 1.9442E
+00
 urtin: -0.48100E+04
 mom-ratio: 0.25009E+02
 ncyc=  2725 ca=   0.0 t= 1.3114E-01 dt= 4.4658E-05 gr=1.451 dcpuodt= 6.9149E+
05
      c8h18= 0.0000E+00 pm= 0.0000E+00 avp= 1.0130E+07 perr= 1.4054E-03 rstr
      iters: y=  0 v= 13 t= 16 p=  7 k= 36 e= 50 big=  2 nfluxs= 7 pgs= 1.9453E
+00
```

Normal rapid mixer run nearing steady state....

```
 ncyc= 3299 ca=  0.0 t= 1.5447E-01 dt= 4.4655E-05 gr= 1.062 dcpuodt= 5.0615E+
05
      c8h18= 0.0000E+00 pm= 0.0000E+00 avp= 1.0155E+07 perr= 1.9643E-04  rstr
      iters: y=  0 v=  3 t=  7 p=  2 k=  6 e=  6 big=  2 nfluxs=  7 pgs= 1.9107E
+00
      dtcon= 6.69053E-06 dtacc= 1.23886E-04 dtrst= 4.46499E-05 dt= 4.46499E-05
 ncyc= 3300 ca=  0.0 t= 1.5451E-01 dt= 4.4650E-05 gr= 1.072 dcpuodt= 5.1069E+
05
      c8h18= 0.0000E+00 pm= 0.0000E+00 avp= 1.0155E+07 perr= 1.3972E-04  rstr
      iters: y=  0 v=  3 t=  7 p=  2 k=  6 e=  6 big=  2 nfluxs=  7 pgs= 1.9111E
+00
```

Initially, to eliminate the numerical anomaly a type of tke clipper was inserted into the code. It determined the average tke considering only the first 4 cells from the centerline along the entire length of the mesh. Then each cell within the 4 cell sweep range was compared with the average tke value and set to the average tke if exceeding it. Averaging was used because physically tke values near the centerline should be rather uniform. This technique prevented localized high spots from forming on the centerline with out altering the jet analysis within the area of interest (k=1 to k=60).

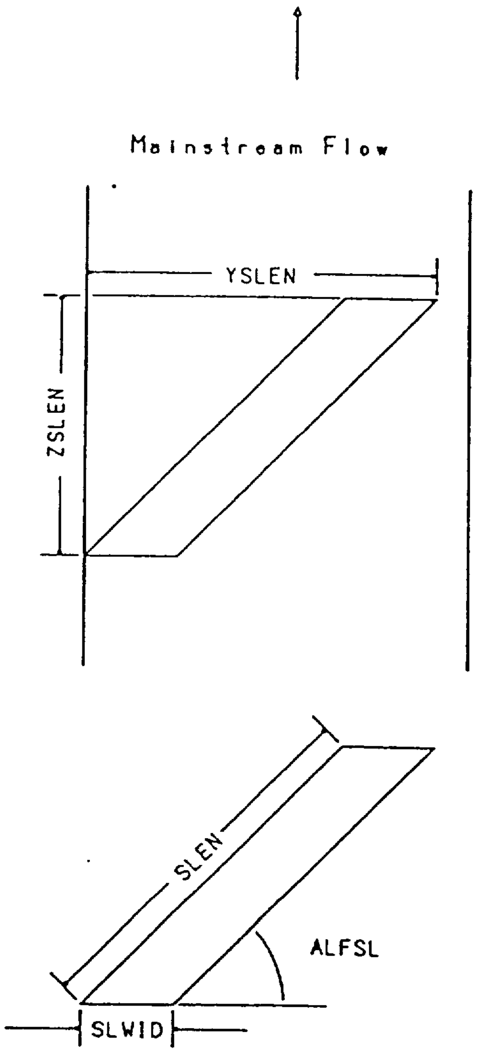

SLEN = 1.25" - SLOT LENGTH

ALFSL = 45 degrees - SLOT ANGLE

SLWID = 0.3125" - SLOT WIDTH

ZSLEN = 0.884" - SLOT LENGTH IN THE AXIAL DIRECTION

YSLEN = 1.196" - SLOT WIDTH IF DRAWN ON A NON-CURVED PLANE

Figure 2-1a

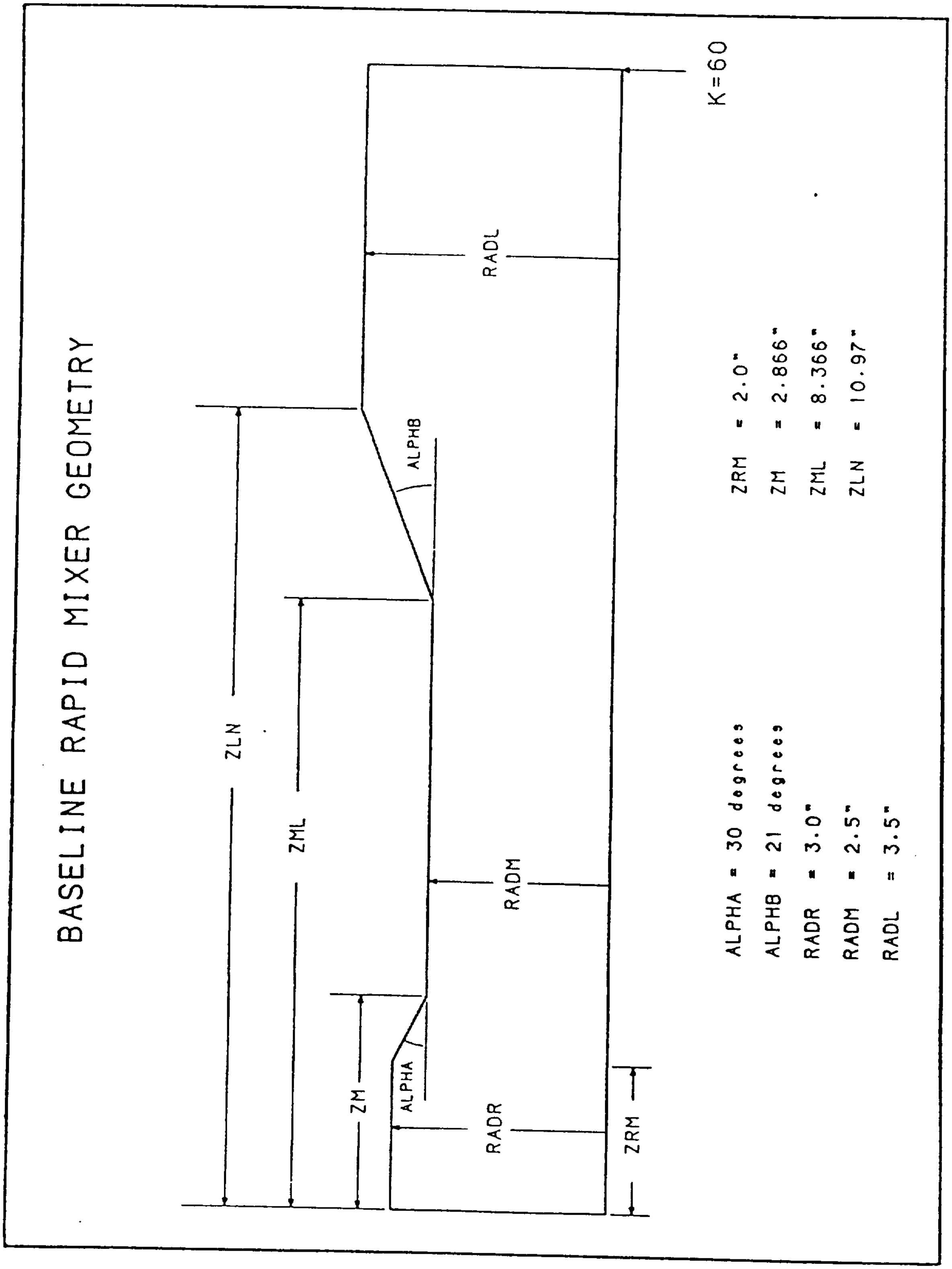
BASELINE RAPID MIXER GEOMETRY
K=60
RADL
ALPHB
ZLN
ZML
RADM
ZM
ALPHA
RADR
ZRM
ALPHA = 30 degrees
ALPHB = 21 degrees
RADR = 3.0"
RADM = 2.5"
RADL = 3.5"
ZRM = 2.0"
ZM = 2.866"
ZML = 8.366"
ZLN = 10.97"

Figure 2-1b

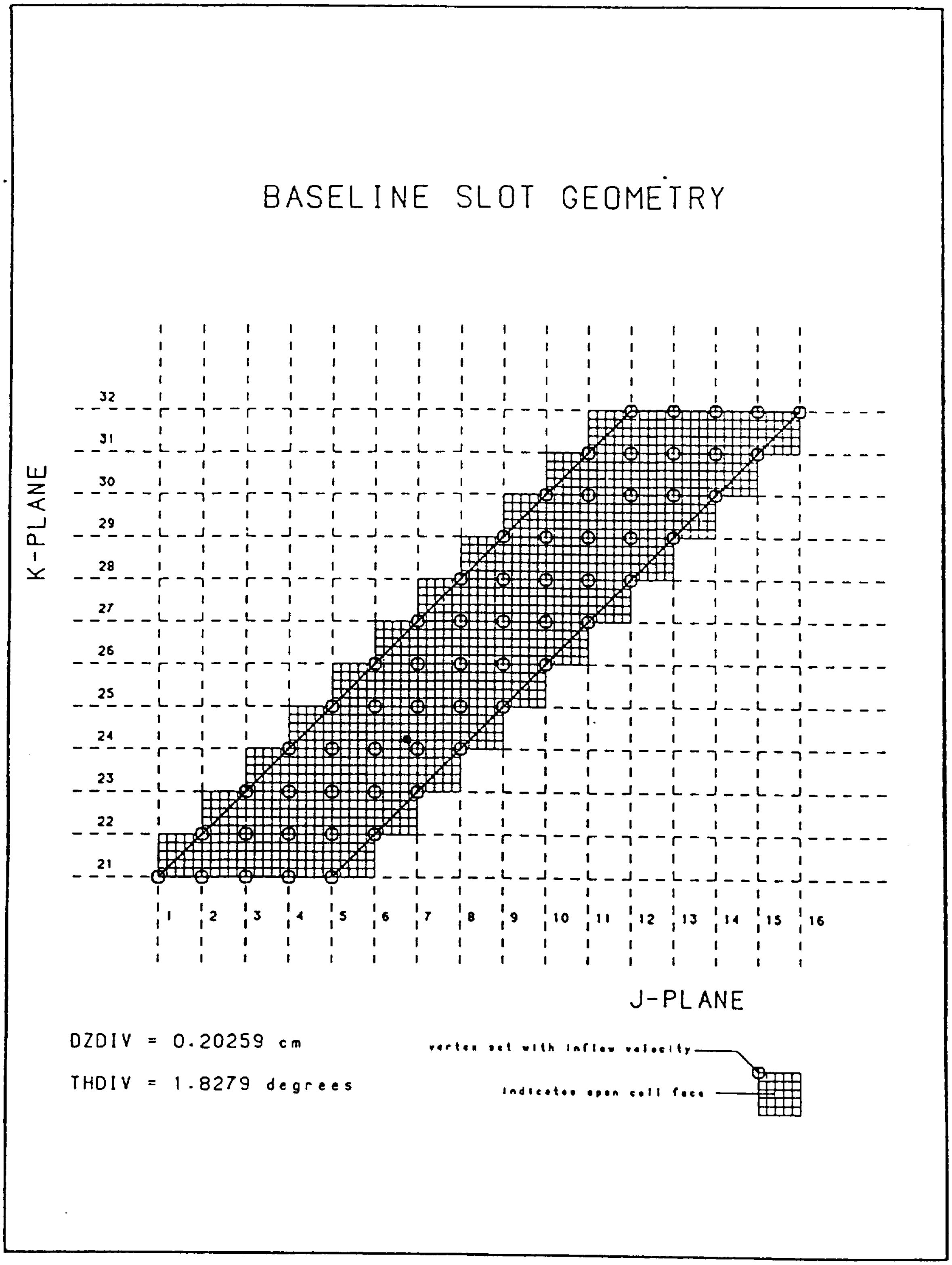
BASELINE SLOT GEOMETRY
K-PLANE
32
31
30
29
28
27
26
25
24
23
22
21
1
2
3
4
5
6
7
8
9
10
11
12
13
14
15
16
J-PLANE
DZDIV = 0.20259 cm
THDIV = 1.8279 degrees
vertex set with inflow velocity
indicates open cell face

Figure 2-2

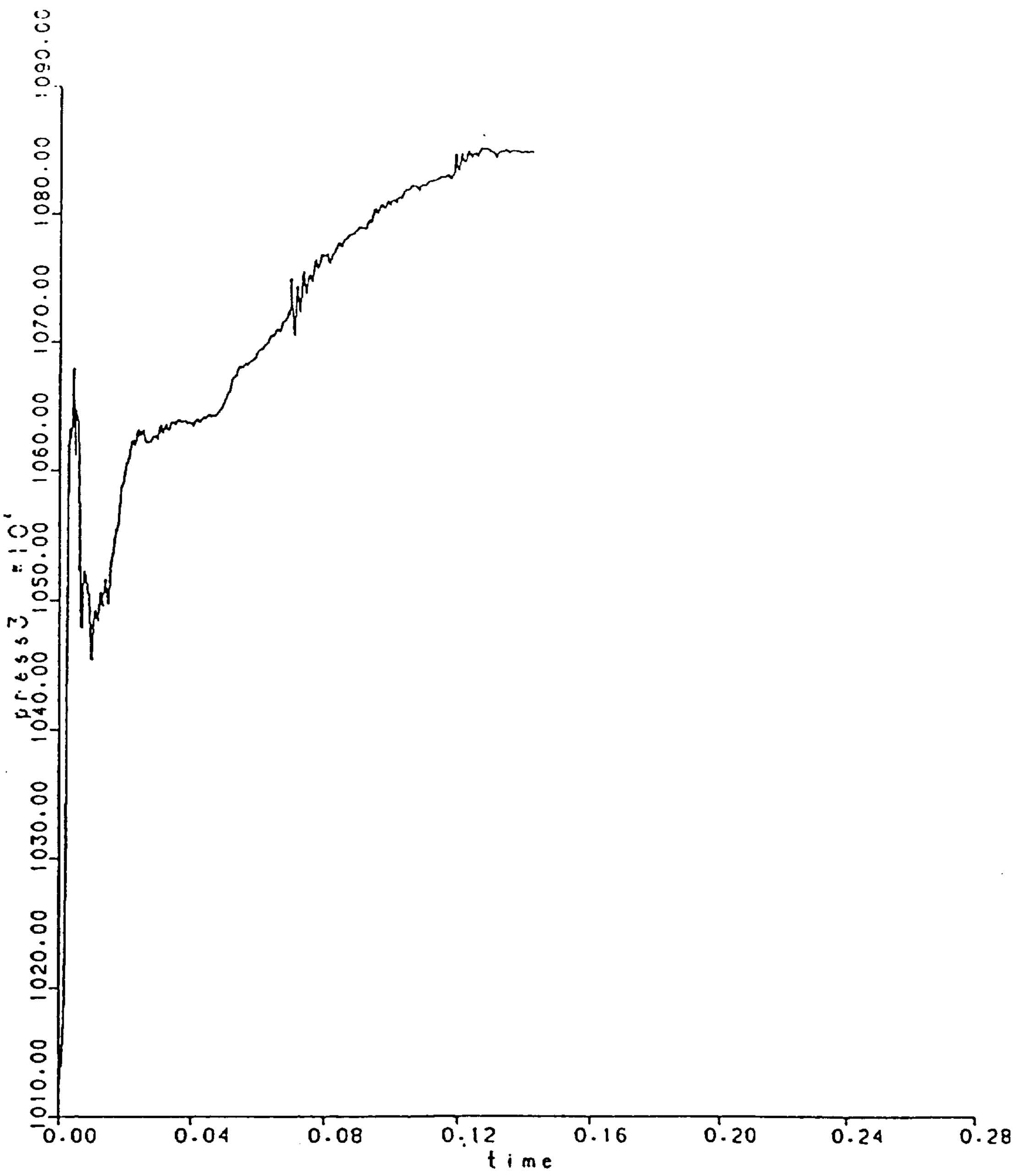

press3 *10'
1010.00
1020.00
1030.00
1040.00
1050.00
1060.00
1070.00
1080.00
1090.00
0.00
0.04
0.08
0.12
0.16
0.20
0.24
0.28
time

Figure 2-3

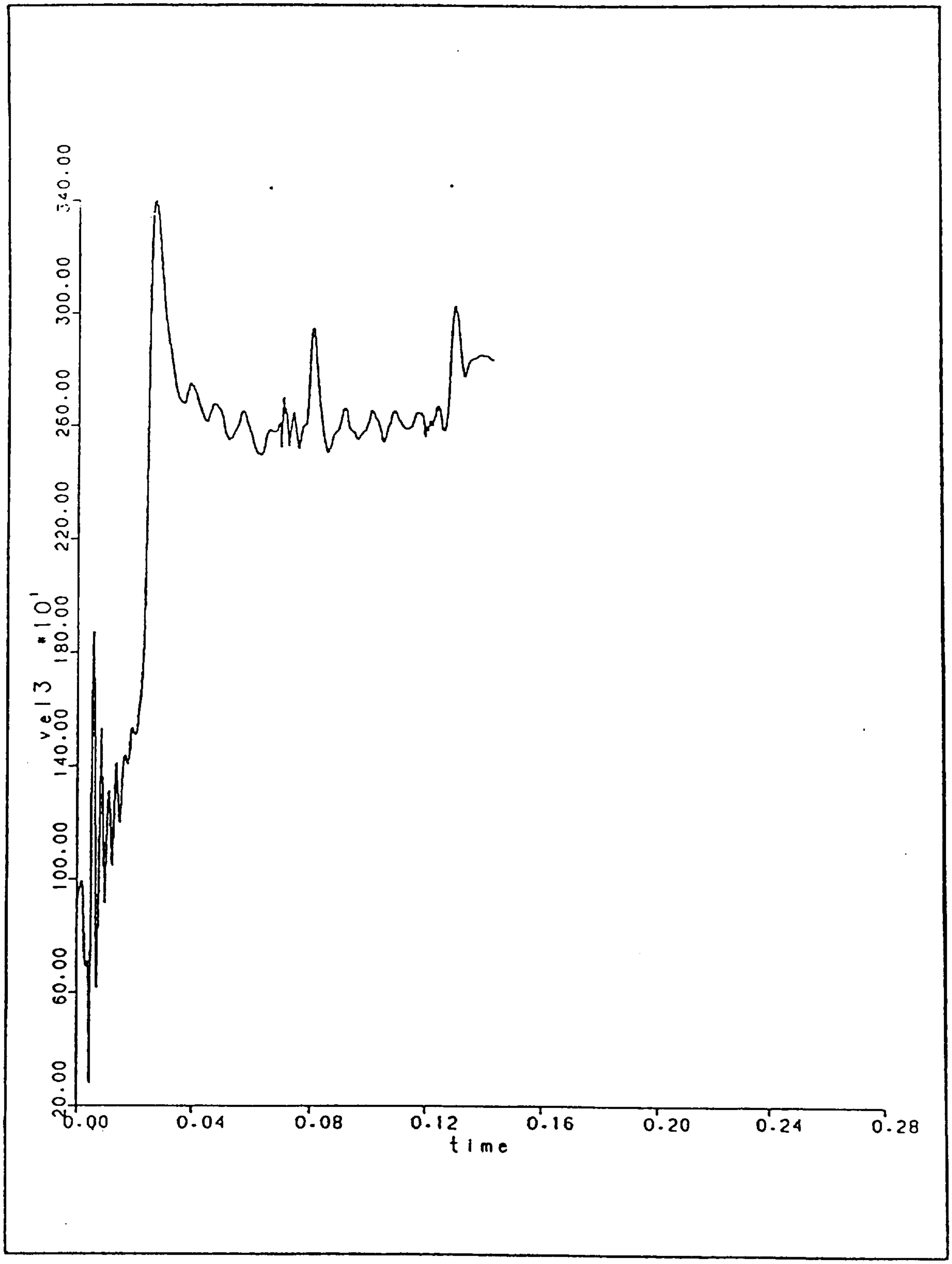

vel3 *10¹
20.00
60.00
100.00
140.00
180.00
220.00
260.00
300.00
340.00
0.00
0.04
0.08
0.12
0.16
0.20
0.24
0.28
time

Figure 2-4

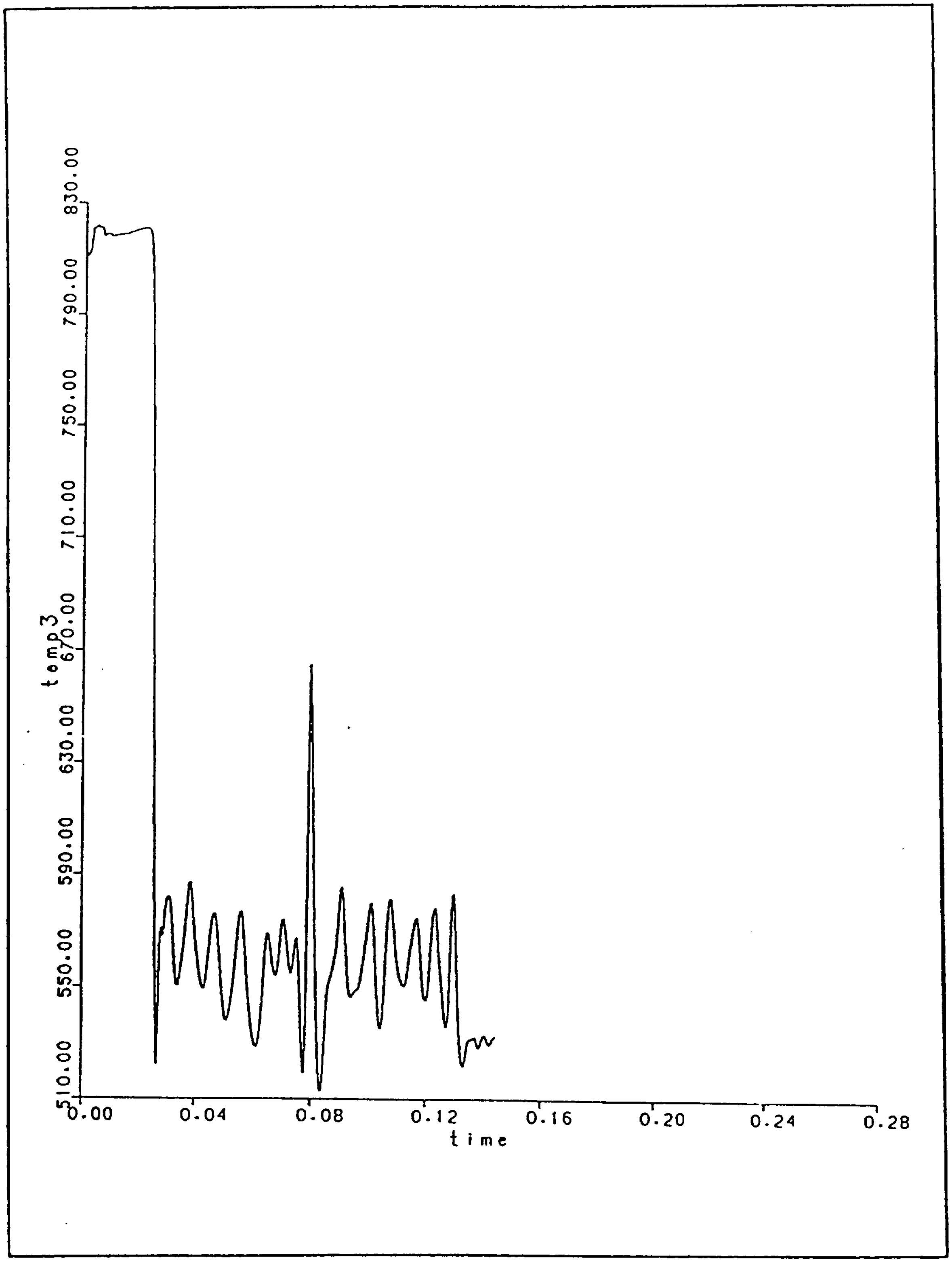
temp3
830.00
790.00
750.00
710.00
670.00
630.00
590.00
550.00
510.00
0.00
0.04
0.08
0.12
0.16
0.20
0.24
0.28
time

Figure 2-5

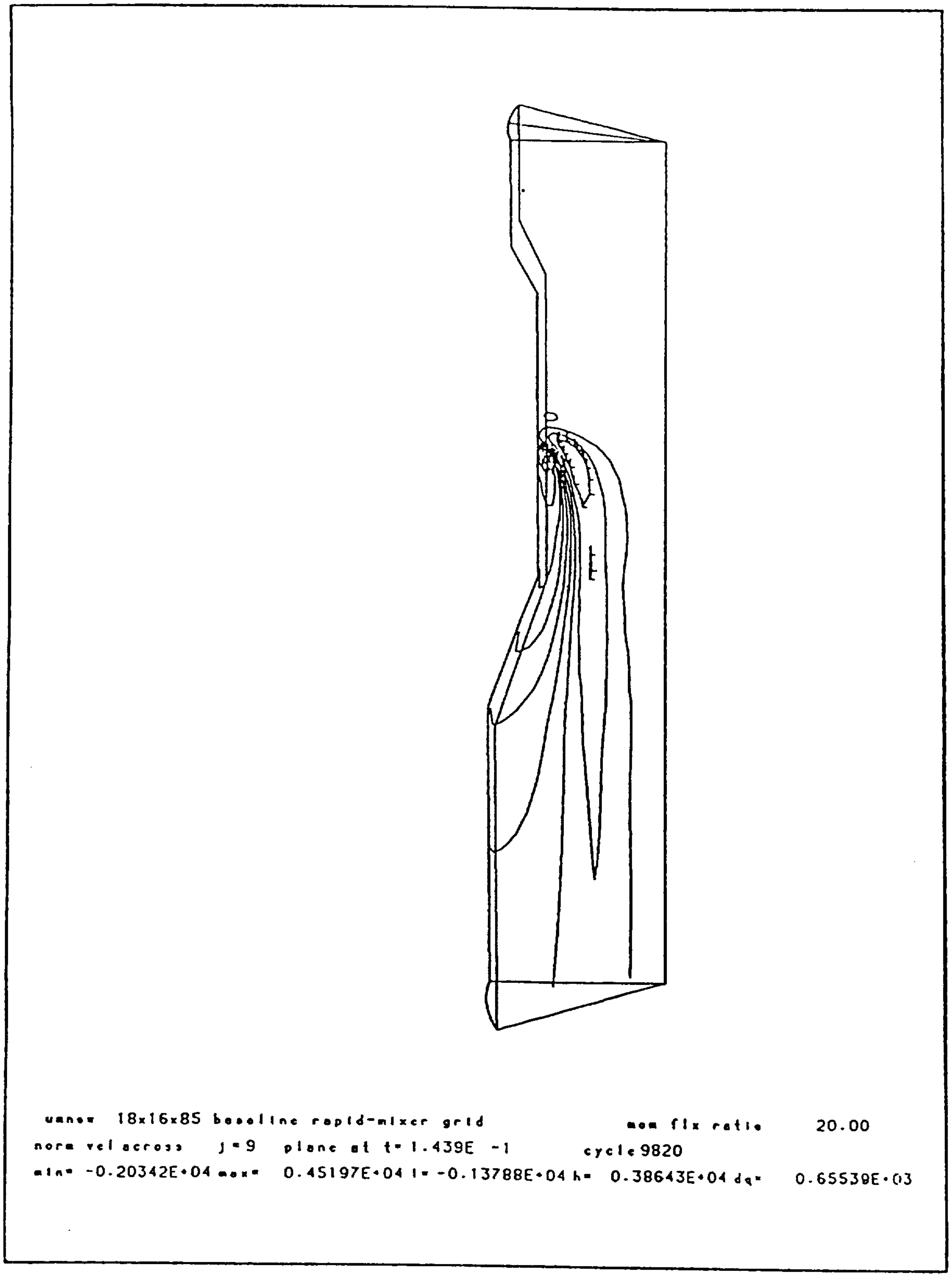
umnew 18x16x85 baseline rapid-mixer grid
mom flx ratio 20.00
norm vel across j=9 plane at t=1.439E -1
cycle 9820
min= -0.20342E+04 max= 0.45197E+04 l= -0.13788E+04 h= 0.38643E+04 dq= 0.65539E+03

Figure 2-6

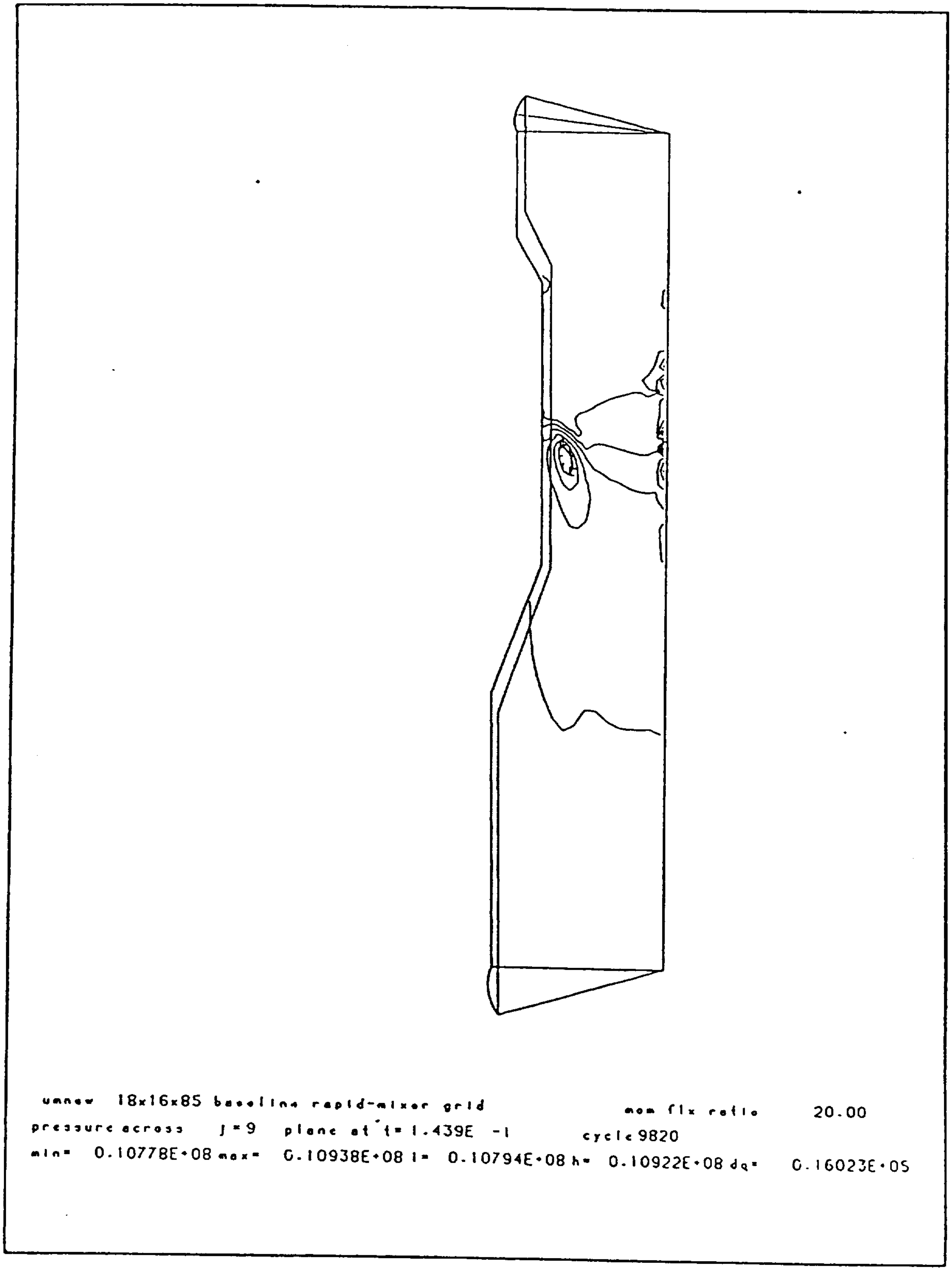
umnew 18x16x85 baseline rapid-mixer grid
mom flx ratio 20.00
pressure across j = 9 plane at t = 1.439E -1
cycle 9820
min= 0.10778E+08 max= 0.10938E+08 l= 0.10794E+08 h= 0.10922E+08 dq= 0.16023E+05

Figure 2-7

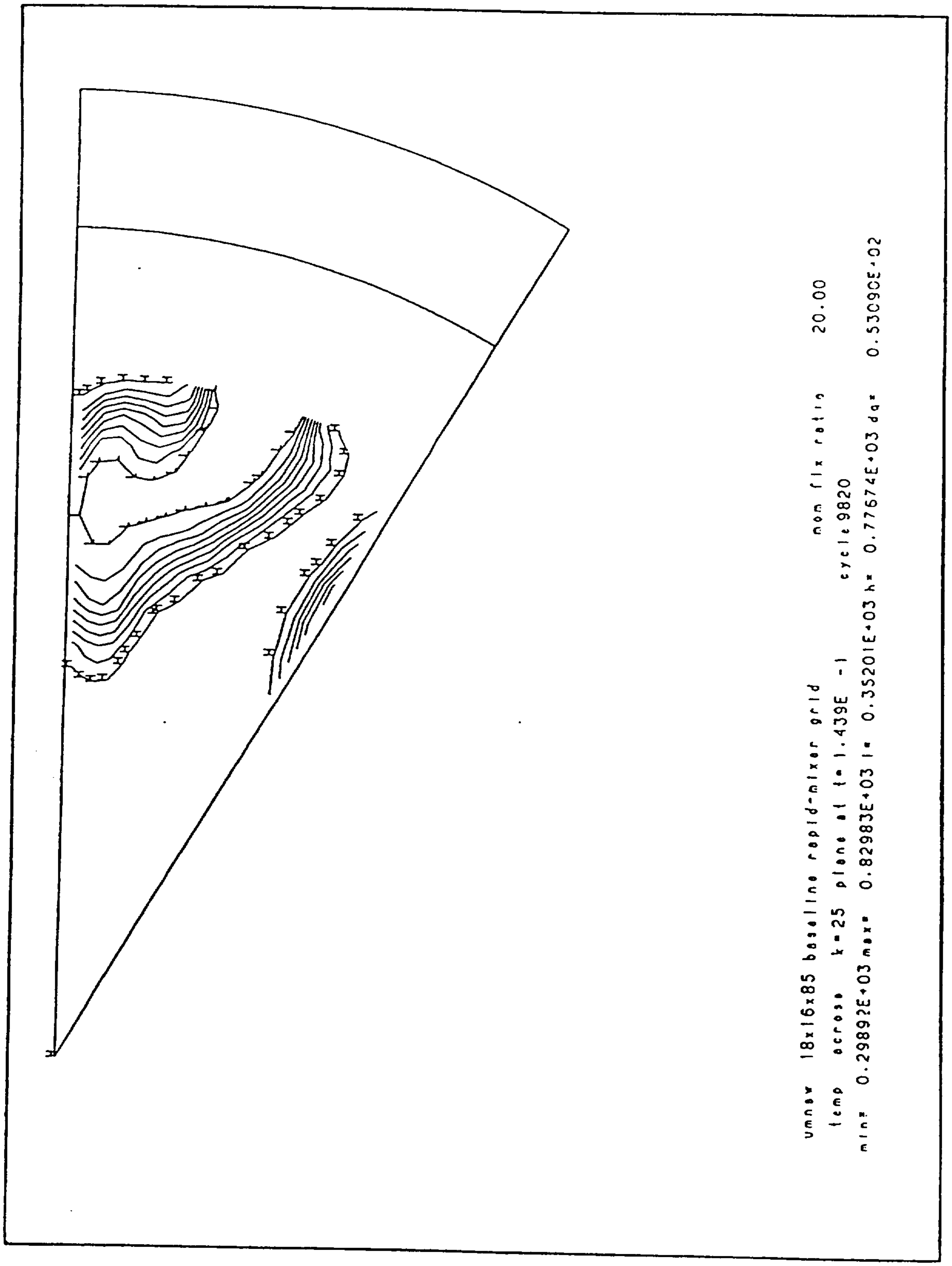
umnew 18x16x85 baseline rapid-mixer grid non flx ratio 20.00
temp across k=25 plane at t= 1.439E -1 cycle=9820
min= 0.29892E+03 max= 0.82983E+03 l= 0.35201E+03 h= 0.77674E+03 dq= 0.53090E+02
H
L

Figure 2-8

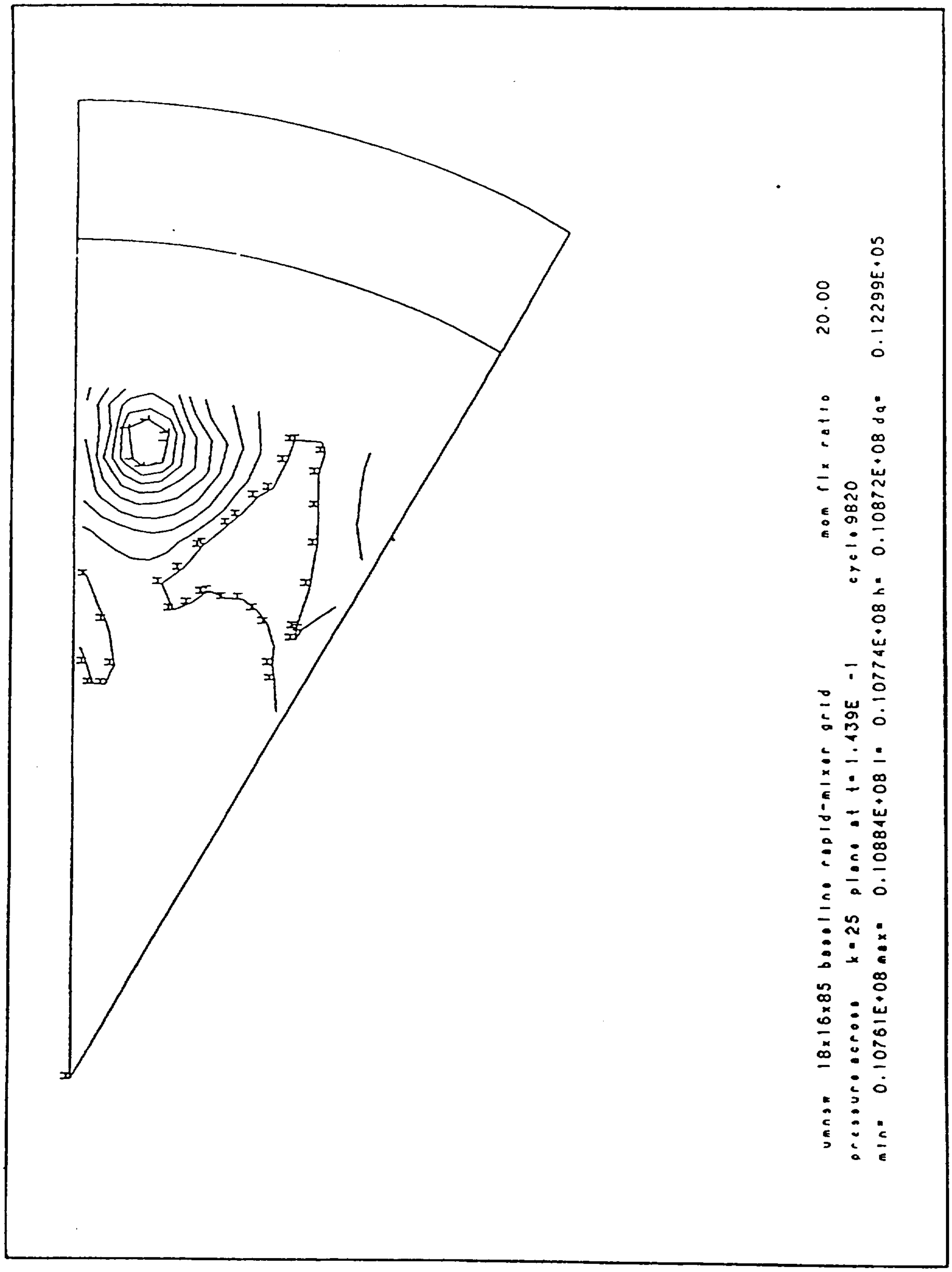
umnsw 18x16x85 baseline rapid-mixer grid mom flx ratio 20.00
pressure across k=25 plane at t=1.439E -1 cycle=9820
min= 0.10761E+08 max= 0.10884E+08 l= 0.10774E+08 h= 0.10872E+08 dq= 0.12299E+05

Figure 2-9

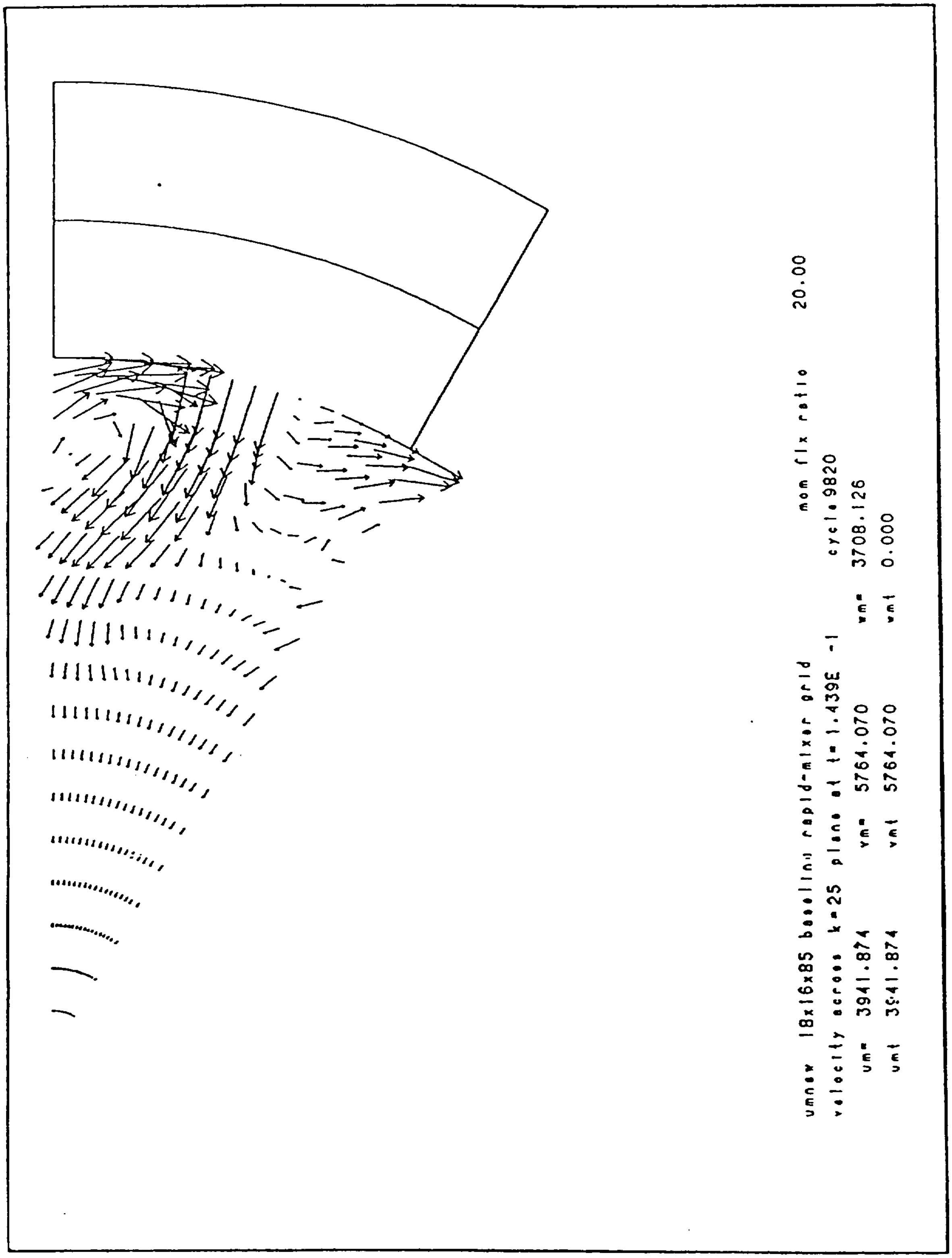
umnew 18x16x85 baseline rapid-mixer grid
mom flx ratio 20.00
velocity across k=25 plane at t= 1.439E -1
cycle 9820
um= 3941.874
vm= 5764.070
wm= 3708.126
umt 3941.874
vmt 5764.070
wmt 0.000

Figure 2-10

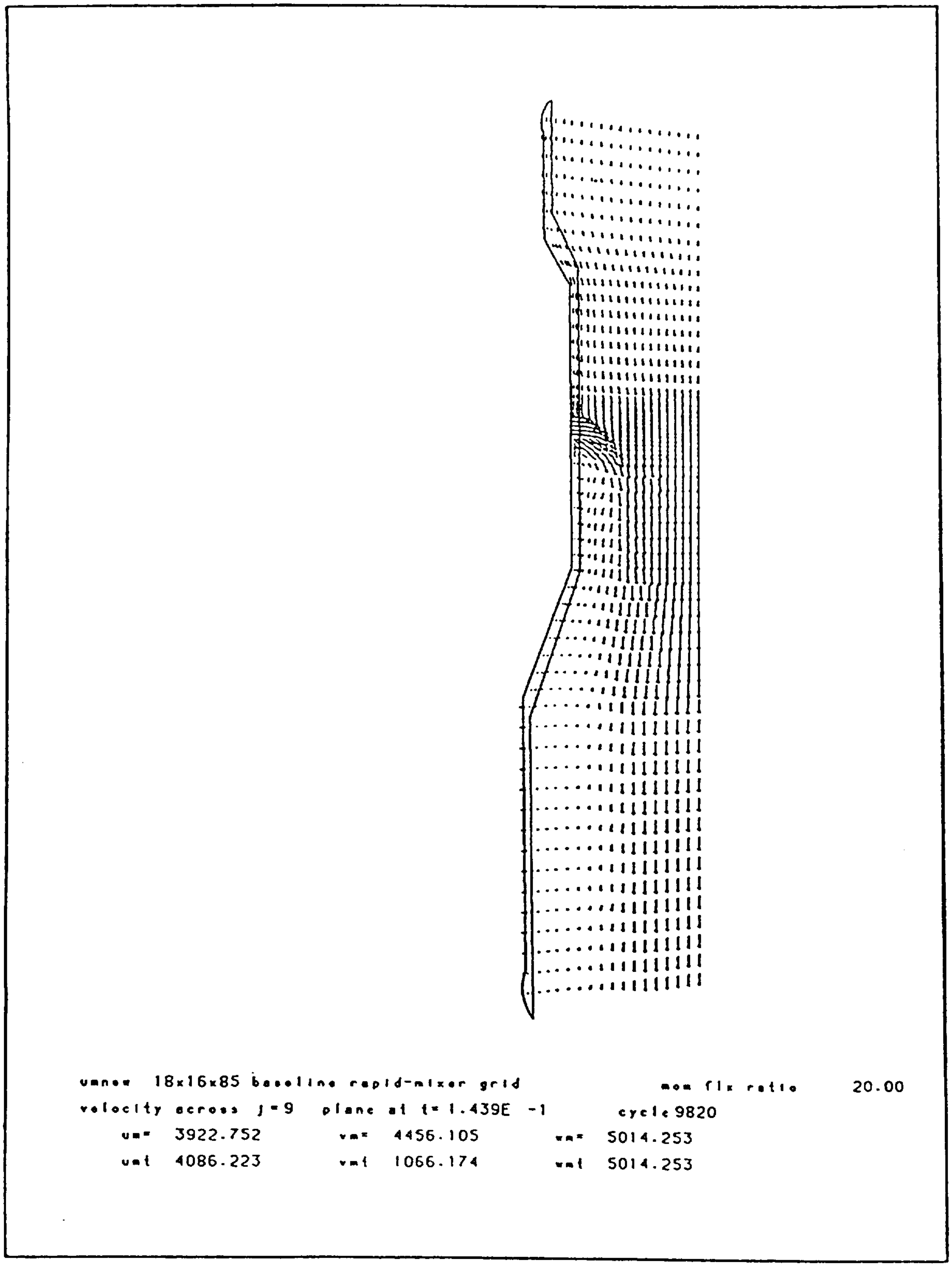
umnew 18x16x85 baseline rapid-mixer grid
mom flx ratio 20.00
velocity across j=9 plane at t=1.439E -1
cycle 9820
um= 3922.752
vm= 4456.105
wm= 5014.253
umt 4086.223
vmt 1066.174
wmt 5014.253

Figure 2-11

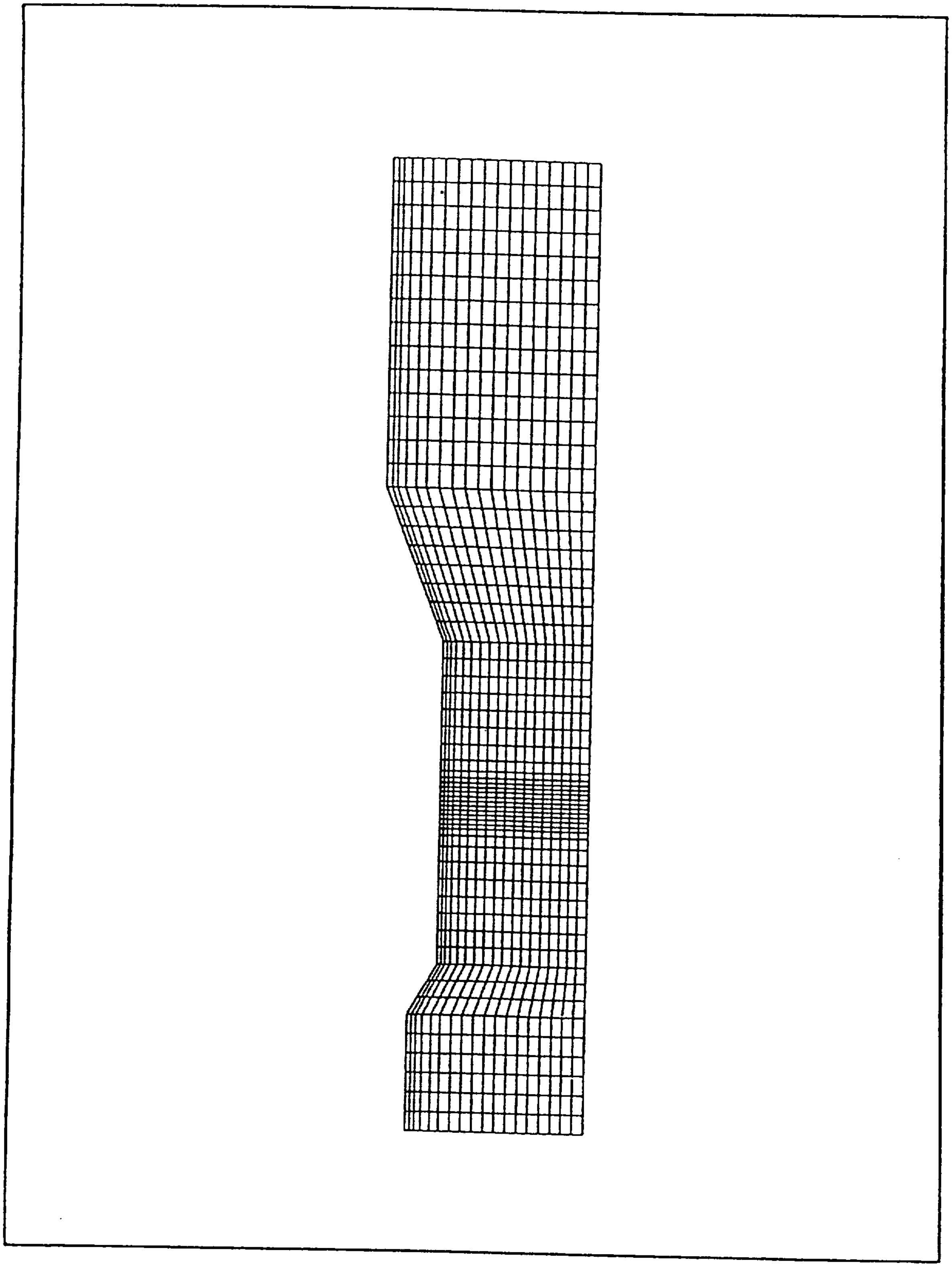

Figure 2-12

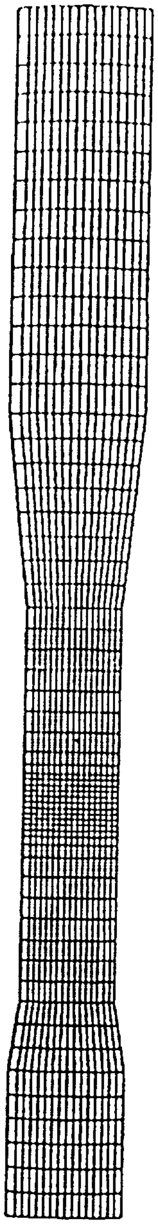

Figure 2-13

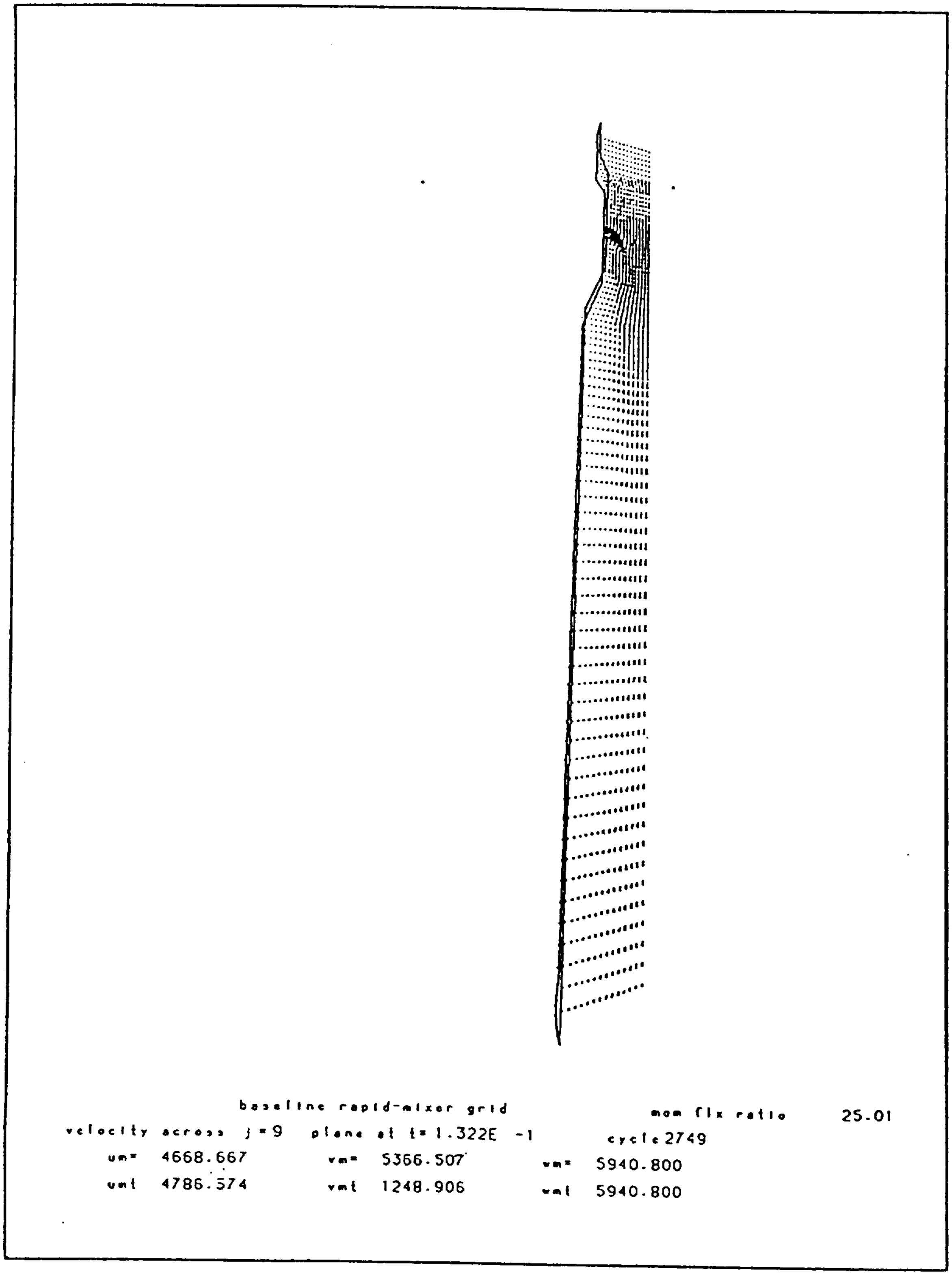
baseline rapid-mixer grid
mom flx ratio 25.01
velocity across j=9 plane at t=1.322E -1
cycle 2749
um= 4668.667
vm= 5366.507
wm= 5940.800
umt 4786.574
vmt 1248.906
wmt 5940.800

Figure 2-14

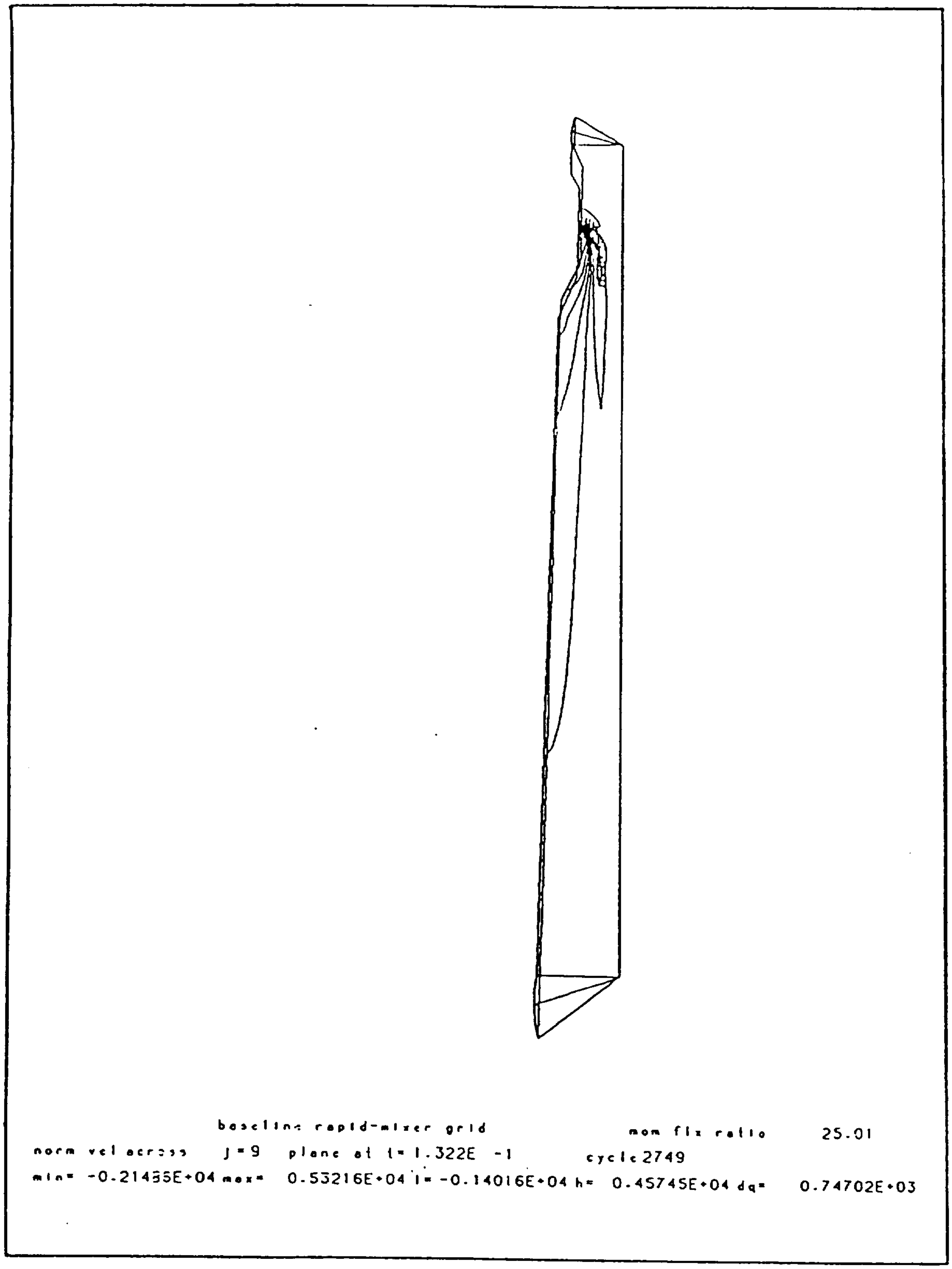
baseline rapid-mixer grid
mom flx ratio 25.01
norm vel across j = 9 plane at i = 1.322E -1
cycle 2749
min= -0.21435E+04 max= 0.53216E+04 l= -0.14016E+04 h= 0.45745E+04 dq= 0.74702E+03

Figure 2-15

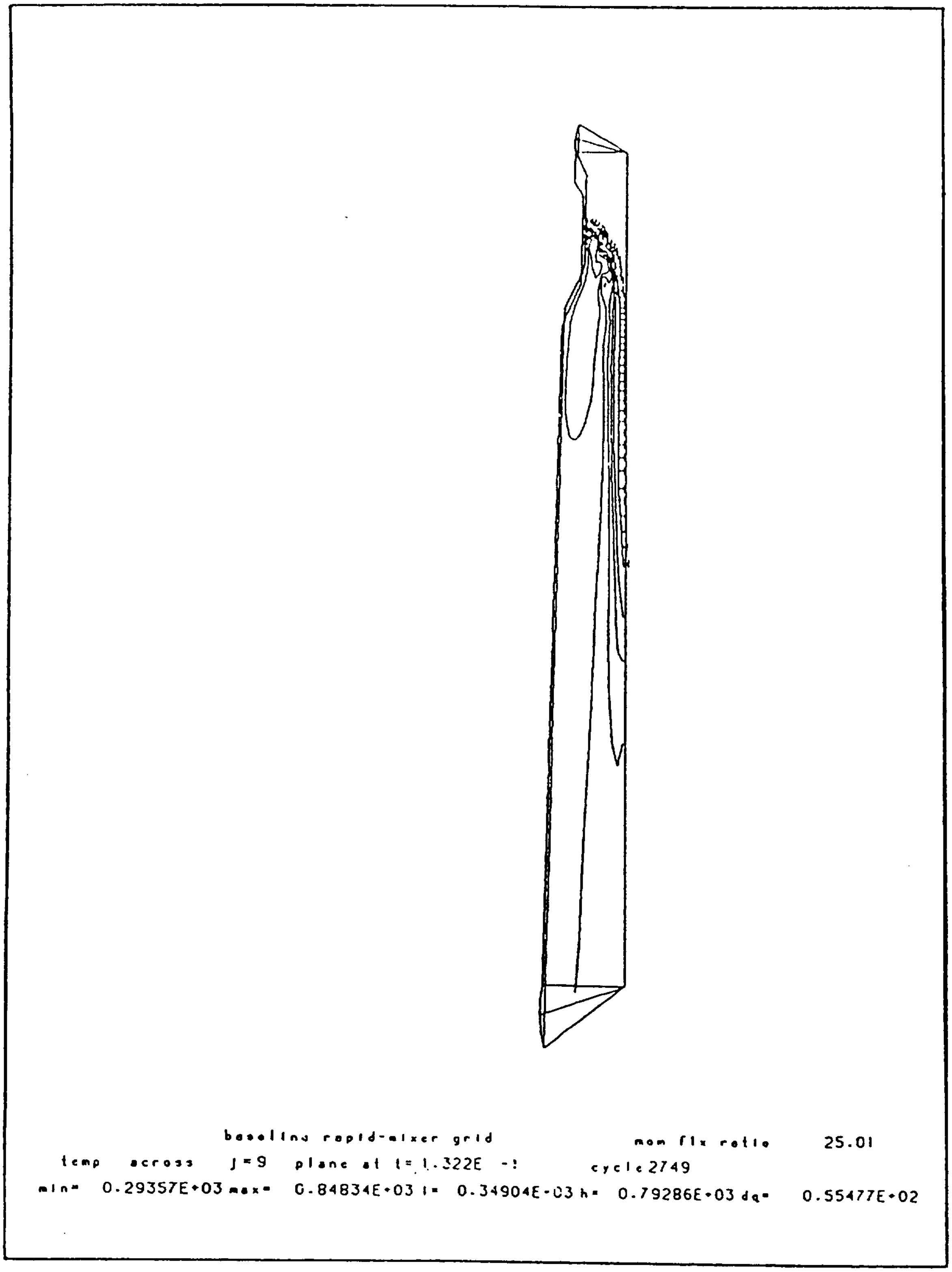
baseline rapid-mixer grid
mom flx ratio 25.01
temp across j=9 plane at t=1.322E -1
cycle 2749
min= 0.29357E+03 max= 0.84834E+03 i= 0.34904E-03 h= 0.79286E+03 dq= 0.55477E+02

Figure 2-16

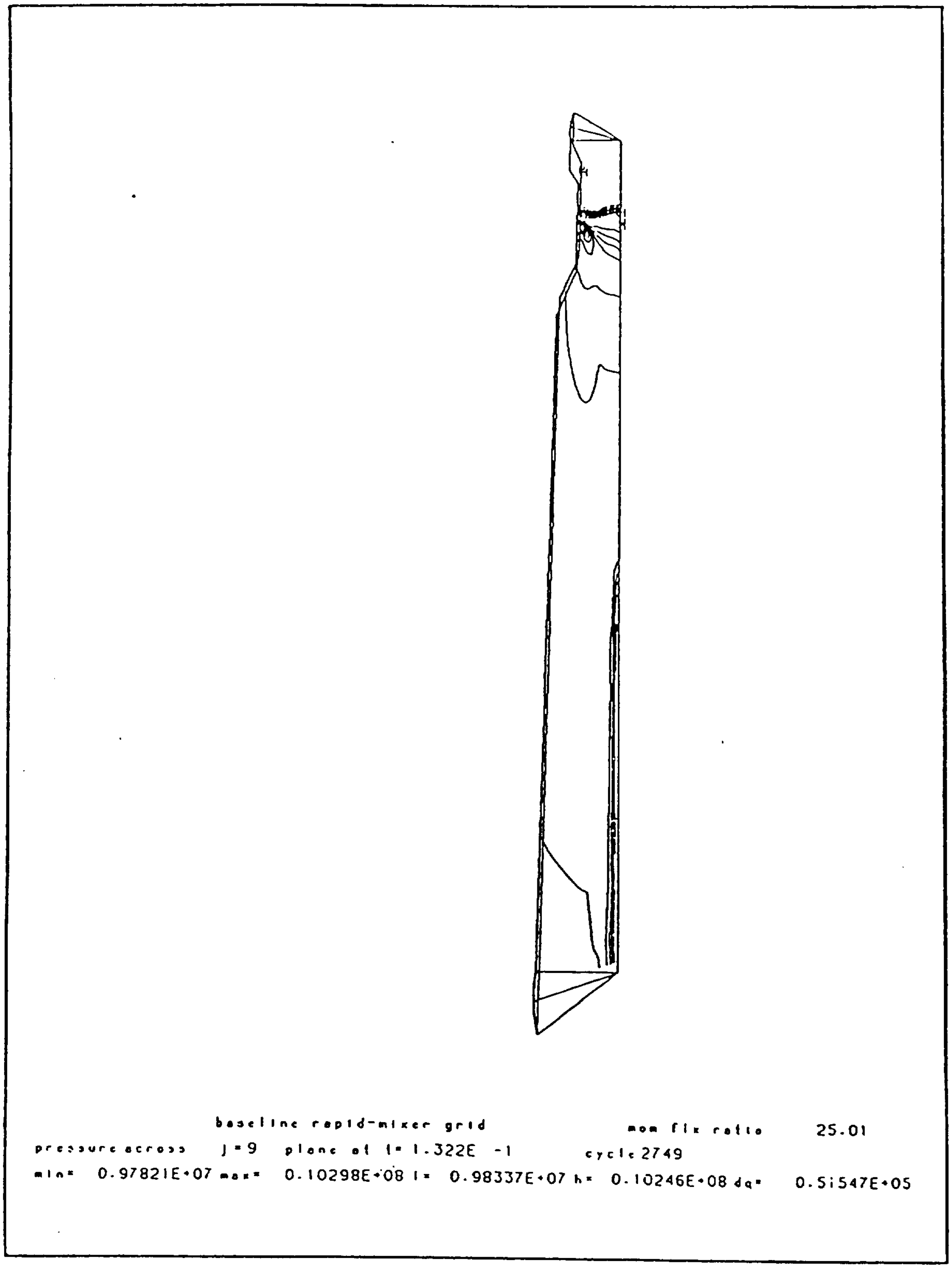
baseline rapid-mixer grid
mom flx ratio 25.01
pressure across j=9 plane at i= 1.322E -1
cycle 2749
min= 0.97821E+07 max= 0.10298E+08 l= 0.98337E+07 h= 0.10246E+08 dq= 0.51547E+05

Figure 2-17

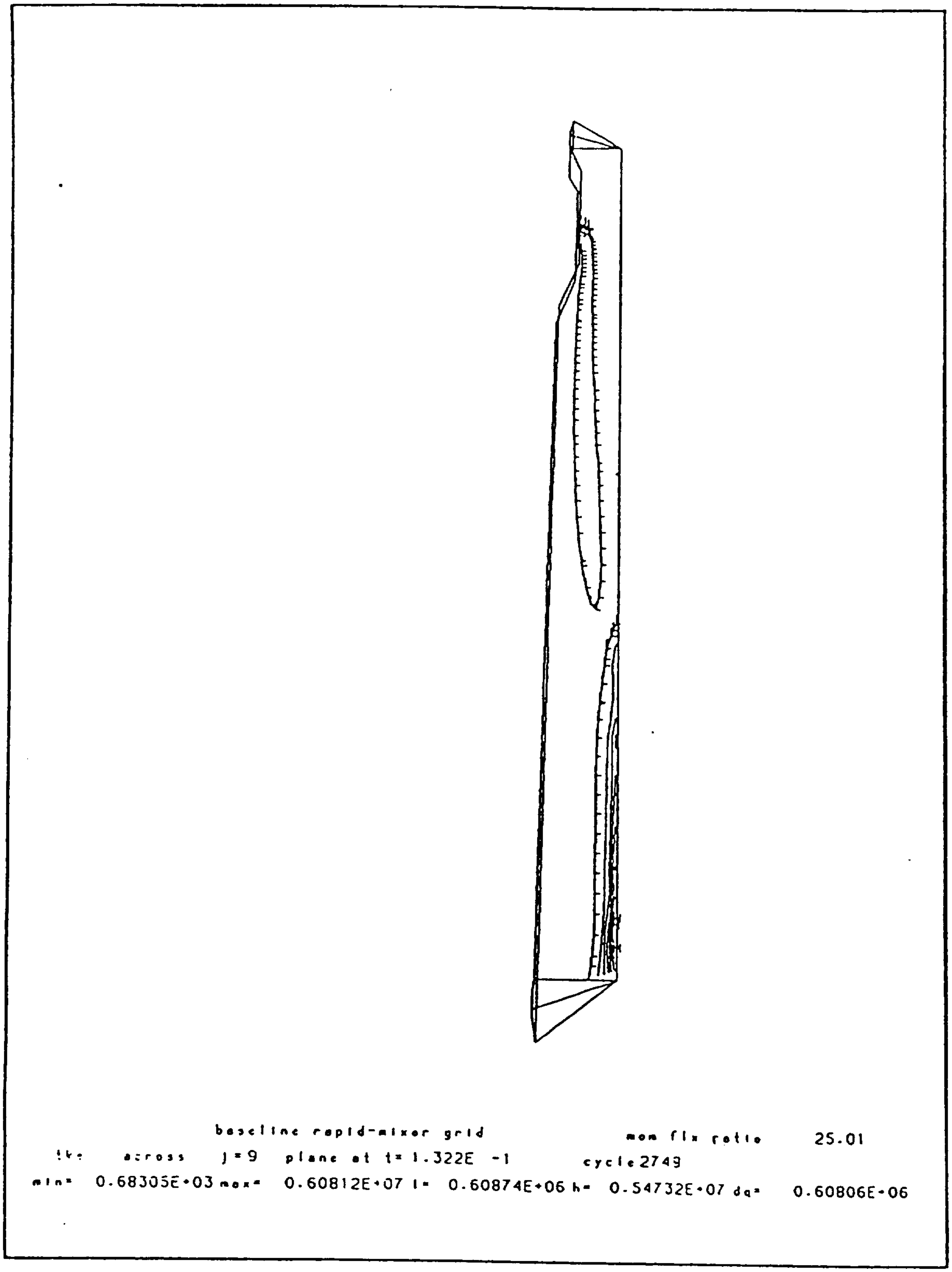
baseline rapid-mixer grid
mom flx ratio 25.01
tke across j=9 plane at t= 1.322E -1
cycle 2749
min= 0.68305E+03 max= 0.60812E+07 l= 0.60874E+06 h= 0.54732E+07 dq= 0.60806E+06

Figure 2-18

CHAPTER III

PROCEDURE

III.1. Initialization of Run Conditions

After comparing the characteristics and cpu requirements of the partially blocked mesh with the fully open mesh the latter was chosen for results generation. This mesh would take typically 3000 time steps from time = 0.0 sec to reach steady state. This corresponds to 0.1-0.14 sec to reach the steady state. Table 3.1 lists several important parameters set in the input file for the mixer runs.

Table 3.1

Variable	Setting	Description
LWALL	1	selects law-of-the-wall boundary conditions
JSECTR	1	sector mesh desired
IREZ	0	eulerian grid
CYL	1.0	cylindrical mesh
PGSSW	1.0	pressure gradient scaling method utilized
DTI	1.04e-06	initial time step (s)
THSECT	30.0	sector mesh of 30 degrees
EPSY	1.0e-03	convergence mass diffusion
EPSV	1.0e-03	convergence momentum diff.
EPSP	1.0e-04	convergence of pressure
EPST	1.0e-03	convergence of heat diff.
EPSK	1.0e-03	convergence for tke diff.
EPSE	1.0e-03	convergence of epsi diff.
TCYLWL	811.0	wall temp = 811° kelvin
PARDON	0	quasi second order upwind differencing
ANC4	0.0	no node coupling
ADIA	0.0	isothermal walls
TKEI	1600.0	2.5% of inlet velocity
SGSL	0.0	use k- ε turb. model
Distamb	0.0	specified outlet pressure directly at nzp plane

III.2. *Inflow/Outflow Boundaries*

The bottom boundary is entirely open for inflow, while the right boundary allows inflow only along the slot and is a solid curved surface elsewhere. Air at 1000° F enters the computing mesh across the bottom boundary, while air at 77° F enters through the slanted slot. Pressure and temperature of the entering air are defined by specifying their stagnation state and using the following insentropic relations:

$$SPDIN(M) = SPDINO(M)\left(\frac{P}{PO}\right)^{1/gamma}$$

SPDINO(M)	- the stagnation density for species m set in the input file.
P	- pressure of the respective cell into which the species is being fluxed.
gamma	- ratio of the specific heats determined at the respective inflow boundary conditions.
PO	- stagnation pressure at the respective inflow boundary set in the input file.

Along the bottom boundary turbulent length scale is set to 0.065, and the tke itself is based upon w′ (fluctuating velocity) specified as 2.4% of the square of the mean flow velocity. Stagnation pressure and temperature are set to 10 atm and 1000° F, respectively.

Along the right inflow boundary the stagnation pressure and temperature are set to 10 atm and 77° F, respectively. Three percent of the perpendicular distance across the slot opening (0.2213 in) is used to calculate both tke and length scale entering with the jet.

A static pressure is applied along the outlet boundary by setting DISTAMB to 0.0 in the input file. DISTAMB is a quantity that allows the applied pressure boundary to be moved away from the physical outflow boundary, which in some cases reduces time to reach steady state. The pressure applied is 10 atm. Acoustic wave reflection was found not to be a problem. It was seen that giving DISTAMB a positive value increased the probability of flow reversal at the outlet boundary.

III.3. Initial Problem Conditions

Species densities of the individual components of air at 10 atm and 1000° F were calculated and set in the input file to initialize the respective densities through out the mesh at time = 0.0 sec. The initial velocity profile was set based upon a relation with the square of the radius at a given axial position in the geometry. This approach reduced required time to reach steady state. The reference velocity of Win and radius of the rich zone are used in the following relation:

$$W(i4) = Win*\left(\frac{R(k)}{R(1)}\right)^2$$

W(i4) - value of axial velocity at time=0.0 sec. set at every vertex during initial setup.

Win - the axial velocity applied to the bottom inflow boundary at k=1.

R(k) - radius at a given k-plane.

This type of initial velocity distribution provided good results in comparison with runs using an initial velocity of 0.0 through out the mesh. Another alternative is ramping the axial inflow velocity (win) linearly, but this required a longer transient than runs using the described initial distribution.

III.4. Jet Development

The jet was ramped from an initial velocity of 0.0 to the desired value of the variable URTIN in the input file. A major advantage of setting the jet velocity in the input file is that subsequent higher values could be set and the run resumed from a previous J^* steady state binary file via KIVA-II's restart capability. This decreased transient time for the new higher J^* steady state by roughly a third from the transient time required for a run starting at time = 0.0 seconds.

The jet is ramped very slowly early in the transient to minimize pressure waves between the right boundary and the centerline. Between cycle 1 and 120 the jet is increased by 0.01 cm/s per 1e-05 sec. From cycle 120 to 800 the ramp is increased to 1.0 cm/s per 1e-05 sec. Ramping the jet based upon time and not cycle early in the transient is advantageous because the time step (dt) fluctuates and drops into the low (1.0e-06 sec...1.2e-06 sec) range at some points. Beyond cycle 800 the jet ramp is raised to 5 cm/s per cycle and up to 10 cm/s per cycle after cycle 1000.

III.5. Steady State Determination

Steady state was determined from visual inspection of history plots produced after a restart. This file contains 9 different histories (3 pressure, 3 temperature, 3 velocity) from three different locations in the mesh. Appendix A lists the specific history locations for all calculations including the partially blocked mesh described in chapter 2. It was observed that steady state would first be established first at the k = 1 plane and last at the outlet. Since the important region of the grid is in the vicinity of the jet, histories indicating steady state at the end of the region of interest (k=60) were used to determine acceptable development of the jet and termination of the run. When one of the history locations was changed to the mesh outlet (k=nz) for the 30 degree slanted slot runs, it was clearly evident that temperature was not steady at cycle 3000 and required several thousand more cycles to approach steady state. Allowing the entire mesh to reach steady state was not realistic with every run due to excessive cpu time requirements, thus only the region of interest was considered for steady state. Appendix B contains history plots at the end of the region of interest used to verify the flow transient had reached steady state for the result cases presented in chapters 4 and 5.

CHAPTER IV

45° SLANTED SLOT RAPID MIXER RESULTS

IV.1. Initial Setup

The baseline mixer utilizes a 45 deg slanted slot orifice to inject 77° F secondary air into the mixing section of the rapid mixer. The slot has a 4 to 1 aspect ratio. The results presented in this chapter were produced with a 20x16x110 open ended mesh utilizing the tke averaging technique discussed in chapter 2. Modifications to the outflow boundary conditions of the KIVA-II code set any components of negative face or vertex velocities to zero. This is only necessary during the transient and does not effect the steady state results, since there is no tendency for the flow field to reverse after the jet has been ramped to is full inflow speed. The mesh is shown in full length in figure (4-1). Figure (4-2) shows the azimuthal cell spacing in the j direction. Figures (4-3) and (4-4) are enlargements of the region of interest (k=1 to k=60). This mesh models 44.2 in of the lean zone which has an actual length of 6 ft.

IV.2. Bulk Swirl Profile

An important characteristic of the flowfield, which enhances thermal mixing, is the swirl profile originating at the 45 degree slanted slot which persists well into the lean zone. Figures (4-5) to (4-11) are k-slice velocity field plots with $J^*=5$, that show the swirling velocity profile along the length of the mixer geometry. Figures

(4-12) to (4-18) are the temperature contour plots at the same axial locations.

Air injected from the slanted slot remains along the outer perimeter surrounding a high temperature inner core. At k=42 the low temperature contour line is distorted from effects of jet penetration radially inwards into the mixer. This is a full 5.27 cm from the downstream edge of the slanted slot. At k=55, which is 17.57 cm from the downstream edge of the slanted slot, the low temperature contour is smoothed from turbulent mixing between the high and low temperature air masses. At k=65 and beyond, the temperature contours assume a circular profile. At higher J^* values the high temperature contour line will intersect the centerline.

The jet interacts with the axial mainstream inducing a CCW spin in the region near the wall. An opposite CW spin develops between this outer CCW swirling profile and the centerline. Figure (4-6) in the 21° expansion region of the grid reveals that as the axial velocity decreases in the expansion the magnitude of swirl velocity increases. A well developed swirl profile is seen at k=55, but at k=65 the swirling profile is beginning to vanish. At k=75,85 and 95 the azimuthal component of velocity has decreased greatly with the entire profile assuming a CW swirl of a small magnitude. Figures (4-19) and (4-42) of normal velocity contours reveal that the defined swirl profile extends only slightly beyond the area of interest (k=60).

IV.3. Higher Momentum Flux Ratios

As jet velocity increases, the jet penetrates further into the mixing region. The vortex directly to the right of the jet shown in figures (4-21) through (4-23) elongates considerably. Temperature and turbulent kinetic energy contours shown in figures (4-24) through (4-29) reveal increased radial penetration of the jet.

At low momentum flux ratios a stagnant low pressure region exists just downstream of the jet near the wall seen in figure (4-33). As J^* increases the low pressure point moves away from the wall following the penetration of the jet (figure (4-34)). In Fig. (4-35) the low pressure region has shifted to the center of the mixer geometry, which indicates the jet is in effect pinching the axial flow. The corresponding temperature contours are shown in figures (4-36) through (4-38). The high temperature contour line moves almost directly radially inward intersecting the centerline in Fig. (4-38). Figures (4-39) through (4-41) reveal high turbulence near the wall at the base of the jet as expected in this region of high shear.

Increased momentum flux ratio increases the extent of the swirling flow as shown in figures (4-45) through (4-50), which correspond to two axial locations.

IV.4. Numerical Accuracy

The mesh used for the results presented in the previous section consists of 39,627 cells. This allows for adequate spatial resolution to resolve the high shear region in the vicinity of the jet. A run with $J^*=25$ was conducted with a coarser mesh to verify grid independence of the generated results. The coarser cell mesh used 16,660 cells (13x16x69) and is shown in figure (4-63). Figures (4-51) to (4-56) generated with the coarse mesh compare well with figures (4-57) to (4-62). Temperature contour values generated with the coarser mesh agree within 4%. Comparing the velocity plots a 4% difference in u and v velocity components, and an 11% difference in w velocity components is noted. The pressure contour plots show agreement within 8%. All quantities compare well with the exception of the turbulent kinetic energy, which is 40-60% lower in the coarser mesh. This is most likely a result of the tke averaging employed with both runs. The tke is averaged from $i=1$ to $i=4$ along the centerline in both runs. The coarse grid having 7 fewer cells in the radial region has a greater portion of the same geometry averaged. At $J^*=120$ the temperature contour in Fig. (4-26) does not indicate any coalescence of the jets. This is a characteristic of quasi-second-order-upwind differencing. When using partial and full donor cell differencing coalescence is observed at much lower momentum flux ratios.

IV.5. Lean Zone Length Effects

A $J^*=60$ run was conducted with a mesh having 20 less k-planes and an axial length decrease of 27.94 cm from the 20x16x110 grid. Results from the run are presented with the equivalent plots from the 44.2 in lean zone grid in figures (4-64) to (4-71). Visual qualitative comparison of plots from the region of interest of both grids reveals very little deviation. Variation of flowfield parameters shown in these figures is tabulated in table 4.1.

TABLE 4.1

Plot	**Variation**		
	UM	VM	WM
Velocity	0.53%	3.59%	1.21%
	L-Contour	H-Contour	
Normal Velocity	2.84%	3.59%	
Pressure	0.87%	0.078%	
Temperature	0.05%	0.27%	

IV.6. Bulk Temperature Profile

Bulk temperature is one characteristic that is of interest when considering nonreactive flow mixing performance of the rapid mixer geometry. Bulk temperature is defined by the following equation:

$$\text{Bulk Temperature} = \frac{\int \rho c_v \vec{u} T dA}{\int \rho c_v \vec{u} dA}$$

ρ - fluid density

$\vec{u}$ - fluid velocity

T - temperature

A - area

c_v - specific heat at constant volume

Bulk temperature is the temperature to which a non-isothermal fluid mixture would reach if allowed to come to an equilibrium state. Bulk temperature profiles for the 20x16x110 grid at J=5,25,40,60 and 120 are presented in figure (4-72). The bulk temperature is plotted verses mixer length within the area of interest. The runs were terminated prior to the entire lean zone reaching steady state due to high cpu time requirements.

Bulk temperature was calculated on each k-plane of the sector mesh once the area of interest reached steady state. The bulk temperature plummets at the point of jet injection. The minimum bulk temperature is lower with increasing momentum flux ratio.

IV.7. Swirl Number Profile

Beer and Chigier [12] proposed the non-dimensional parameter Swirl Number. This parameter characterizes the amount of rotation in a given axial flow. Swirl number is defined by the following equations:

$$G_m = \int 2\pi r \vec{W} r \rho \vec{U} dr$$

$$G_t = \int 2\pi r \rho \vec{U}^2 dr + \int 2\pi r p dr$$

$\vec{U}$ - axial velocity

$\vec{W}$ - tangetial velocity

p - static pressure

r - radius

ρ - fluid density

$$\text{Swirl number} = G_m/G_t$$

This quantity like bulk temperature was calculated on each k-plane once the area of interest had reached steady state.

Lefebvre [1] states most fixed vane swirlers of practical interest operate in the range of (SN>0.6). The fixed vane swirler physically surrounds the fuel injector and its purpose is to induce rotation of the secondary air which creates a recirculation region within the primary zone.

The swirl number profiles for all five momentum flux ratios are plotted verses axial location in figure (4-73). Except for a spike at the point of jet injection the swirl number remains between 3.0e-04 and -5.0e-04, which is essentially zero compared to 0.6 in conventional gas turbines utilizing fixed vane swirlers. The swirl profile indicates the conservation of angular momentum within the flowfield. Angular momentum of the outer CCW rotating field is virtually offset by the inner CW rotating core.

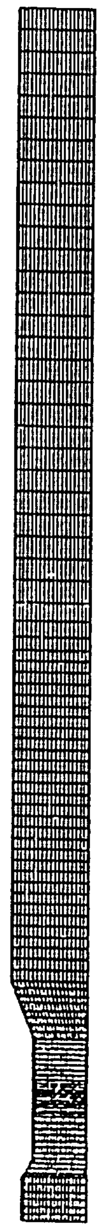

Figure 4-1

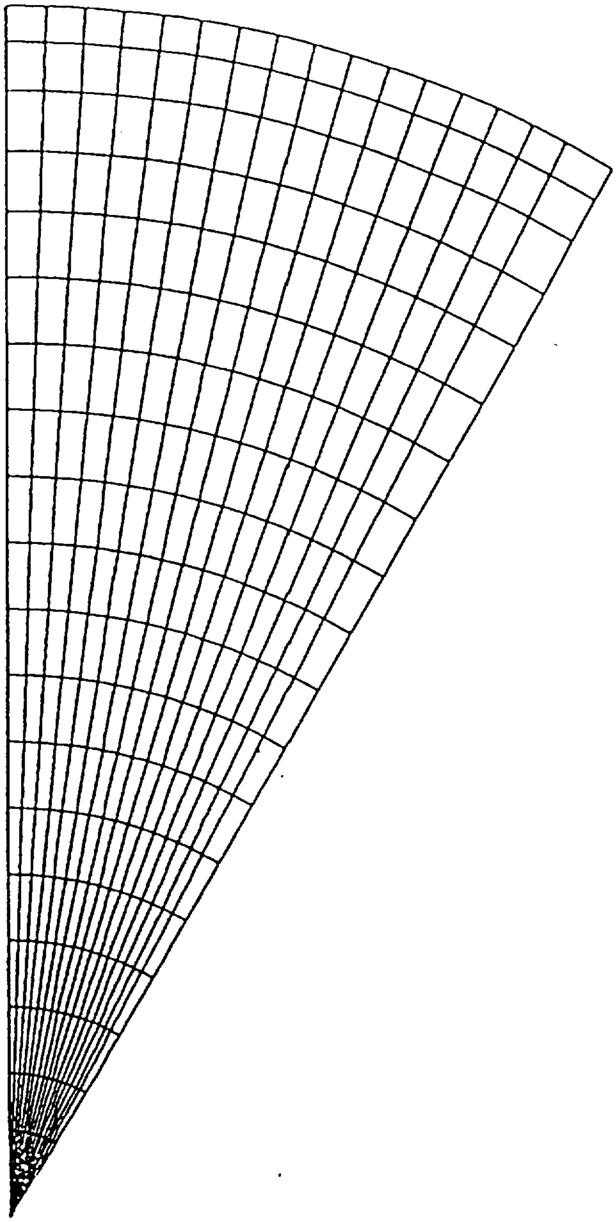

Figure 4-2

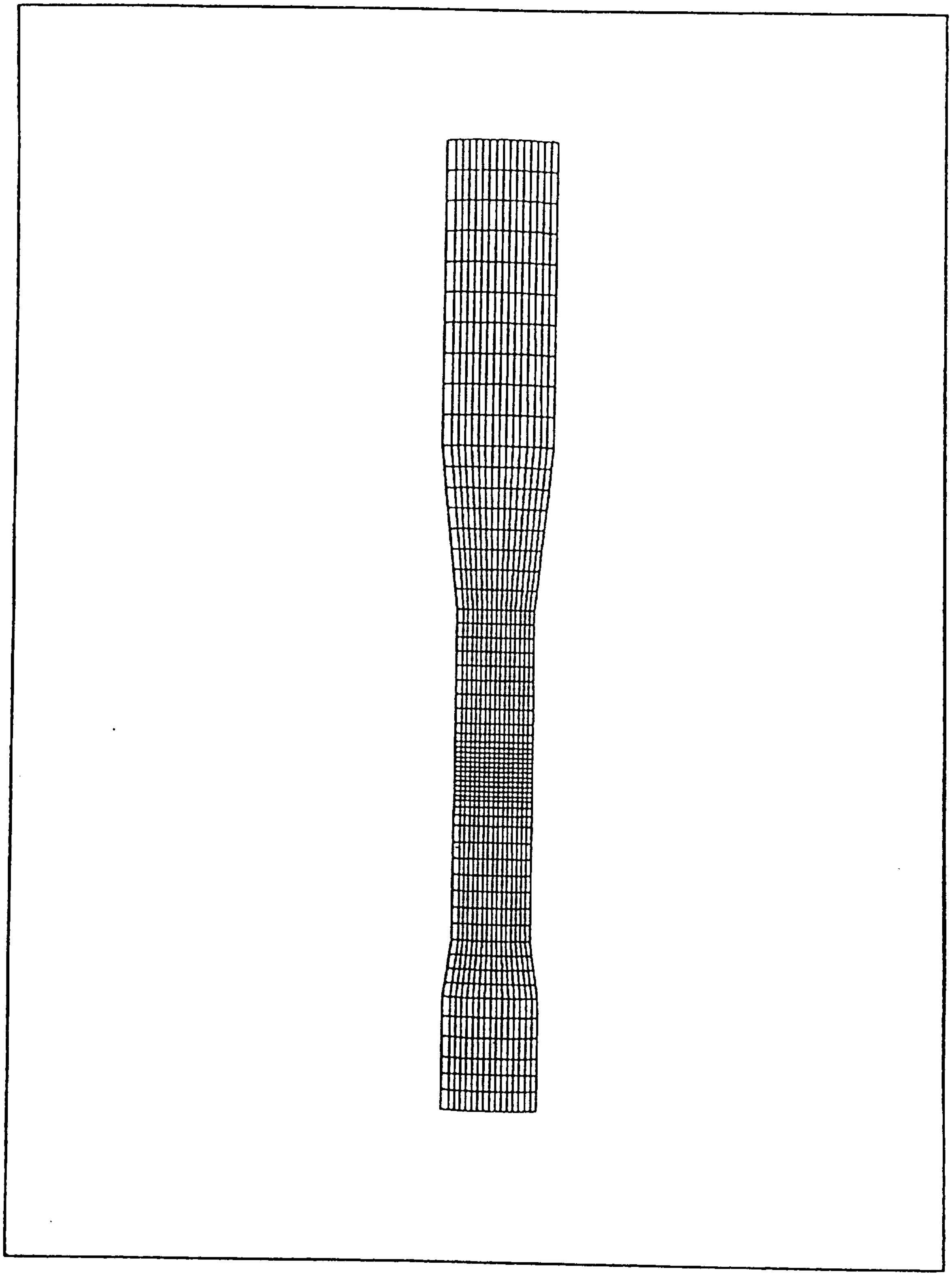

Figure 4-3

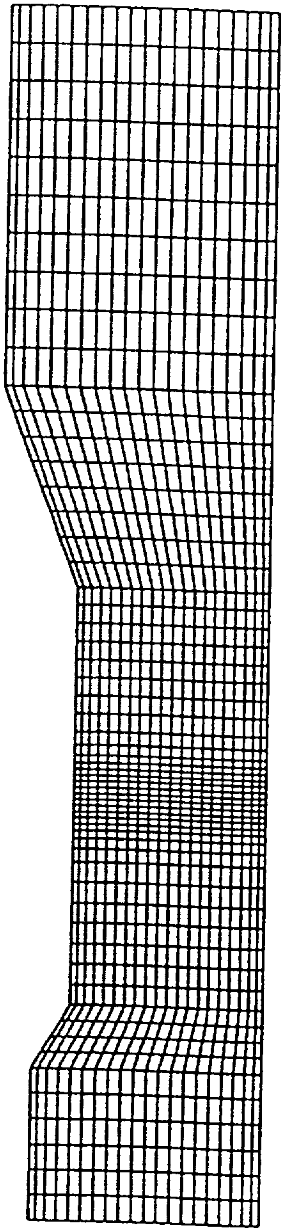

Figure 4-4

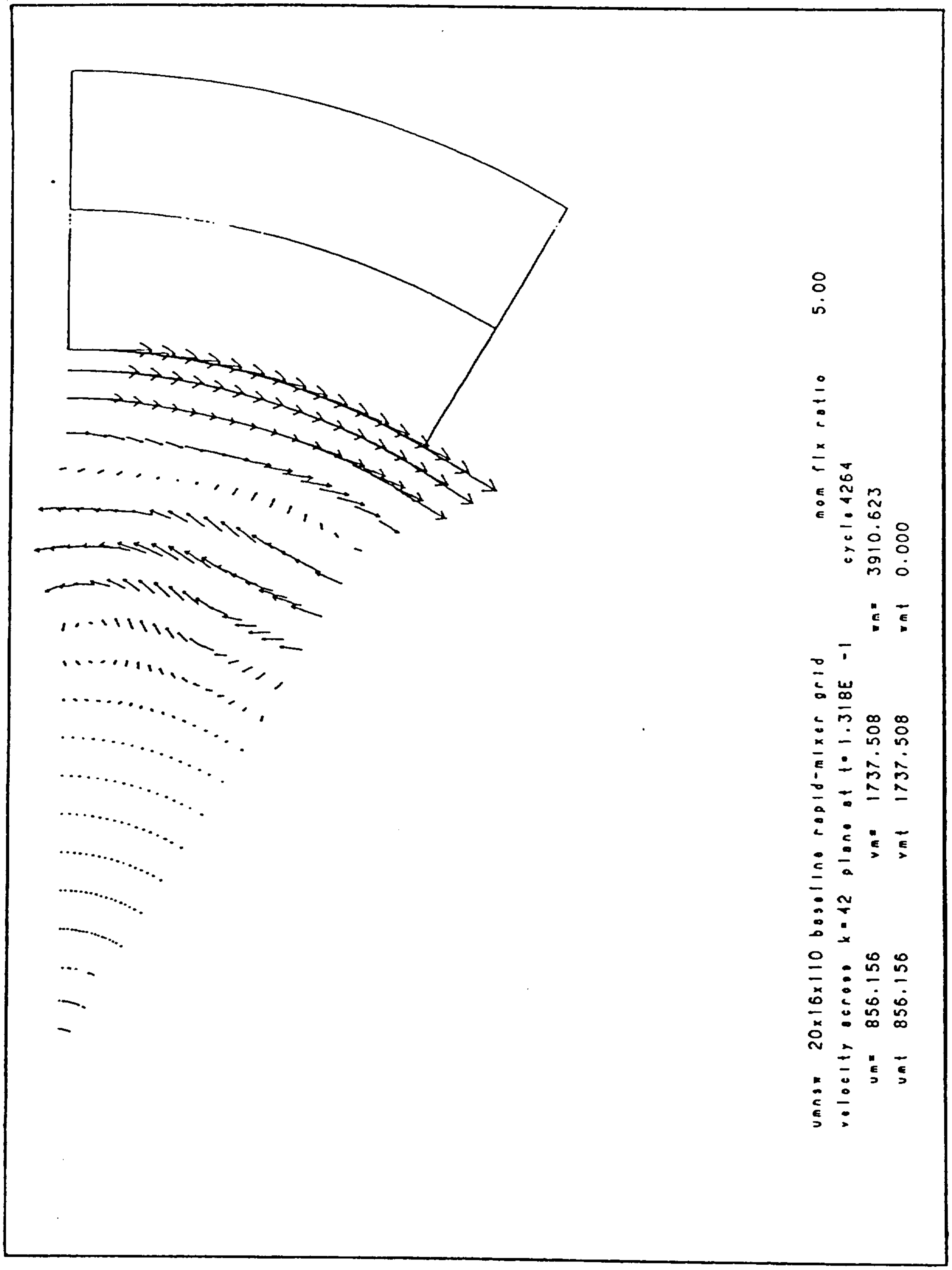
umnsw 20x16x110 baseline rapid-mixer grid
mom flx ratio 5.00
velocity across k=42 plane at t= 1.318E -1
cycle=4264
um= 856.156
vm= 1737.508
wm= 3910.623
umt 856.156
vmt 1737.508
wmt 0.000

Figure 4-5

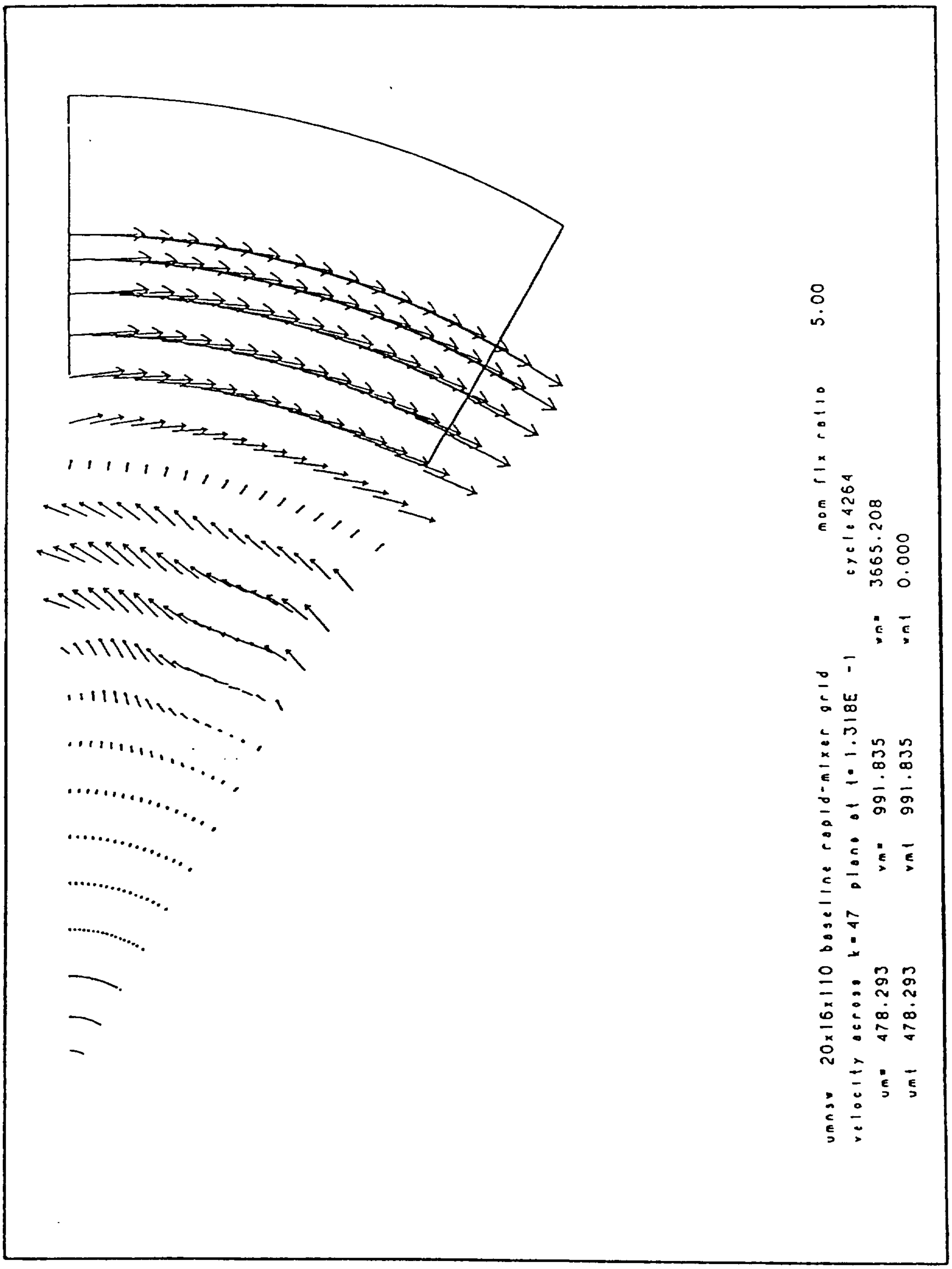
umnsw 20x16x110 baseline rapid-mixer grid
mom flx ratio 5.00
velocity across k=47 plane at t=1.318E -1
cycle=4264
um= 478.293
vm= 991.835
wm= 3665.208
uml 478.293
vml 991.835
wml 0.000

Figure 4-6

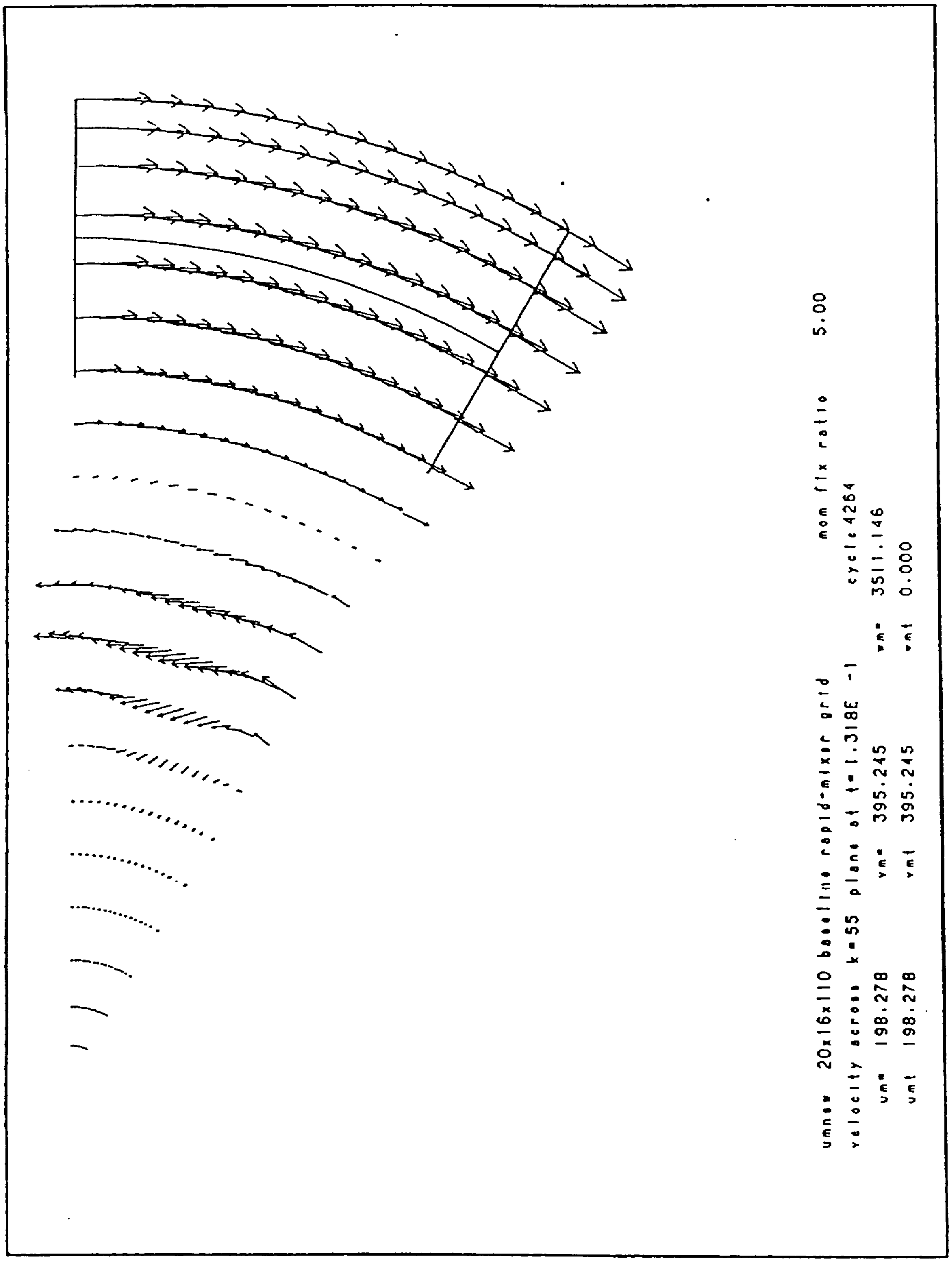
umnew 20x16x110 baseline rapid-mixer grid
mom flx ratio 5.00
velocity across k=55 plane at t=1.318E -1
cycle 4264
um= 198.278
vm= 395.245
wm= 3511.146
umt 198.278
vmt 395.245
wmt 0.000

Figure 4-7

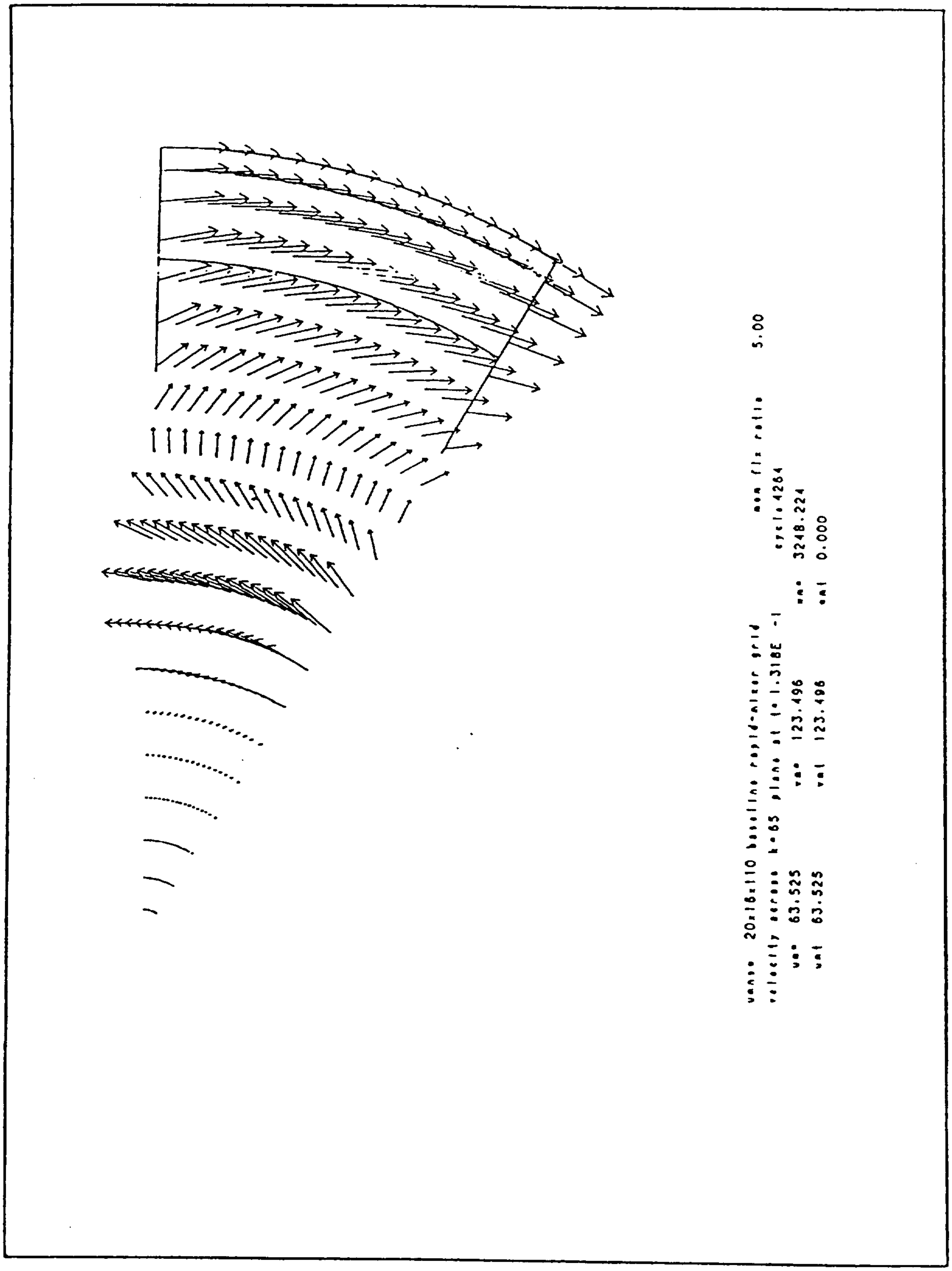
vanse 20x18x110 baseline rapid-mixer grid
mom flx ratio 5.00
velocity across k=65 plane at t= 1.318E -1
cycle 4264
um= 63.525
vm= 123.496
wm= 3248.224
uml 63.525
vml 123.496
wml 0.000

Figure 4-8

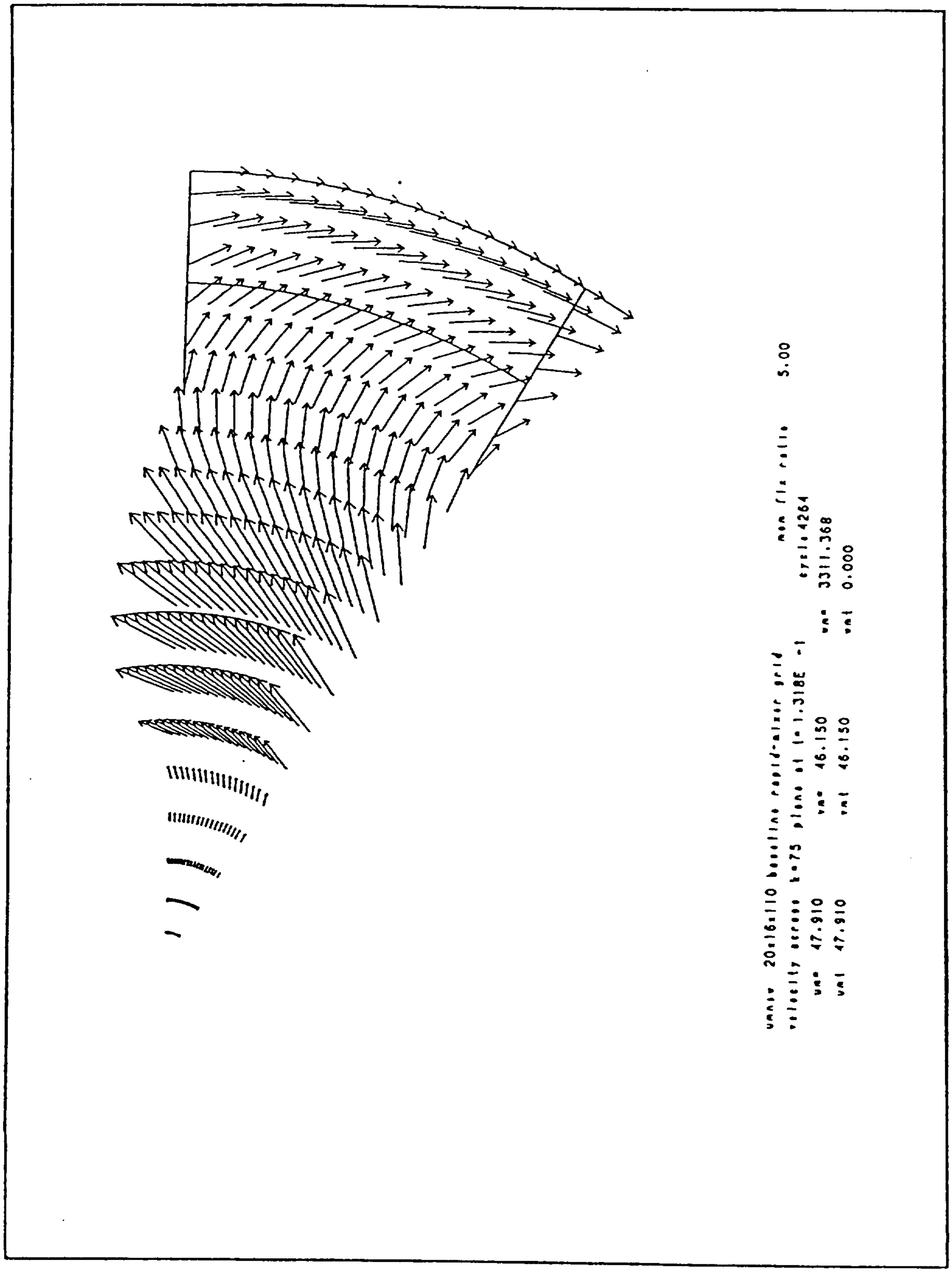
vmnsv 20x16x110 baseline rapid-mixer grid
mom flx ratio 5.00
velocity across k=75 plane at l= 1.318E -1
cycle 4264
um= 47.910
vm= 46.150
wm= 3311.368
uml 47.910
vml 46.150
wml 0.000

Figure 4-9

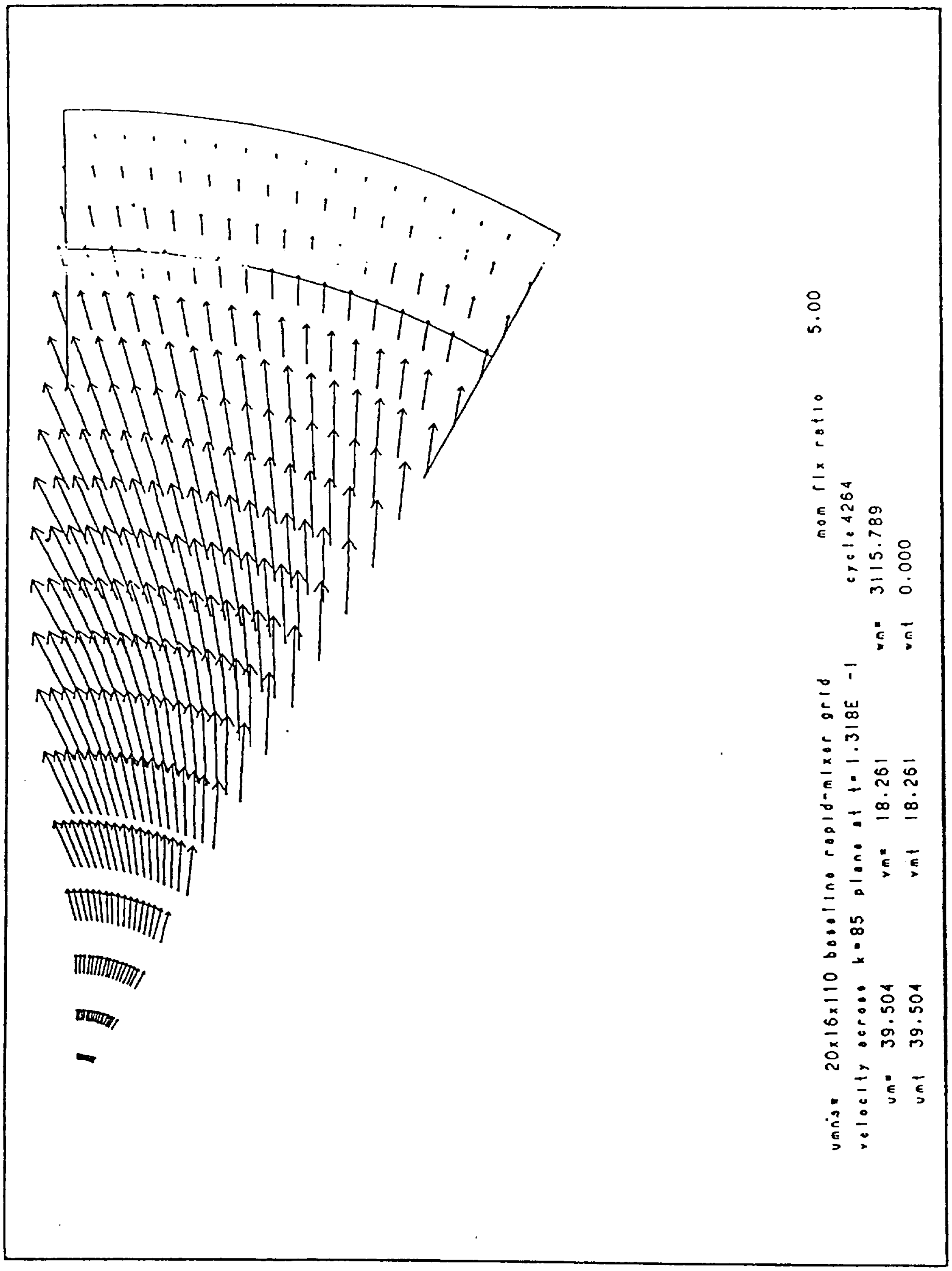
umnsw 20x16x110 baseline rapid-mixer grid
mom flx ratio 5.00
velocity across k=85 plane at t=1.318E -1
cycle 4264
um= 39.504
vm= 18.261
wn= 3115.789
umt 39.504
vmt 18.261
wnt 0.000

Figure 4-10

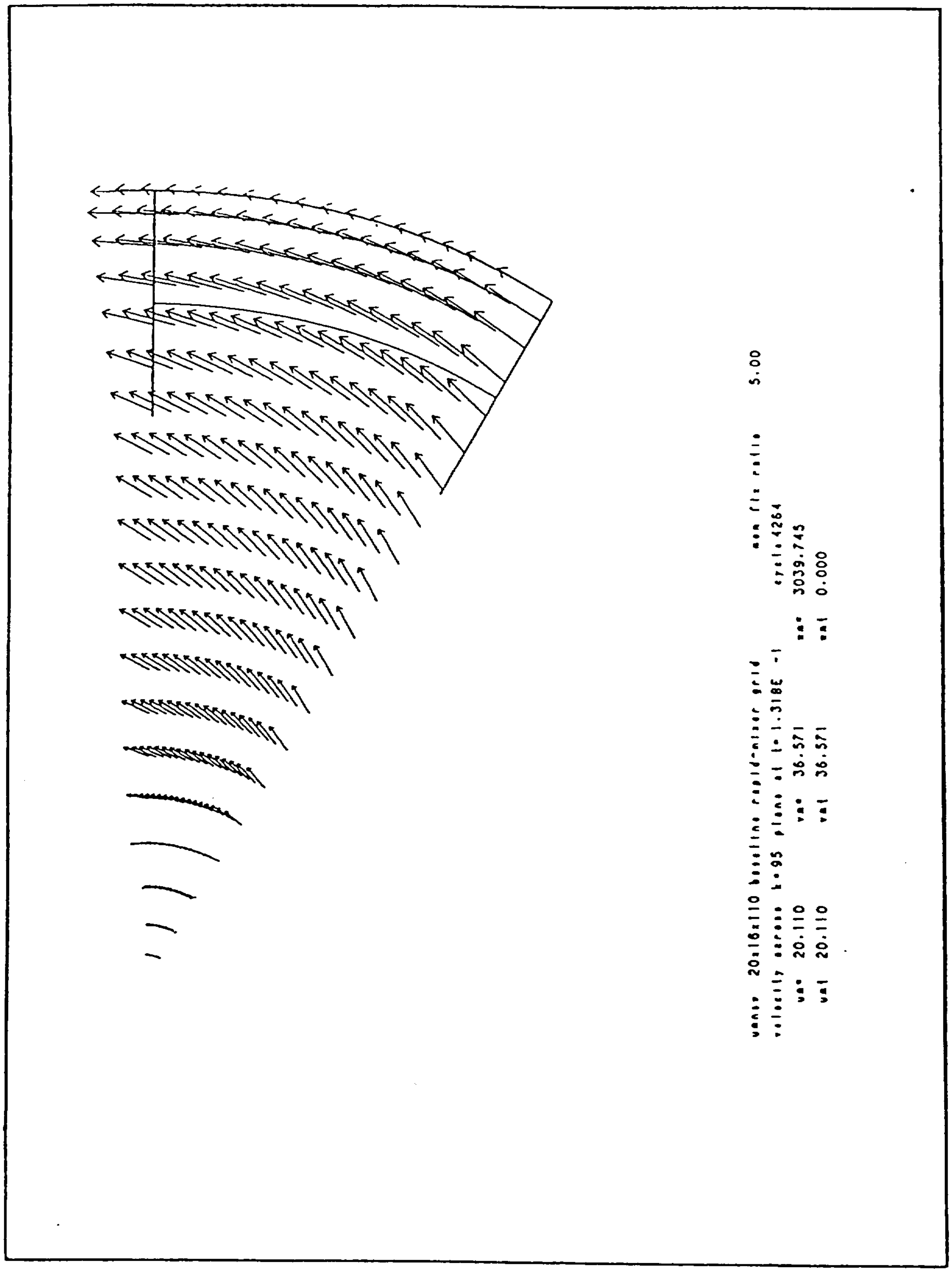
vanes 20x16x110 baseline rapid-mixer grid
mom flx ratio 5.00
velocity across k=95 plane at t=1.318E -1
cycle=4264
vmx 20.110
vmx 36.571
vmx 3039.745
vmi 20.110
vmi 36.571
vmi 0.000

Figure 4-11

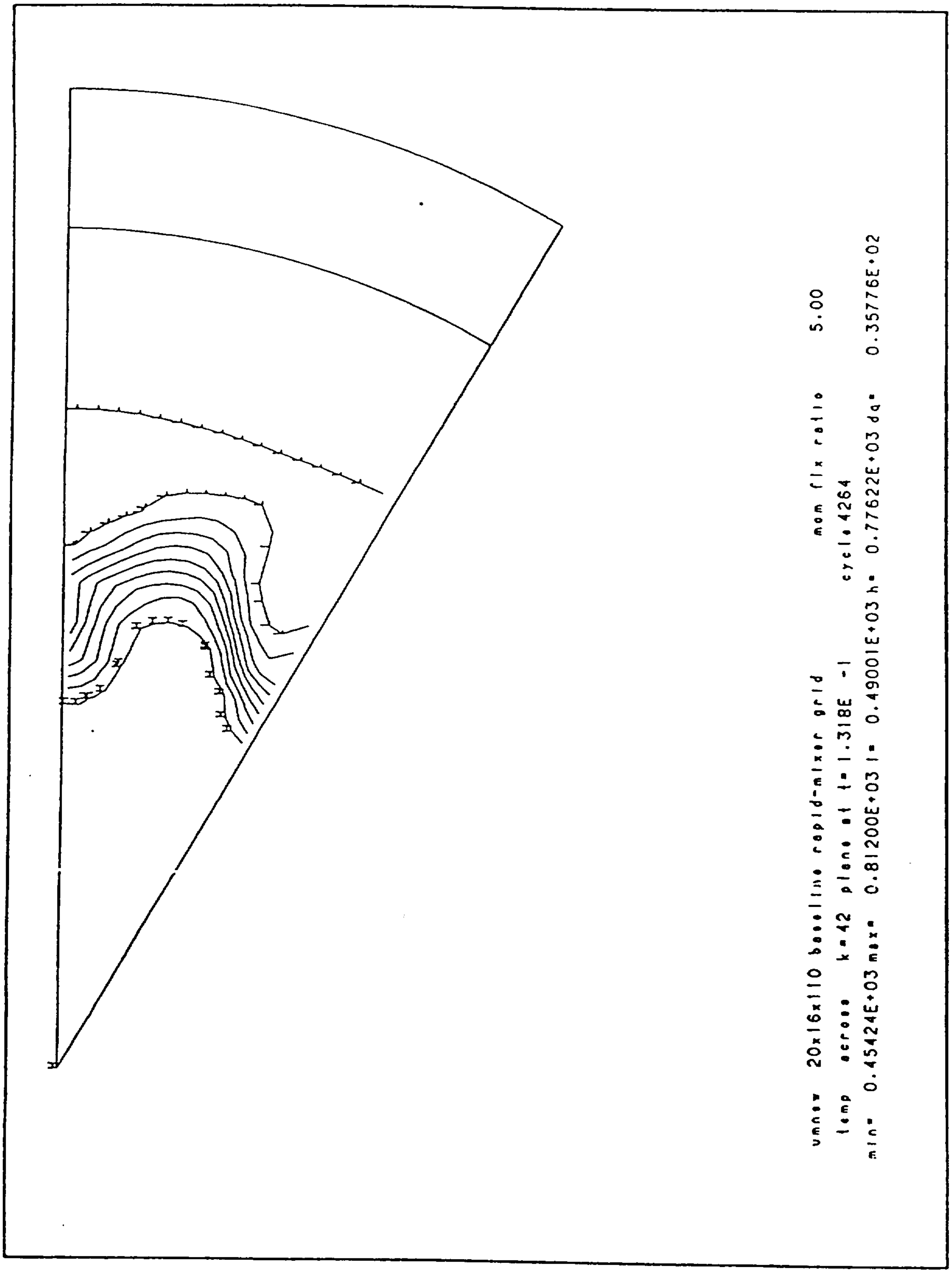
vmnew 20x16x110 baseline rapid-mixer grid mom flx ratio 5.00
temp across k=42 plane at t= 1.318E -1 cycle=4264
min= 0.45424E+03 max= 0.81200E+03 l= 0.49001E+03 h= 0.77622E+03 dq= 0.35776E+02

Figure 4-12

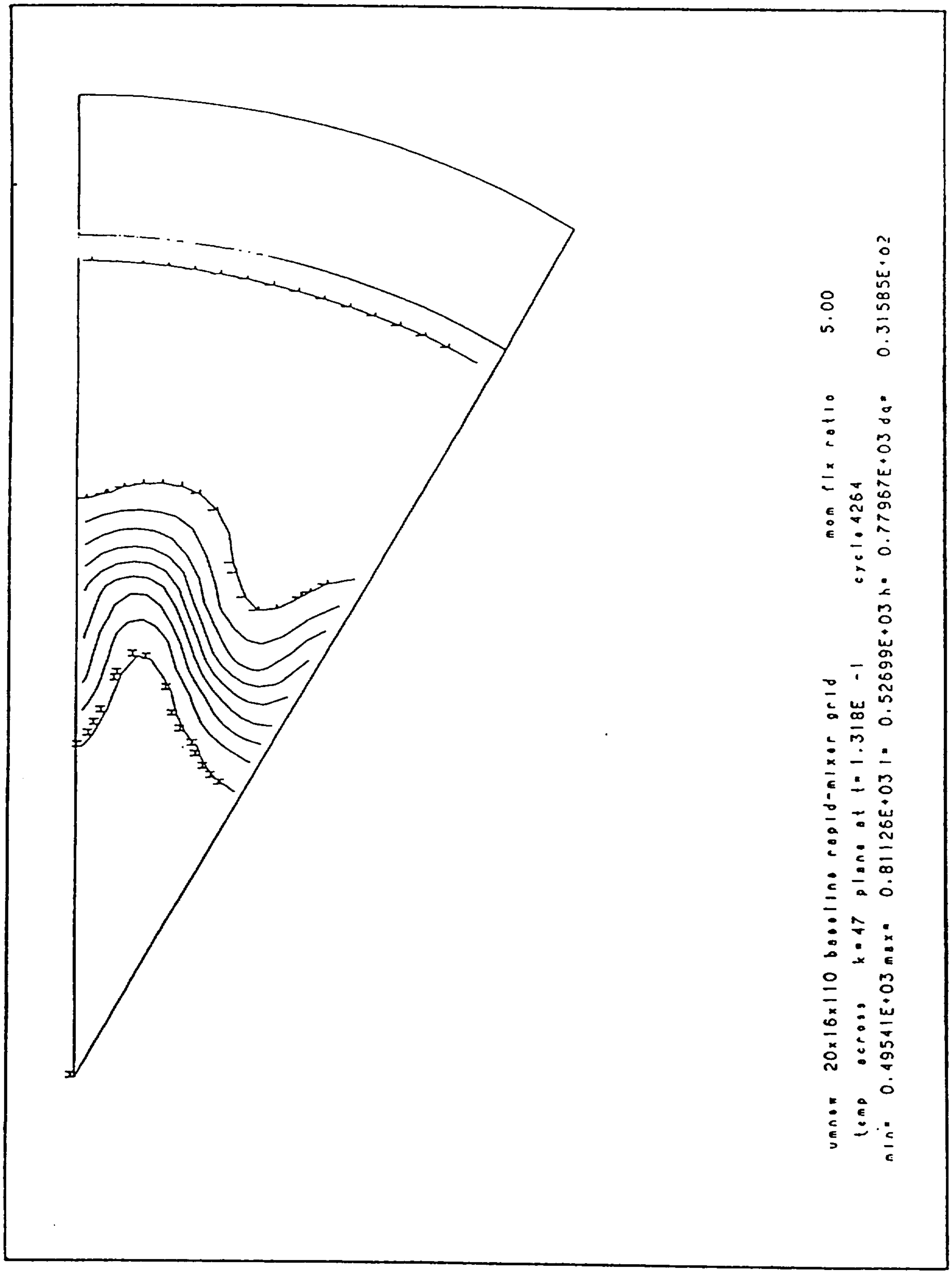
umnew 20x16x110 baseline rapid-mixer grid mom flx ratio 5.00
temp across k=47 plane at t= 1.318E -1 cycle 4264
min= 0.49541E+03 max= 0.81126E+03 l= 0.52699E+03 h= 0.77967E+03 dq= 0.31585E+02

Figure 4-13

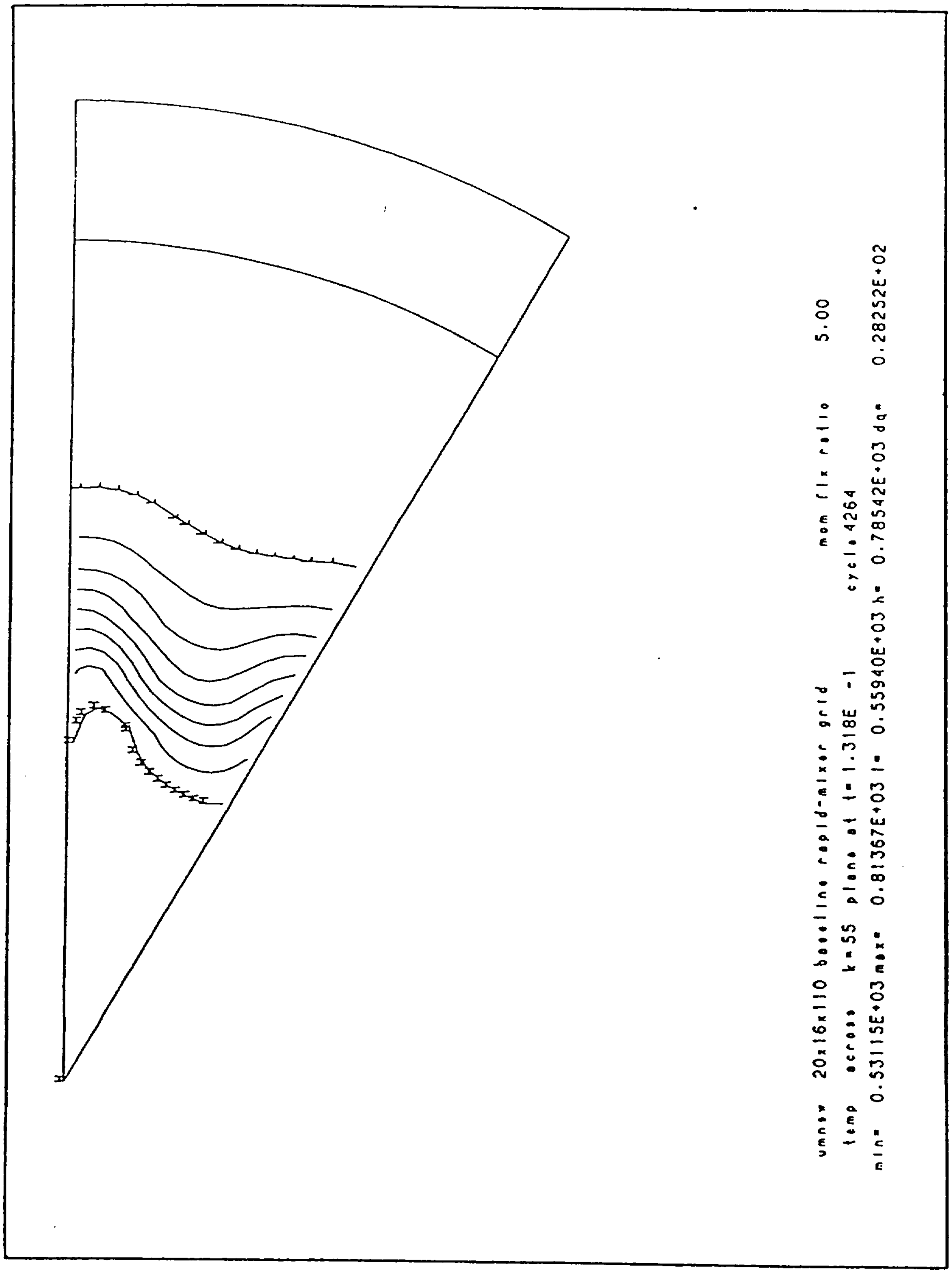
umnew 20x16x110 baseline rapid-mixer grid mom flx ratio 5.00
temp across k=55 plane at t= 1.318E -1 cycle=4264
min= 0.53115E+03 max= 0.81367E+03 l= 0.55940E+03 h= 0.78542E+03 dq= 0.28252E+02

Figure 4-14

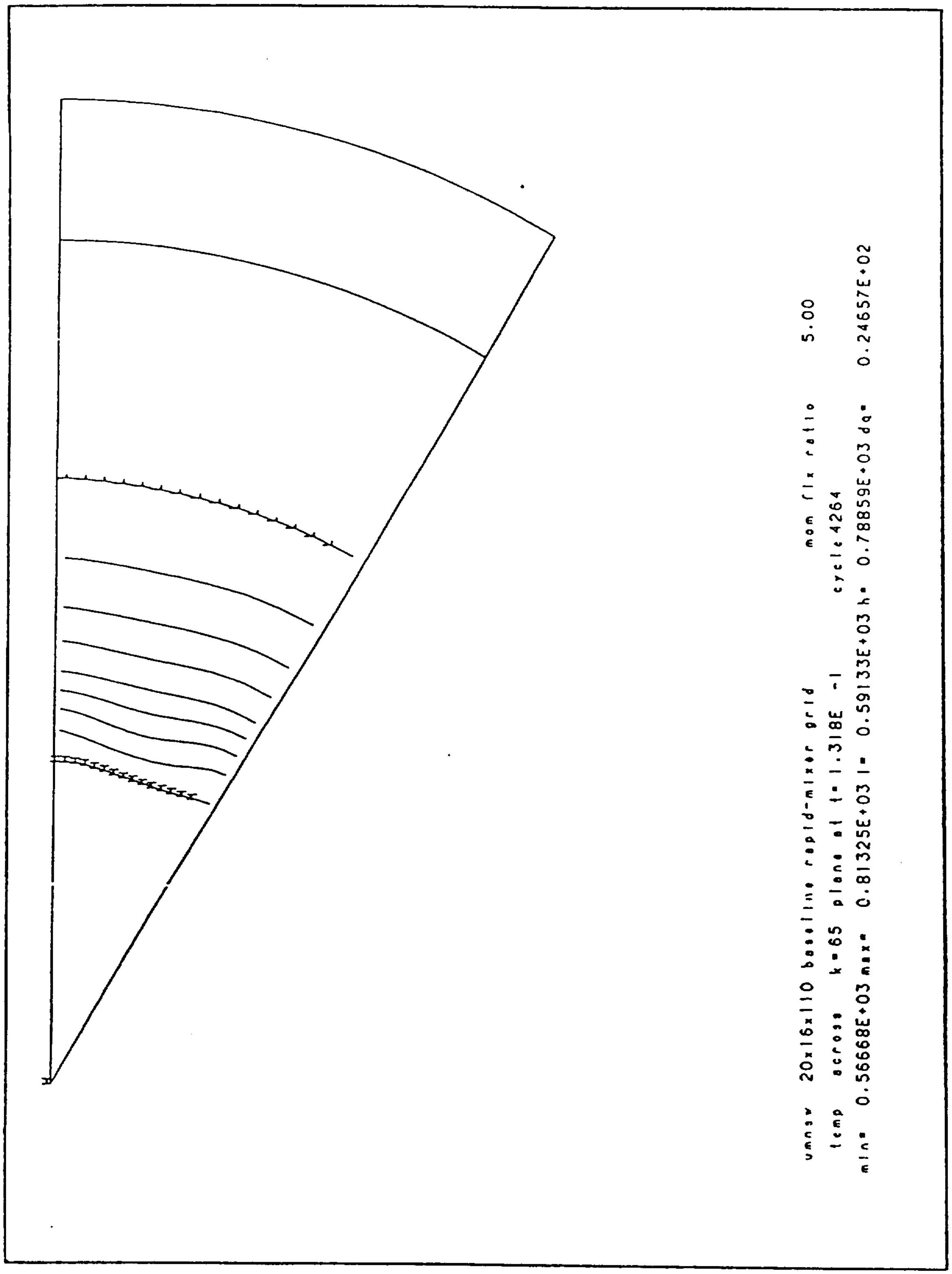
vmnsv 20x16x110 baseline rapid-mixer grid mom flx ratio 5.00
temp across k=65 plane at t= 1.318E -1 cycle 4264
min= 0.56668E+03 max= 0.81325E+03 l= 0.59133E+03 h= 0.78859E+03 dq= 0.24657E+02

Figure 4-15

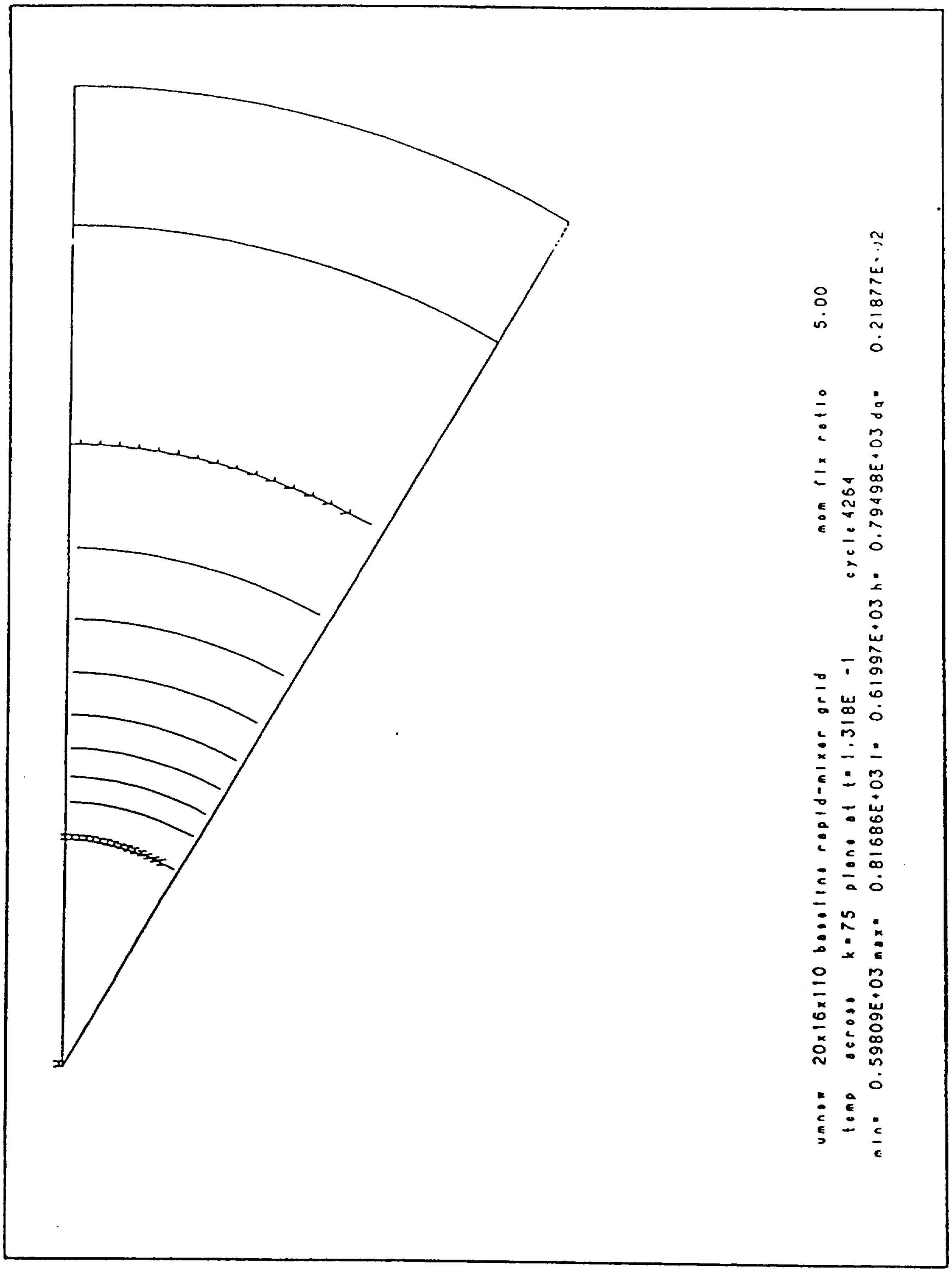
umnew 20x16x110 baseline rapid-mixer grid mom flx ratio 5.00
temp across k=75 plane at t=1.318E -1 cycle=4264
min= 0.59809E+03 max= 0.81686E+03 l= 0.61997E+03 h= 0.79498E+03 dq= 0.21877E+02

Figure 4-16

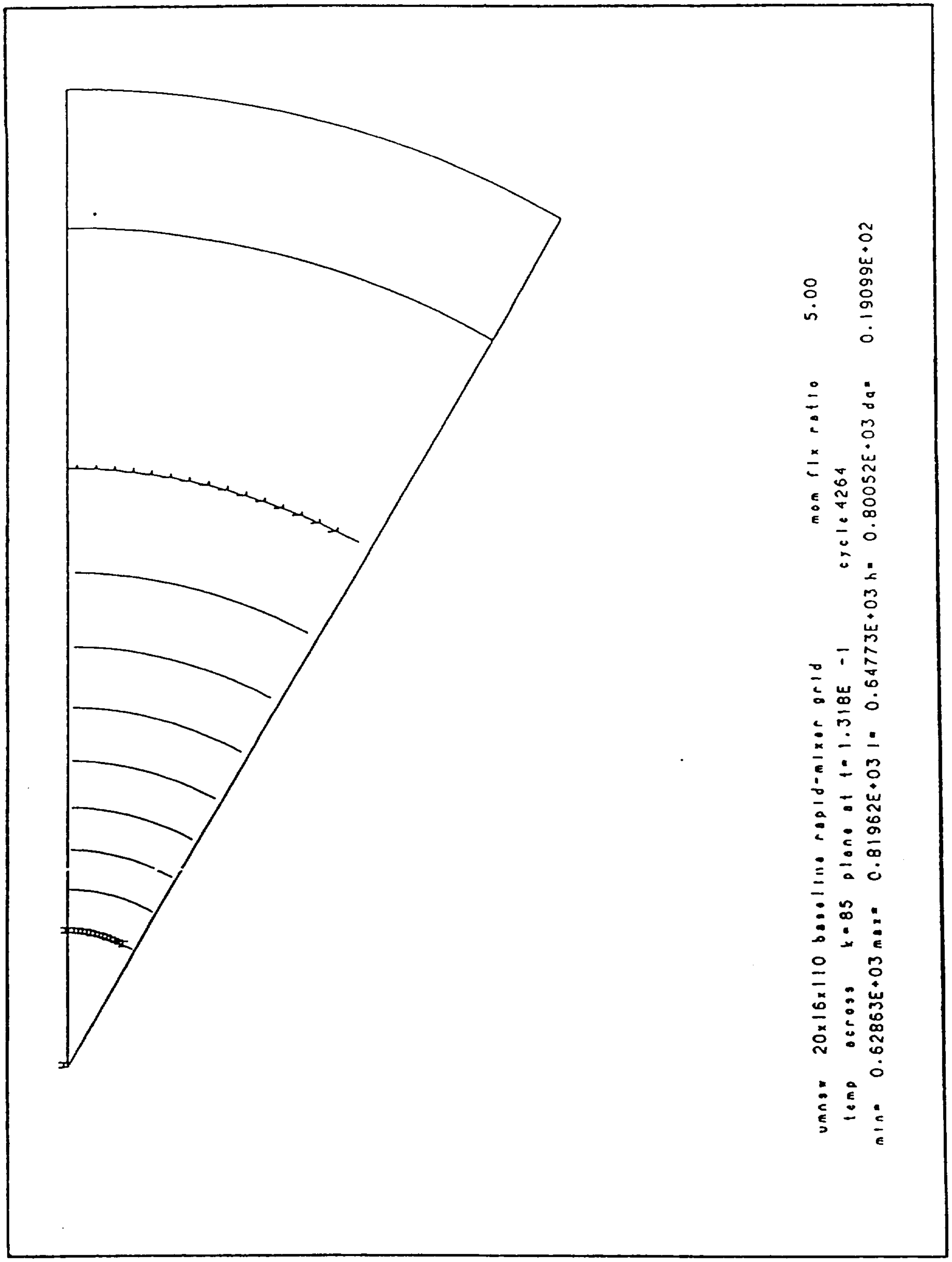
umnsw 20x16x110 baseline rapid-mixer grid
mom flx ratio 5.00
temp across k=85 plane at t= 1.318E -1
cycle 4264
min= 0.62863E+03 max= 0.81962E+03 l= 0.64773E+03 h= 0.80052E+03 da= 0.19099E+02

Figure 4-17

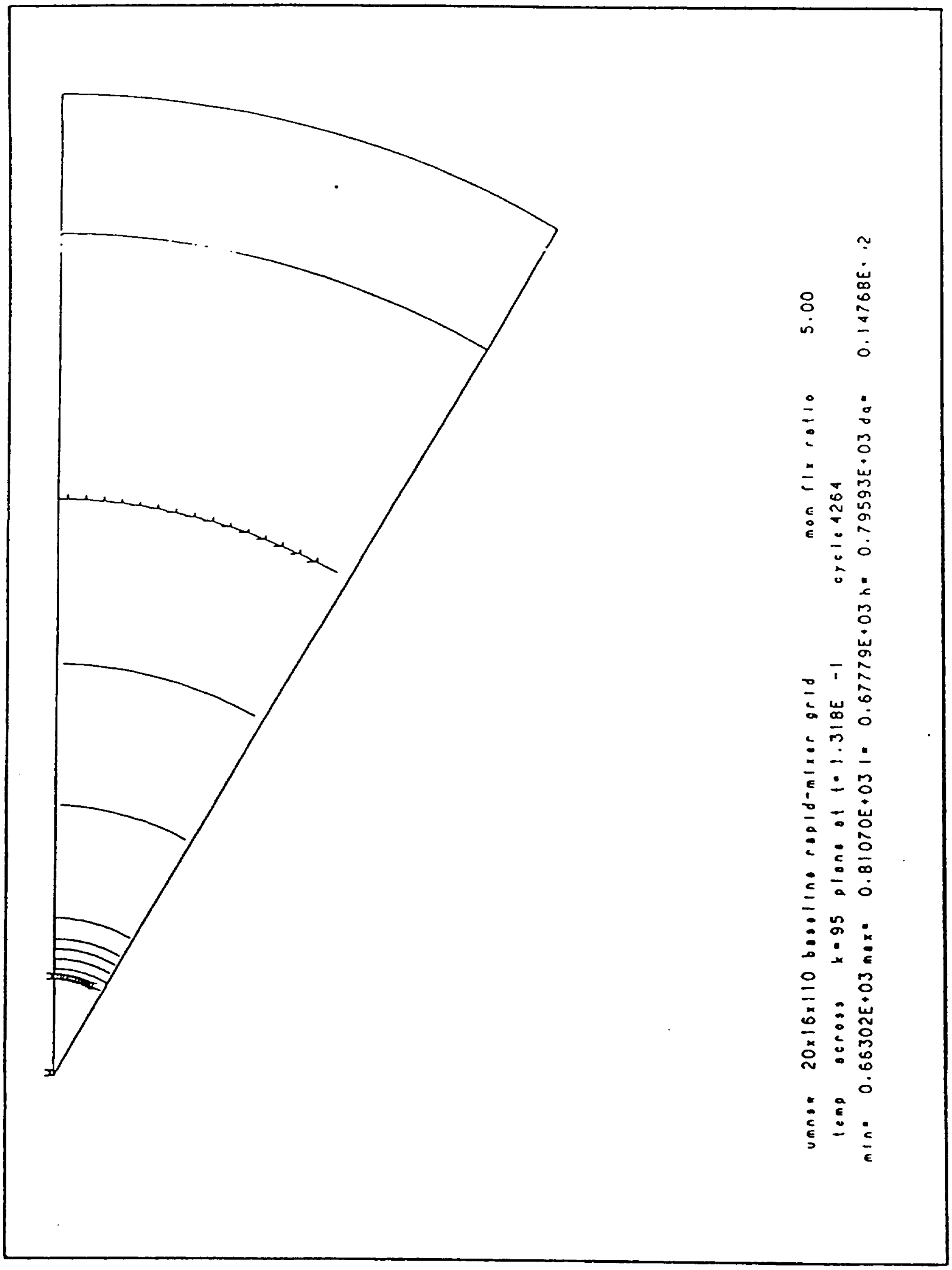
umnew 20x16x110 baseline rapid-mixer grid mon flx ratio 5.00
temp across k=95 plane at t= 1.318E -1 cycle 4264
min= 0.66302E+03 max= 0.81070E+03 l= 0.67779E+03 h= 0.79593E+03 dq= 0.14768E+2

Figure 4-18

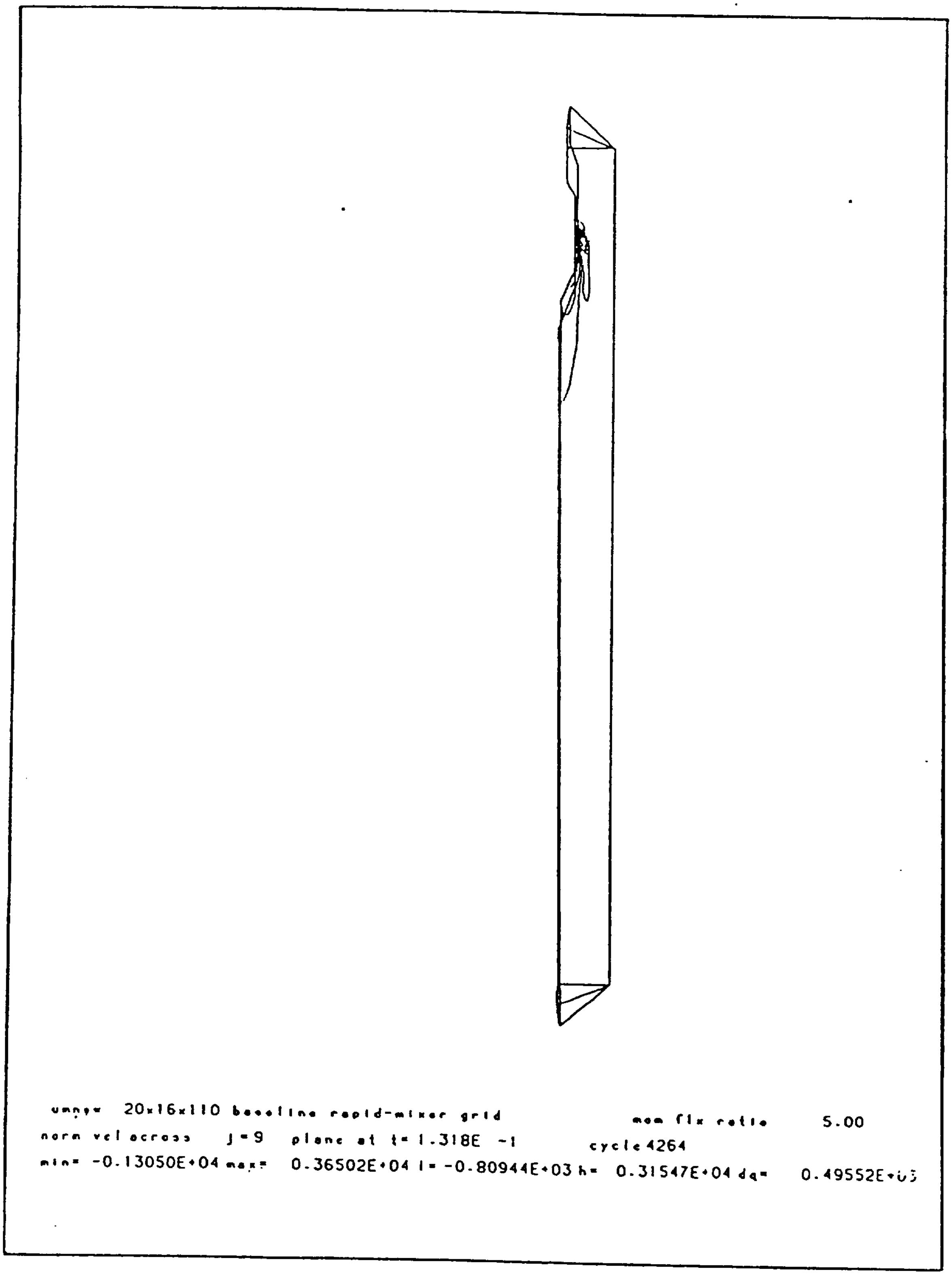
umnew 20x16x110 baseline rapid-mixer grid
mom flx ratio 5.00
norm vel across j=9 plane at t= 1.318E -1
cycle 4264
min= -0.13050E+04 max= 0.36502E+04 l= -0.80944E+03 h= 0.31547E+04 dq= 0.49552E+03

Figure 4-19

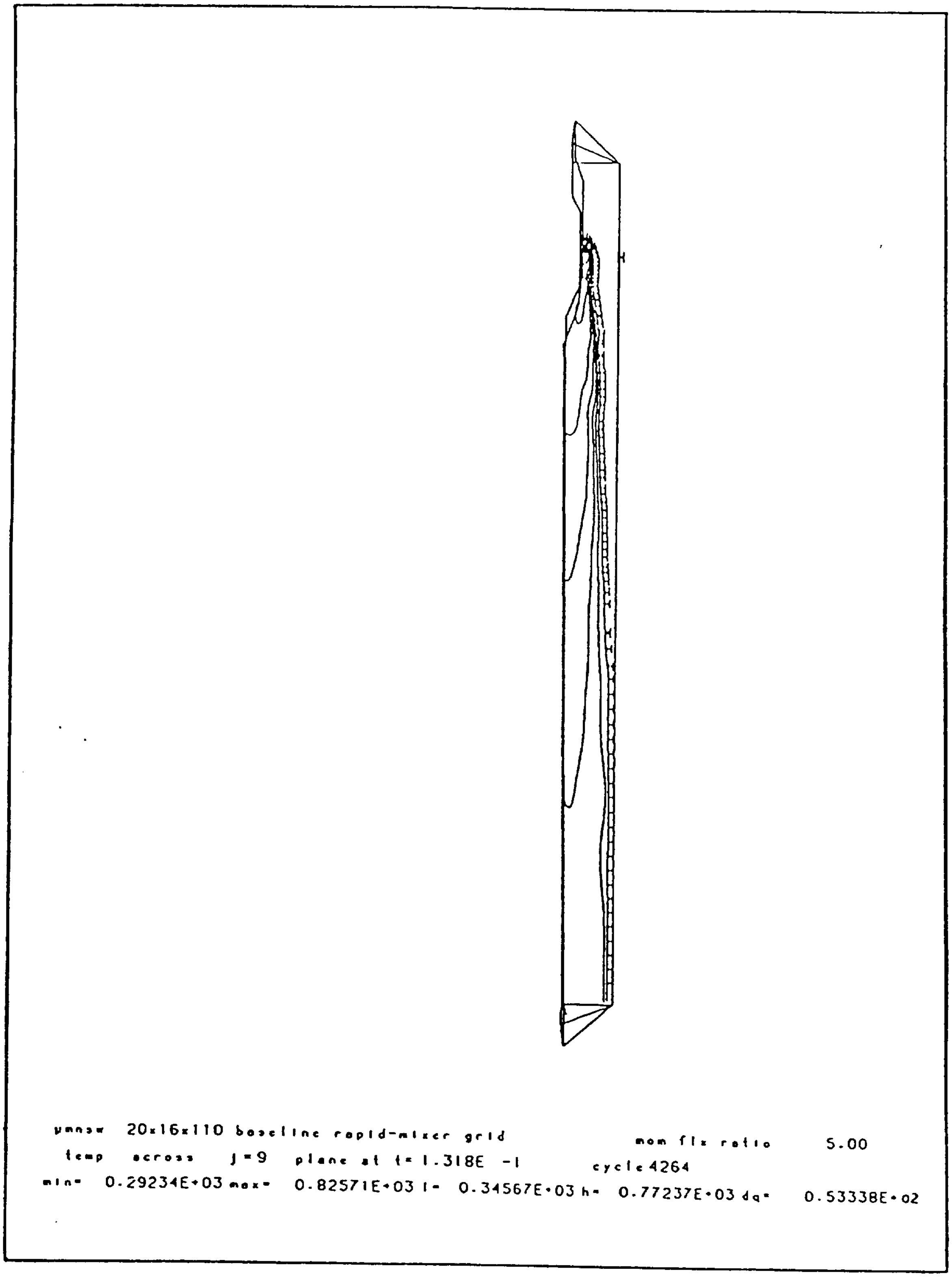
ymnsw 20x16x110 baseline rapid-mixer grid
mom flx ratio 5.00
temp across j=9 plane at t= 1.318E -1
cycle 4264
min= 0.29234E+03 max= 0.82571E+03 l= 0.34567E+03 h= 0.77237E+03 dq= 0.53338E+02

Figure 4-20

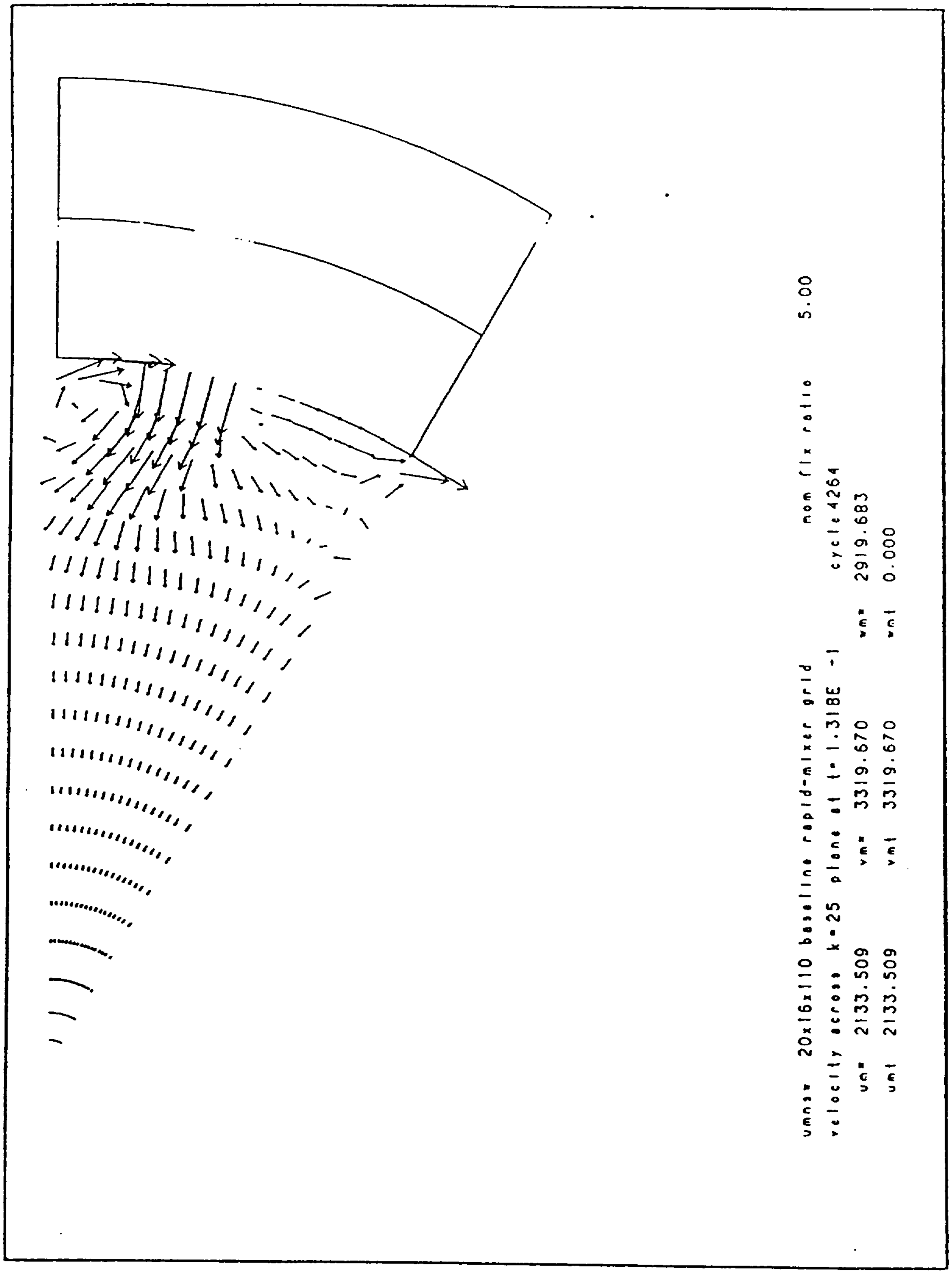
umnsw 20x16x110 baseline rapid-mixer grid
nom flx ratio 5.00
velocity across k=25 plane at t=1.318E -1
cycle 4264
un= 2133.509
vm= 3319.670
wm= 2919.683
uml 2133.509
vml 3319.670
wml 0.000

Figure 4-21

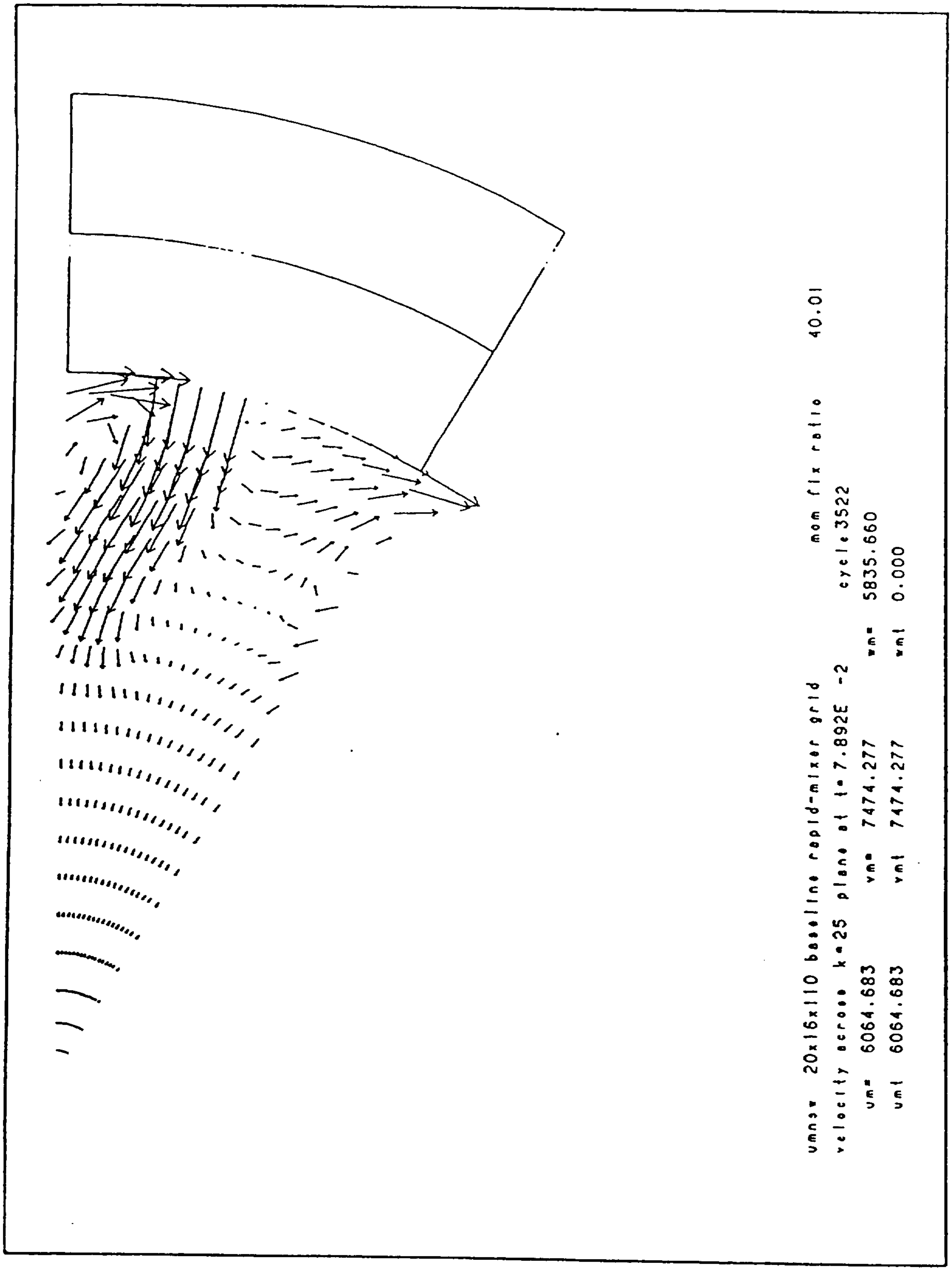
vmnsw 20x16x110 baseline rapid-mixer grid
mom flx ratio 40.01
velocity across k=25 plane at t= 7.892E -2
cycle 3522
um= 6064.683
vm= 7474.277
wm= 5835.660
umt 6064.683
vmt 7474.277
wmt 0.000

Figure 4-22

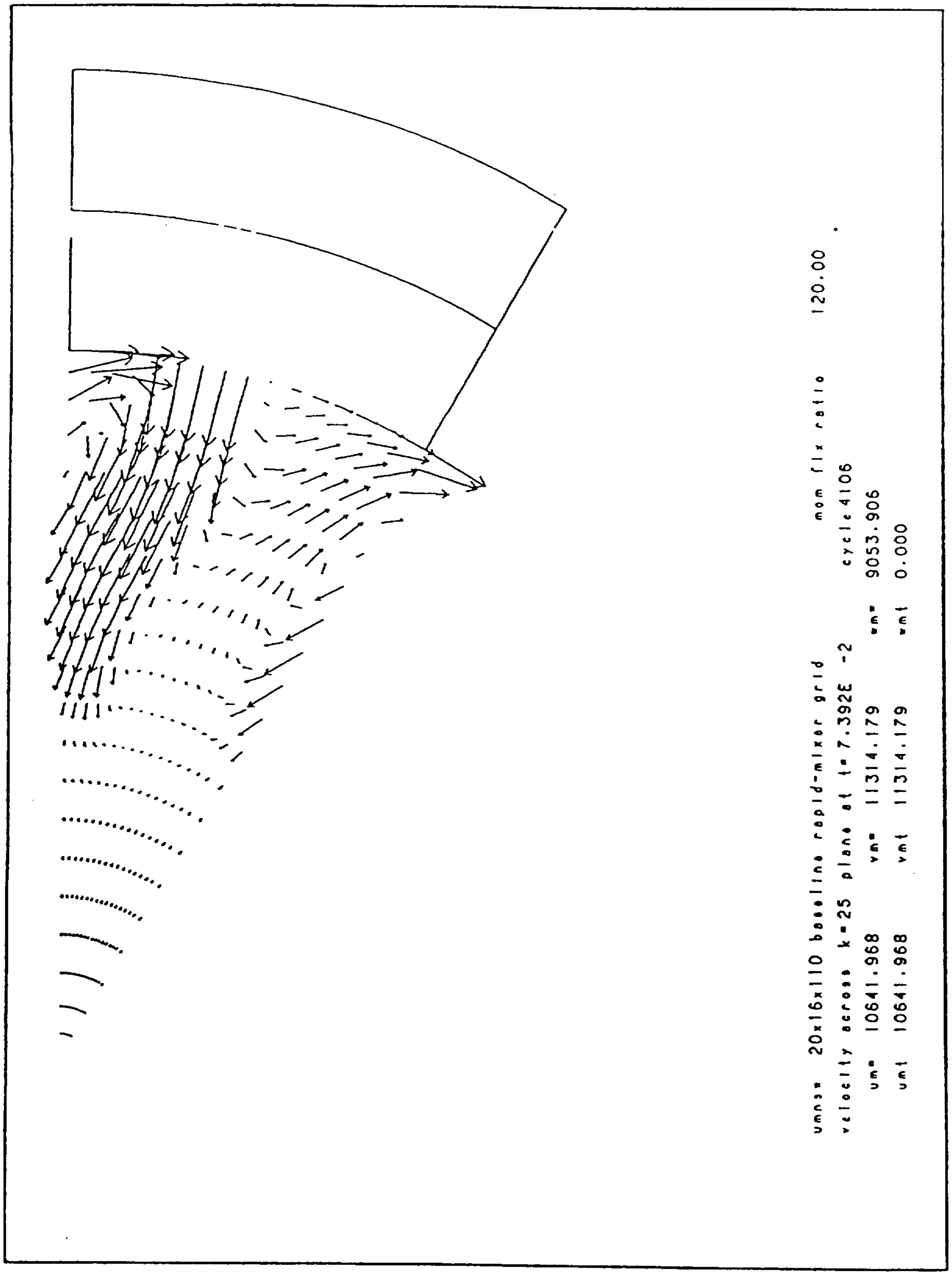
umnsa 20x16x110 baseline rapid-mixer grid
mom flx ratio 120.00
velocity across k=25 plane at t=7.392E -2
cycle 4106
um= 10641.968
vm= 11314.179
wm= 9053.906
umt 10641.968
vmt 11314.179
wmt 0.000

Figure 4-23

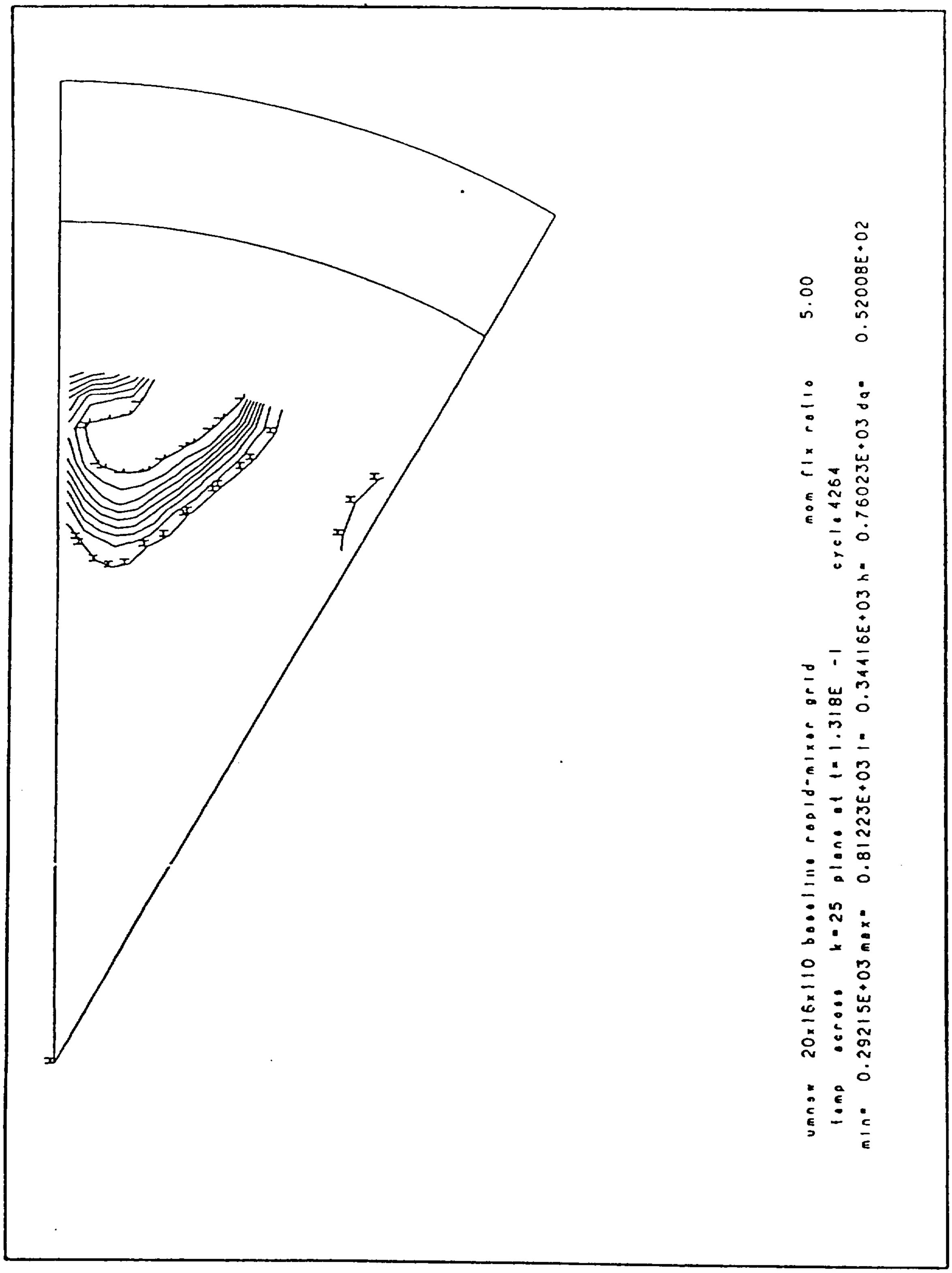
umnsw 20x16x110 baseline rapid-mixer grid mom flx ratio 5.00
temp across k=25 plane at t= 1.318E -1 cycle 4264
min= 0.29215E+03 max= 0.81223E+03 l= 0.34416E+03 h= 0.76023E+03 dq= 0.52008E+02

Figure 4-24

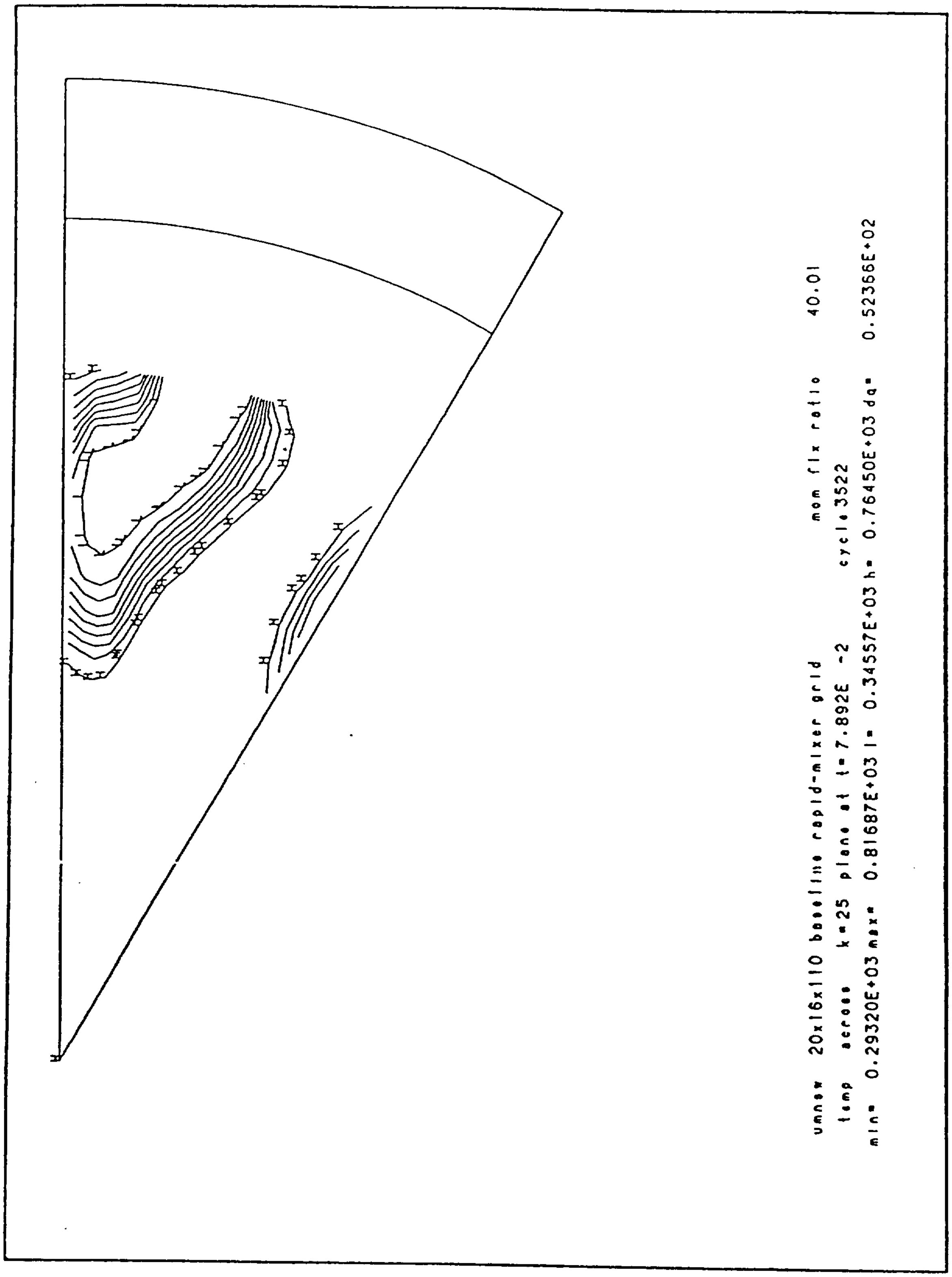
unnew 20x16x110 baseline rapid-mixer grid mom flx ratio 40.01
temp across k=25 plane at t= 7.892E -2 cycle=3522
min= 0.29320E+03 max= 0.81687E+03 l= 0.34557E+03 h= 0.76450E+03 dq= 0.52366E+02

Figure 4-25

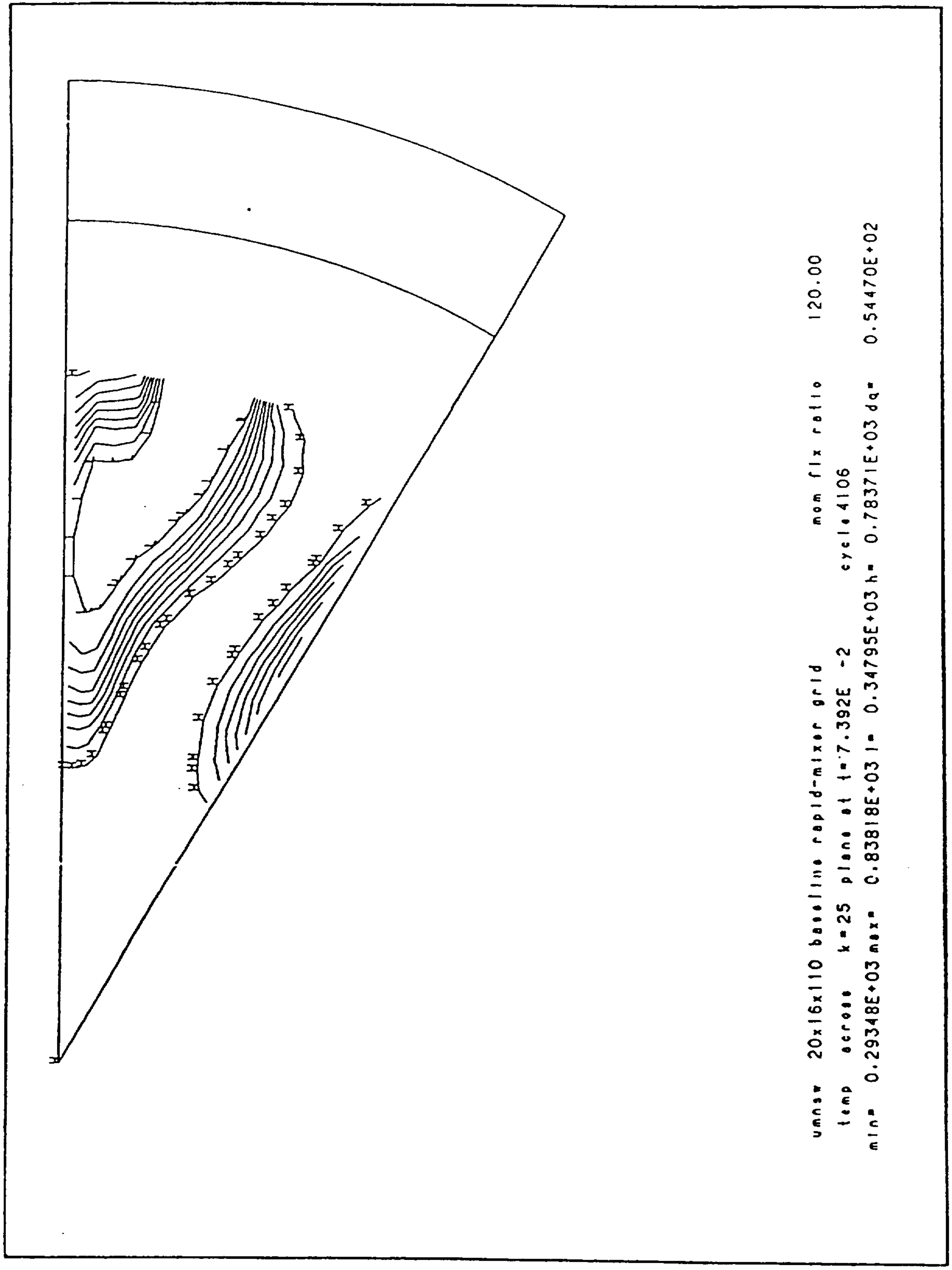
umnsw 20x16x110 baseline rapid-mixer grid mom flx ratio 120.00
temp across k=25 plane at t=7.392E -2 cycle=4106
min= 0.29348E+03 max= 0.83818E+03 l= 0.34795E+03 h= 0.78371E+03 dq= 0.54470E+02
H

Figure 4-26

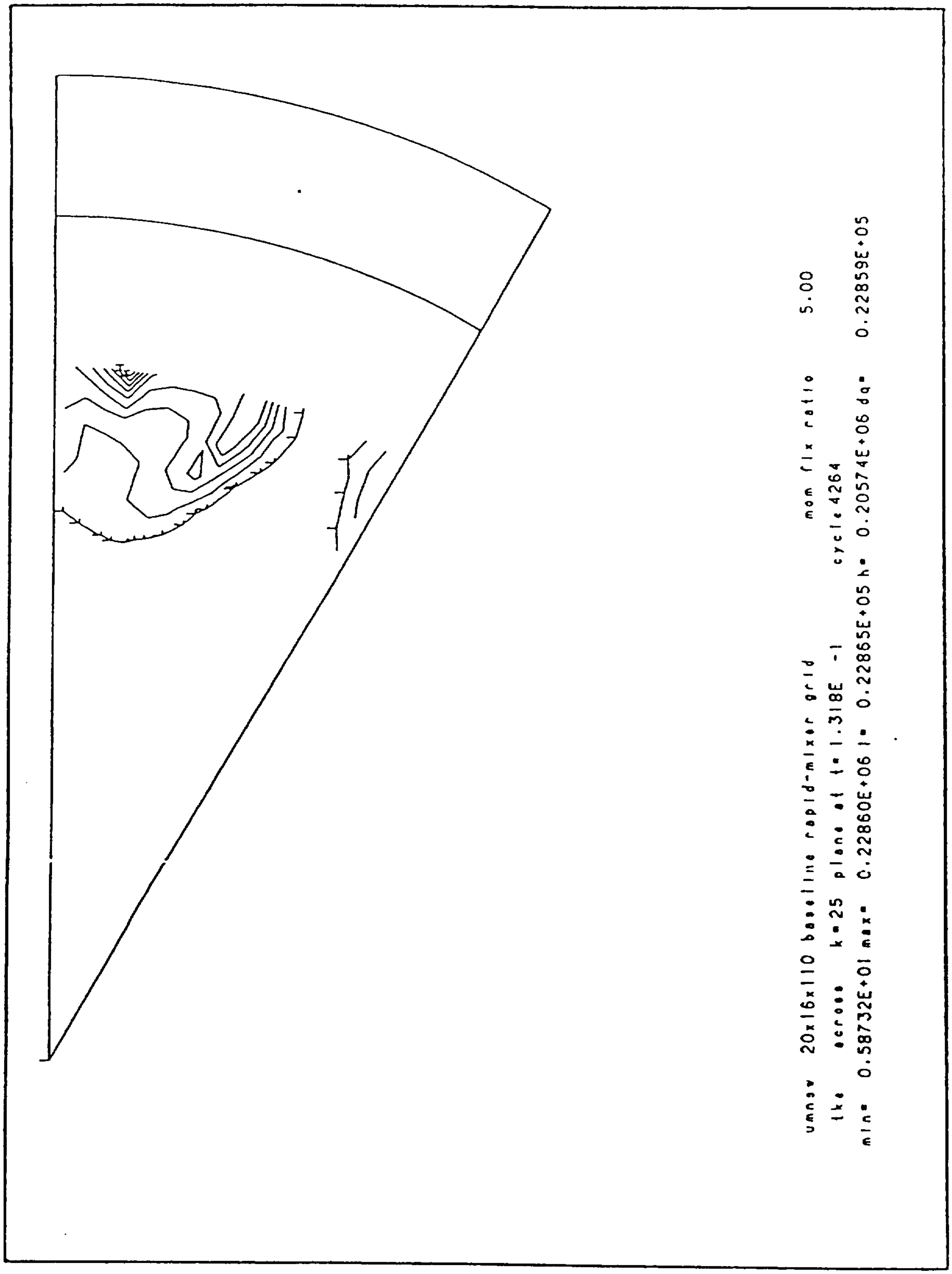
umnsv 20x16x110 baseline rapid-mixer grid mom flx ratio 5.00
tke across k=25 plane at t= 1.318E -1 cycle=4264
min= 0.58732E+01 max= 0.22860E+06 l= 0.22865E+05 h= 0.20574E+06 dq= 0.22859E+05

Figure 4-27

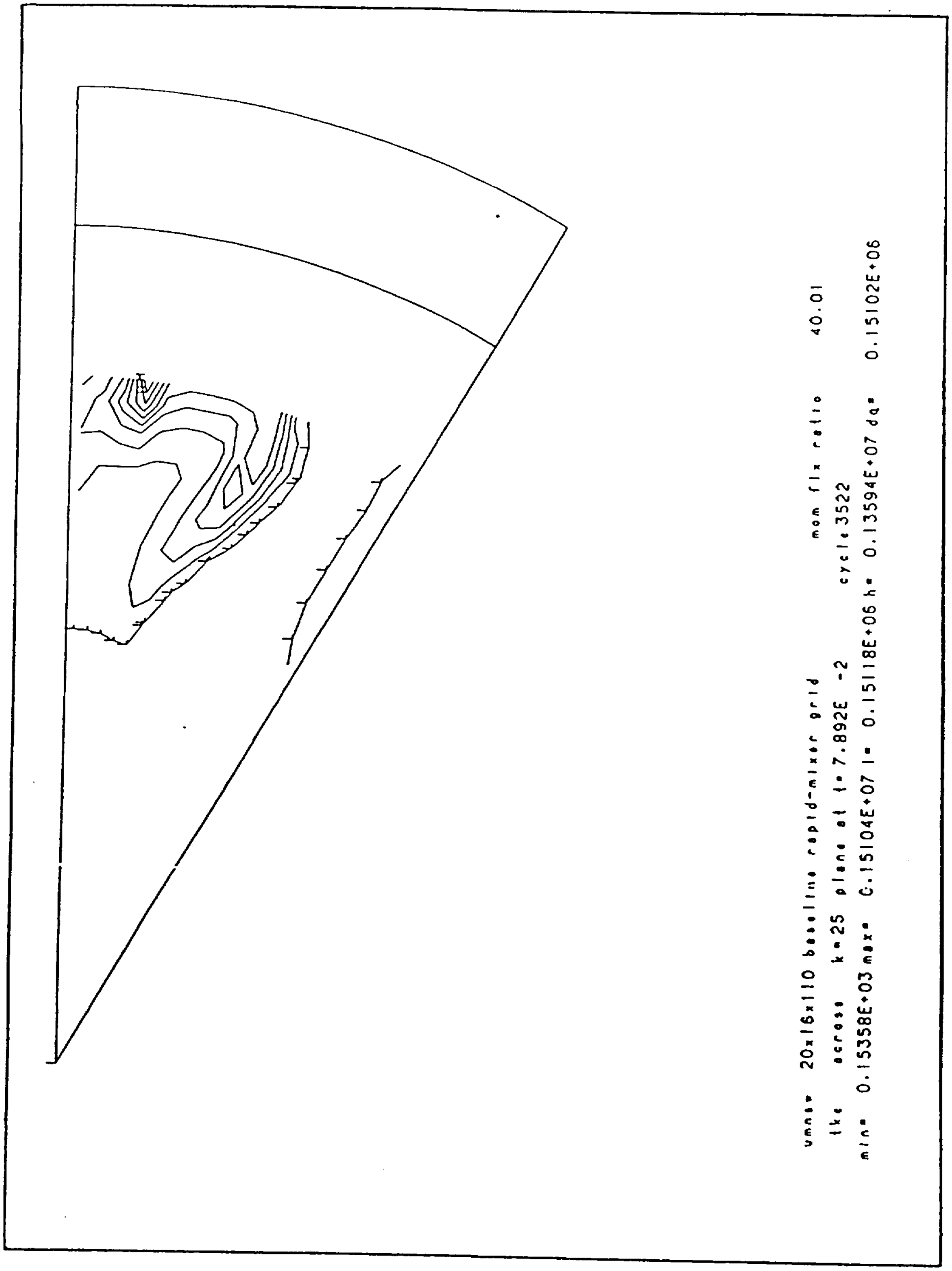
vmnew 20x16x110 baseline rapid-mixer grid mom flx ratio 40.01
tke across k=25 plane at t=7.892E -2 cycle 3522
min= 0.15358E+03 max= 0.15104E+07 l= 0.15118E+06 h= 0.13594E+07 dq= 0.15102E+06

Figure 4-28

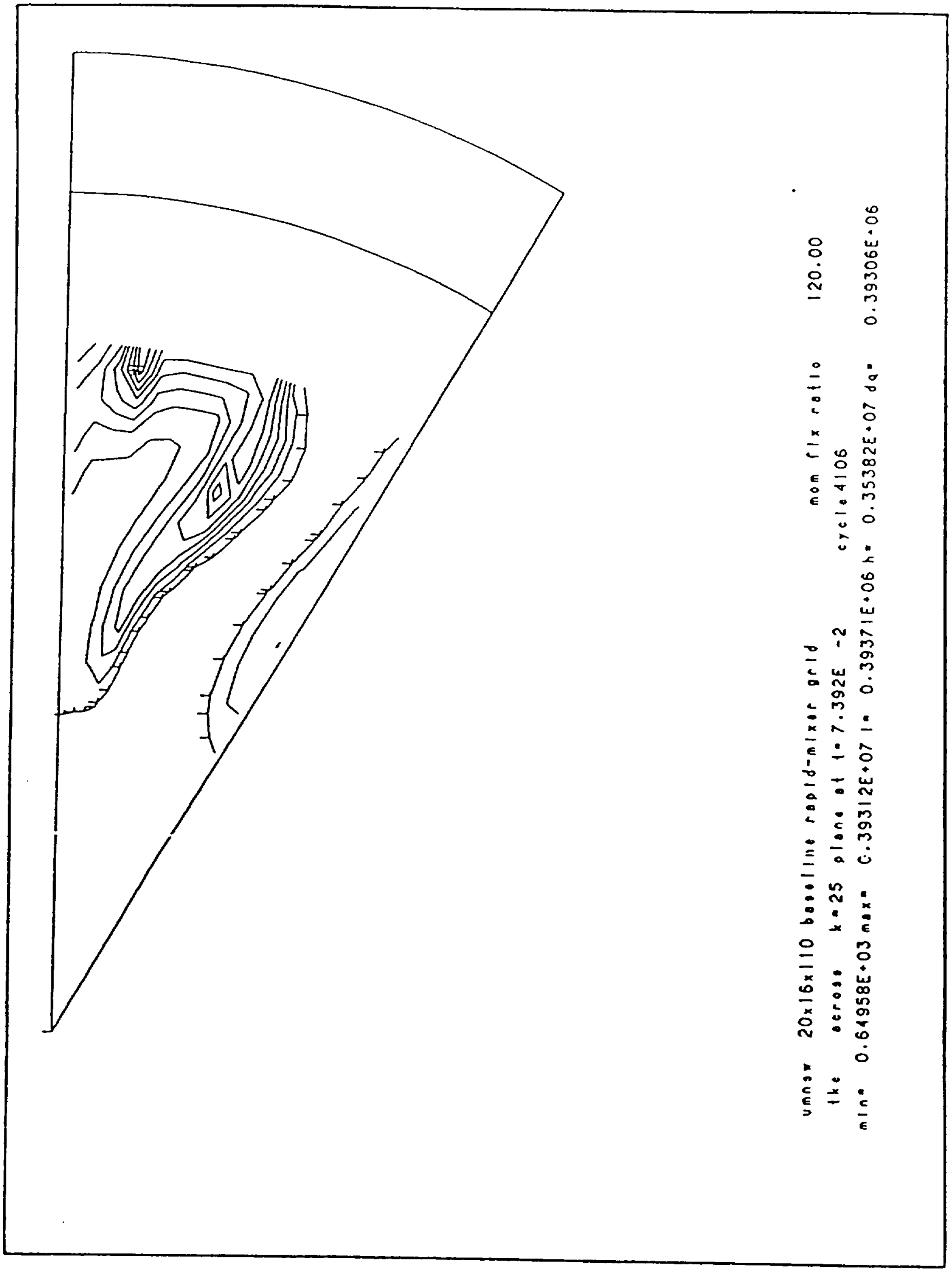
umnsw 20x16x110 baseline rapid-mixer grid
mom flx ratio 120.00
tke across k=25 plane at t= 7.392E -2
cycle 4106
min= 0.64958E+03 max= 0.39312E+07 l= 0.39371E+06 h= 0.35382E+07 dq= 0.39306E+06

Figure 4-29

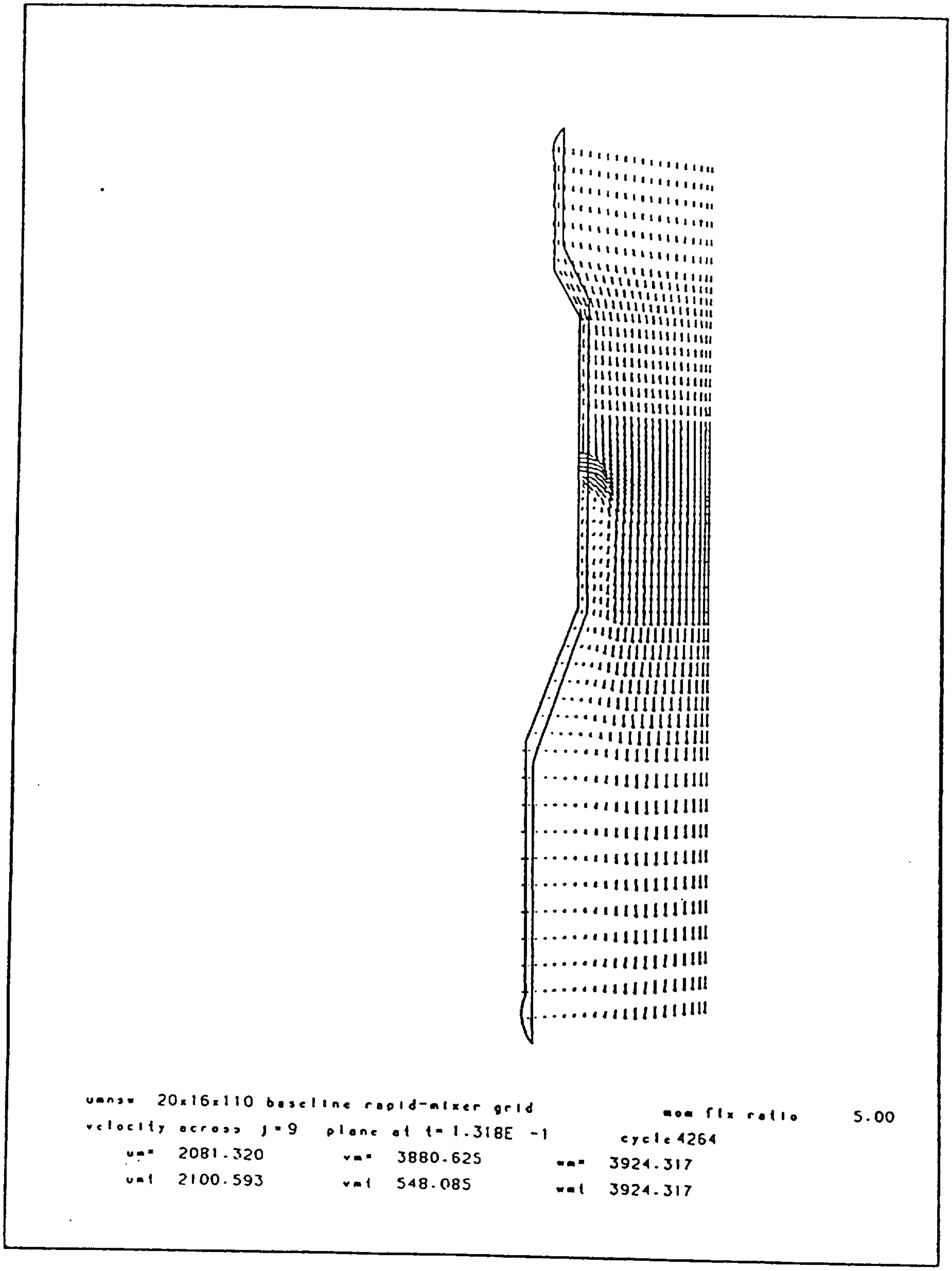
umnsw 20x16x110 baseline rapid-mixer grid
mom flx ratio 5.00
velocity across j=9 plane at t= 1.318E -1
cycle 4264
um= 2081.320
vm= 3880.625
wm= 3924.317
uml 2100.593
vml 548.085
wml 3924.317

Figure 4-30

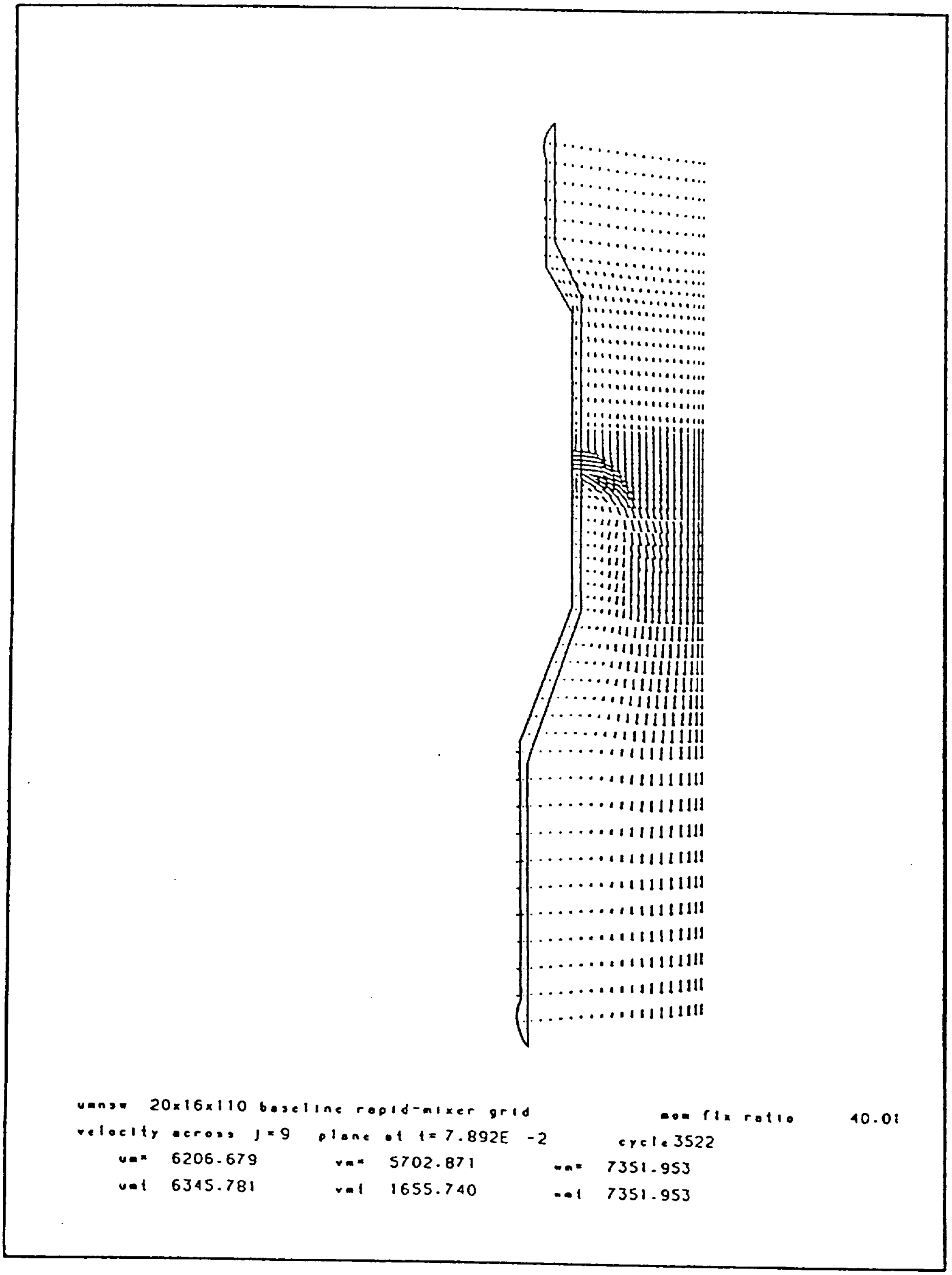
umnsw 20x16x110 baseline rapid-mixer grid
mom flx ratio 40.01
velocity across j=9 plane at t=7.892E -2
cycle 3522
um= 6206.679
vm= 5702.871
wm= 7351.953
uml 6345.781
vml 1655.740
wml 7351.953

Figure 4-31

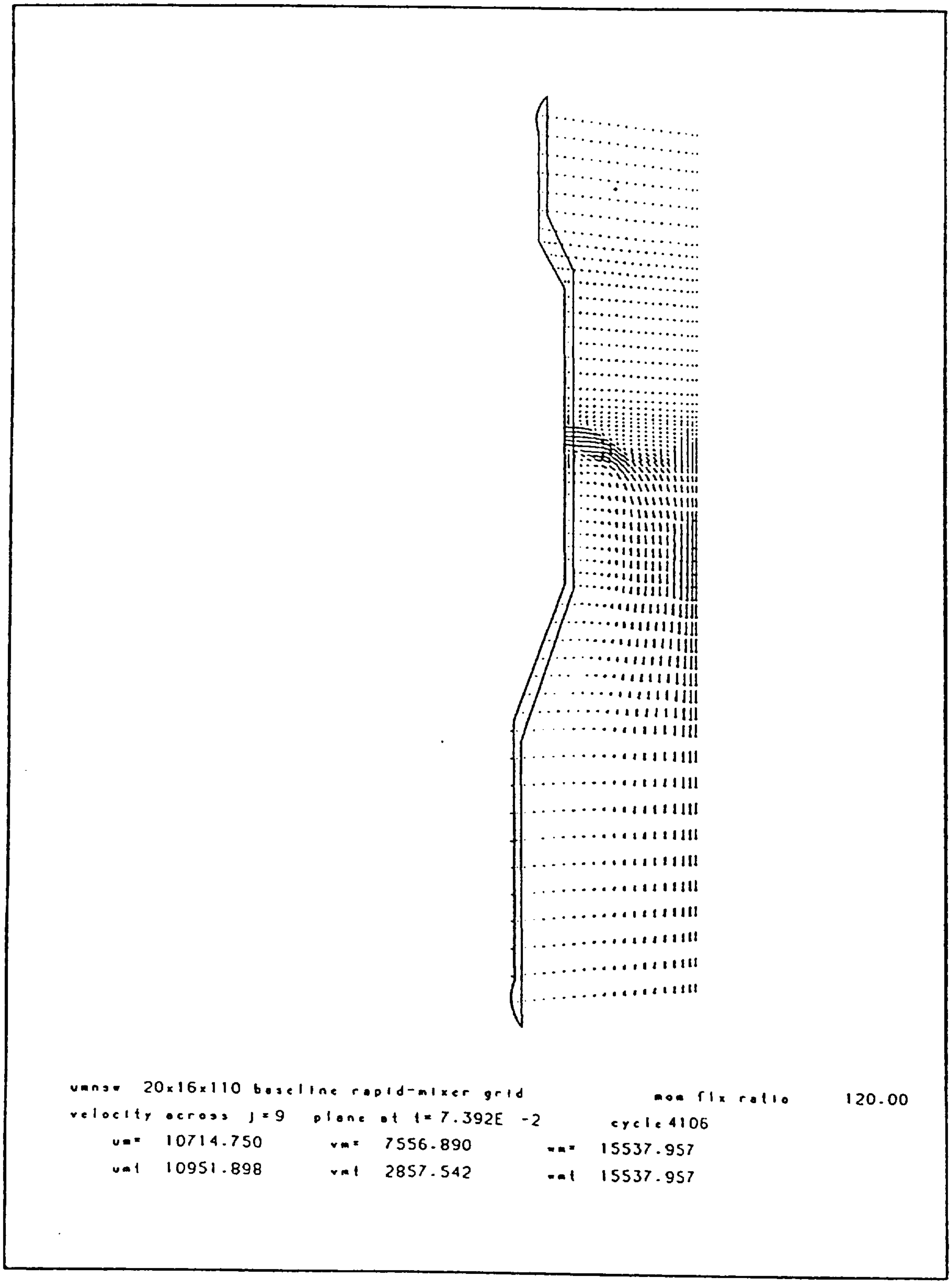
vmnsw 20x16x110 baseline rapid-mixer grid
mom flx ratio 120.00
velocity across j=9 plane at t=7.392E -2
cycle 4106
um= 10714.750
vm= 7556.890
wm= 15537.957
uml 10951.898
vml 2857.542
wml 15537.957

Figure 4-32

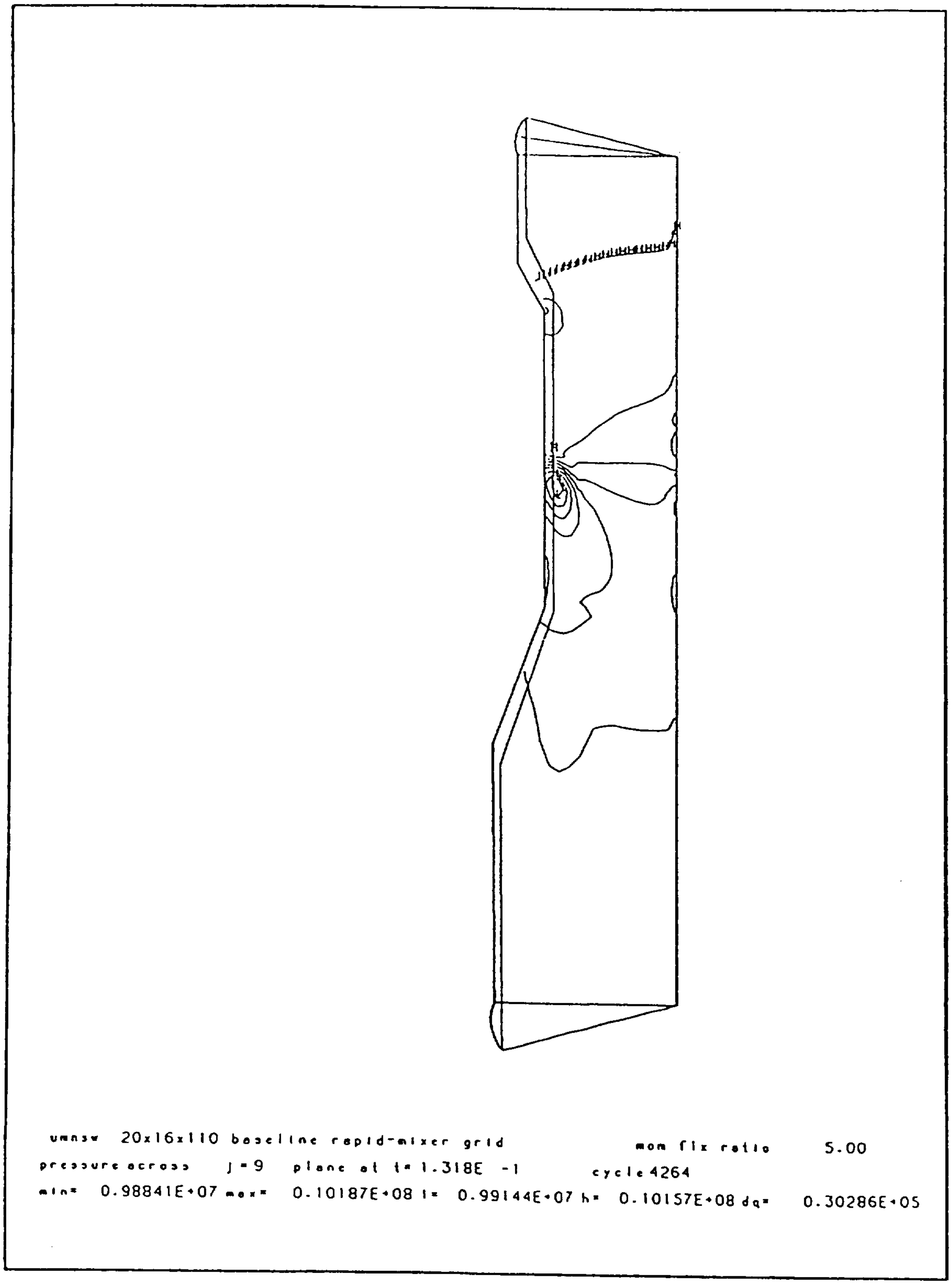
umnsw 20x16x110 baseline rapid-mixer grid
mom flx ratio 5.00
pressure across j = 9 plane at t= 1.318E -1
cycle 4264
min= 0.98841E+07 max= 0.10187E+08 l= 0.99144E+07 h= 0.10157E+08 dq= 0.30286E+05

Figure 4-33

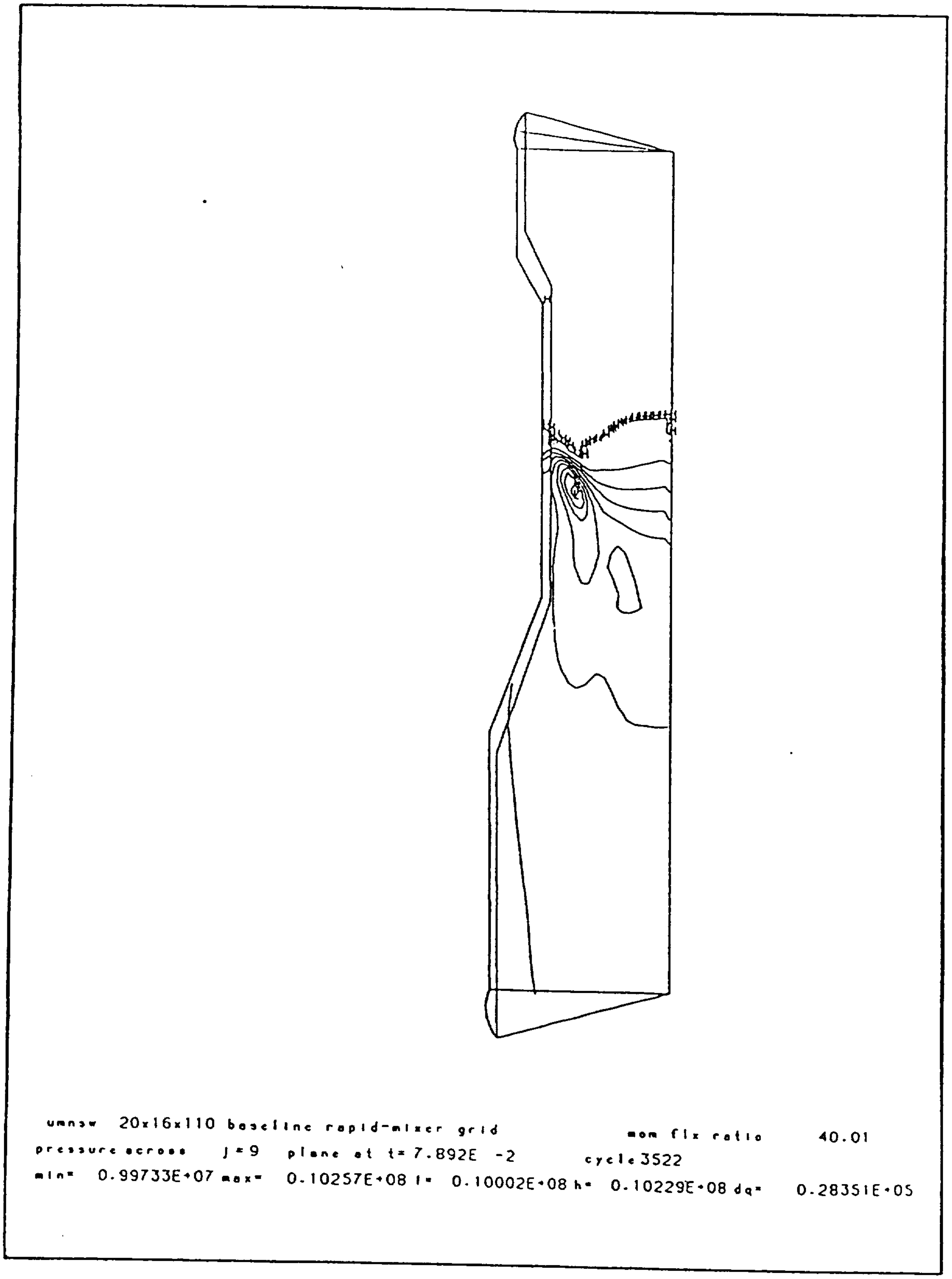
umnsw 20x16x110 baseline rapid-mixer grid
mom flx ratio 40.01
pressure across j = 9 plane at t = 7.892E -2
cycle 3522
min= 0.99733E+07 max= 0.10257E+08 l= 0.10002E+08 h= 0.10229E+08 dq= 0.28351E+05

Figure 4-34

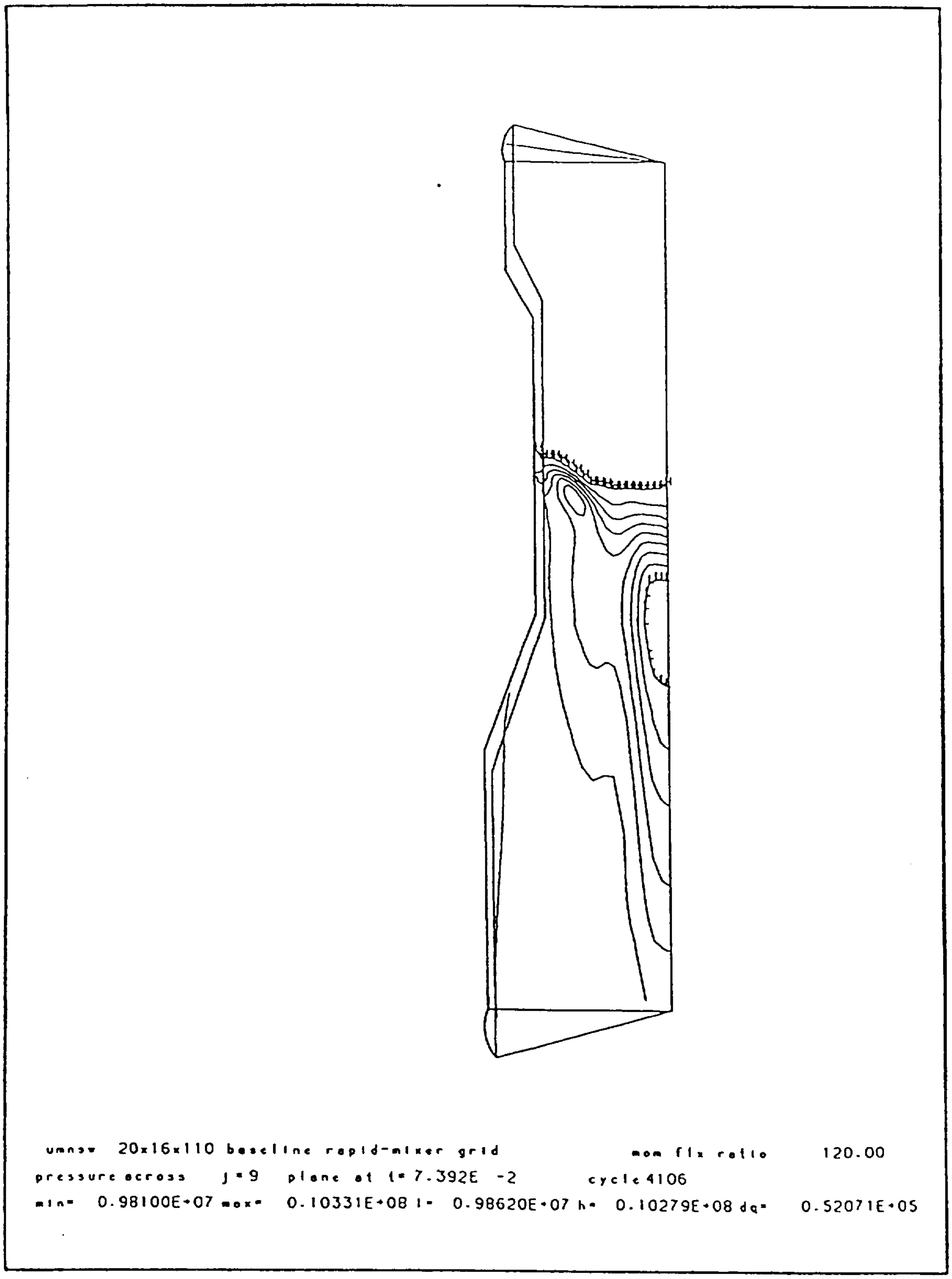
umnsw 20x16x110 baseline rapid-mixer grid
mom flx ratio 120.00
pressure across j=9 plane at t= 7.392E -2
cycle 4106
min= 0.98100E+07 max= 0.10331E+08 l= 0.98620E+07 h= 0.10279E+08 dq= 0.52071E+05

Figure 4-35

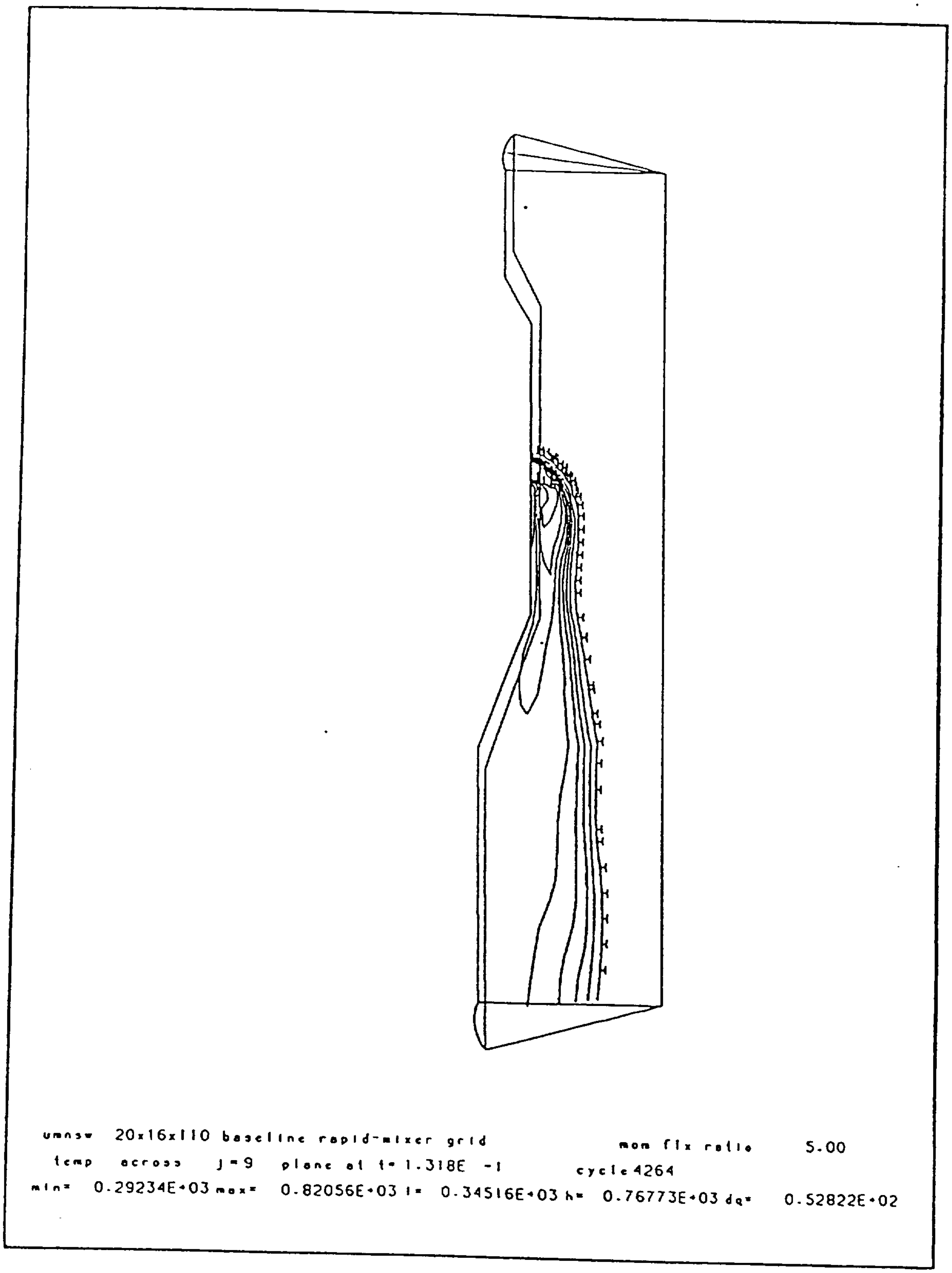

Figure 4-36

C-2

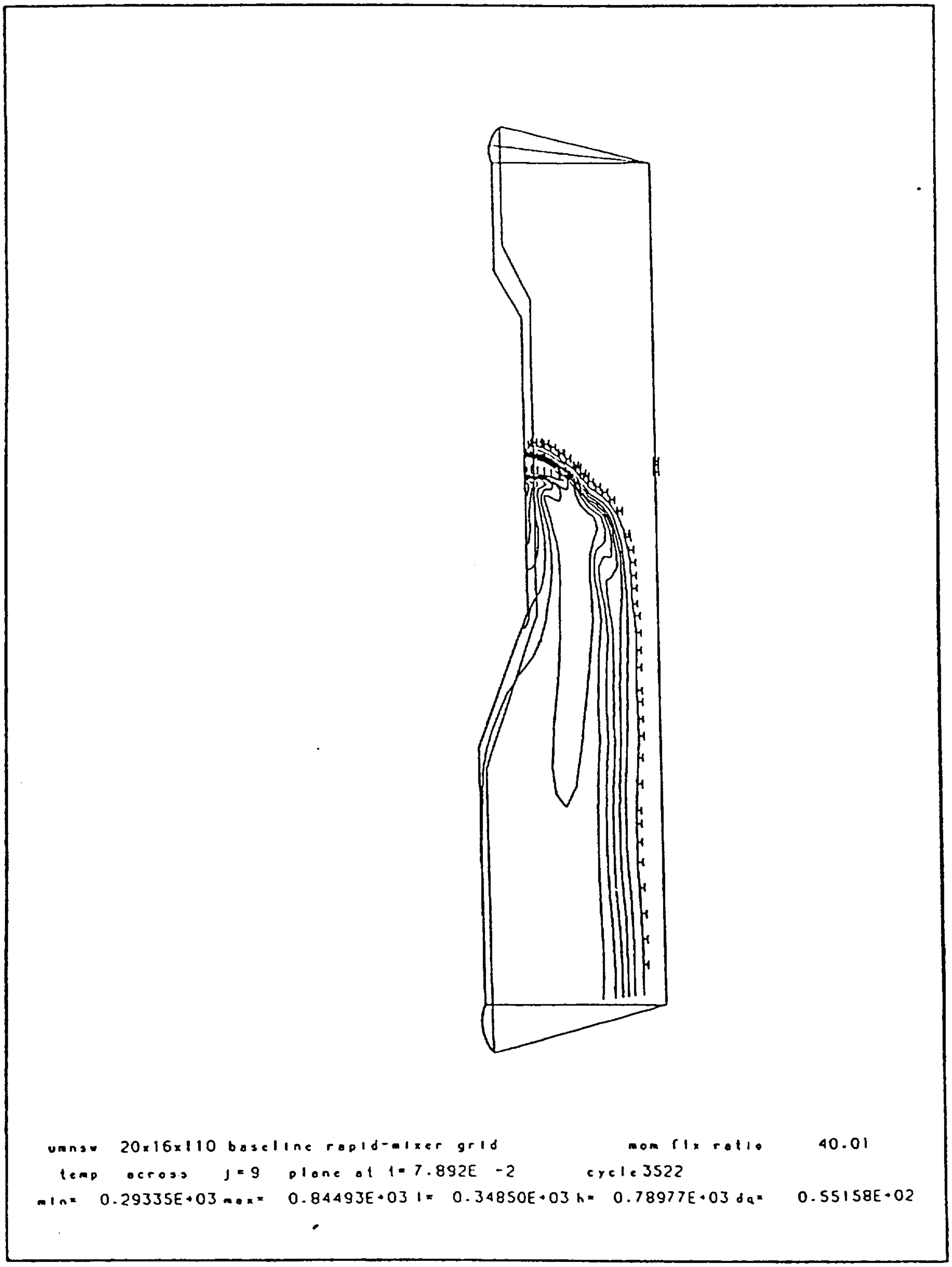
umnsw 20x16x110 baseline rapid-mixer grid mom flx ratio 40.01
temp across j=9 plane at i=7.892E -2 cycle 3522
min= 0.29335E+03 max= 0.84493E+03 l= 0.34850E+03 h= 0.78977E+03 dq= 0.55158E+02

Figure 4-37

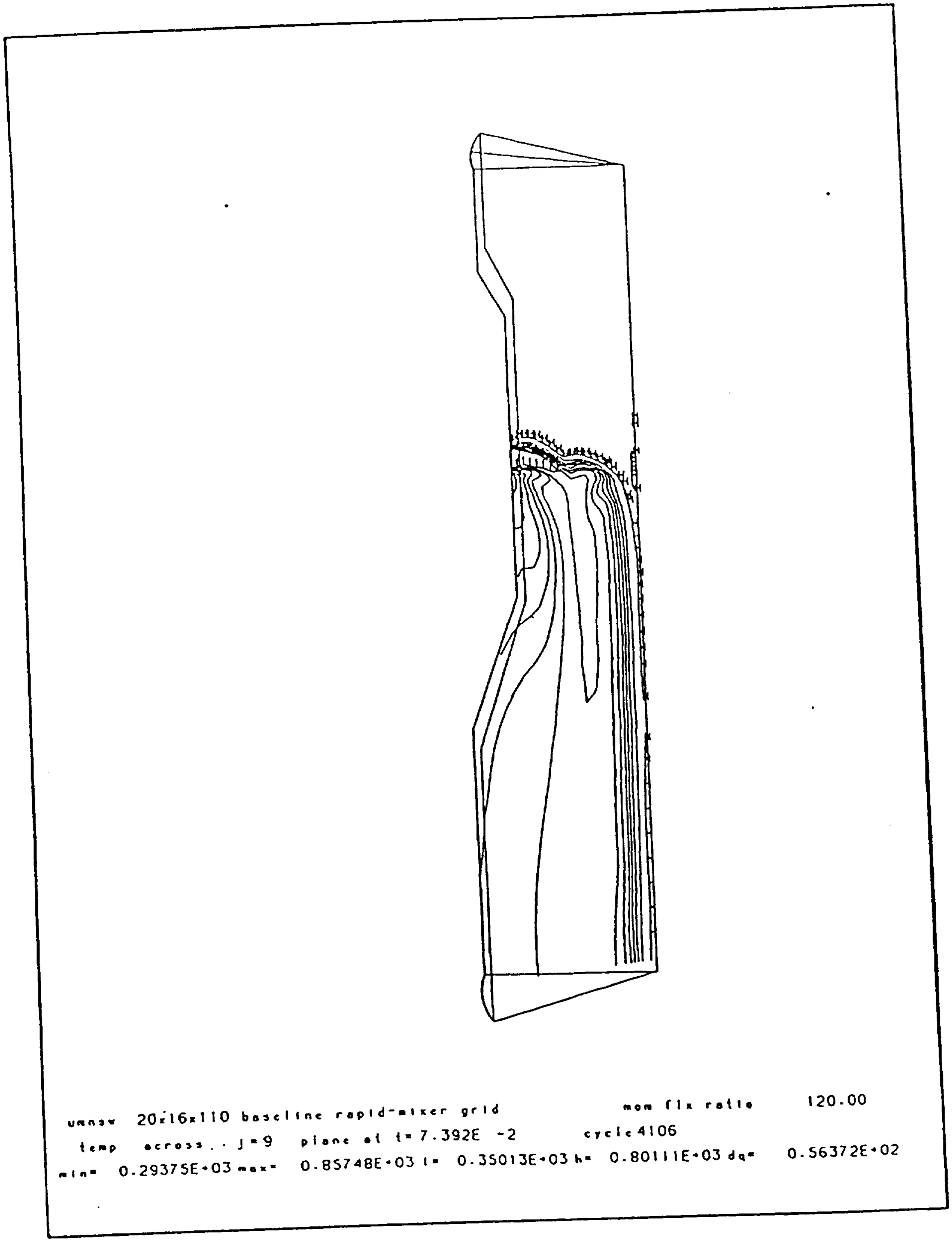
umnsw 20x16x110 baseline rapid-mixer grid
mom flx ratio 120.00
temp across . . j = 9 plane at i = 7.392E -2
cycle 4106
min= 0.29375E+03 max= 0.85748E+03 l= 0.35013E+03 h= 0.80111E+03 dq= 0.56372E+02

Figure 4-38

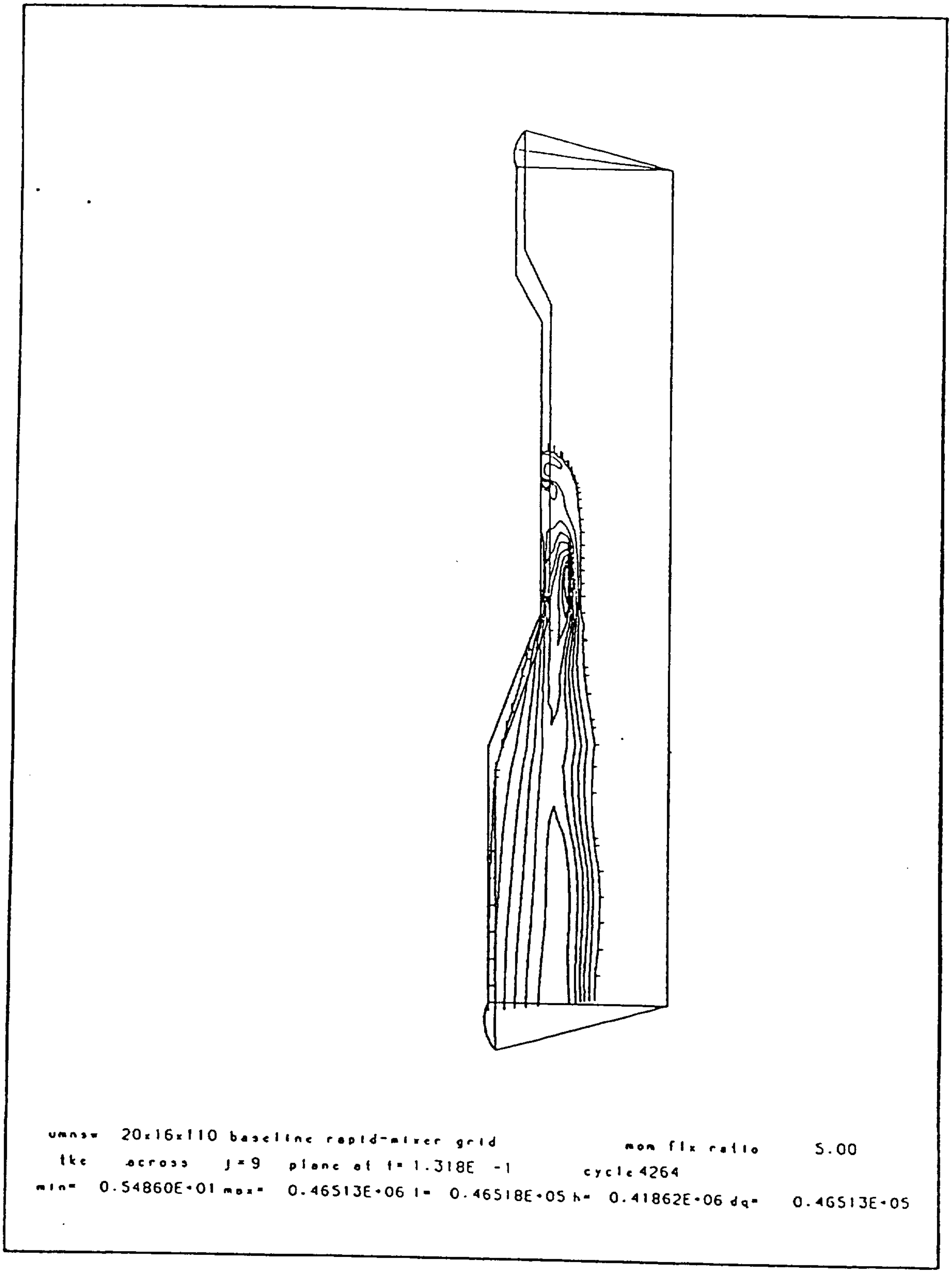
umnsw 20x16x110 baseline rapid-mixer grid
mom flx ratio 5.00
tke across j=9 plane at t= 1.318E -1
cycle 4264
min= 0.54860E+01 max= 0.46513E+06 l= 0.46518E+05 h= 0.41862E+06 dq= 0.46513E+05

Figure 4-39

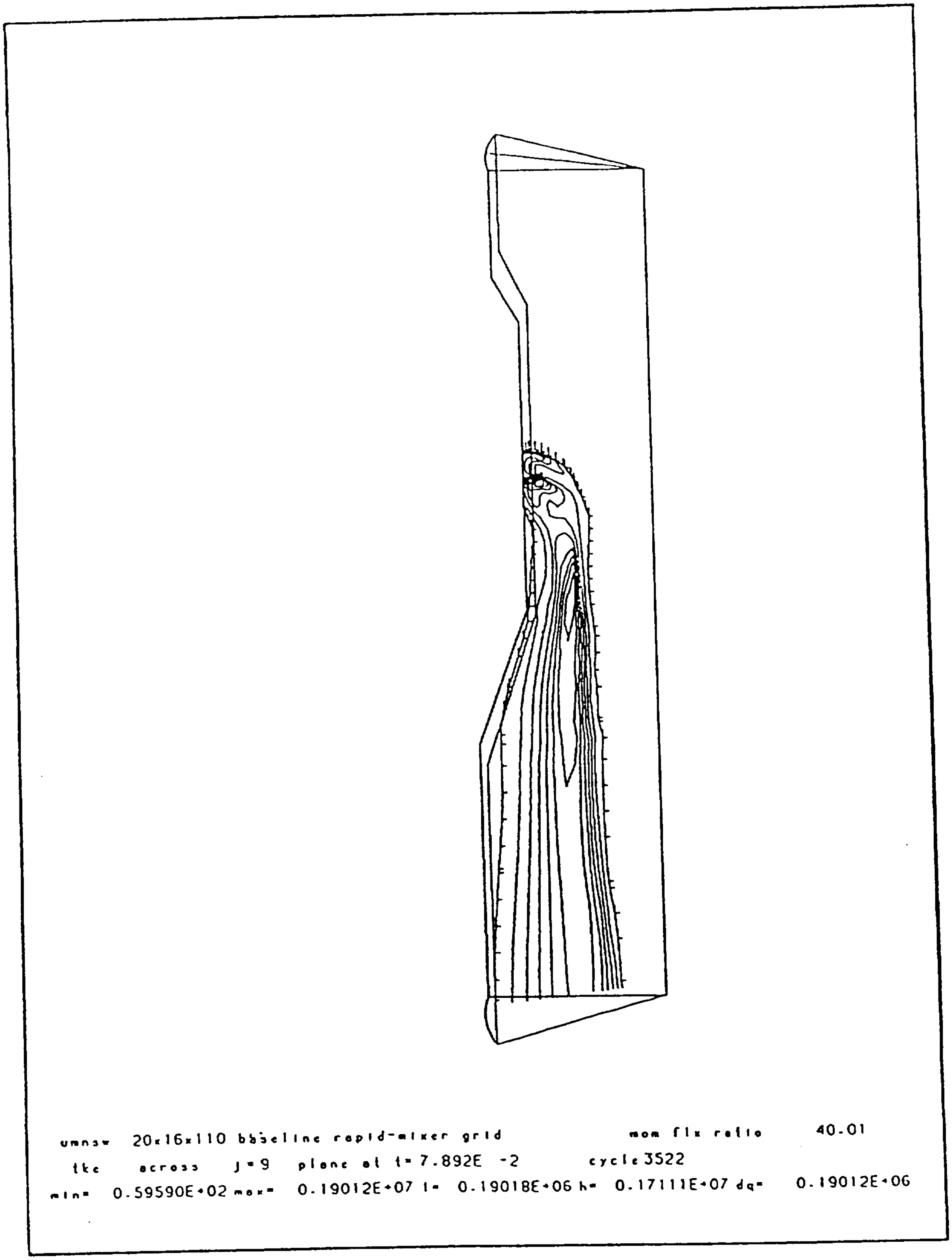
umnsw 20x16x110 baseline rapid-mixer grid
mom flx ratio 40.01
tke across j=9 plane at t= 7.892E -2
cycle 3522
min= 0.59590E+02 max= 0.19012E+07 l= 0.19018E+06 h= 0.17111E+07 dq= 0.19012E+06

Figure 4-40

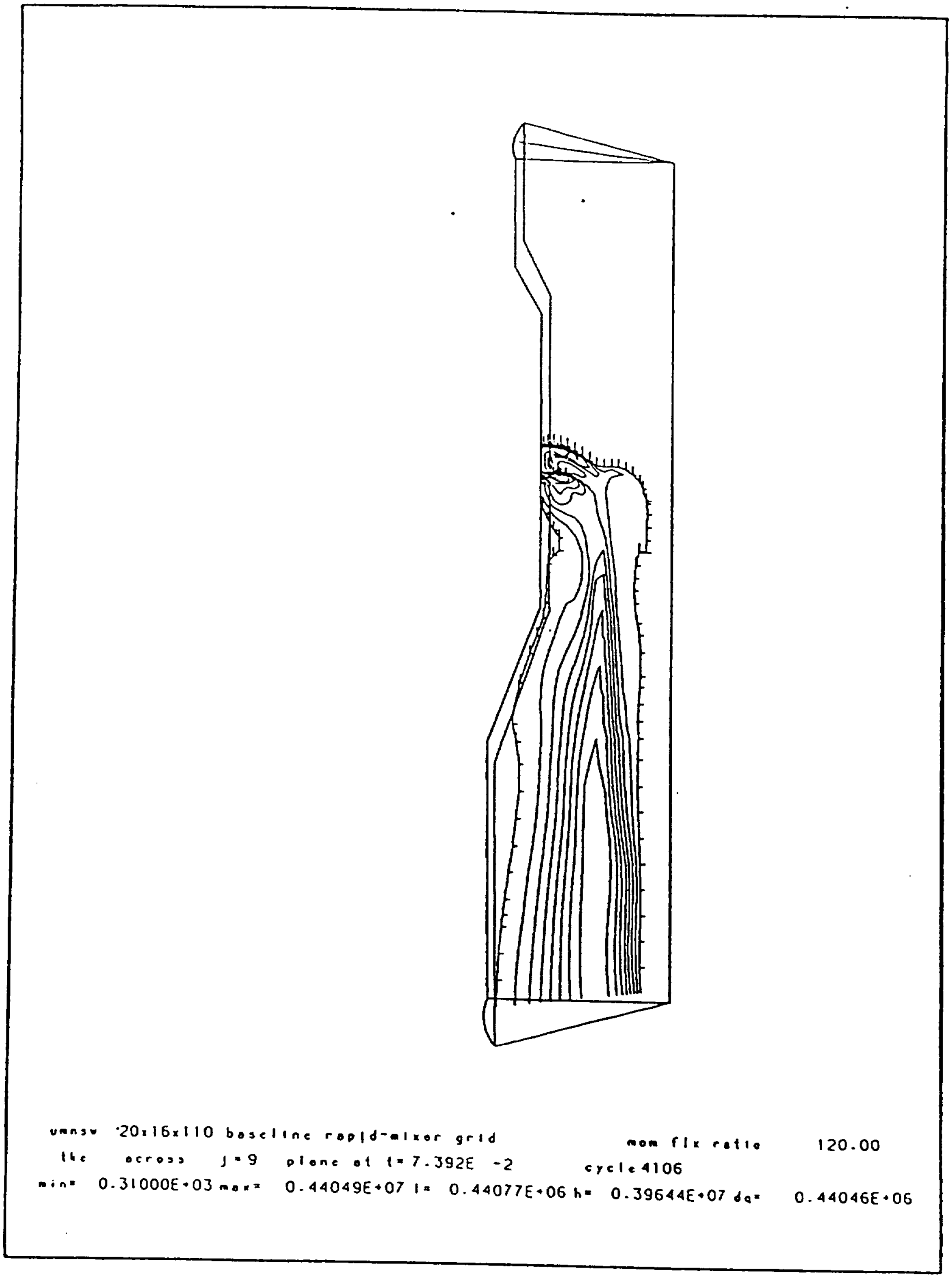
umnsw 20x16x110 baseline rapid-mixer grid
mom flx ratio 120.00
tke across j=9 plane at t=7.392E -2
cycle 4106
min= 0.31000E+03 max= 0.44049E+07 l= 0.44077E+06 h= 0.39644E+07 dq= 0.44046E+06

Figure 4-41

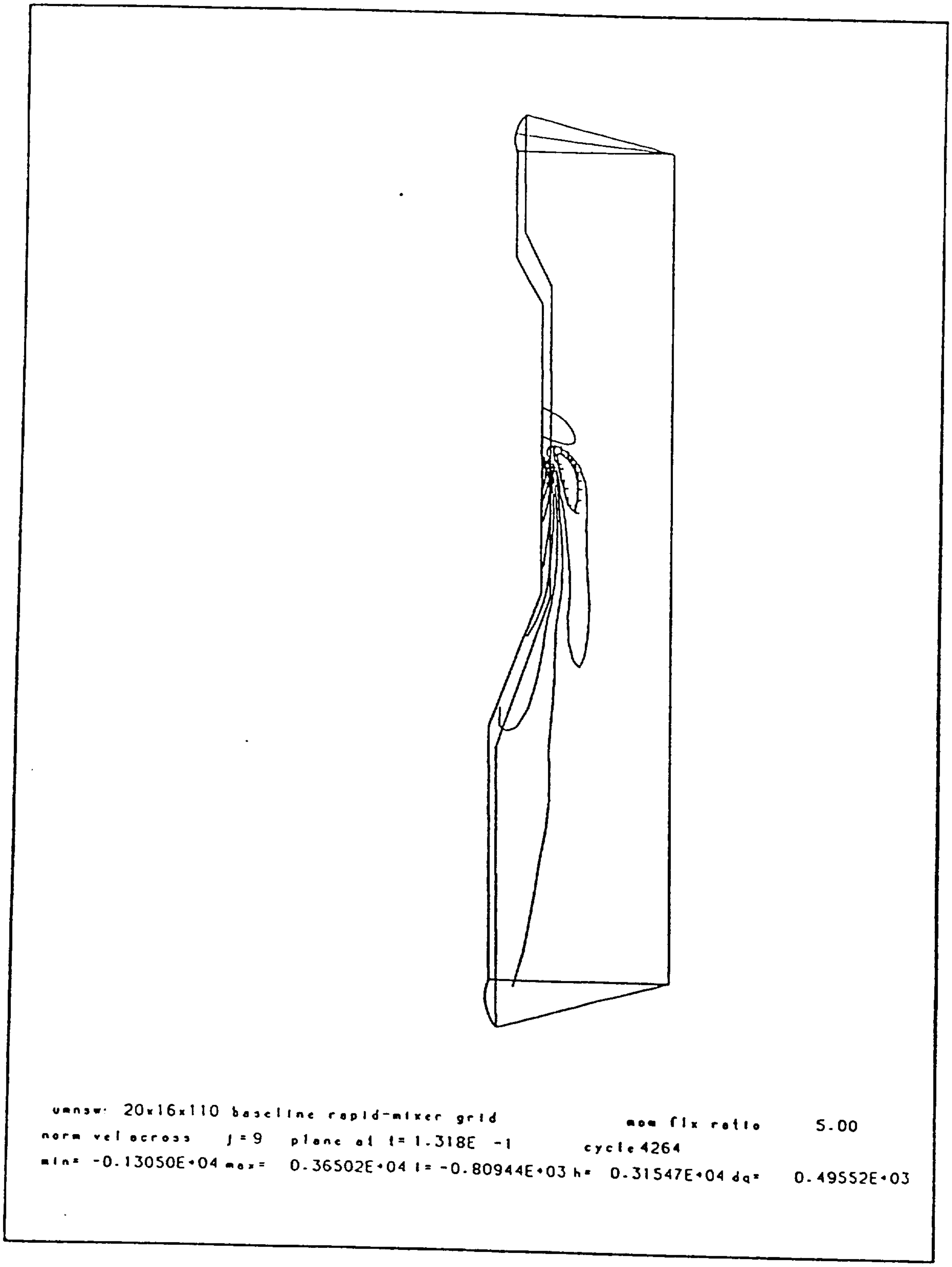

```
umnsw: 20x16x110 baseline rapid-mixer grid                    mom flx ratio     5.00
norm vel across   j = 9   plane at t= 1.318E  -1        cycle 4264
min= -0.13050E+04 max=  0.36502E+04 l= -0.80944E+03 h=  0.31547E+04 dq=   0.49552E+03
```

Figure 4-42

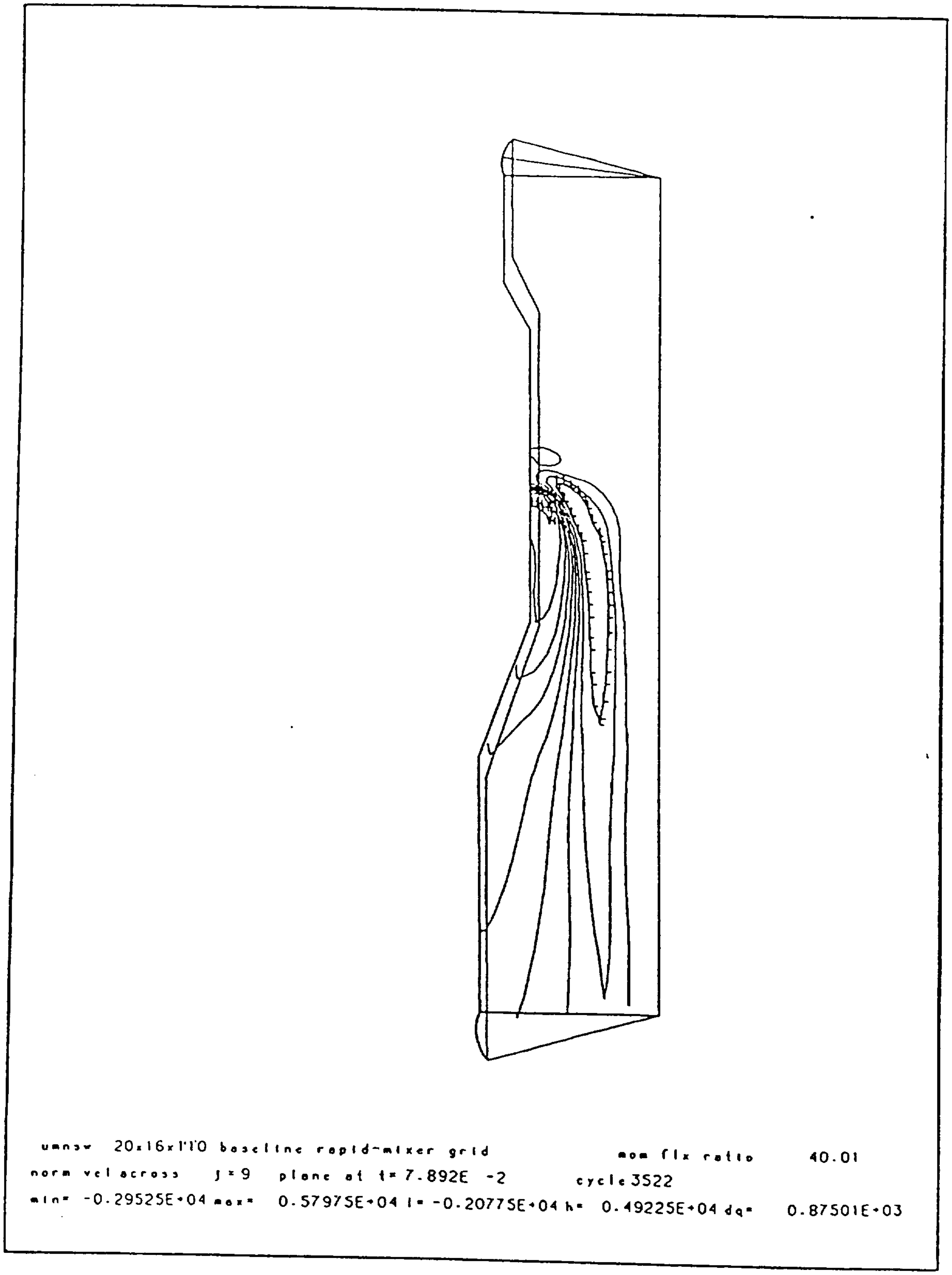
umnsw 20x16x110 baseline rapid-mixer grid
mom flx ratio 40.01
norm vel across j = 9 plane at i = 7.892E -2
cycle 3522
min= -0.29525E+04 max= 0.57975E+04 l= -0.20775E+04 h= 0.49225E+04 dq= 0.87501E+03

Figure 4-43

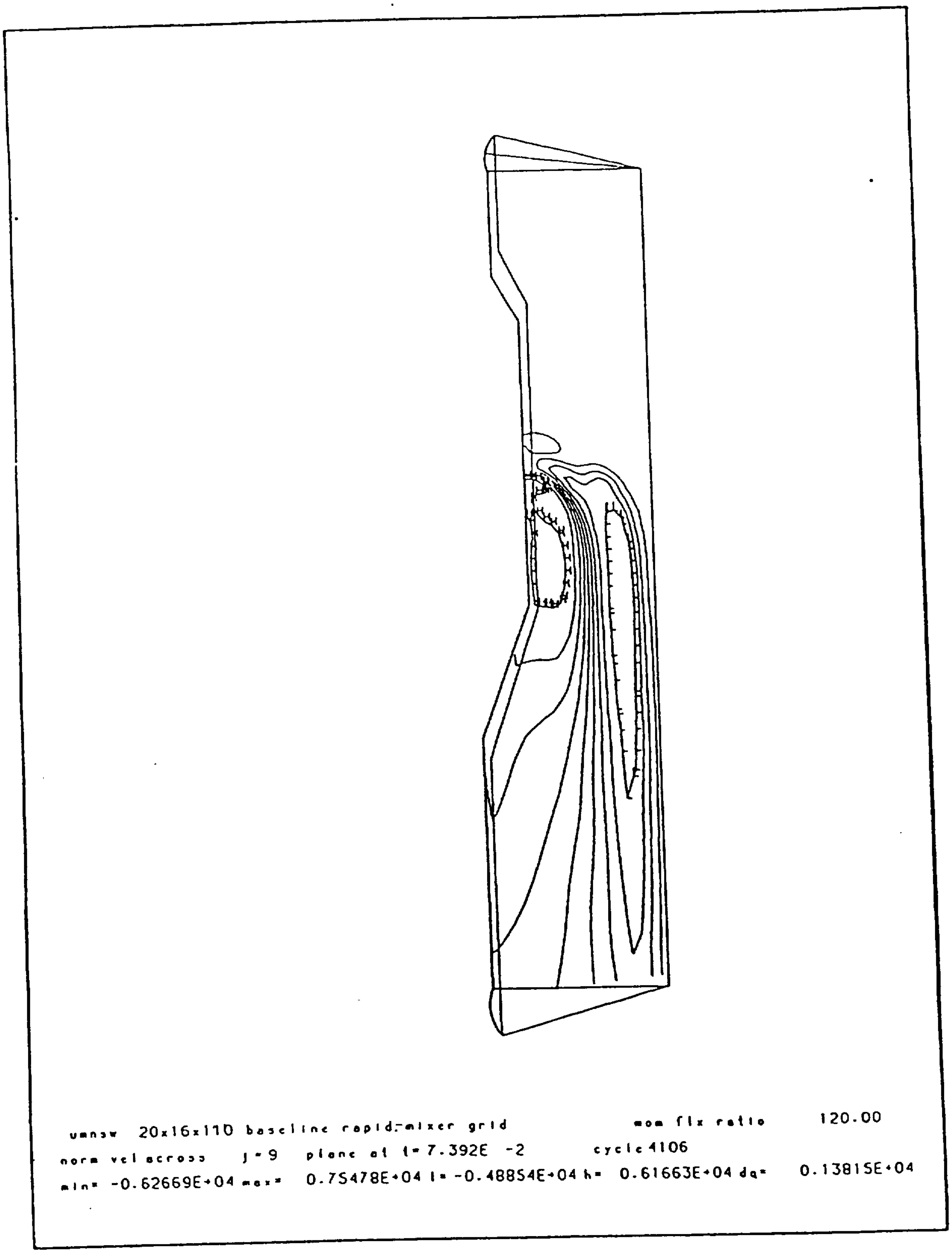
umnsw 20x16x110 baseline rapid-mixer grid
mom flx ratio 120.00
norm vel across j = 9 plane at i = 7.392E -2
cycle 4106
min= -0.62669E+04 max= 0.75478E+04 l= -0.48854E+04 h= 0.61663E+04 dq= 0.13815E+04

Figure 4-44

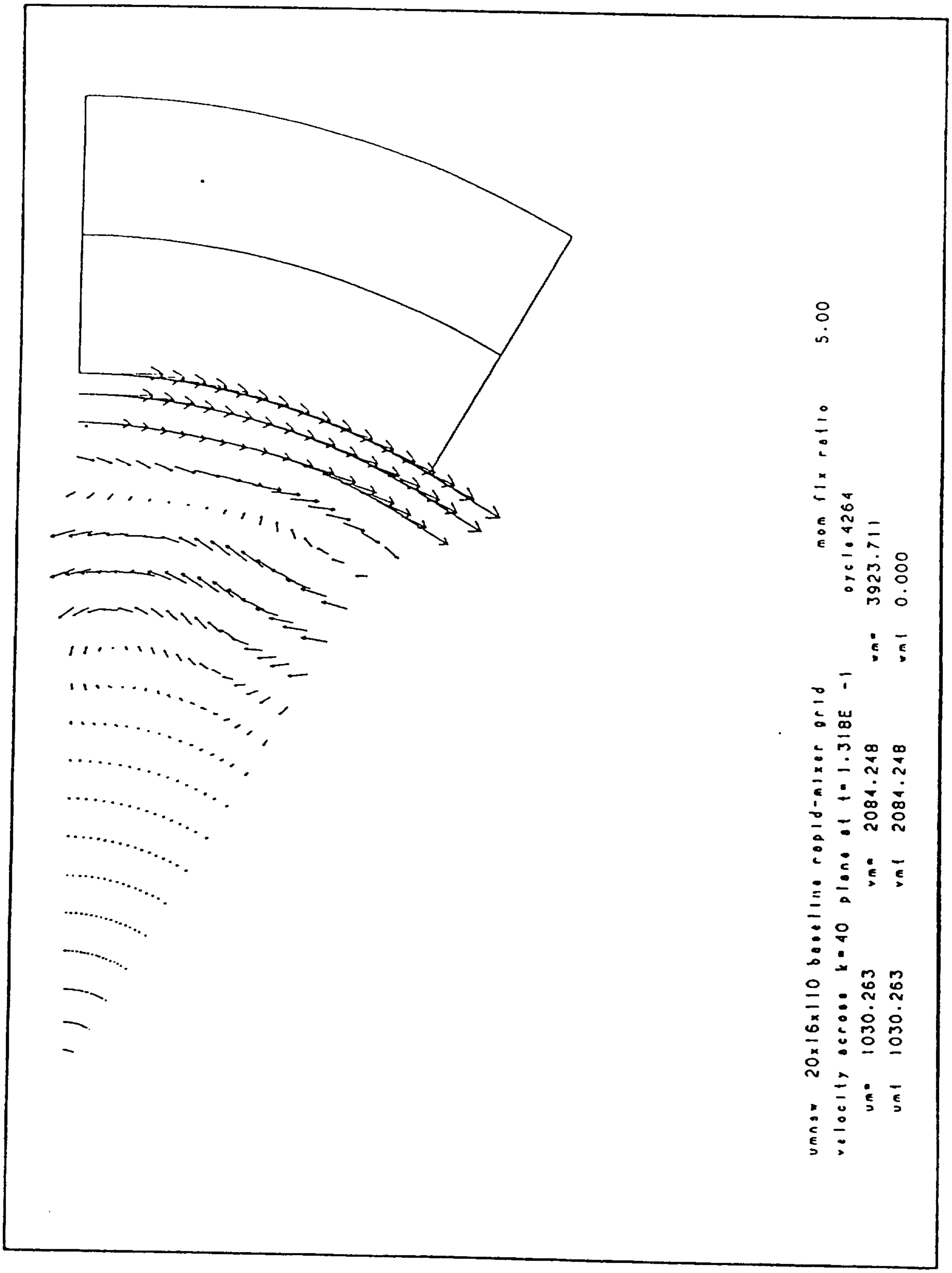
vmnsw 20x16x110 baseline rapid-mixer grid
mom flx ratio 5.00
velocity across k=40 plane at t=1.318E -1
cycle=4264
um= 1030.263
vm= 2084.248
wm= 3923.711
uml 1030.263
vml 2084.248
wml 0.000

Figure 4-45

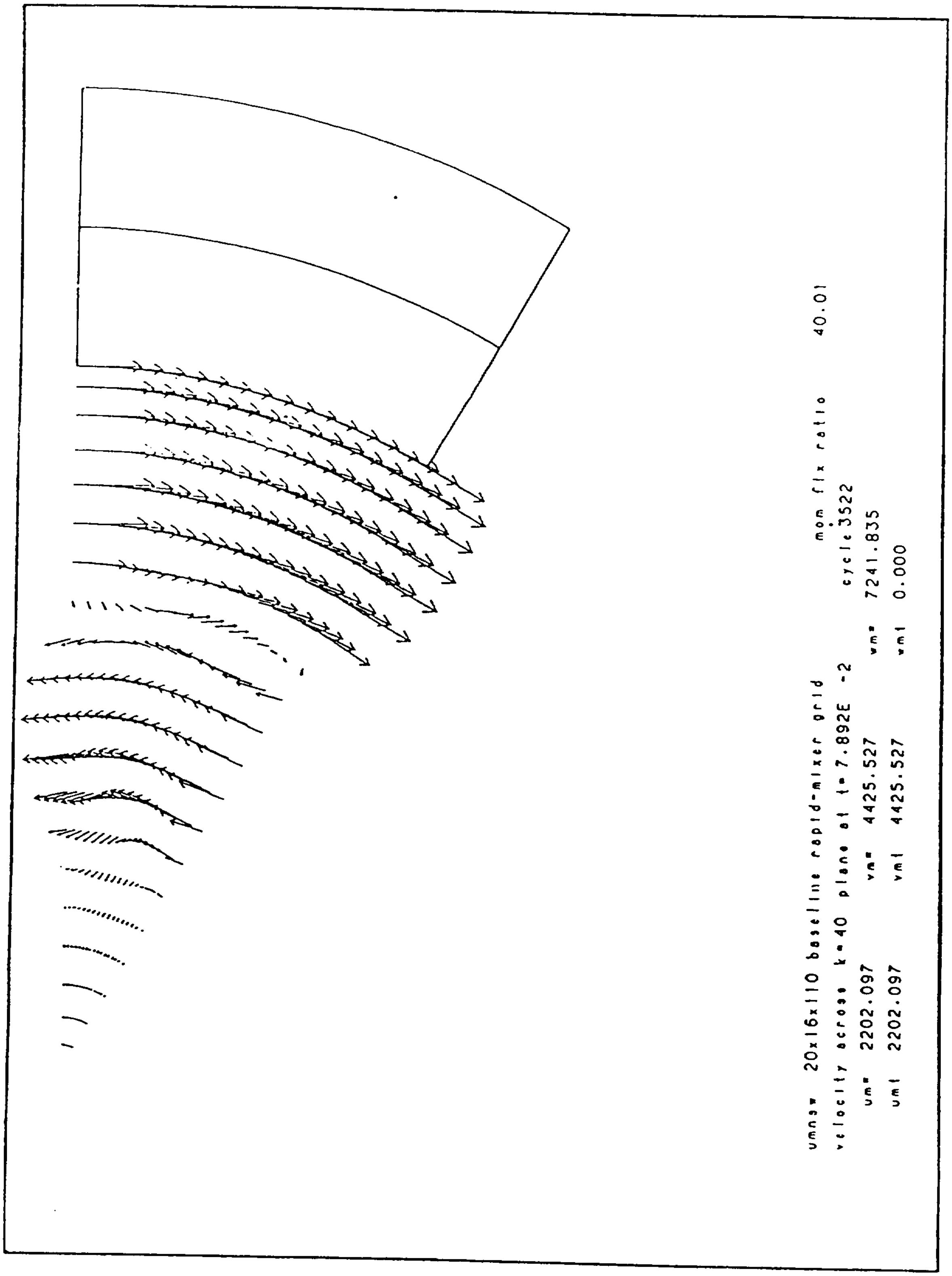
umnsw 20x16x110 baseline rapid-mixer grid
mom flx ratio 40.01
velocity across k=40 plane at t= 7.892E -2
cycle 3522
um= 2202.097
vm= 4425.527
vm= 7241.835
uml 2202.097
vml 4425.527
vml 0.000

Figure 4-46

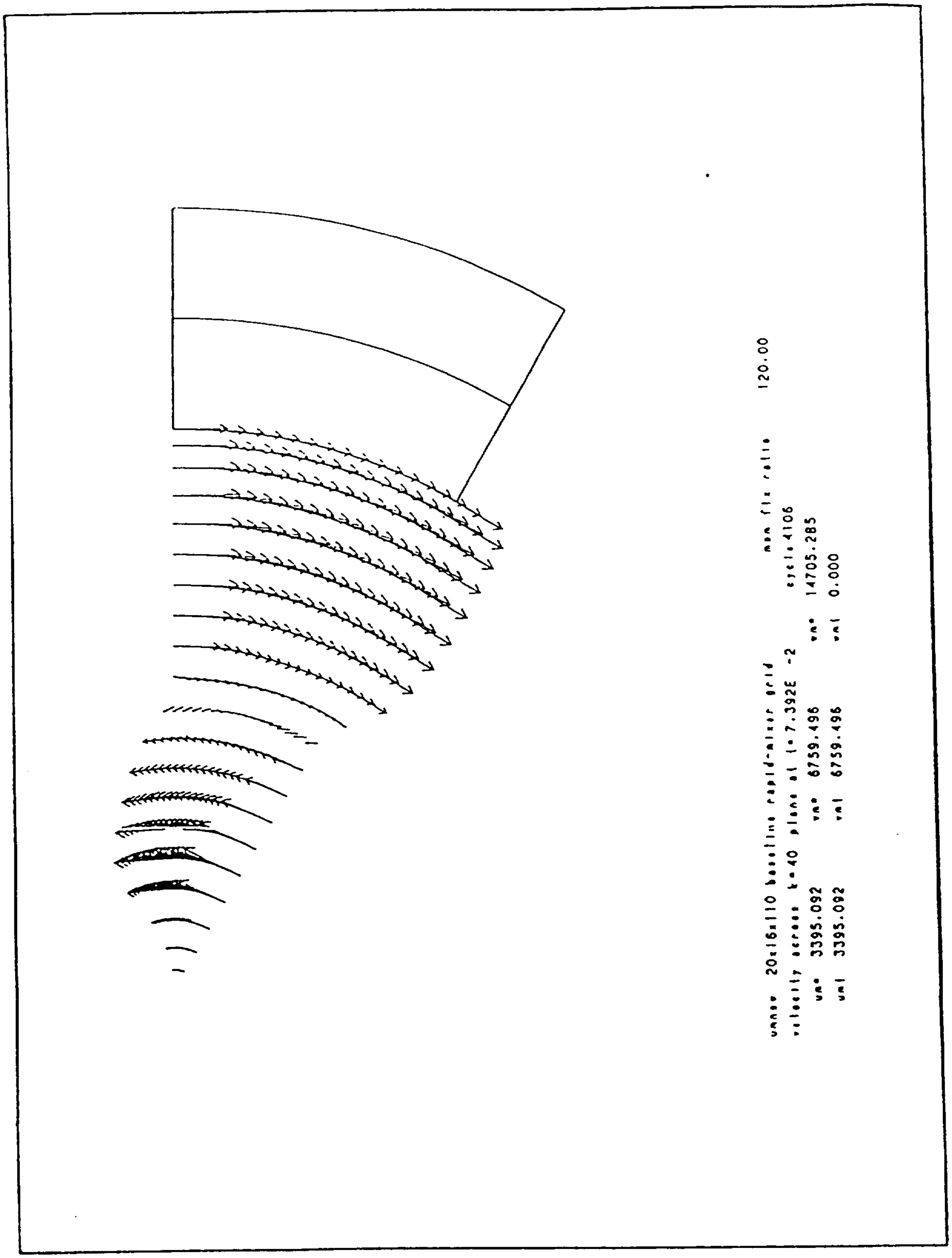
vnnse 20x16x110 baseline rapid-mixer grid
max flx ratio 120.00
velocity across k=40 plane at t=7.392E -2
cycle=4106
vm= 3395.092
vm= 6759.496
vm= 14705.285
vml 3395.092
vml 6759.496
vml 0.000

Figure 4-47

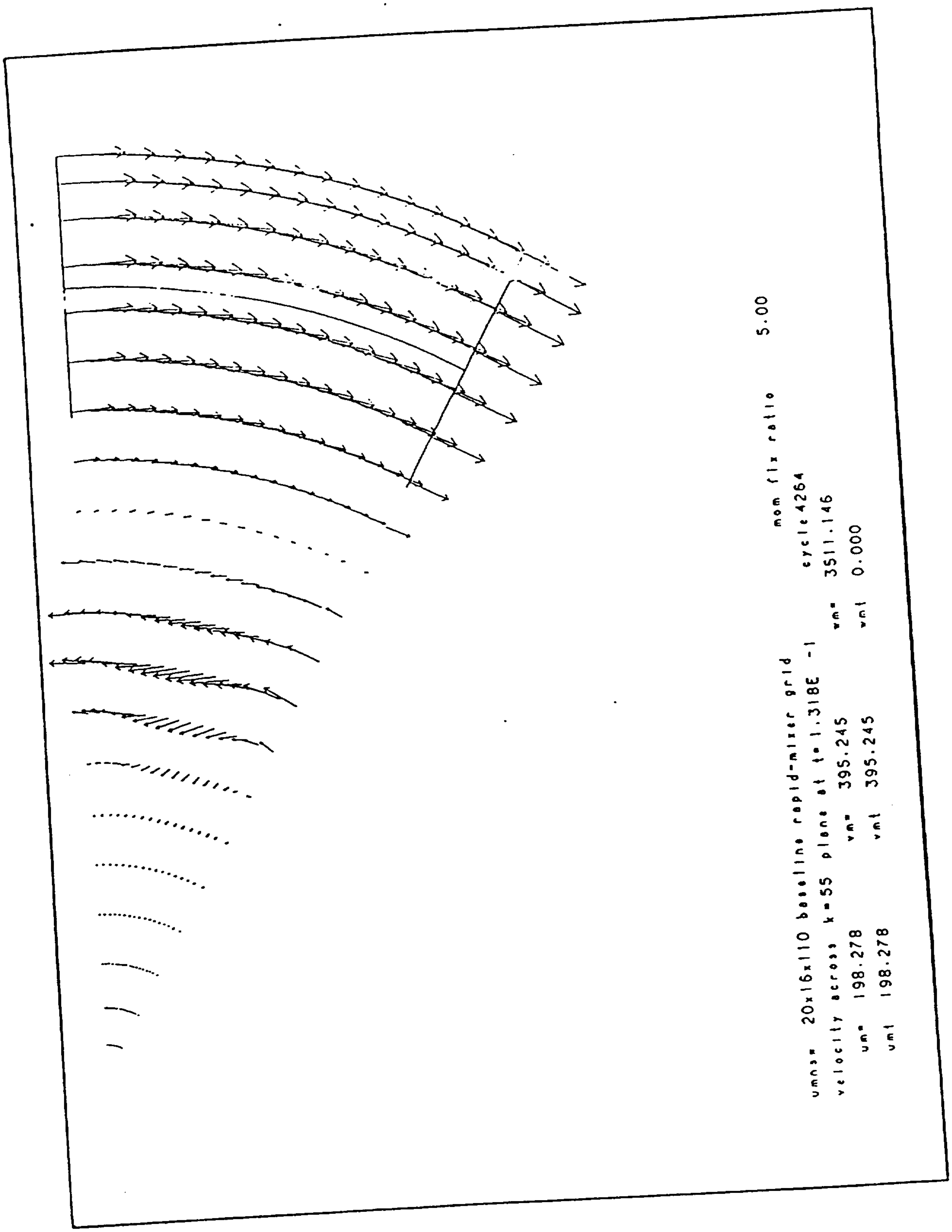mom flx ratio 5.00
umns= 20x16x110 baseline rapid-mixer grid
cycle 4264
velocity across k=55 plane at t= 1.318E -1
vm= 198.278
vm= 395.245
vm= 3511.146
vnl 198.278
vnl 395.245
vnl 0.000

Figure 4-48

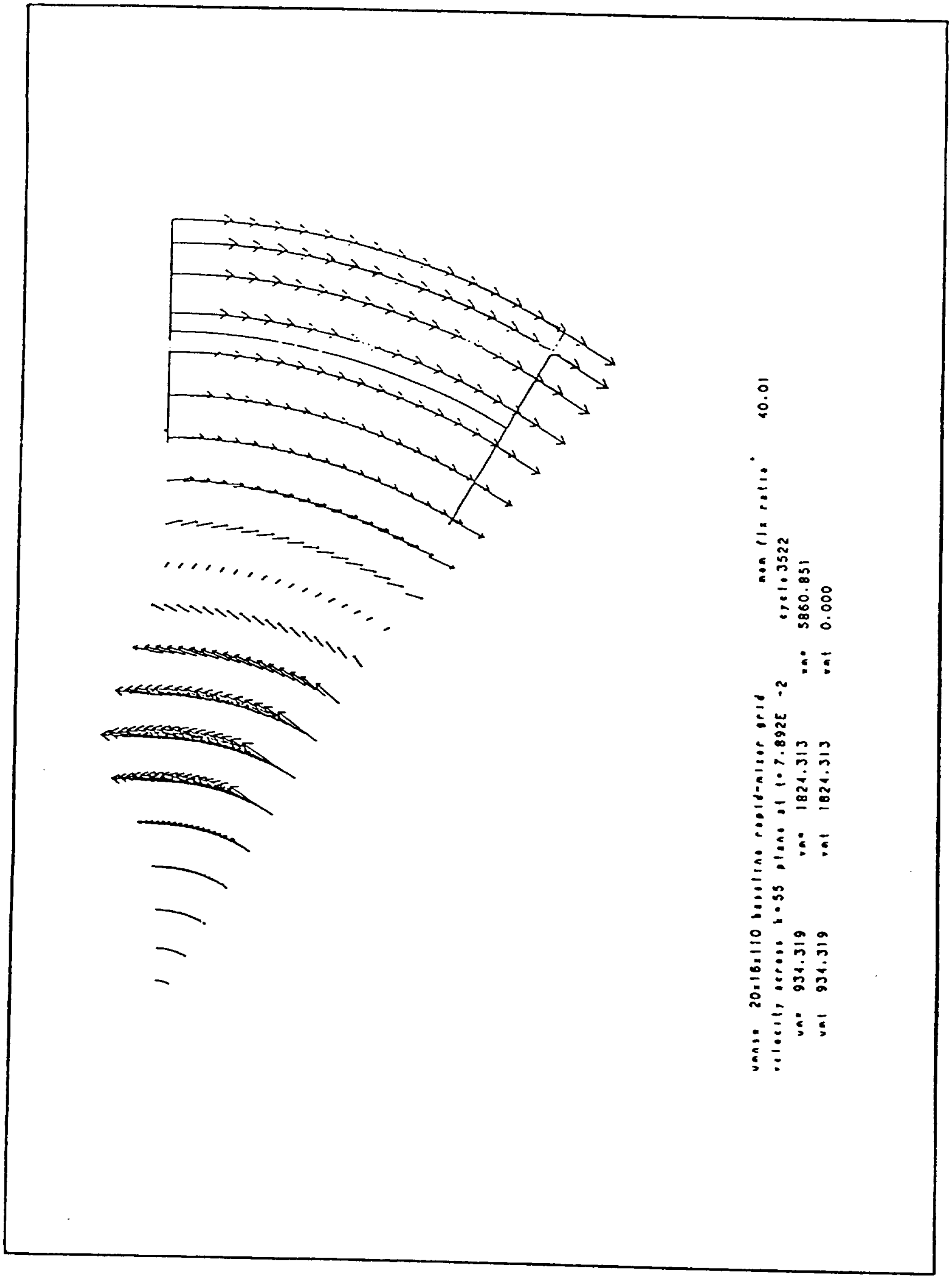
vanes 20x16x110 baseline rapid-mixer grid
mom flx ratio' 40.01
velocity across k=55 plane at t=7.892E -2
cycle=3522
vm* 934.319
vm* 1824.313
vm* 5860.851
vmt 934.319
vmt 1824.313
vmt 0.000

Figure 4-49

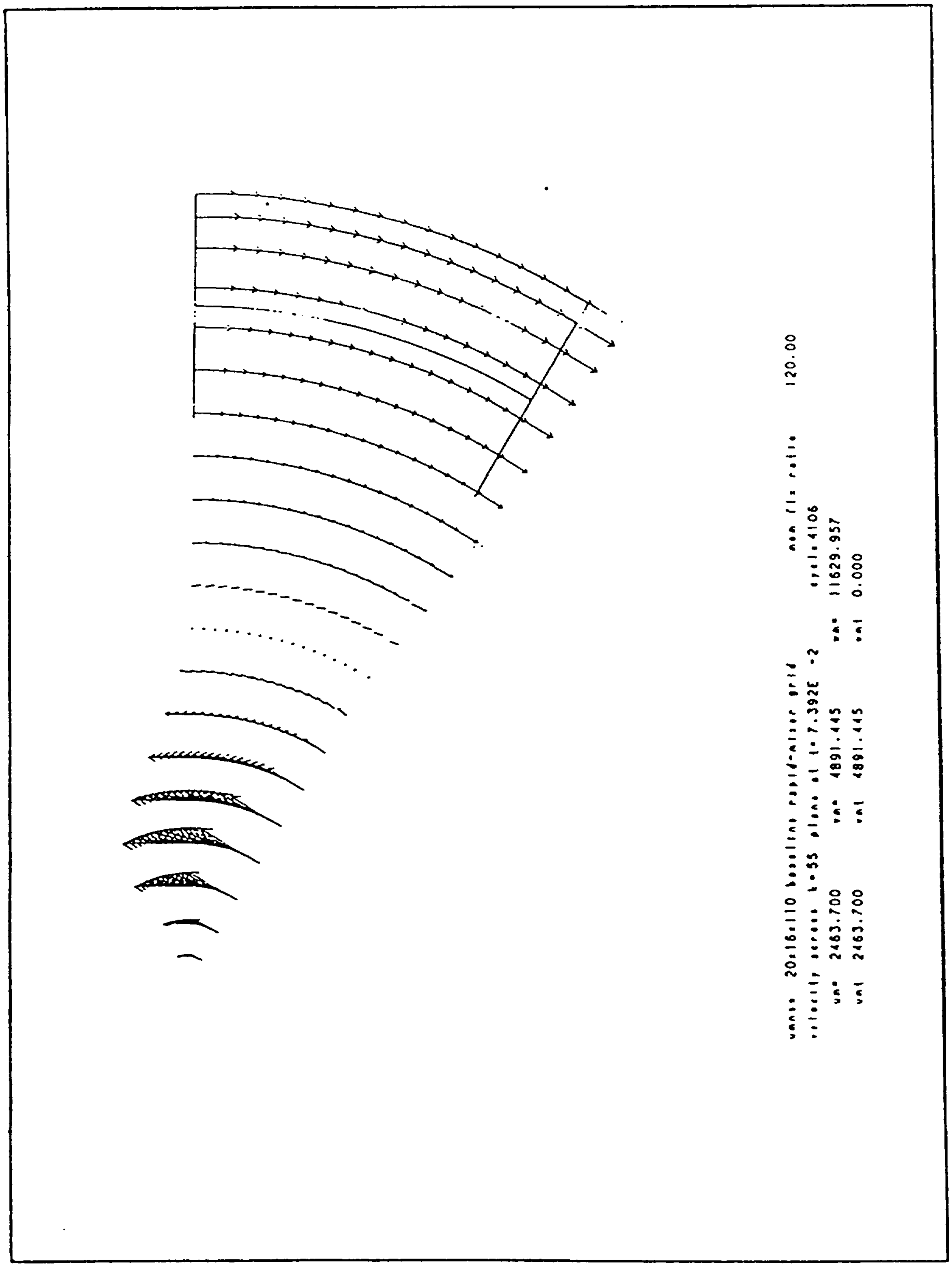
vanes 20x16x110 baseline rapid-mixer grid
mom flx ratio 120.00
velocity across k=55 plane at t=7.392E -2
cycle=4106
vn= 2463.700
vn= 4891.445
vn= 11629.957
vnl 2463.700
vnl 4891.445
vnl 0.000

Figure 4-50

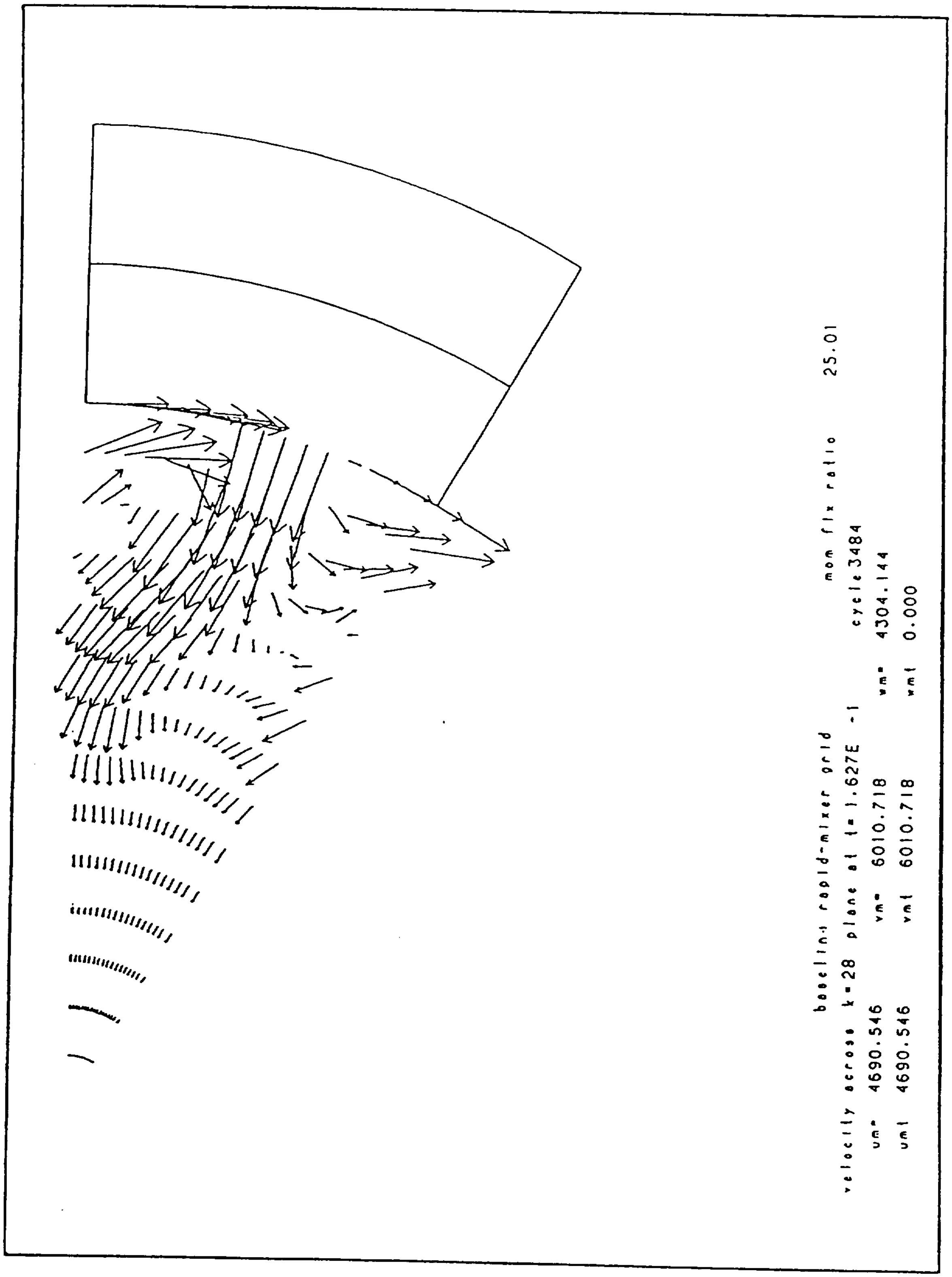
baseline rapid-mixer grid
velocity across k=28 plane at t=1.627E -1
mom flx ratio 25.01
cycle 3484
um= 4690.546
vm= 6010.718
wm= 4304.144
umt 4690.546
vmt 6010.718
wmt 0.000

Figure 4-51

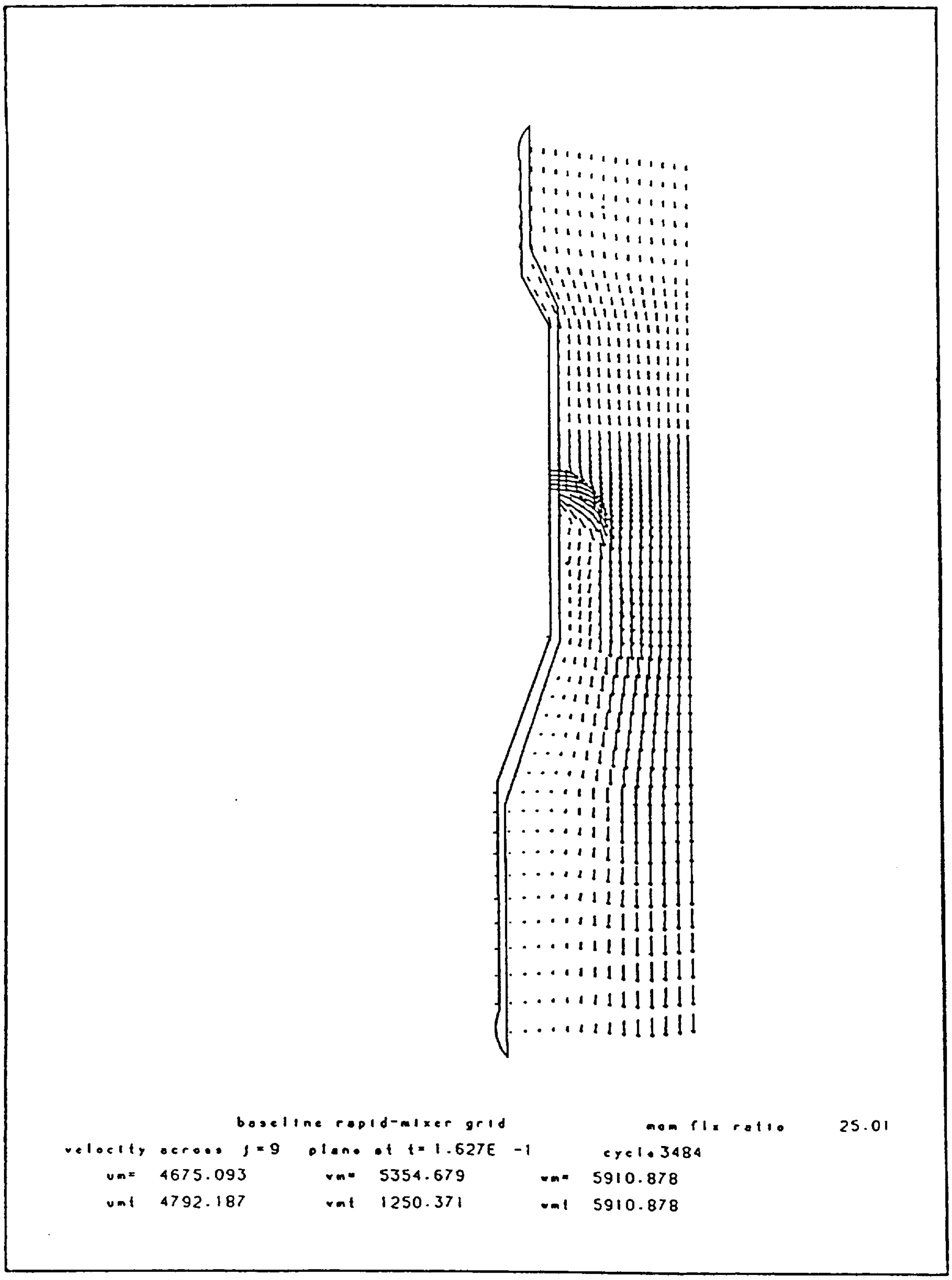
baseline rapid-mixer grid
mom flx ratio 25.01
velocity across j=9 plane at t= 1.627E -1
cycle=3484
um= 4675.093
vm= 5354.679
wm= 5910.878
uml 4792.187
vml 1250.371
wml 5910.878

Figure 4-52

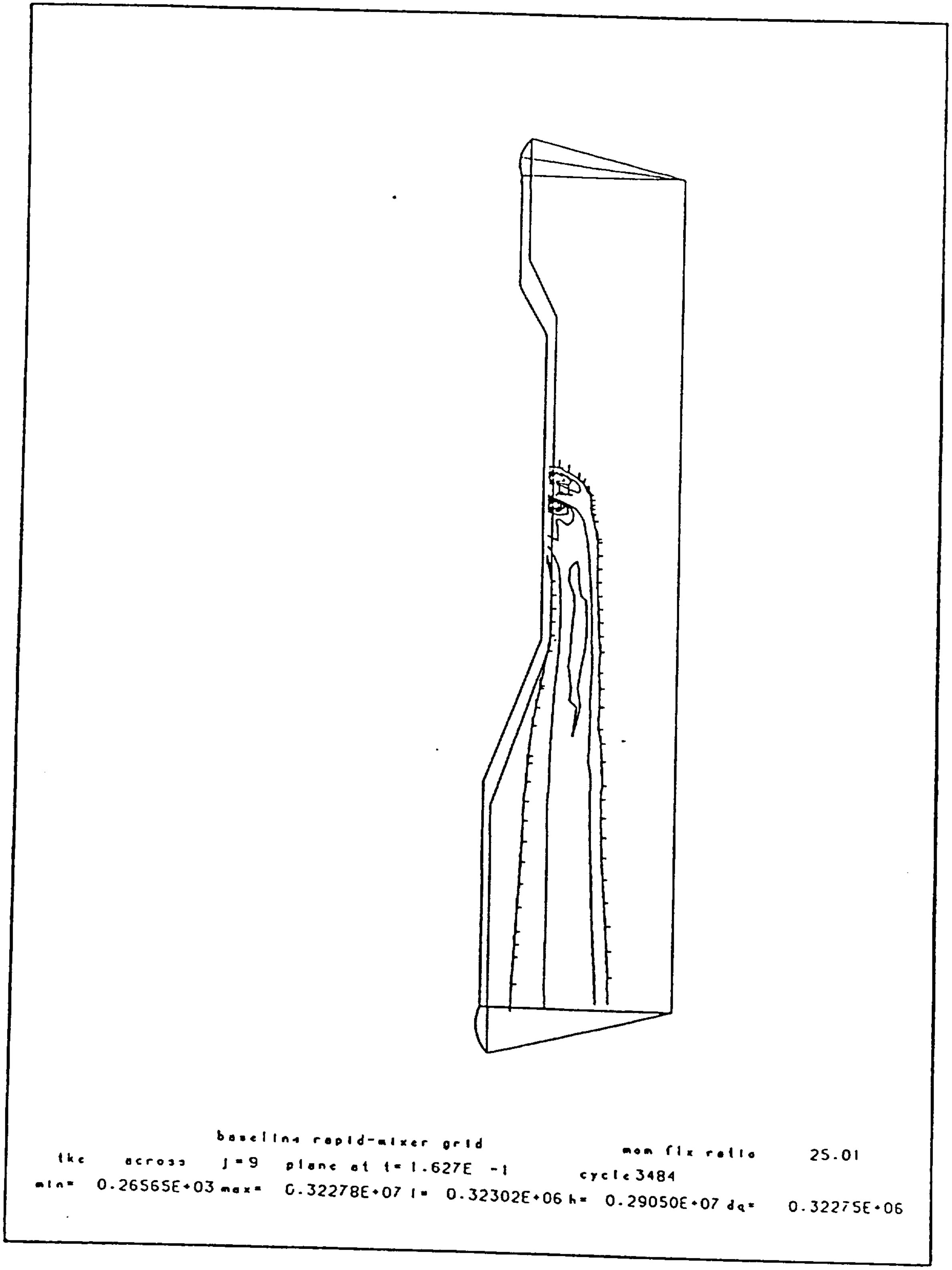
baseline rapid-mixer grid
mom flx ratio 25.01
tke across j=9 plane at i=1.627E -1
cycle 3484
min= 0.26565E+03 max= 0.32278E+07 l= 0.32302E+06 h= 0.29050E+07 dq= 0.32275E+06

Figure 4-53

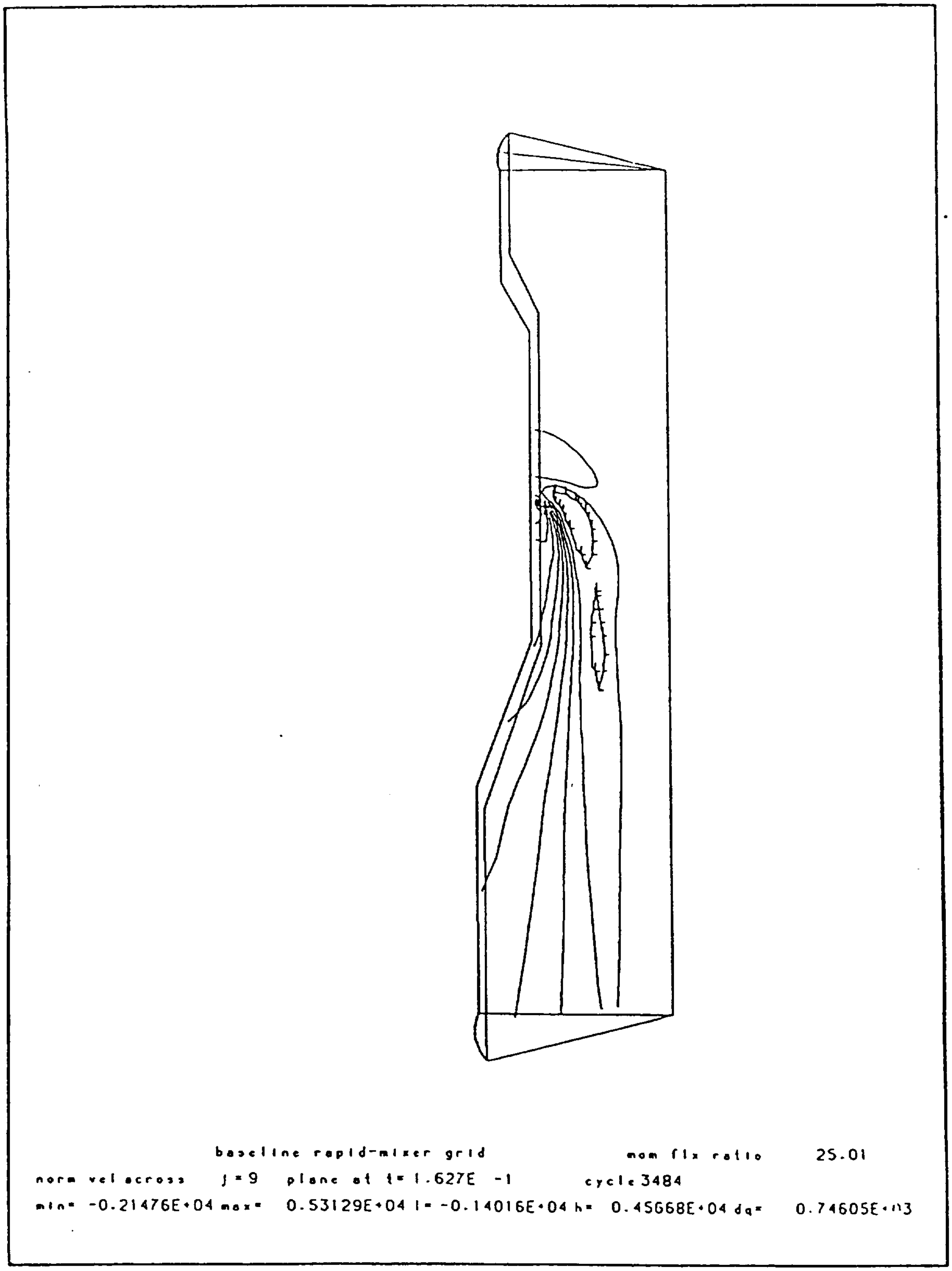
baseline rapid-mixer grid
mom flx ratio 25.01
norm vel across j = 9 plane at t= 1.627E -1
cycle 3484
min= -0.21476E+04 max= 0.53129E+04 l= -0.14016E+04 h= 0.45668E+04 dq= 0.74605E+03

Figure 4-54

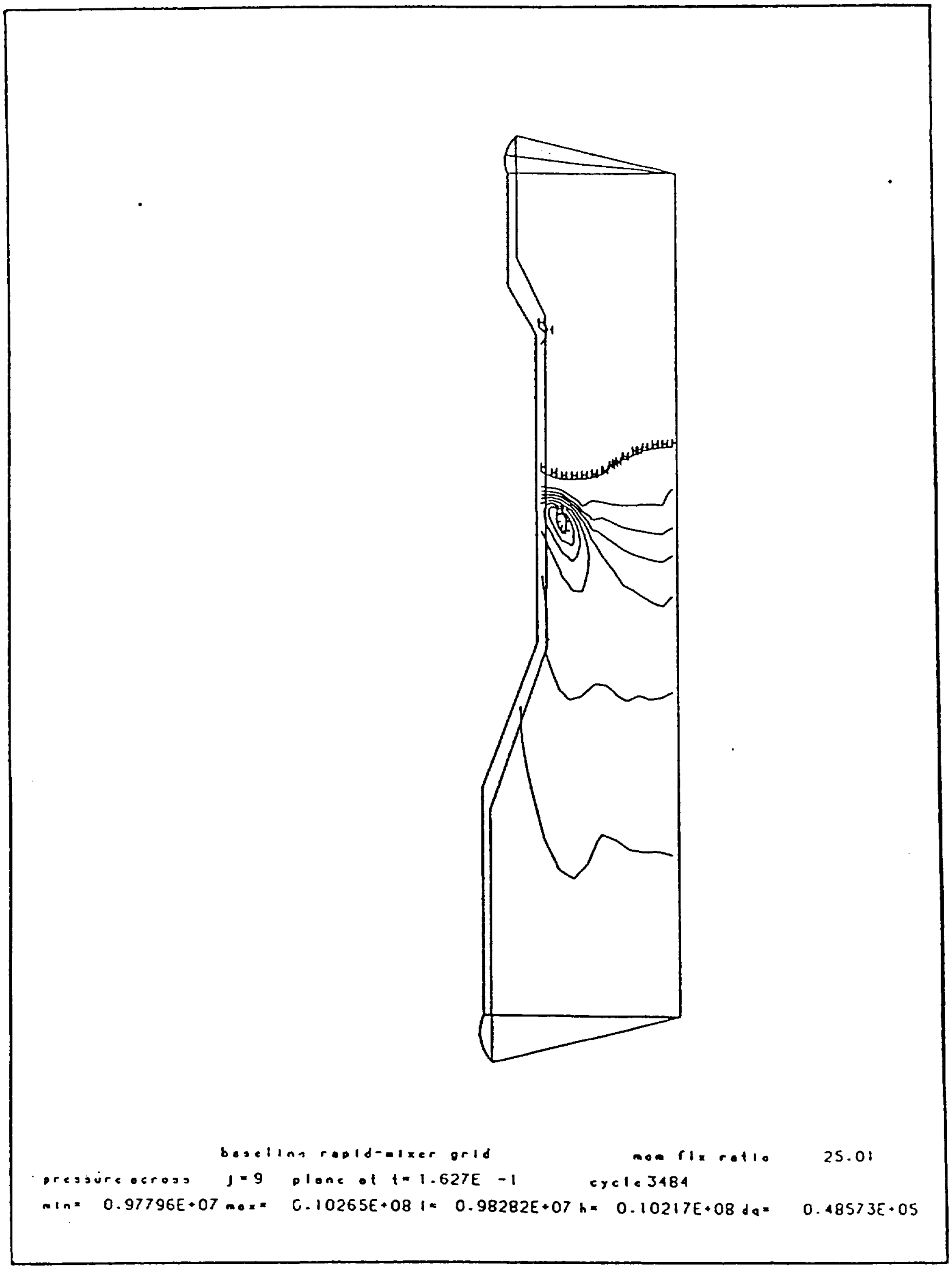
baseline rapid-mixer grid
mom flx ratio 25.01
pressure across j=9 plane at i=1.627E -1
cycle 3484
min= 0.97796E+07 max= 0.10265E+08 l= 0.98282E+07 h= 0.10217E+08 dq= 0.48573E+05

Figure 4-55

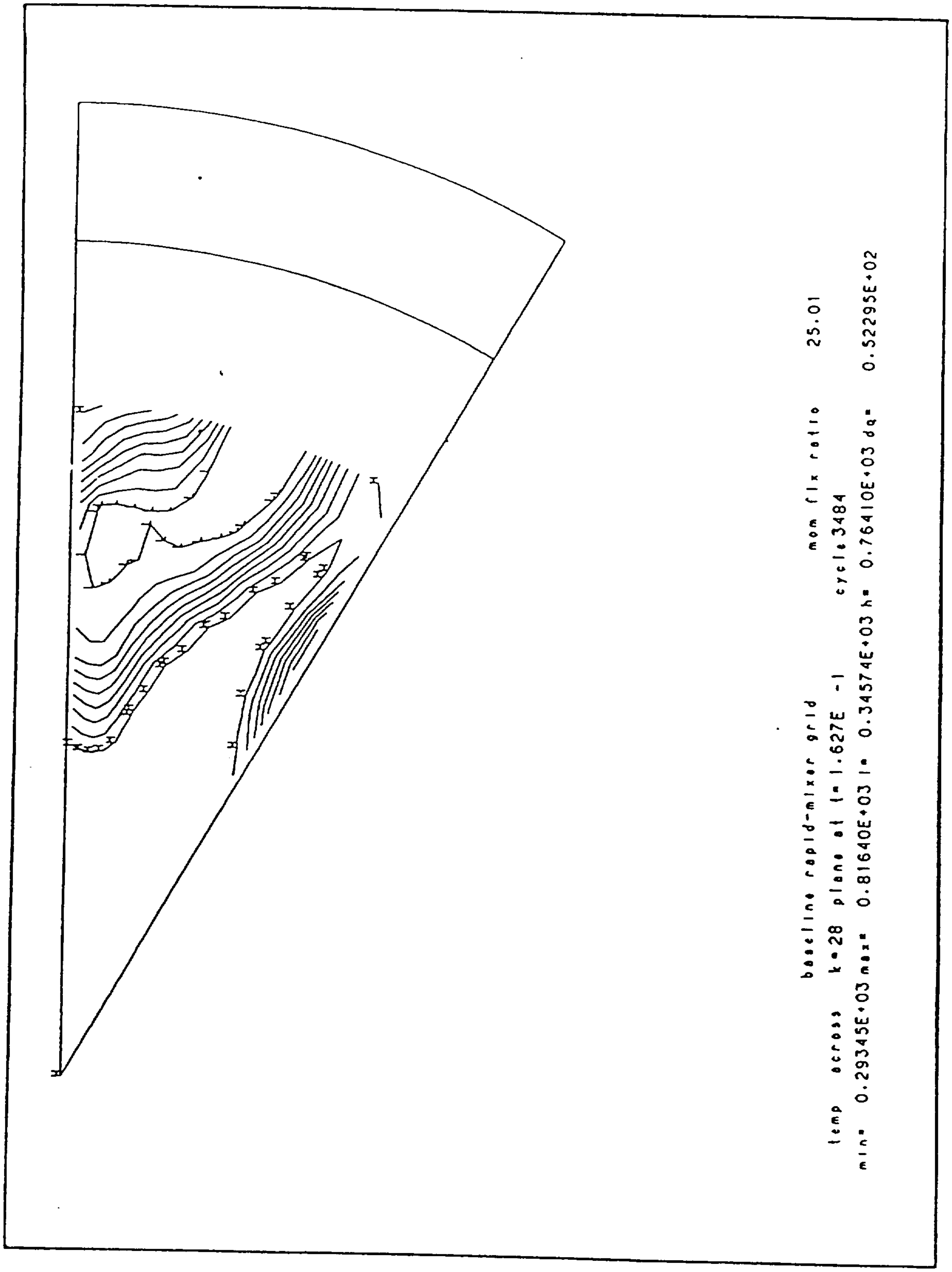
baseline rapid-mixer grid mom flx ratio 25.01
temp across k=28 plane at t= 1.627E -1 cycle=3484
min= 0.29345E+03 max= 0.81640E+03 l= 0.34574E+03 h= 0.76410E+03 dq= 0.52295E+02

Figure 4-56

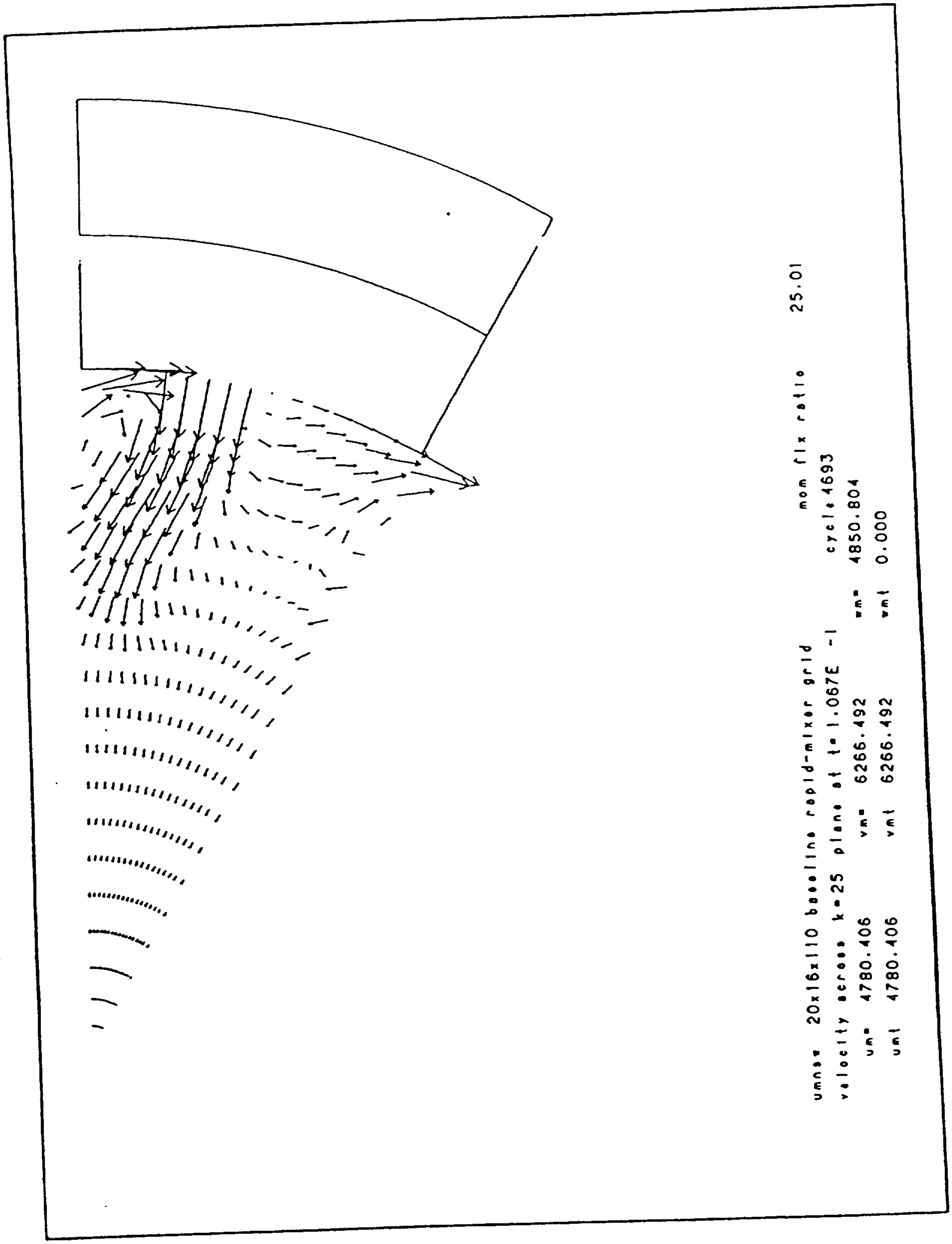
umnsw 20x16x110 baseline rapid-mixer grid
mom flx ratio 25.01
velocity across k=25 plane at t= 1.067E -1
cycle4693
um= 4780.406
vm= 6266.492
wm= 4850.804
uml 4780.406
vml 6266.492
wml 0.000

Figure 4-57

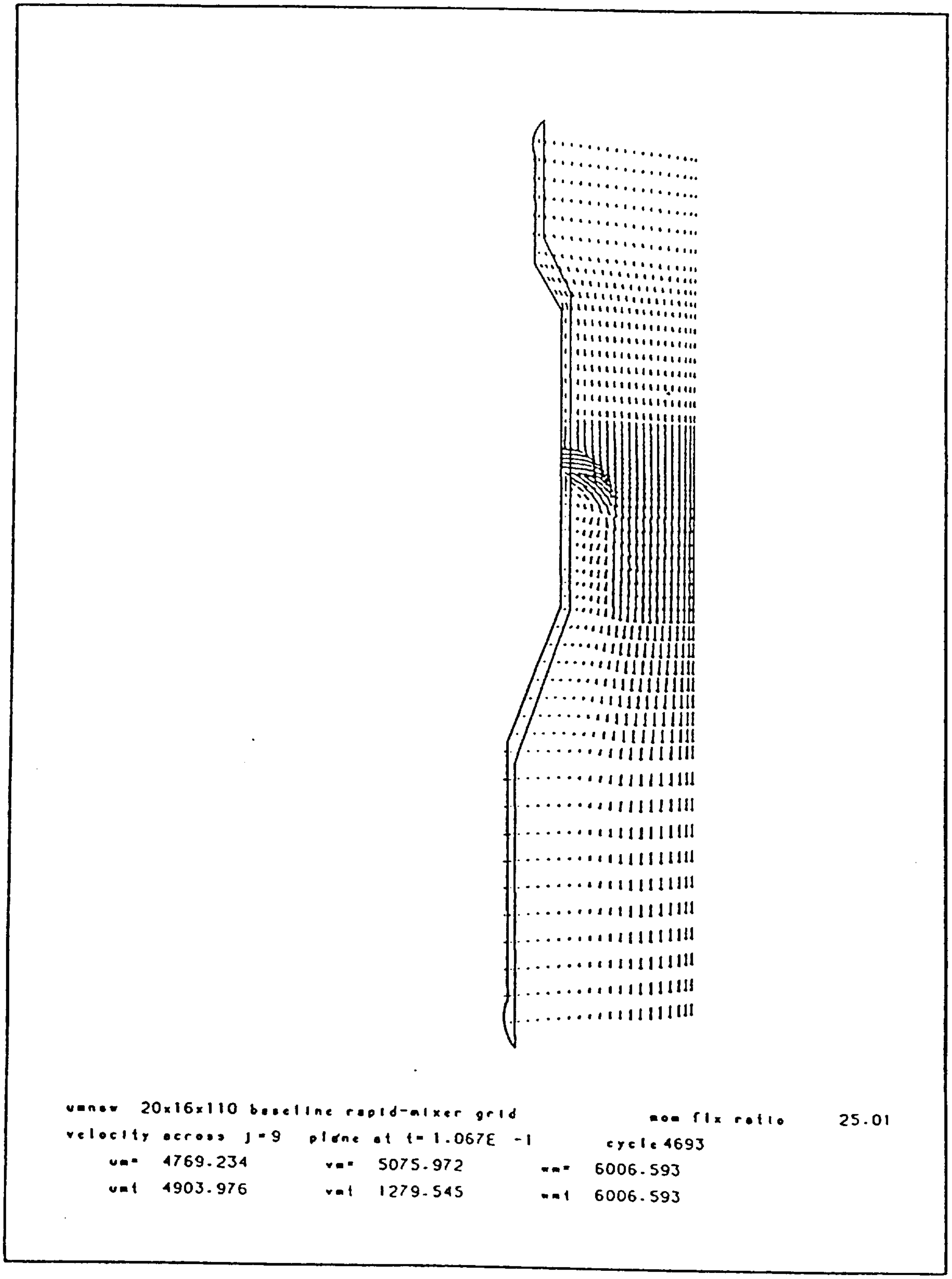
umnew 20x16x110 baseline rapid-mixer grid
mom flx ratio 25.01
velocity across j=9 plane at t= 1.067E -1
cycle 4693
um= 4769.234
vm= 5075.972
wm= 6006.593
uml 4903.976
vml 1279.545
wml 6006.593

Figure 4-58

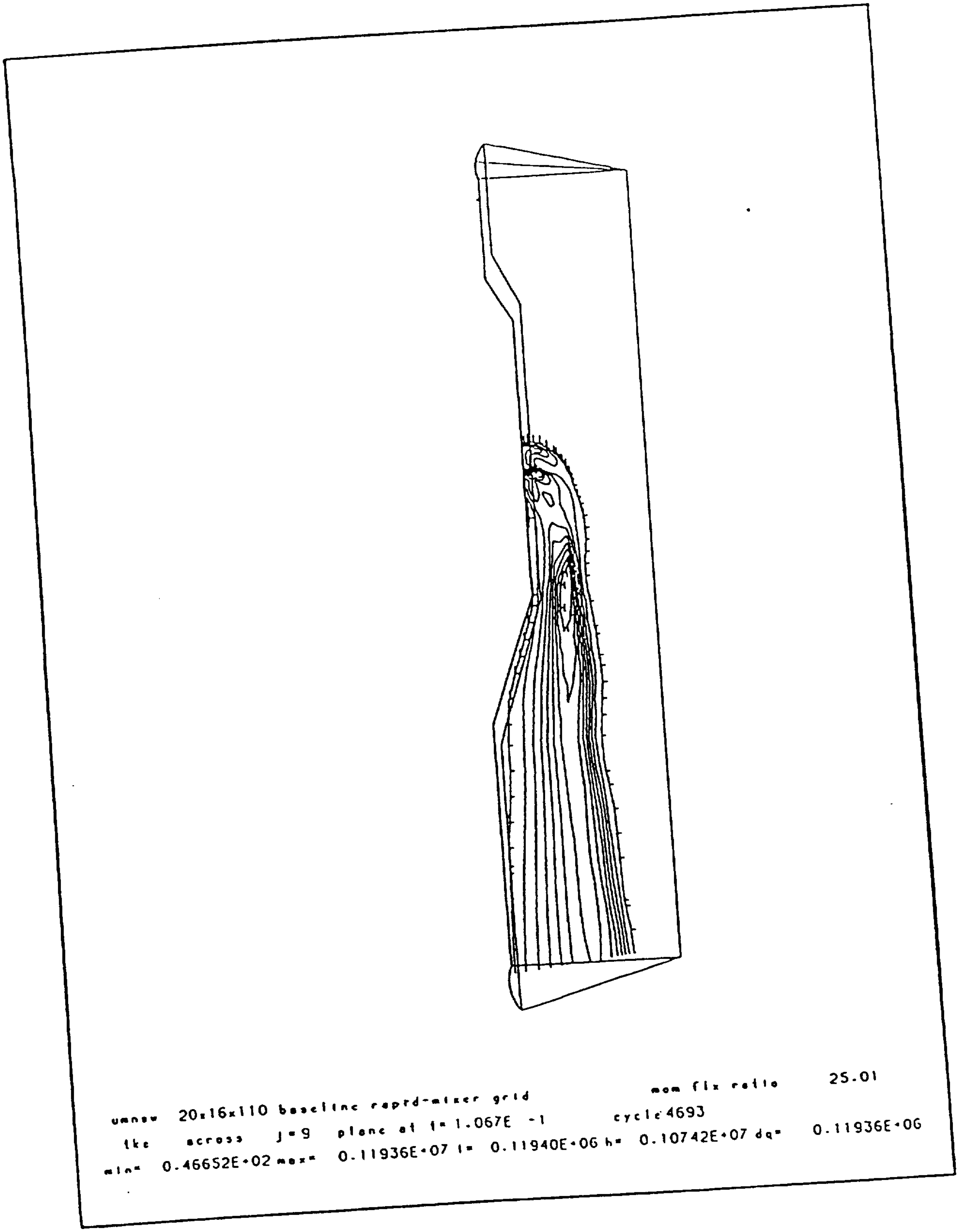
umnsw 20x16x110 baseline raprd-mixer grid
mom flx ratio 25.01
tke across j=9 plane at i= 1.067E -1
cycle 4693
min= 0.46652E+02 max= 0.11936E+07 l= 0.11940E+06 h= 0.10742E+07 dq= 0.11936E+06

Figure 4-59

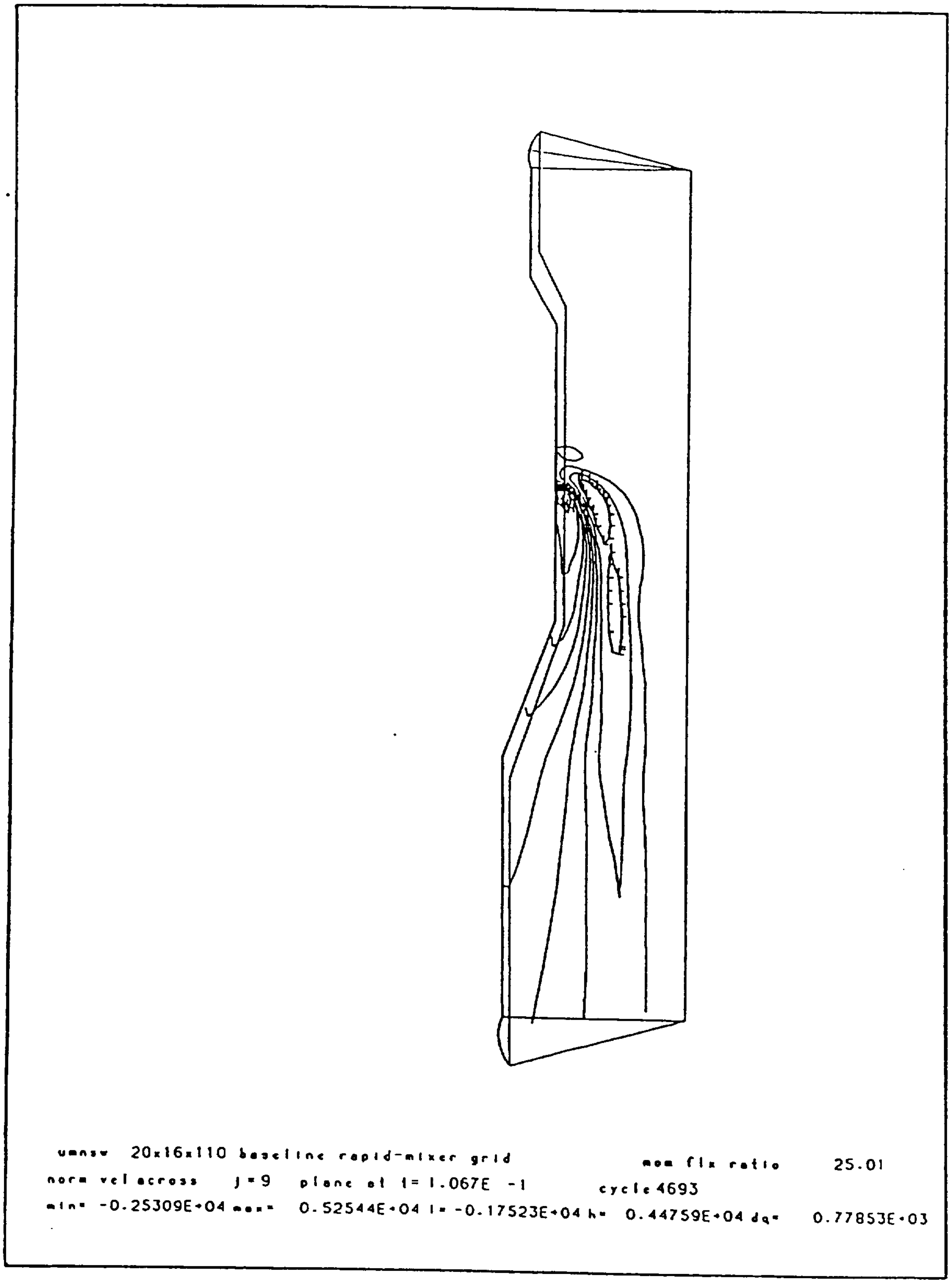

```
umnsw  20x16x110 baseline rapid-mixer grid                    mom flx ratio      25.01
norm vel across    j=9   plane at  i= 1.067E  -1          cycle 4693
min= -0.25309E+04 max=   0.52544E+04 l= -0.17523E+04 h=  0.44759E+04 dq=    0.77853E+03
```

Figure 4-60

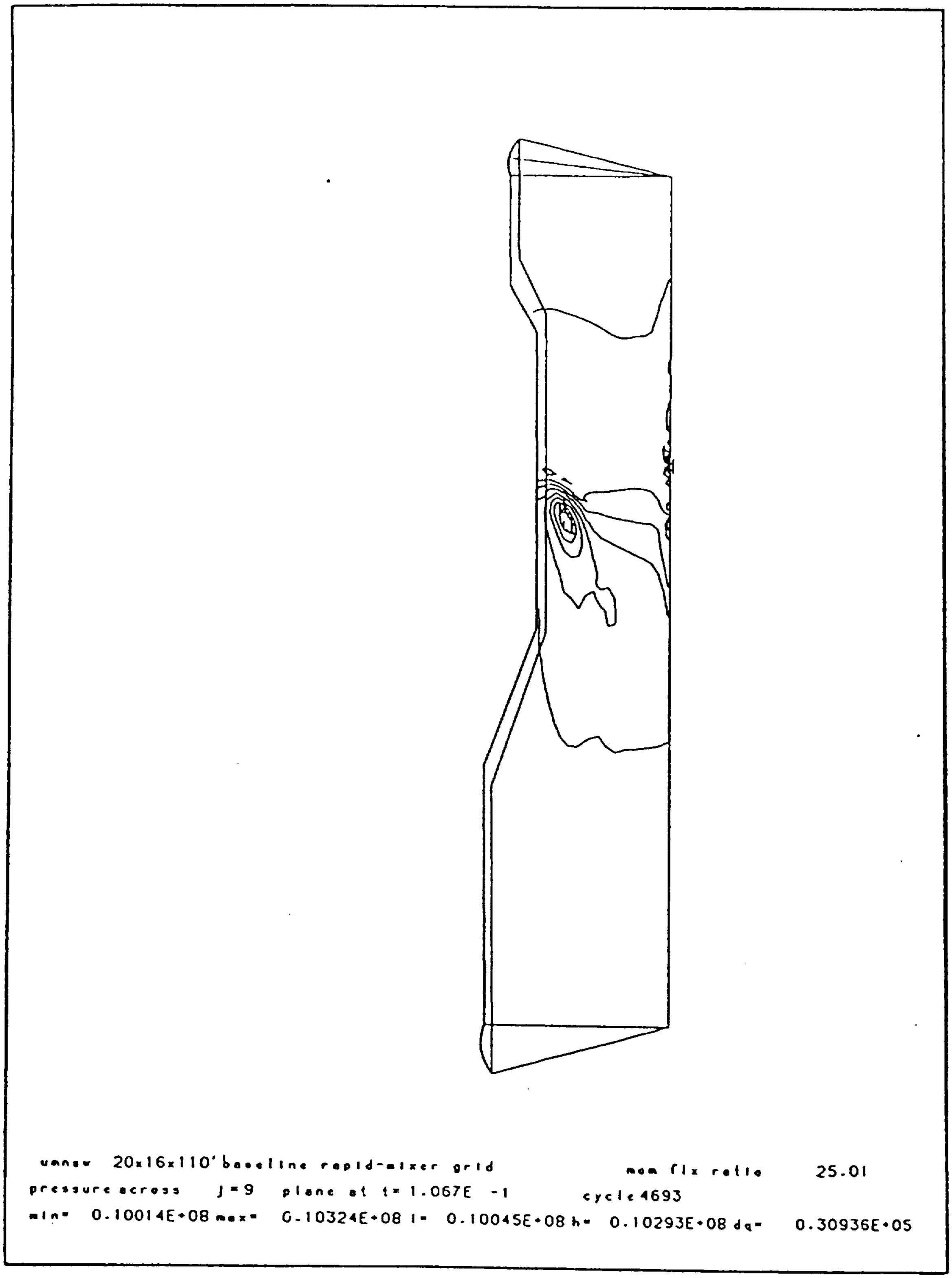
umnsw 20x16x110' baseline rapid-mixer grid
mom flx ratio 25.01
pressure across j = 9 plane at t = 1.067E -1
cycle 4693
min= 0.10014E+08 max= 0.10324E+08 l= 0.10045E+08 h= 0.10293E+08 dq= 0.30936E+05

Figure 4-61

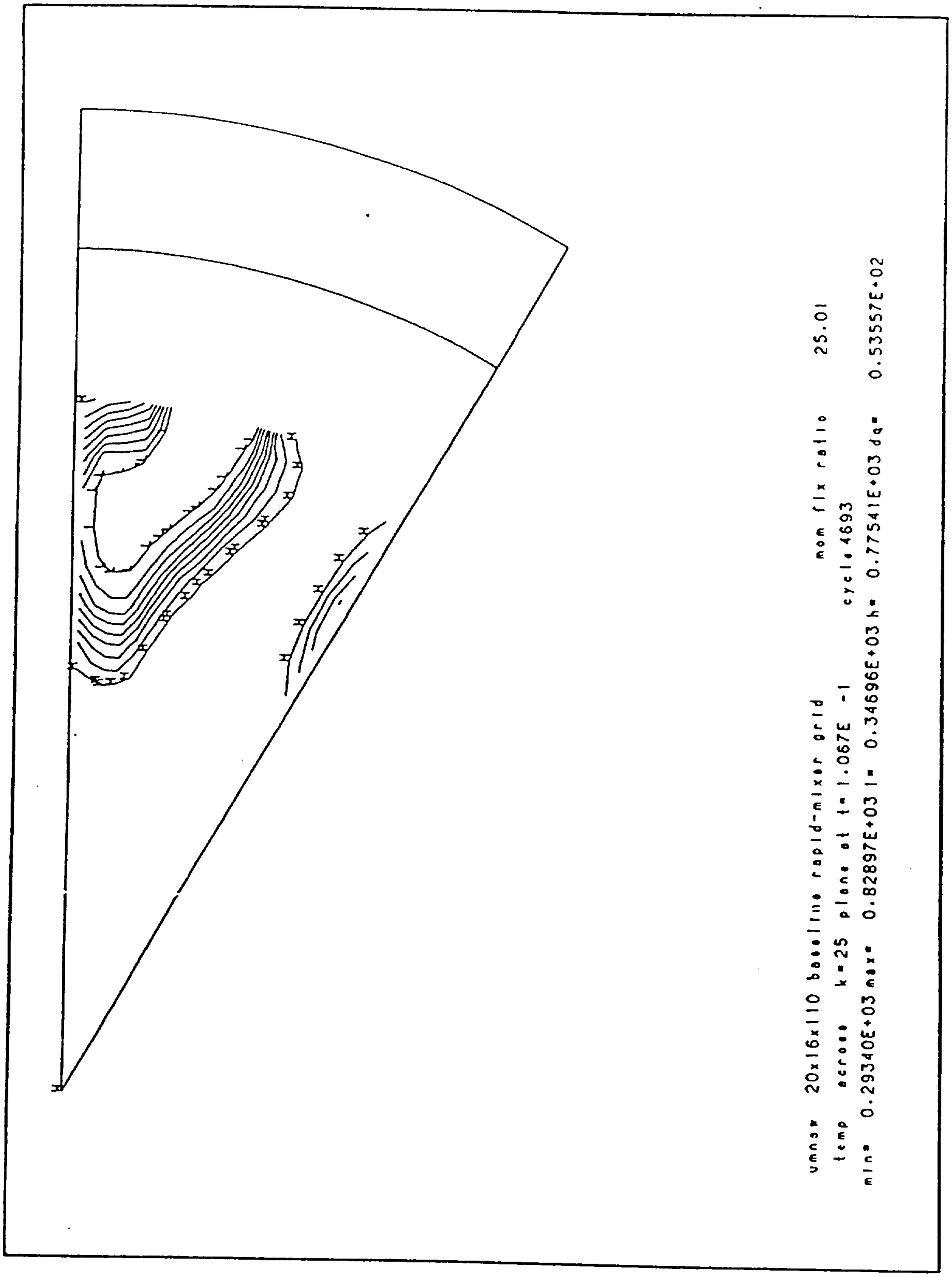
vmnsw 20x16x110 baseline rapid-mixer grid mom flx ratio 25.01
temp across k=25 plane at t= 1.067E -1 cycle=4693
min= 0.29340E+03 max= 0.82897E+03 l= 0.34696E+03 h= 0.77541E+03 dq= 0.53557E+02

Figure 4-62

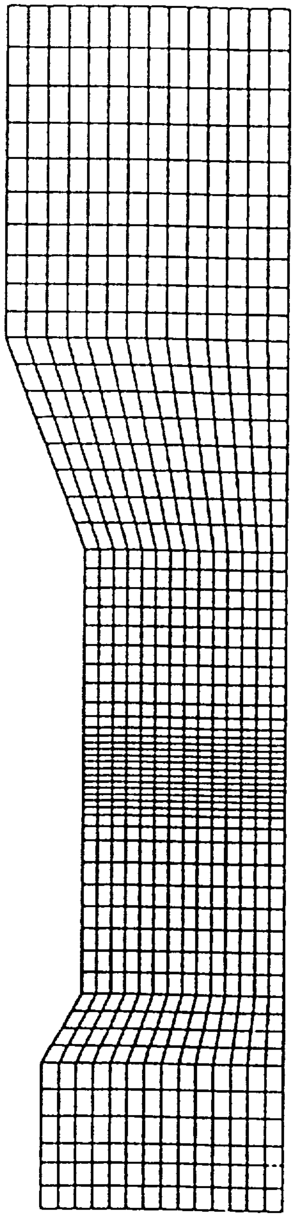

Figure 4-63

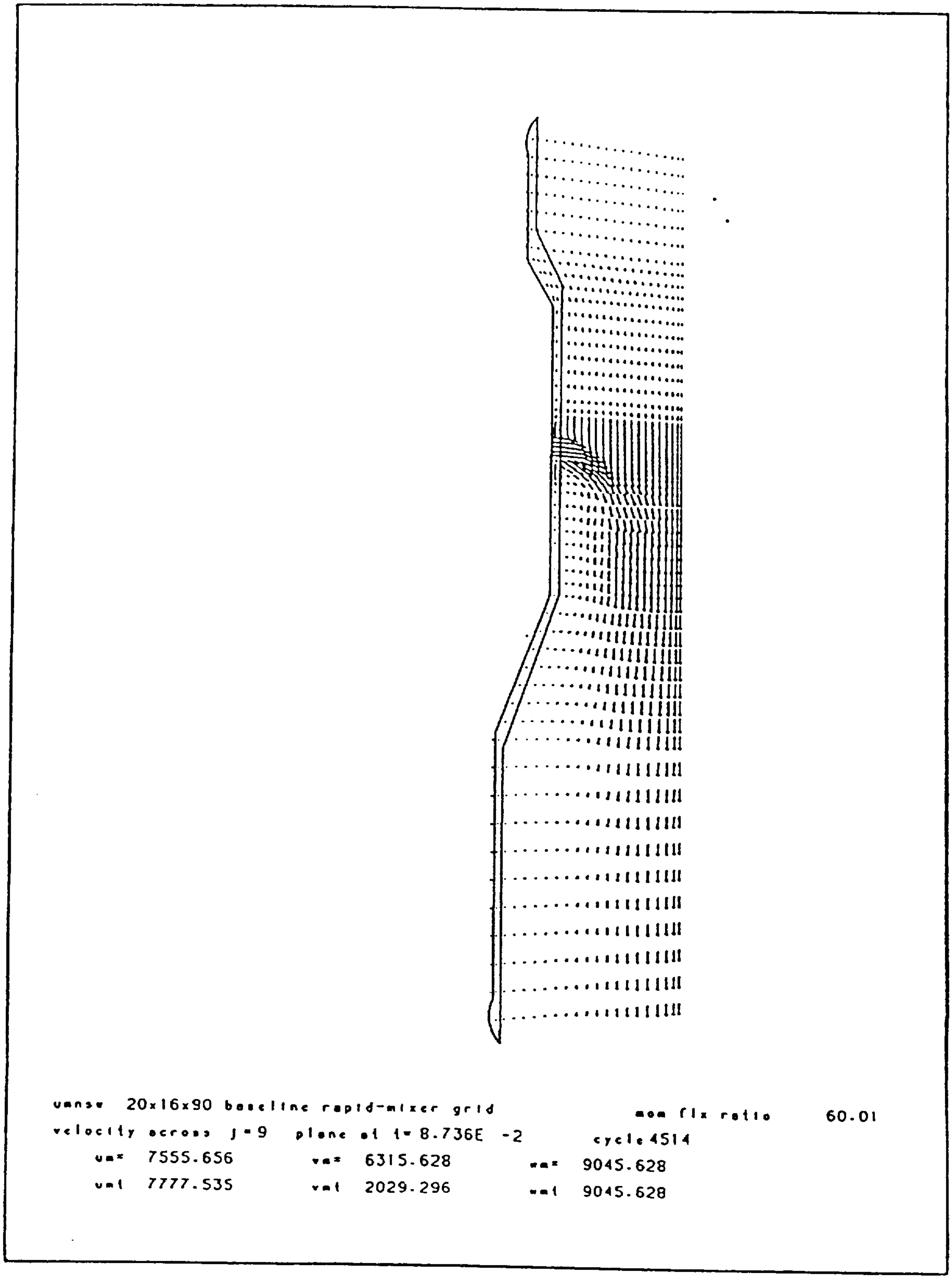
vmnsw 20x16x90 baseline rapid-mixer grid
mom flx ratio 60.01
velocity across j=9 plane at t= 8.736E -2
cycle 4514
umx 7555.656
vmx 6315.628
wmx 9045.628
umt 7777.535
vmt 2029.296
wmt 9045.628

Figure 4-64

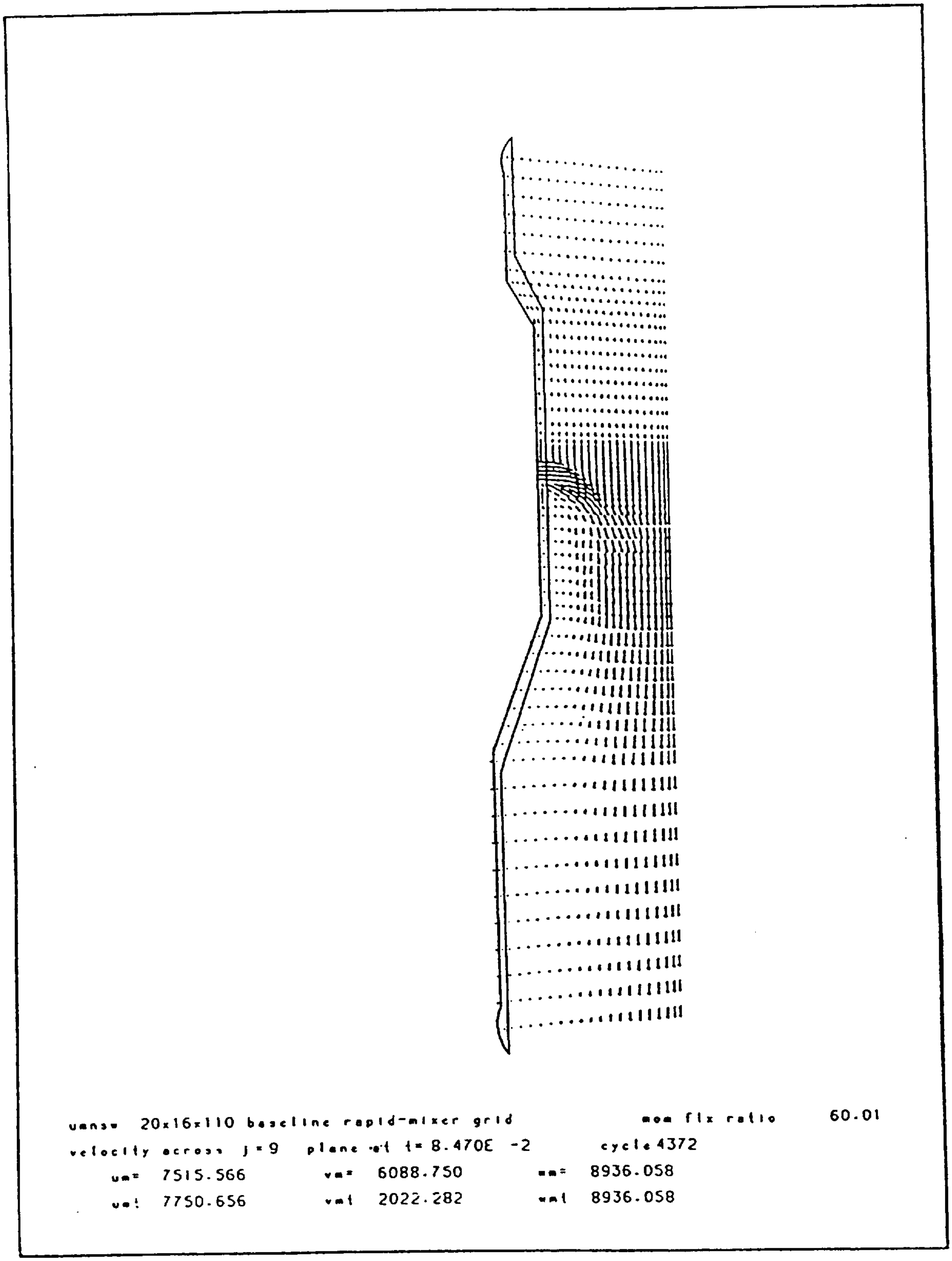
umnsw 20x16x110 baseline rapid-mixer grid
mom flx ratio 60.01
velocity across j=9 plane at t= 8.470E -2
cycle 4372
um= 7515.566
vm= 6088.750
wm= 8936.058
um! 7750.656
vml 2022.282
wml 8936.058

Figure 4-65

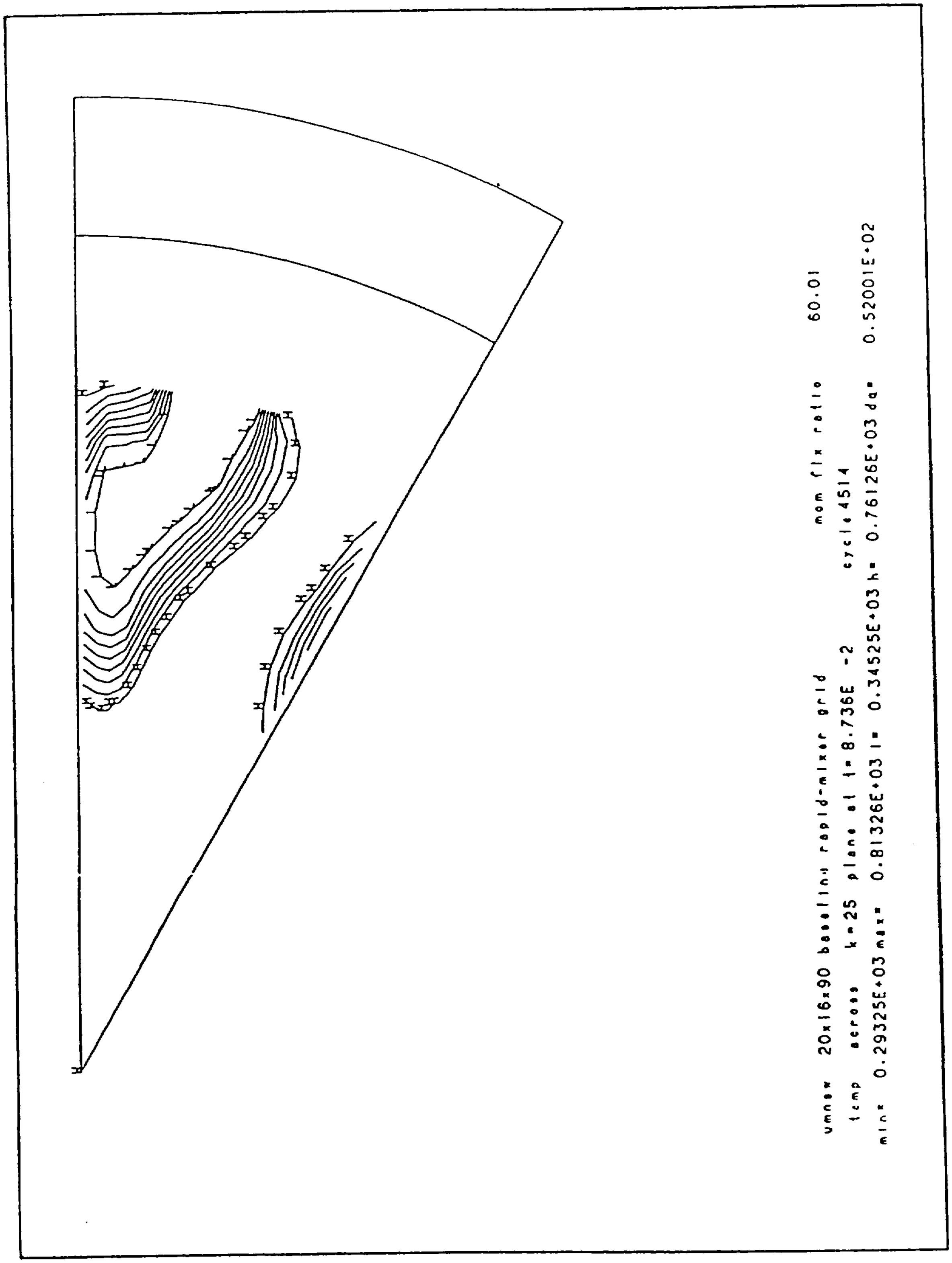
vmnew 20x16x90 baseline rapid-mixer grid
mom flx ratio 60.01
temp across k=25 plane at j= 8.736E -2
cycle 4514
min= 0.29325E+03 max= 0.81326E+03 l= 0.34525E+03 h= 0.76126E+03 da= 0.52001E+02

Figure 4-66

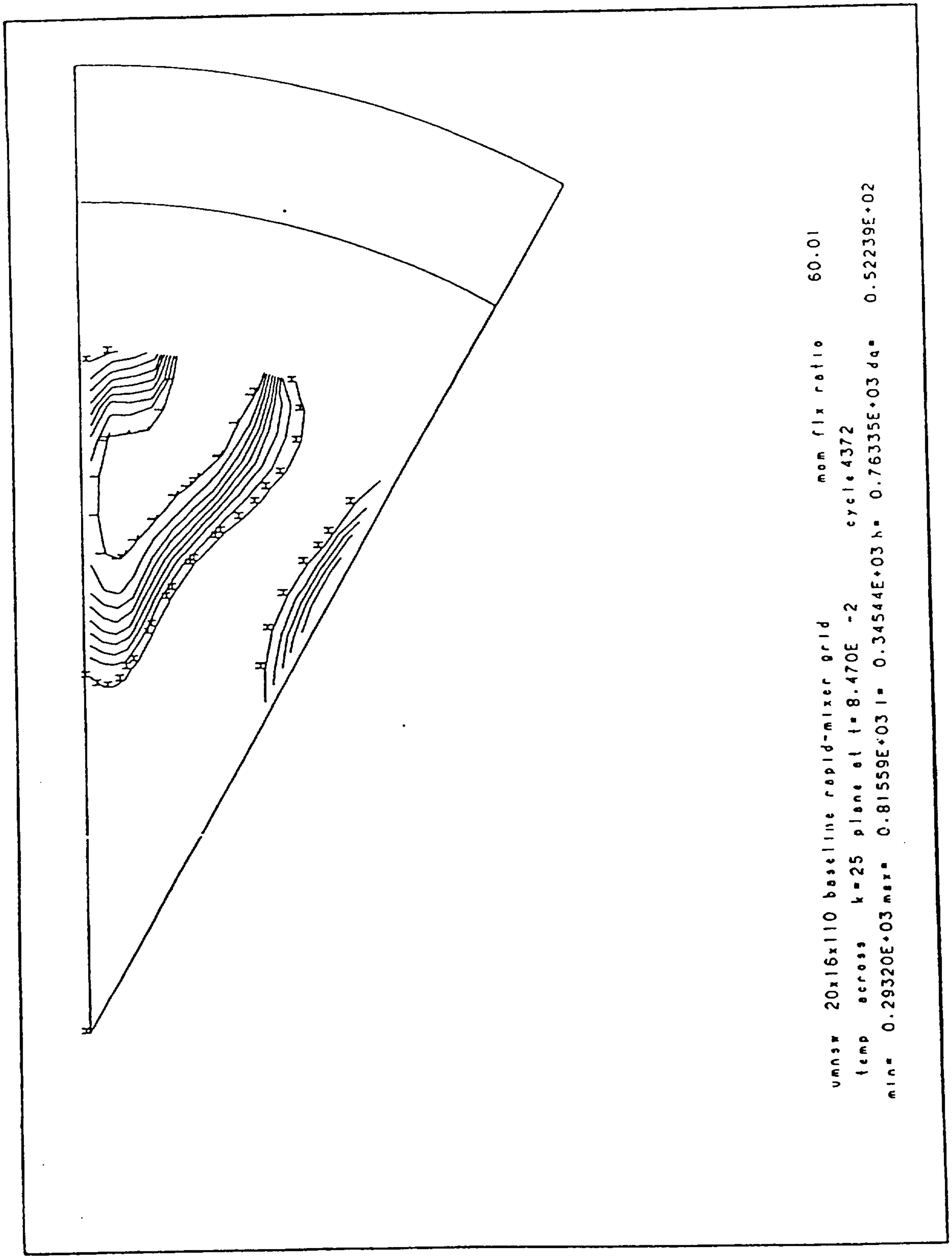
umnsw 20x16x110 baseline rapid-mixer grid mom flx ratio 60.01
temp across k=25 plane at t= 8.470E -2 cycle 4372
min= 0.29320E+03 max= 0.81559E+03 l= 0.34544E+03 h= 0.76335E+03 dq= 0.52239E+02

Figure 4-67

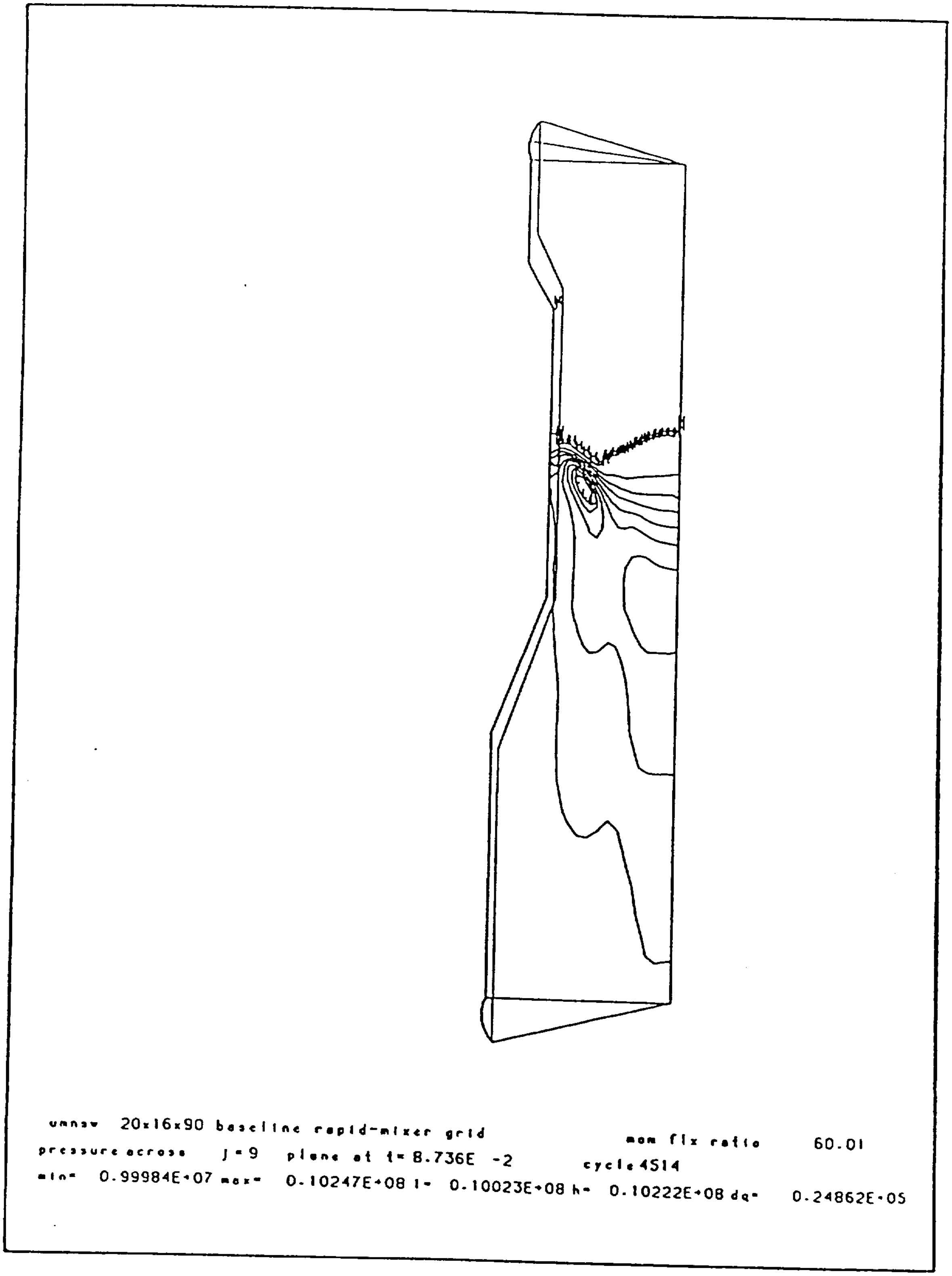
umnsw 20x16x90 baseline rapid-mixer grid
mom flx ratio 60.01
pressure across j = 9 plane at i = 8.736E -2
cycle 4514
min= 0.99984E+07 max= 0.10247E+08 l= 0.10023E+08 h= 0.10222E+08 dq= 0.24862E+05

Figure 4-68

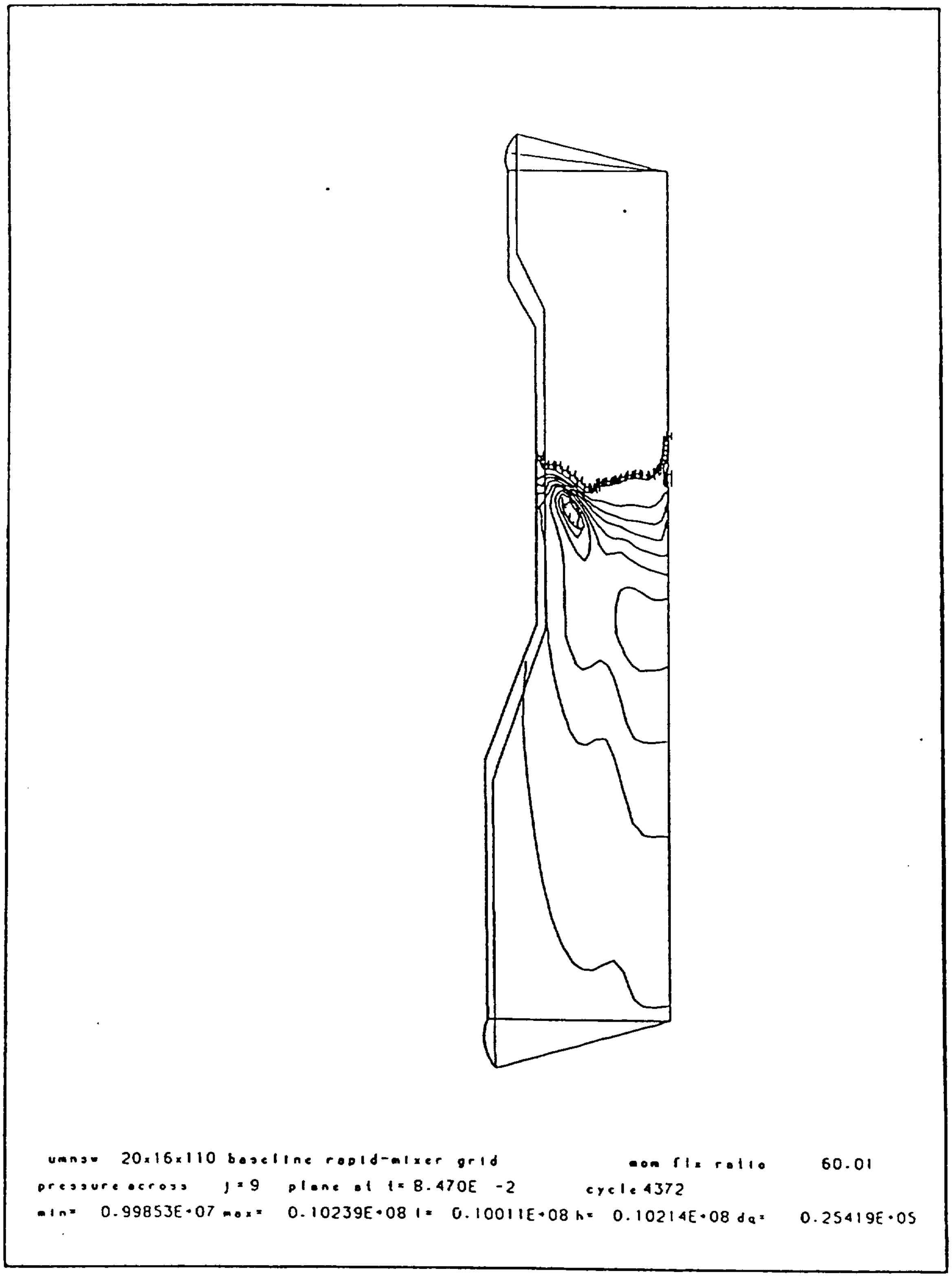
umnsw 20x16x110 baseline rapid-mixer grid
mom flx ratio 60.01
pressure across j=9 plane at t= 8.470E -2
cycle 4372
min= 0.99853E+07 max= 0.10239E+08 l= 0.10011E+08 h= 0.10214E+08 dq= 0.25419E+05

Figure 4-69

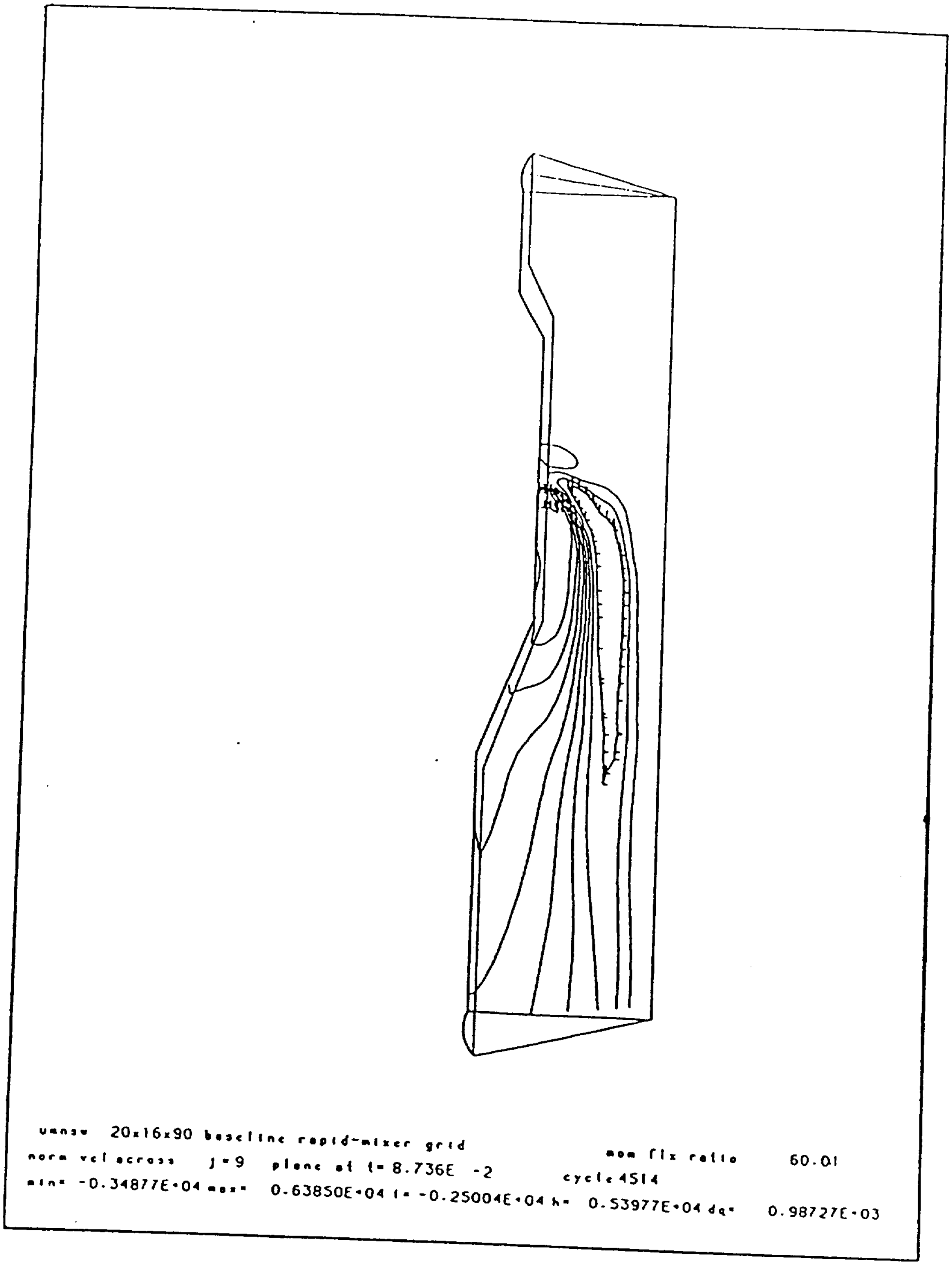
umnsw 20x16x90 baseline rapid-mixer grid
norm vel across j=9 plane at i= 8.736E -2
mom flx ratio 60.01
cycle 4514
min= -0.34877E+04 max= 0.63850E+04 l= -0.25004E+04 h= 0.53977E+04 dq= 0.98727E-03

Figure 4-70

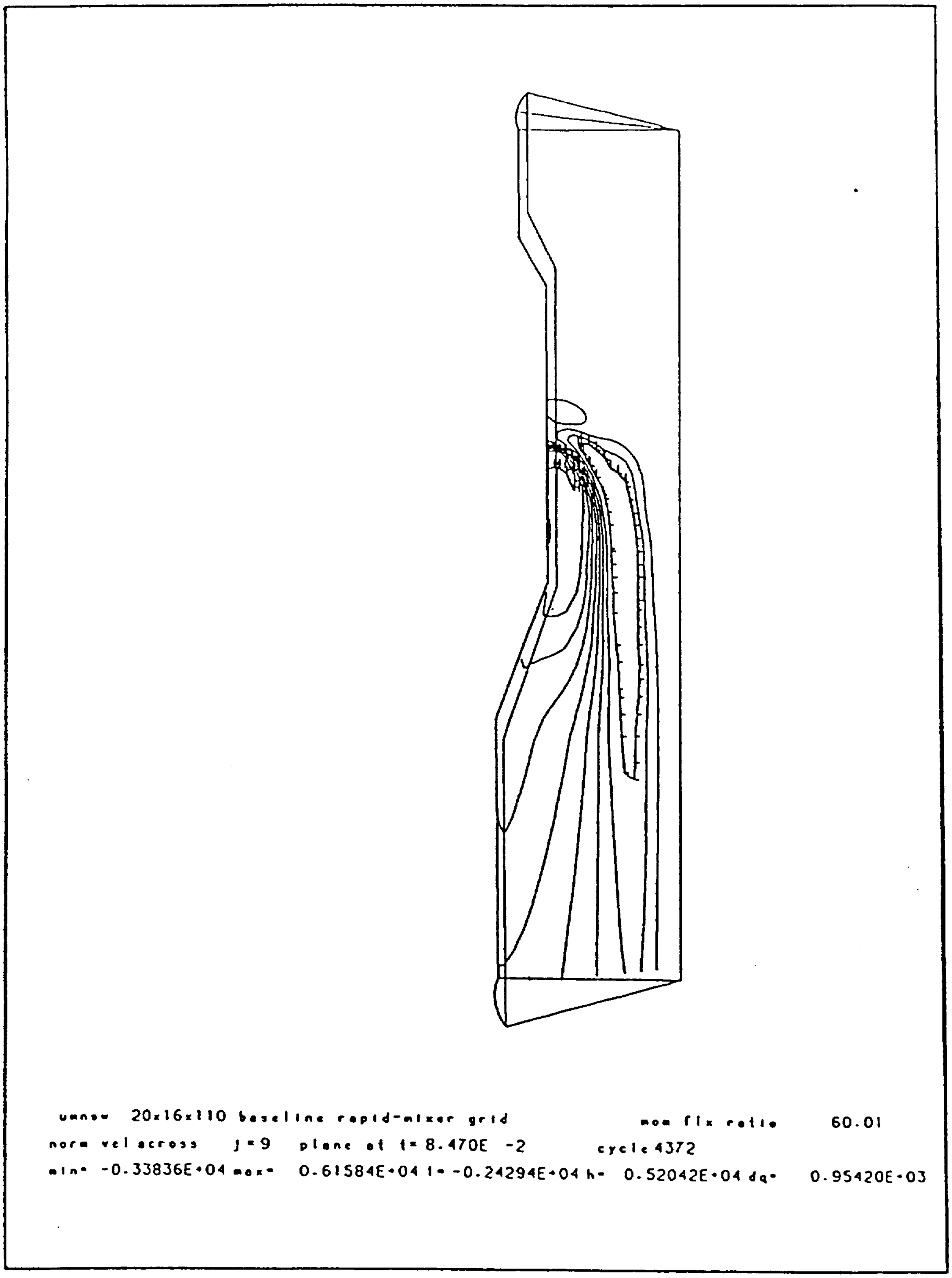
umnsw 20x16x110 baseline rapid-mixer grid
mom flx ratio 60.01
norm vel across j=9 plane at i=8.470E -2
cycle 4372
min= -0.33836E+04 max= 0.61584E+04 l= -0.24294E+04 h= 0.52042E+04 dq= 0.95420E+03

Figure 4-71

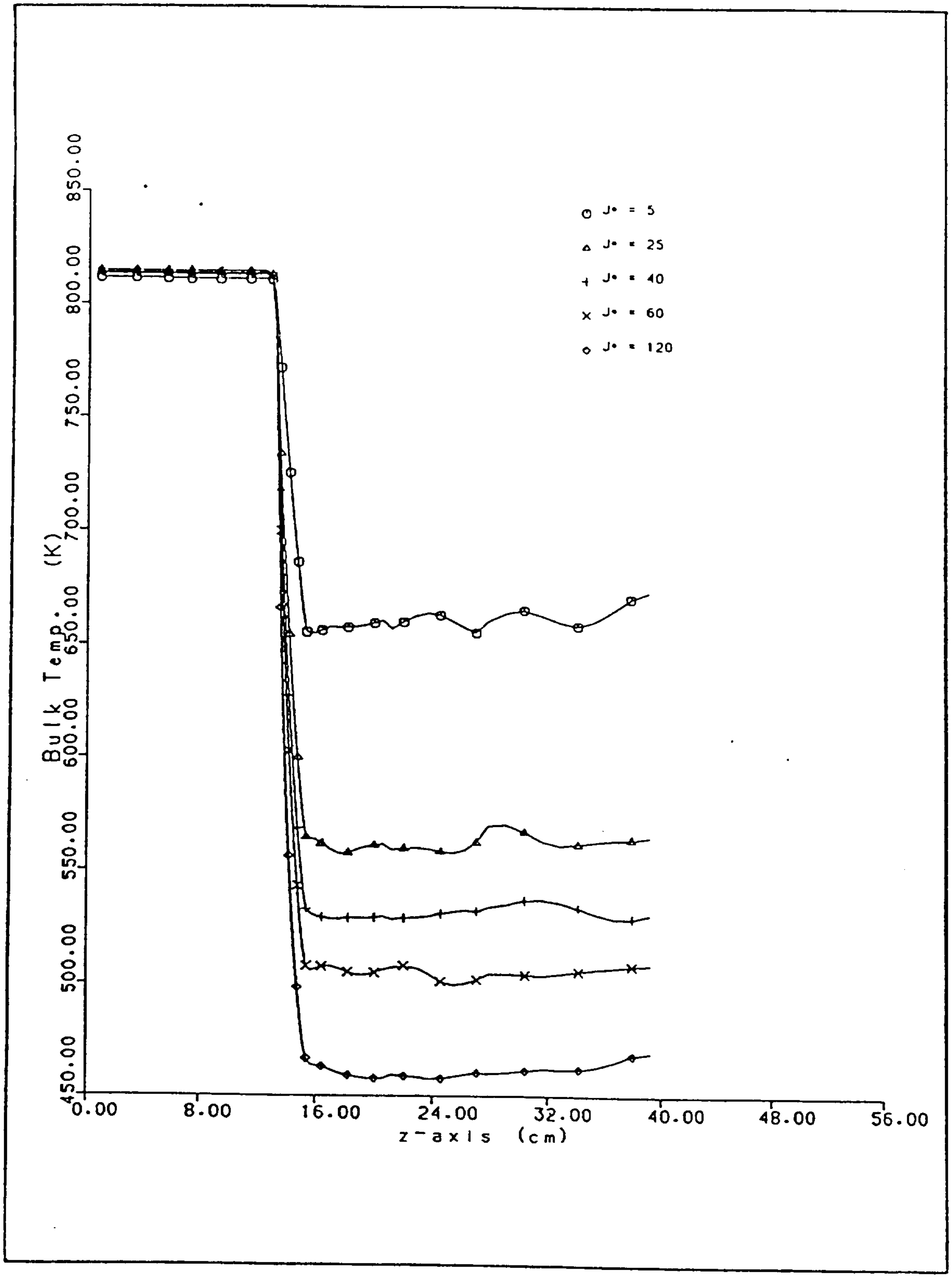
Bulk Temp. (K)
850.00
800.00
750.00
700.00
650.00
600.00
550.00
500.00
450.00
0.00
8.00
16.00
24.00
32.00
40.00
48.00
56.00
z-axis (cm)
J* = 5
J* = 25
J* = 40
J* = 60
J* = 120

Figure 4-72

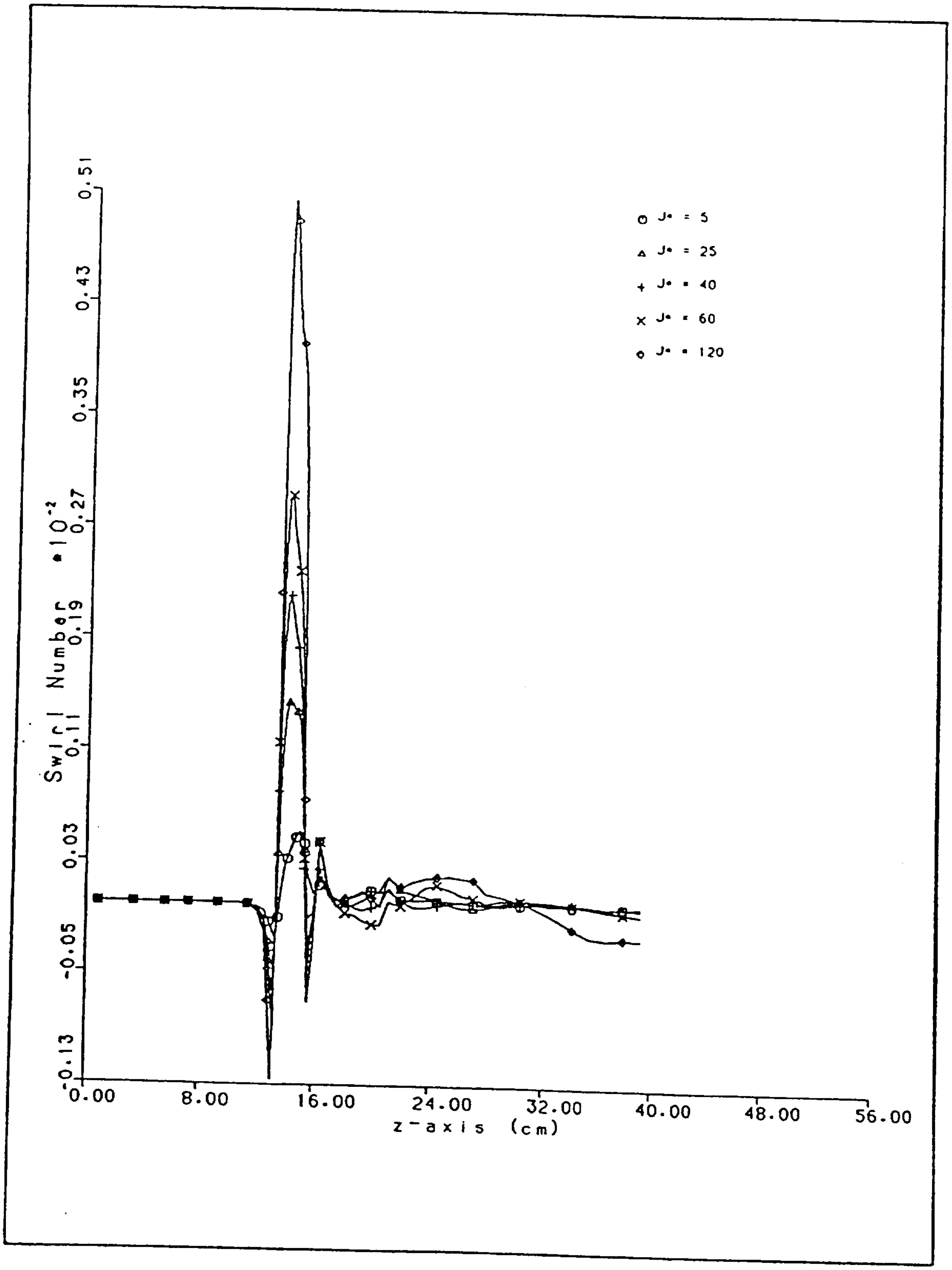

J* = 5
J* = 25
J* = 40
J* = 60
J* = 120
Swirl Number *10⁻²
0.51
0.43
0.35
0.27
0.19
0.11
0.03
-0.05
-0.13
0.00
8.00
16.00
24.00
32.00
40.00
48.00
56.00
z-axis (cm)

Figure 4-73

CHAPTER V

30° SLANTED SLOT RESULTS

V.1. 30° Slanted Slot Geometry

As discussed in chapter 2 the 30° slanted slot was modeled in a similar fashion to the 45° slot. This approach required an additional 5 j-planes, which increased the mesh size to 51,282 cells. Figures (5-1) and (5-2) show the mesh within the region of interest (k=1 to k=60), and figure (5-3) shows azimuthal spacing of the j-planes. Effect of momentum flux ratio variation was conducted using J^{*}=5,25,40,60 and 120 at a fixed density ratio of 2.76. These runs also utilized tke averaging along the mesh centerline from i=1 to 4 to prevent the development of localized turbulent kinetic energy high spots.

V.2. Jet Description

The slanted slot jet interaction with the axial mainstream is similar to that for the 45° slanted slot. Holdeman et al. [10] theorized 45° slots produce less penetration and mixing performance than equivalent area parallel slots. The 30° slanted slot having less slant produces greater radial penetration into the mixing region of the mesh. Jet penetration can be visually characterized in figures (5-4) to (5-9). Comparing these velocity and temperature profiles across the slanted slot with corresponding figures in chapter 4 the increased penetration is readily evident. The 30° slanted slot geometry having increased jet penetration develops a low pressure region just downstream of the jet along the centerline and at lower momentum flux ratios than the 45° slot geometry. The low pressure region is developed at $J^*=40$ while it was not evident until $J^*=60$ with the 45° slot. Regardless of the difference in jet penetration, the bulk temperature profiles shown in figure (5-23) drop to values similar to the profiles generated with the 45° slot.

V.3. Swirl Profile

The 30° slots having a smaller inclination with the centerline, deflects less of the mainstream into the outer CCW swirl region. Accordingly the inner CW rotating bulk swirl profile encompasses a greater portion of the cross sectional area.

The j-plane normal velocity plots shown in figures (5-19) to (5-21) clearly indicate a reduced magnitude of the azimuthal velocity in the outer CCW profile in comparison with the 45° slanted slot. An increase in magnitude of azimuthal velocity in the inner CW profile is most evident at higher momentum flux ratios.

As with the 45° slanted slot, the swirl number variation with axial distance in fig. (5-22), reveals a net cancelation of angular momentum. These values in comparison with those referenced by Lefebvre [1] are effectively zero.

V.4. tke Averaging with the 30° Slot

The averaging out of high tke spots near the centerline is one solution to remedy this problem. This method works well if the jet does not penetrate into the region undergoing tke averaging (i=1 to i=4). When the jet physically enters this region its interaction with the mainstream results in high turbulence that tke averaging alters. This is a problem with the 30° slanted slot at J^*=120. A simpler method preventing the numerical high tke high spots is decreasing velocity convergence criteria to 1.0e-04 and pressure convergence criteria to 1.0e-05. This alternative eliminates the need to "smooth" the centerline tke high spots and is recommended in general.

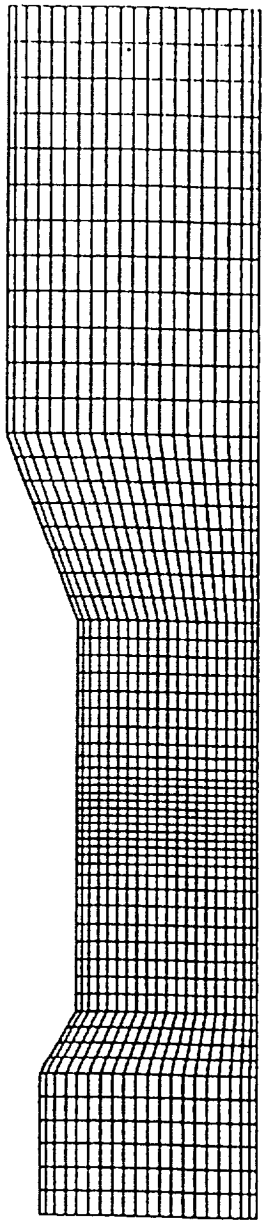

Figure 5-1

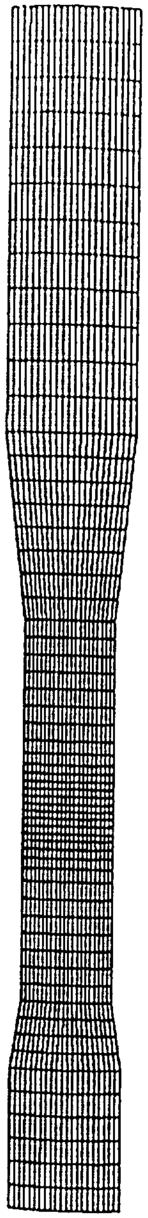

Figure 5-2

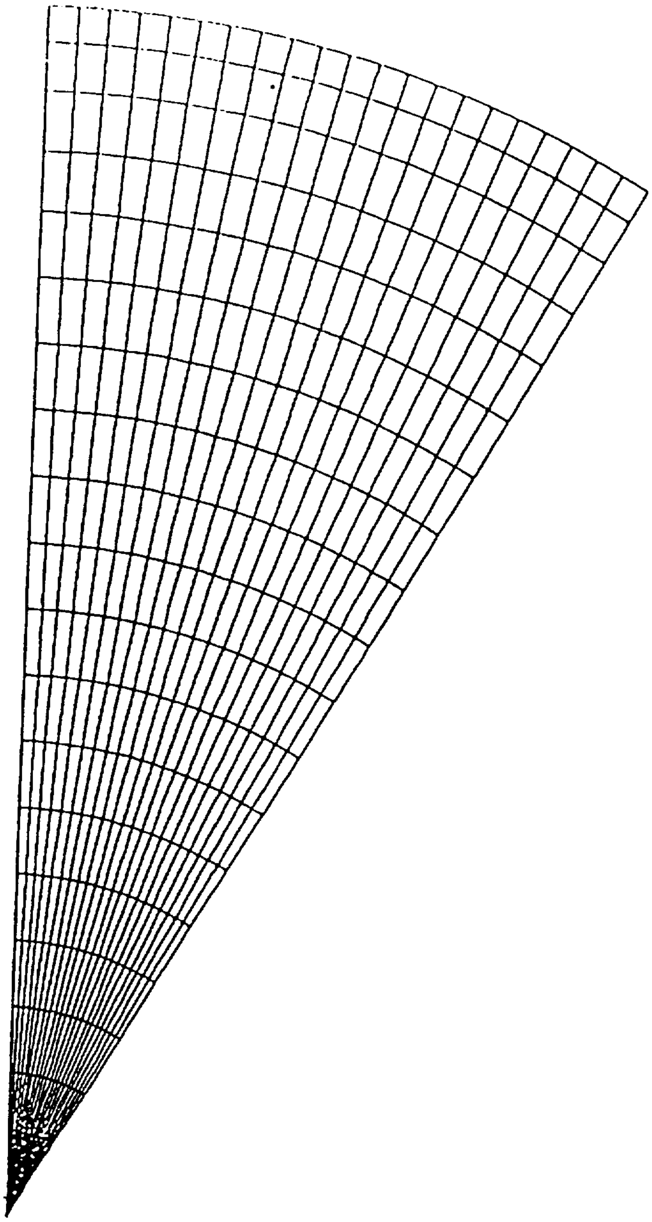

Figure 5-3

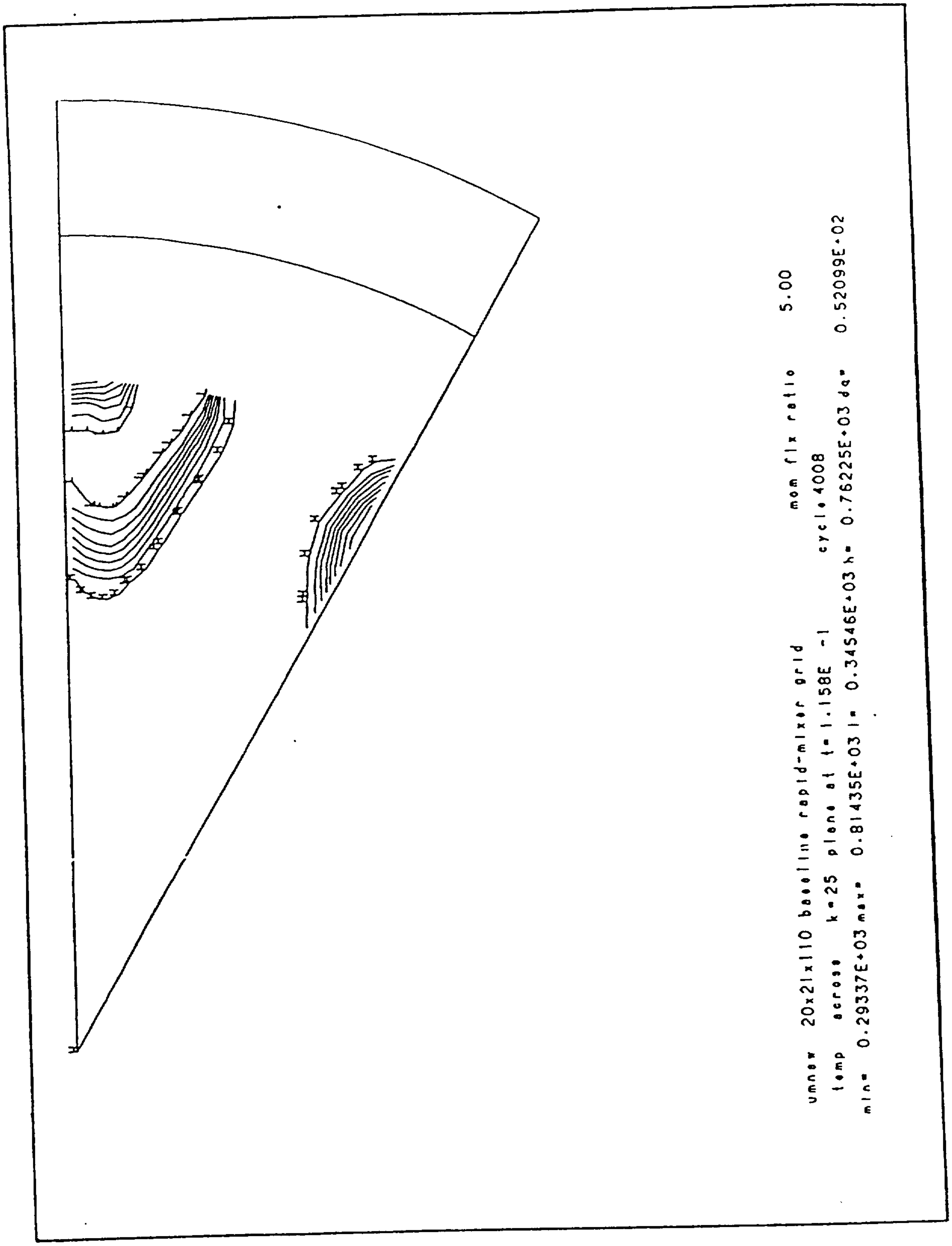
umnew 20x21x110 baseline rapid-mixer grid
mom flx ratio 5.00
temp across k=25 plane at t= 1.158E -1
cycle 4008
min= 0.29337E+03 max= 0.81435E+03 l= 0.34546E+03 h= 0.76225E+03 dq= 0.52099E-02

Figure 5-4

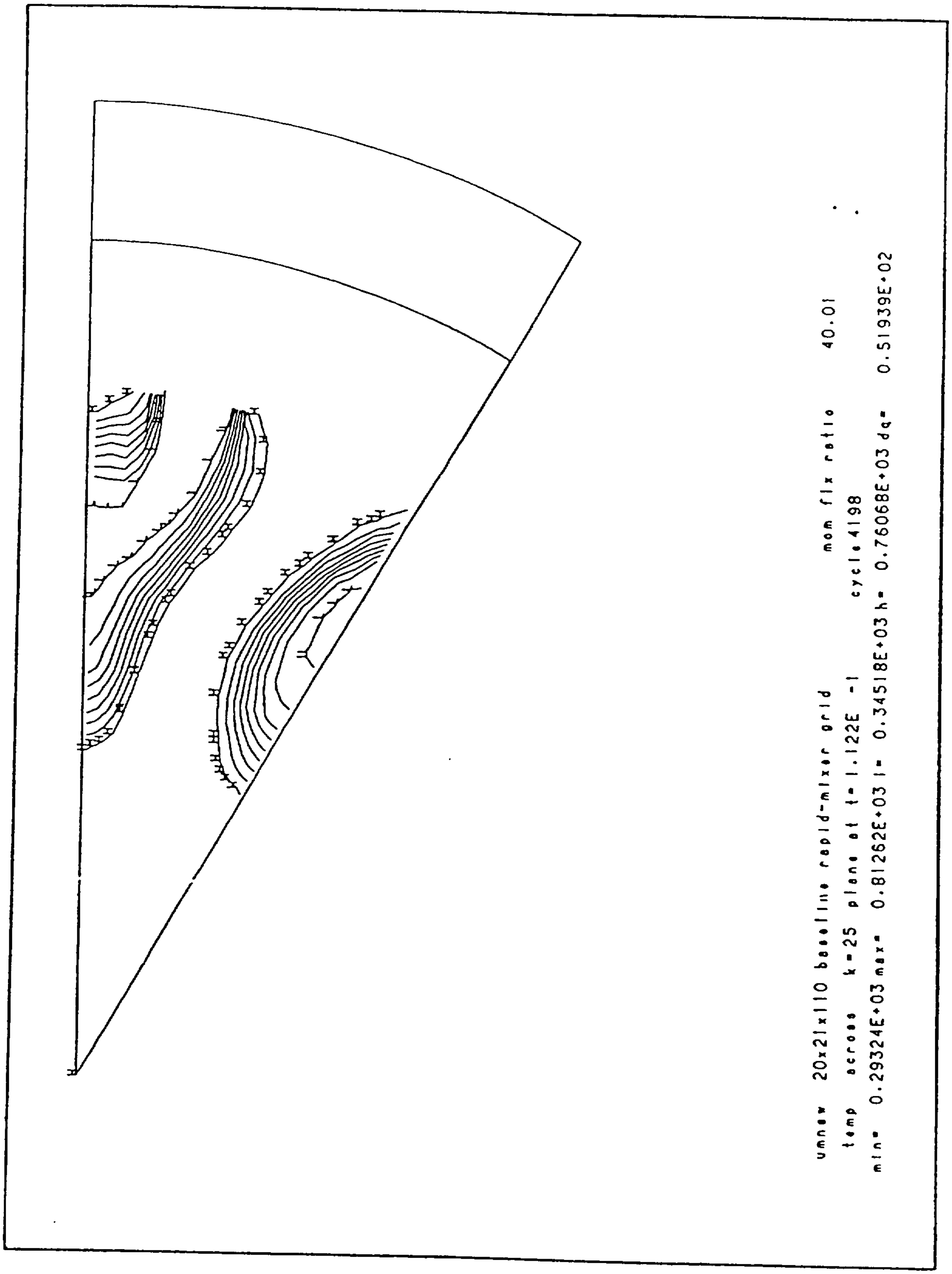
umnew 20x21x110 baseline rapid-mixer grid mom flx ratio 40.01
temp across k=25 plane at t= 1.122E -1 cycle=4198
min= 0.29324E+03 max= 0.81262E+03 l= 0.34518E+03 h= 0.76068E+03 dq= 0.51939E+02
H
L

Figure 5-5

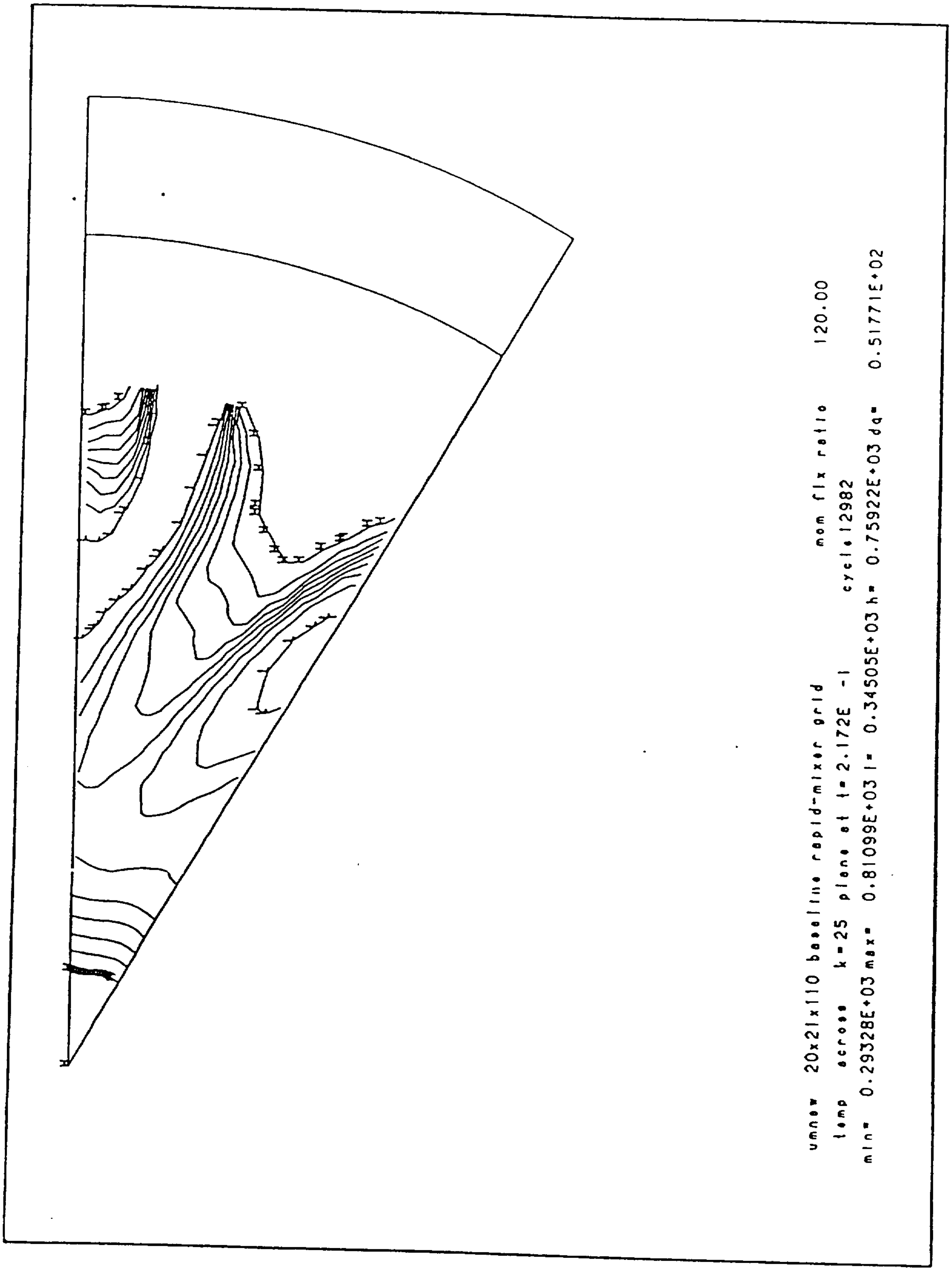
umnew 20x21x110 baseline rapid-mixer grid
mom flx ratio 120.00
temp across k=25 plane at t= 2.172E -1
cycle 12982
min= 0.29328E+03 max= 0.81099E+03 l= 0.34505E+03 h= 0.75922E+03 dq= 0.51771E+02

Figure 5-6

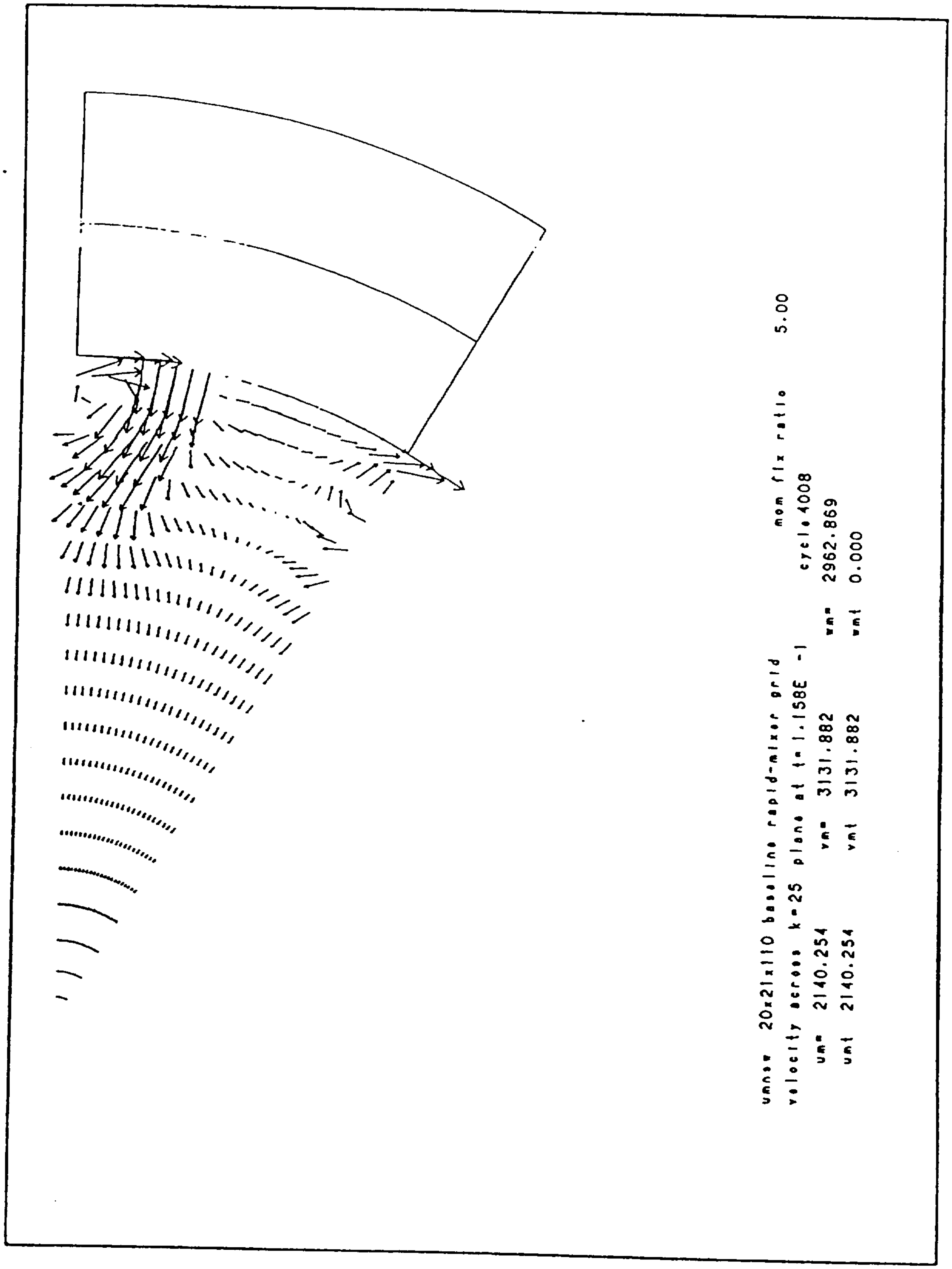
unnew 20x21x110 baseline rapid-mixer grid
mom flx ratio 5.00
velocity across k=25 plane at t=1.158E -1
cycle=4008
um= 2140.254
vm= 3131.882
wm= 2962.869
umt 2140.254
vmt 3131.882
wmt 0.000

Figure 5-7

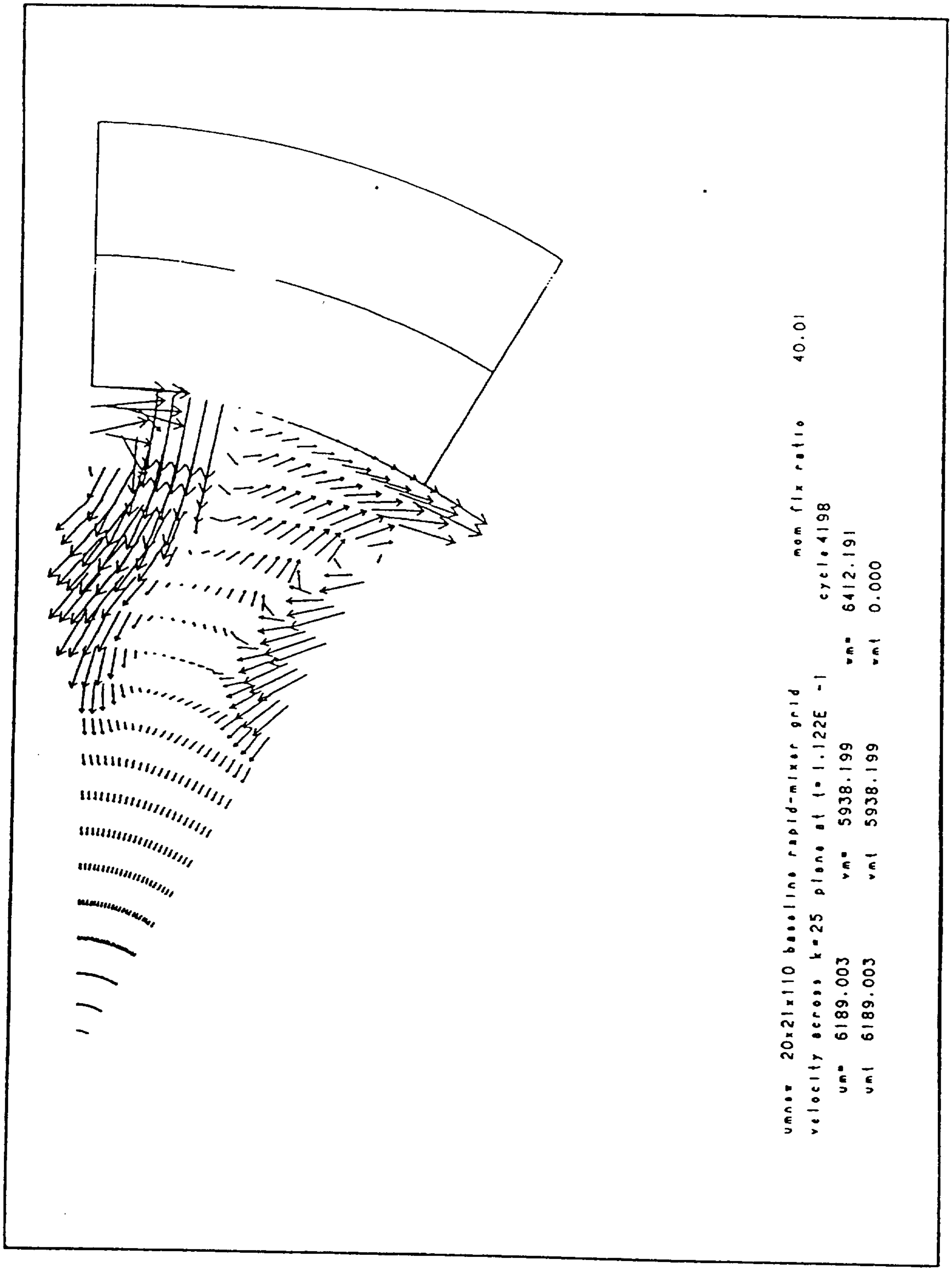
umnew 20x21x110 baseline rapid-mixer grid
mom flx ratio 40.01
velocity across k=25 plane at t= 1.122E -1
cycle 4198
um= 6189.003
vm= 5938.199
wm= 6412.191
uml 6189.003
vml 5938.199
wml 0.000

Figure 5-8

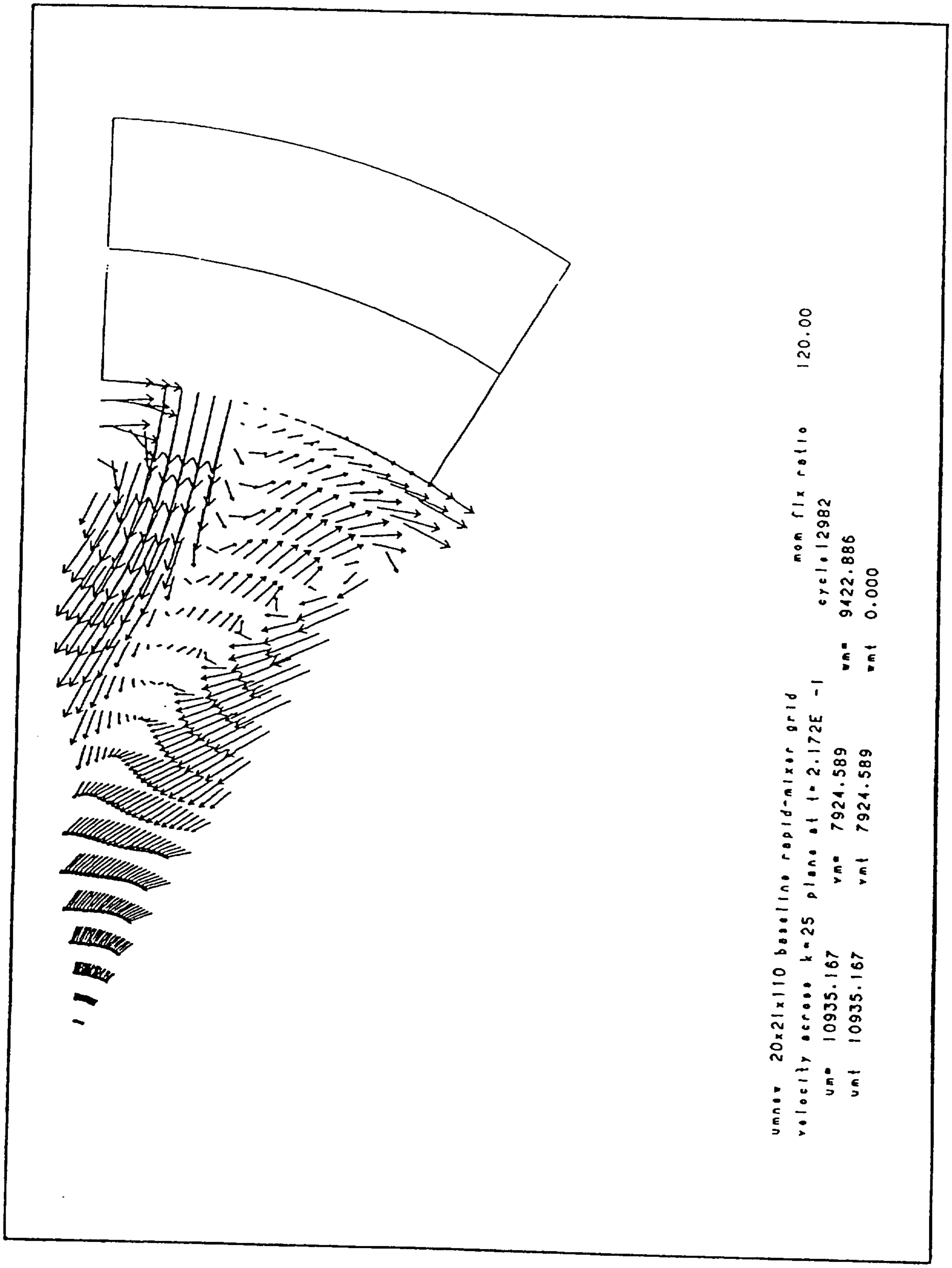
umnew 20x21x110 baseline rapid-mixer grid
mom flx ratio 120.00
velocity across k=25 plane at t=2.172E -1
cycle=12982
um= 10935.167
vm= 7924.589
wm= 9422.886
umt 10935.167
vmt 7924.589
wmt 0.000

Figure 5-9

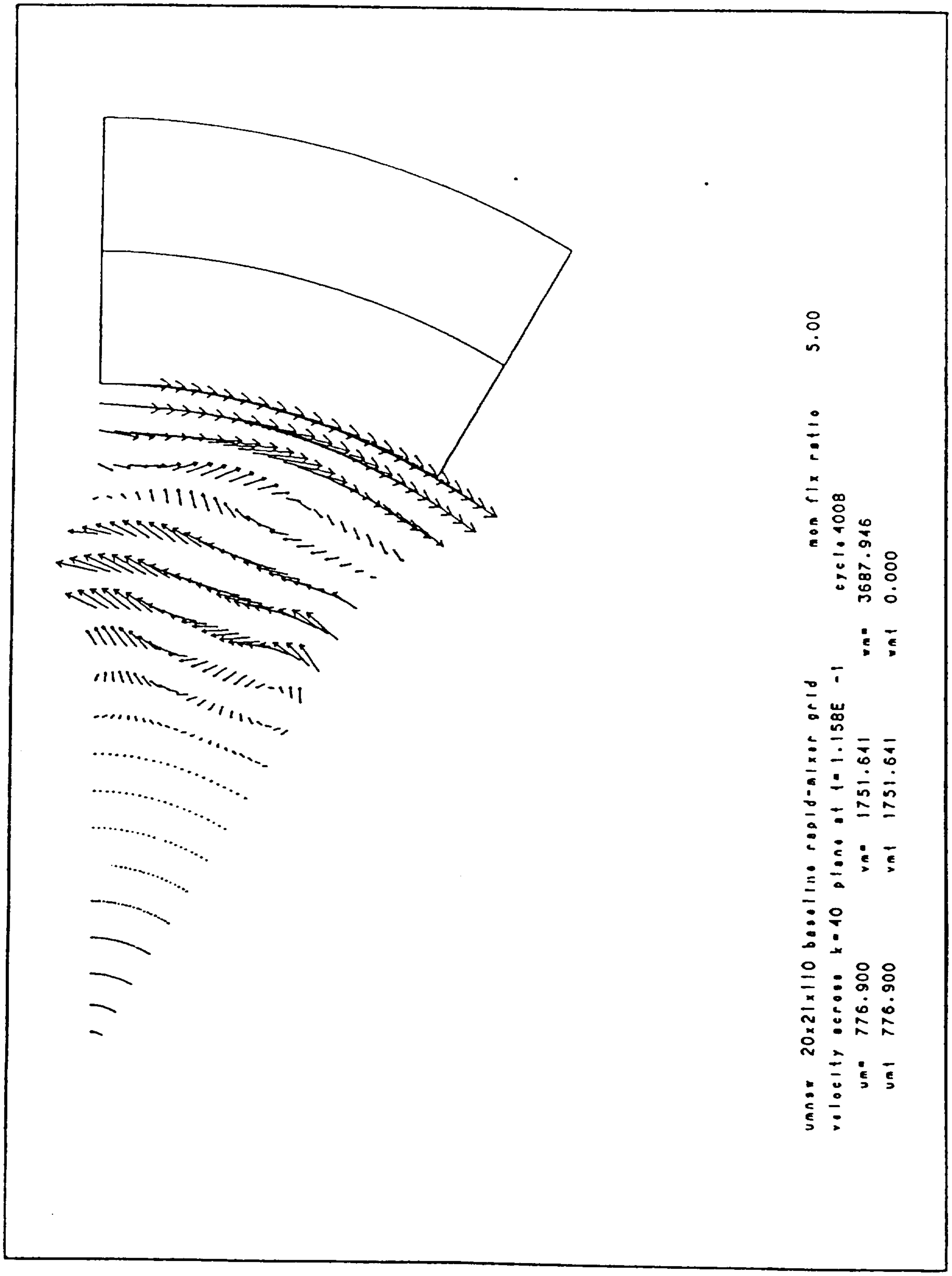
unnsw 20x21x110 baseline rapid-mixer grid
mom flx ratio 5.00
velocity across k=40 plane at t=1.158E -1
cycle=4008
um= 776.900
vm= 1751.641
wm= 3687.946
uml 776.900
vml 1751.641
wml 0.000

Figure 5-10

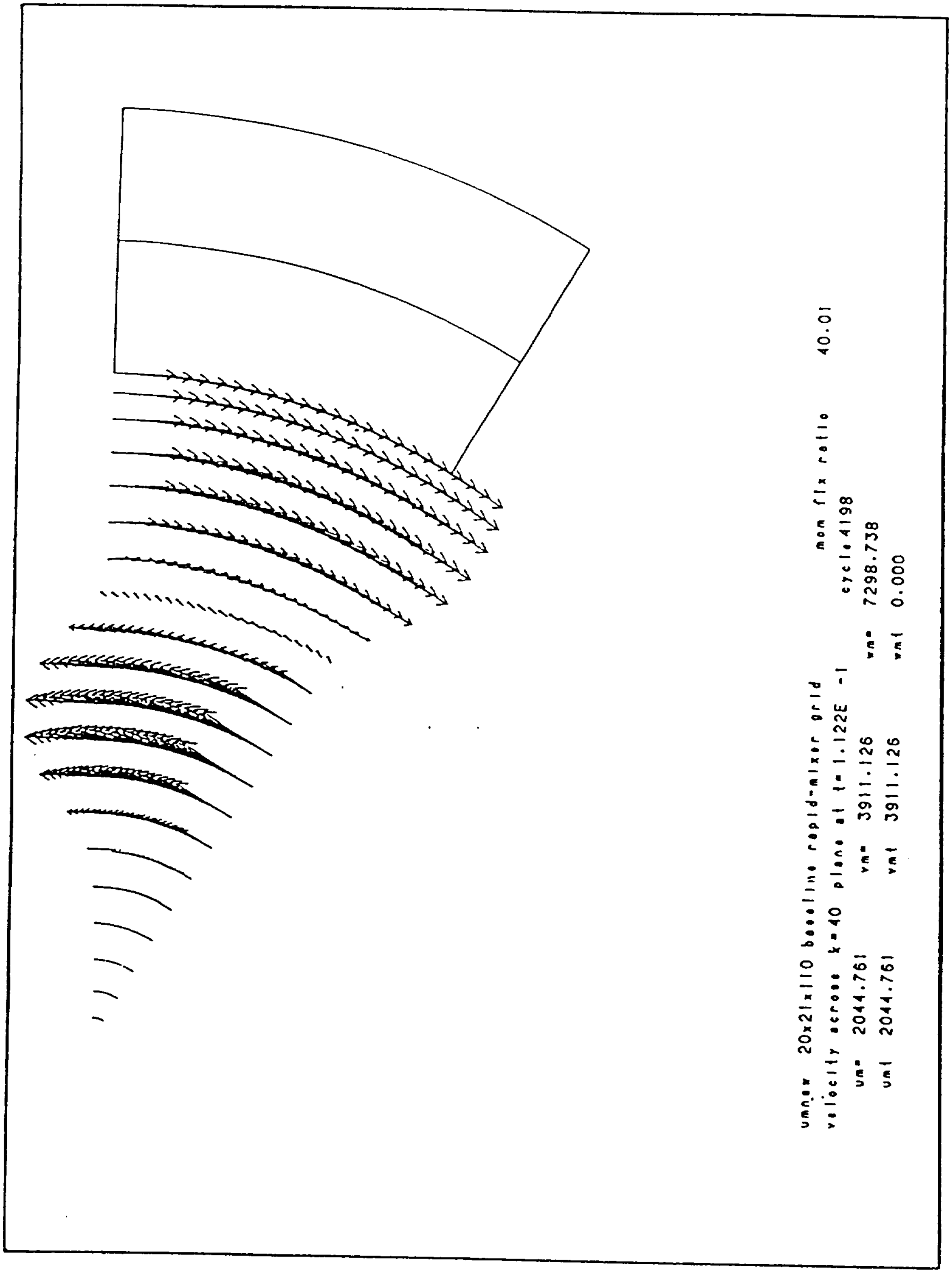
umnew 20x21x110 baseline rapid-mixer grid
velocity across k=40 plane at t= 1.122E -1
um= 2044.761
uml 2044.761
vm= 3911.126
vml 3911.126
mon flx ratio
cycle=4198
wm= 7298.738
wml 0.000
40.01

Figure 5-11

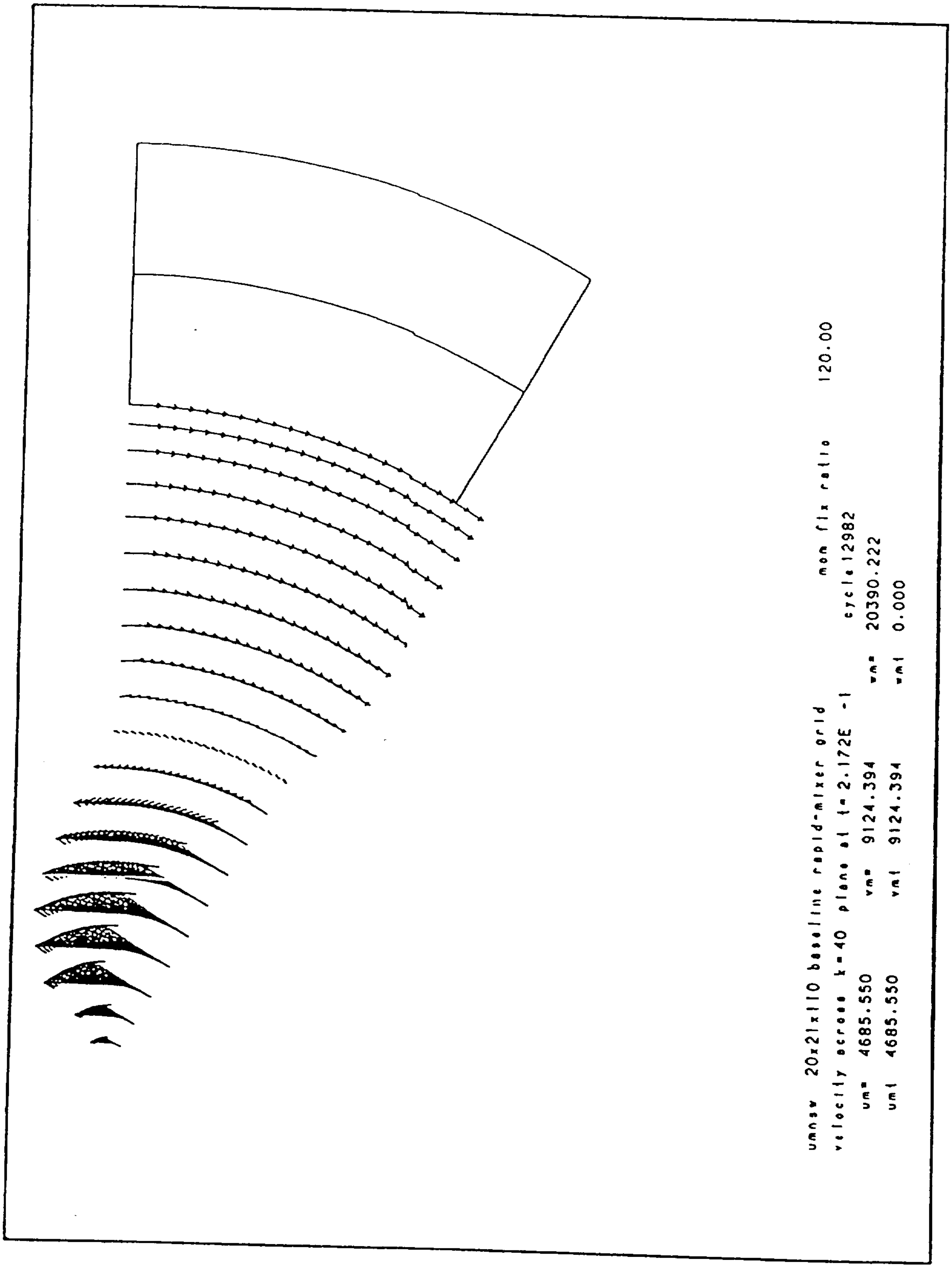
umnsw 20x21x110 baseline rapid-mixer grid
mon flx ratio 120.00
velocity across k=40 plane at t=2.172E -1
cycle 12982
um= 4685.550
vm= 9124.394
wm= 20390.222
uml 4685.550
vml 9124.394
wml 0.000

Figure 5-12

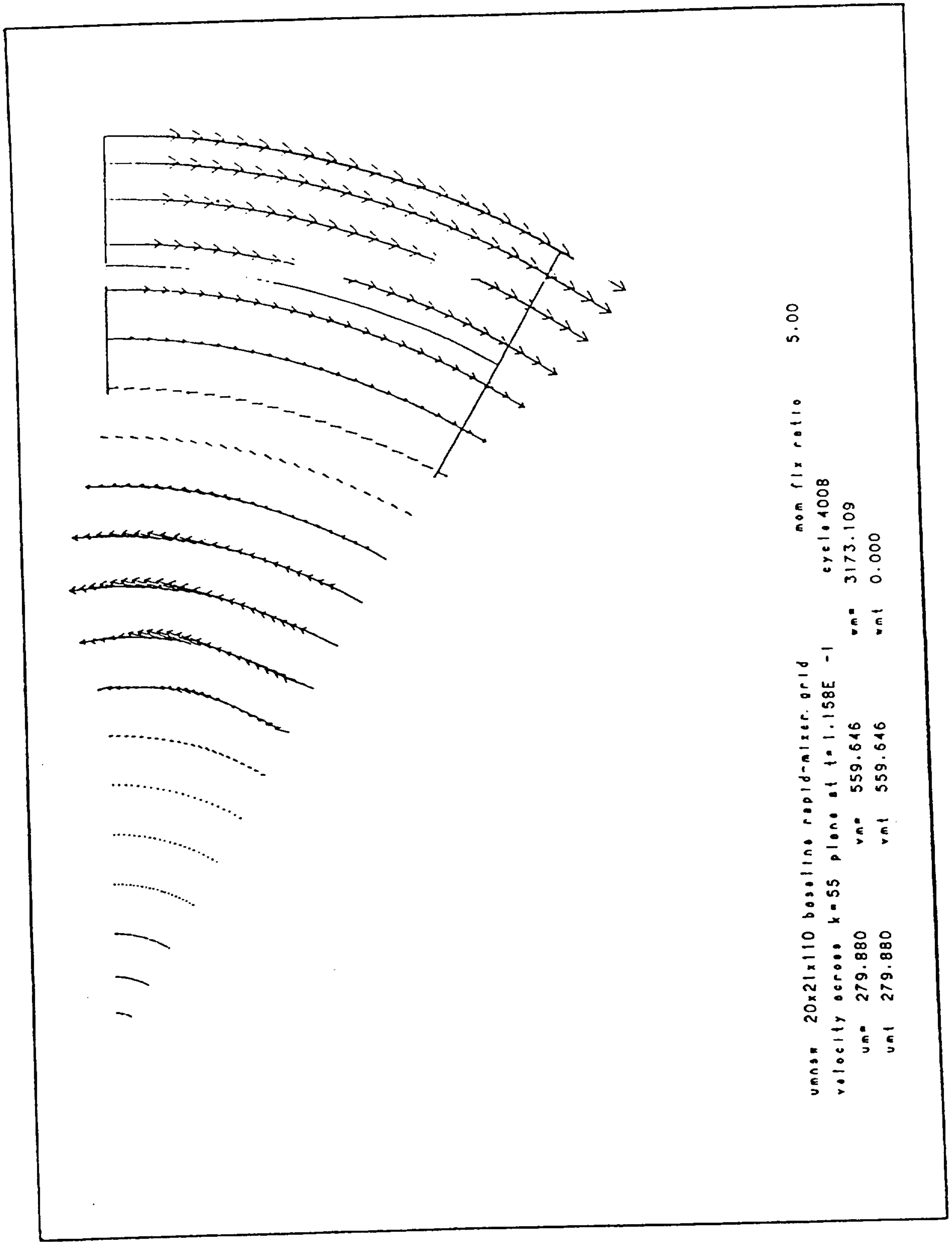
umnsw 20x21x110 baseline rapid-mixer.grid
velocity across k=55 plane at t=1.158E -1
um= 279.880
vmt 279.880
vm= 559.646
vmt 559.646
wm= 3173.109
wmt 0.000
mom flx ratio 5.00
cycle=4008

Figure 5-13

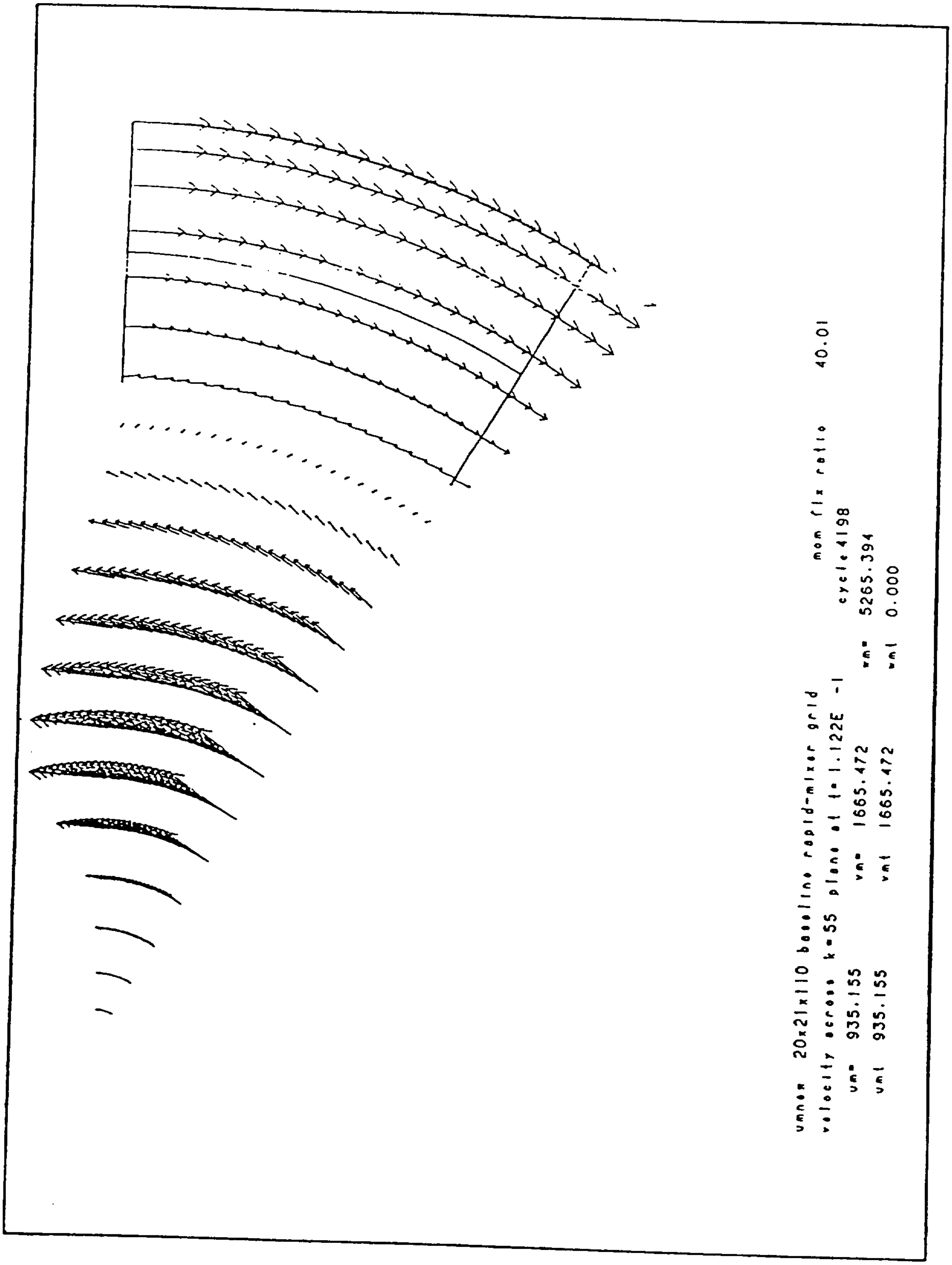
vnnex 20x21x110 baseline rapid-mixer grid
velocity across k=55 plane at t=1.122E -1
vn= 935.155
vnl 935.155
vm= 1665.472
vml 1665.472
wm= 5265.394
wml 0.000
cycle=4198
mom flx ratio 40.01

Figure 5-14

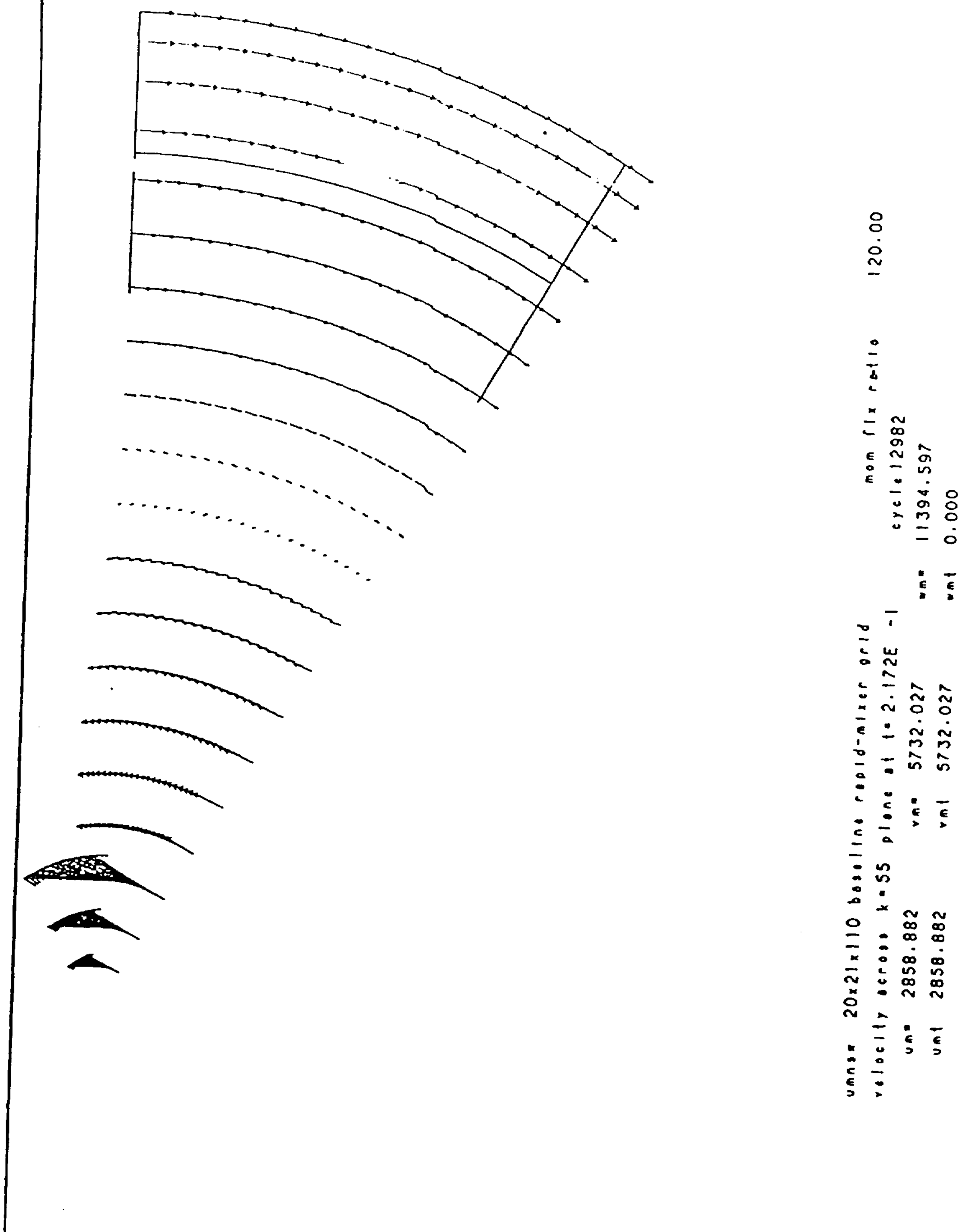
umnsw 20x21x110 baseline rapid-mixer grid
velocity across k=55 plane at t=2.172E -1
um= 2858.882
umt 2858.882
vm= 5732.027
vmt 5732.027
wm= 11394.597
wmt 0.000
mom flx ratio 120.00
cycle12982

Figure 5-15

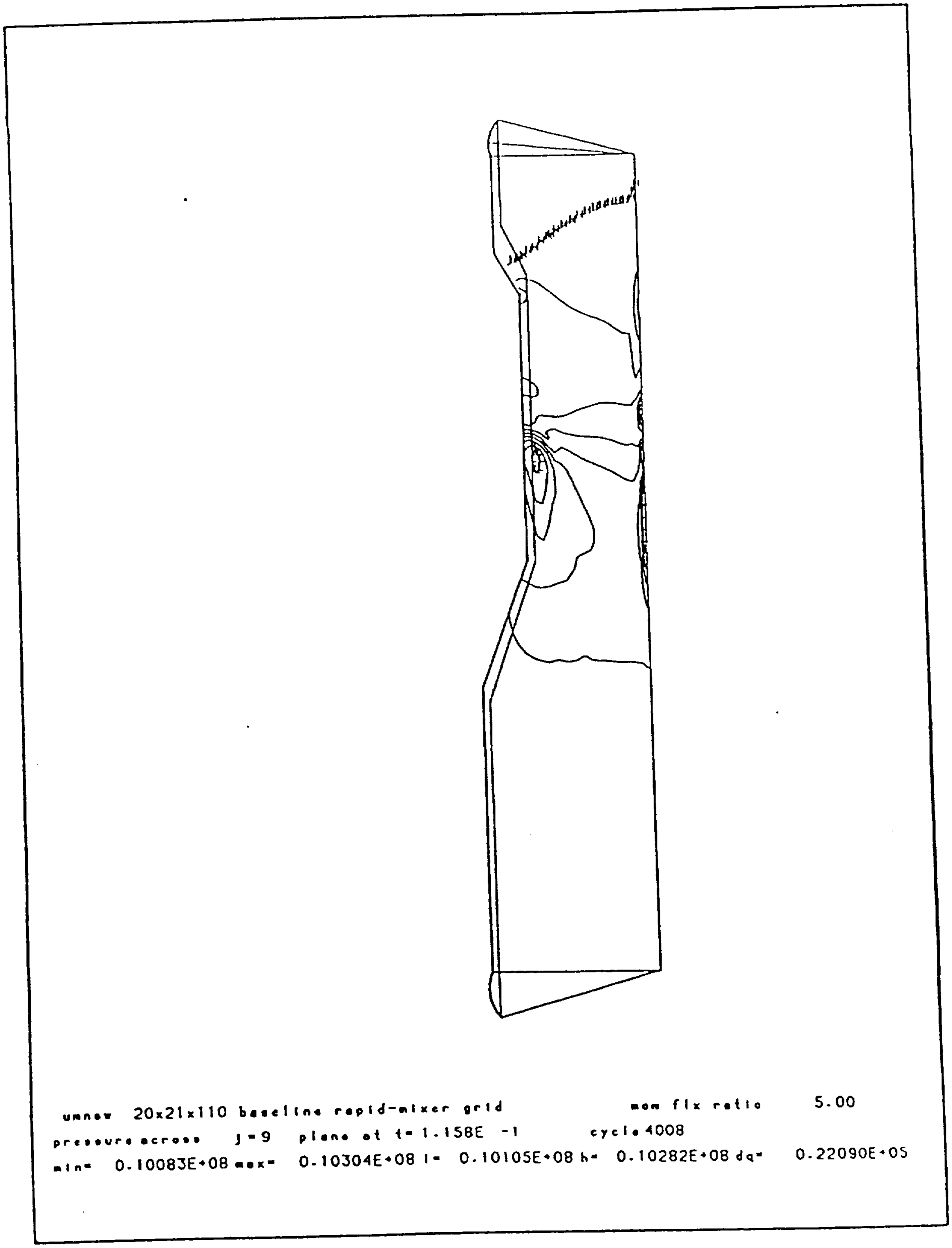
umnew 20x21x110 baseline rapid-mixer grid
mom flx ratio 5.00
pressure across j=9 plane at t= 1.158E -1
cycle 4008
min= 0.10083E+08 max= 0.10304E+08 l= 0.10105E+08 h= 0.10282E+08 dq= 0.22090E+05

Figure 5-16

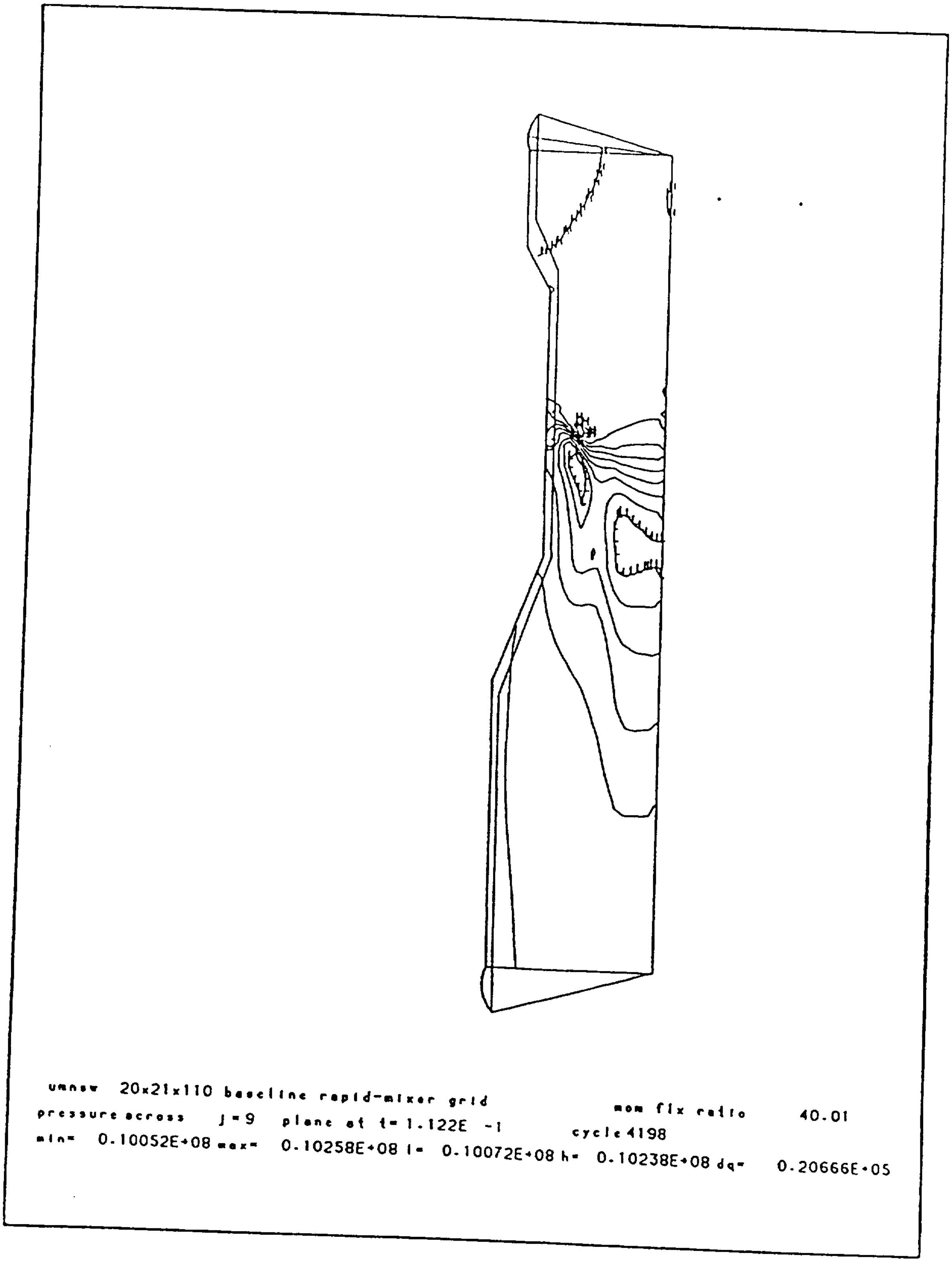
umnew 20x21x110 baseline rapid-mixer grid
pressure across j = 9 plane at t= 1.122E -1
min= 0.10052E+08 max= 0.10258E+08 l= 0.10072E+08 h= 0.10238E+08 dq= 0.20666E+05
mom flx ratio 40.01
cycle 4198

Figure 5-17

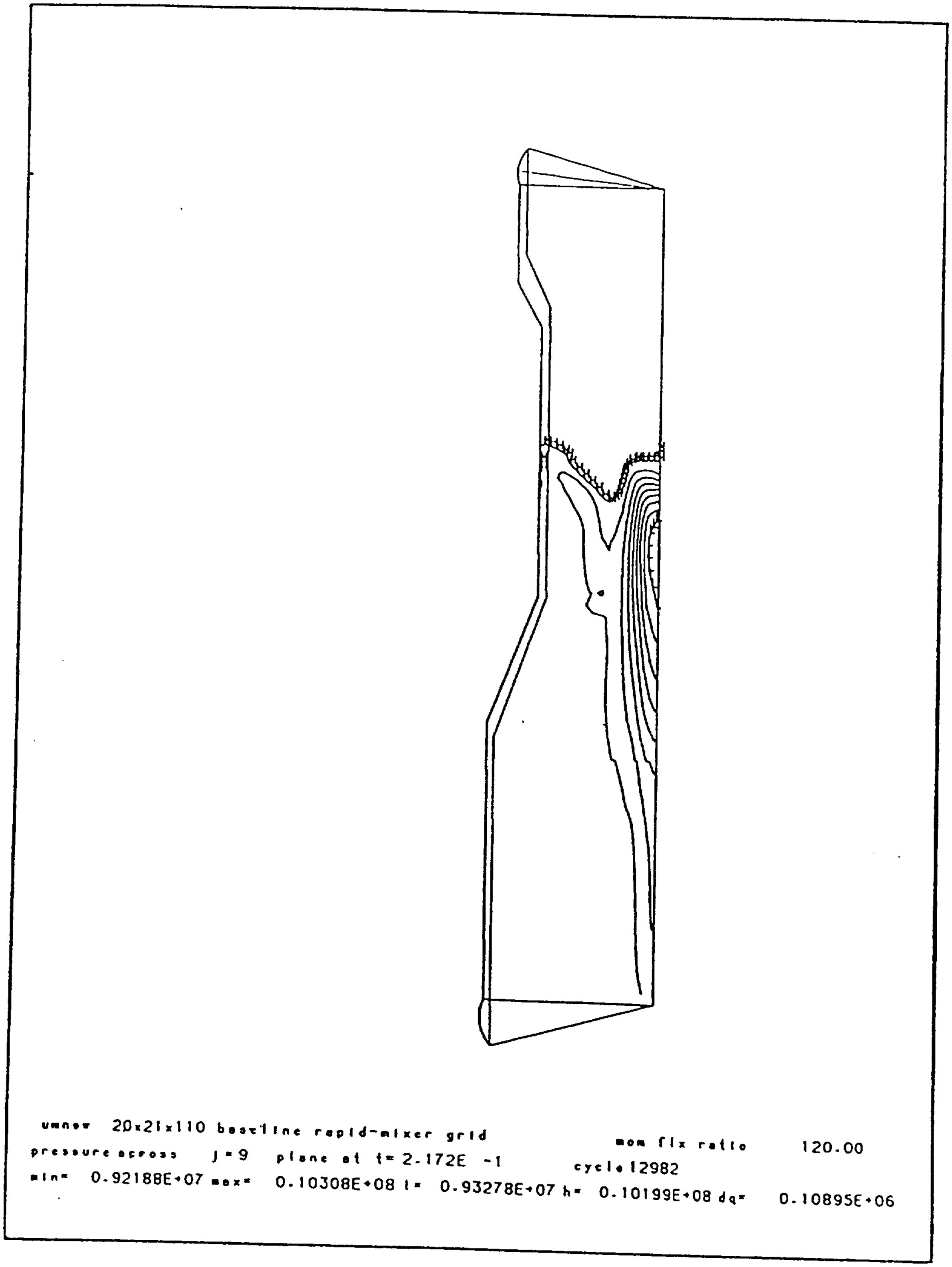
umnew 20x21x110 baseline rapid-mixer grid
mom flx ratio 120.00
pressure across j = 9 plane at t= 2.172E -1
cycle 12982
min= 0.92188E+07 max= 0.10308E+08 l= 0.93278E+07 h= 0.10199E+08 dq= 0.10895E+06

Figure 5-18

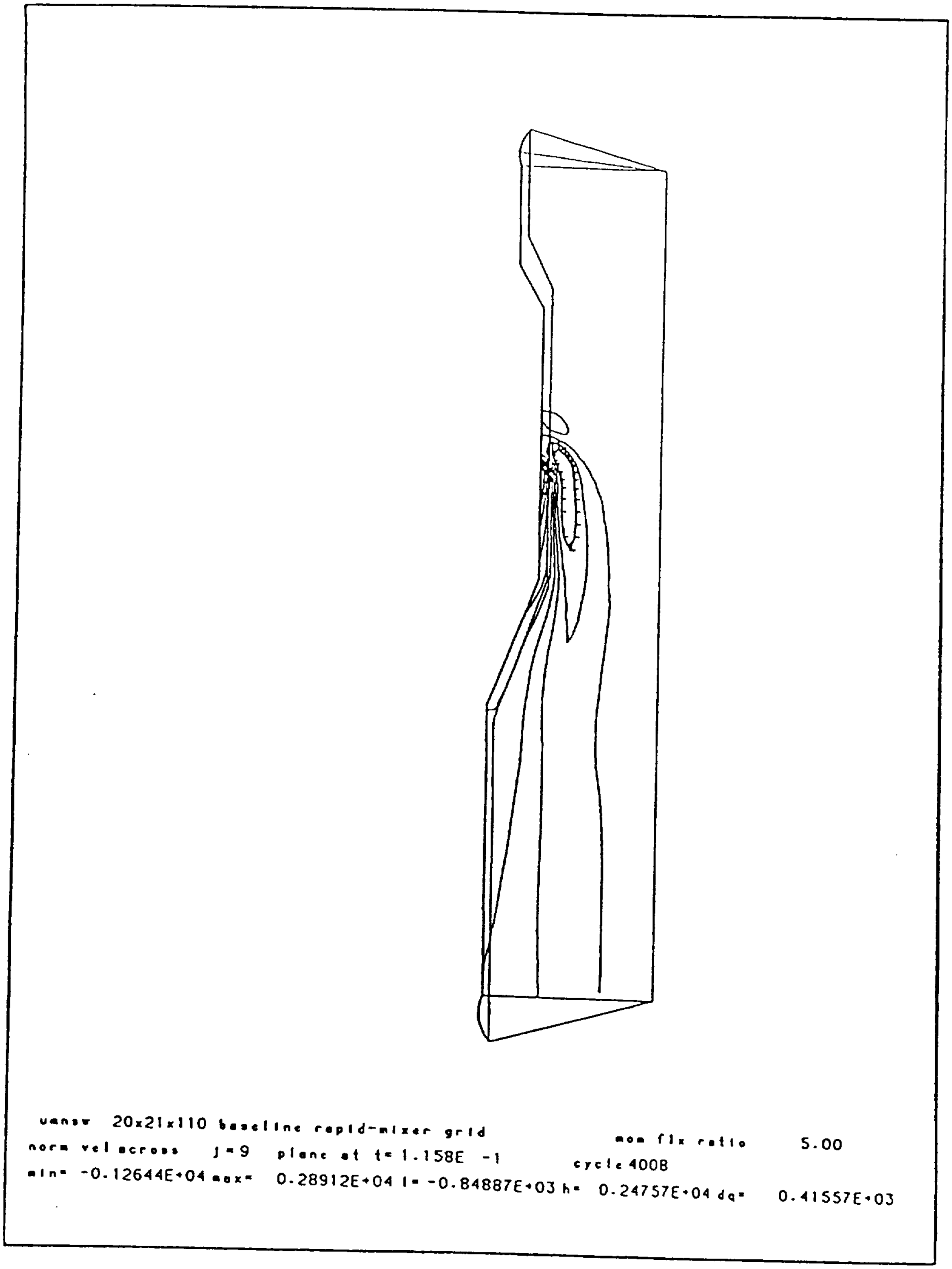
umnsw 20x21x110 baseline rapid-mixer grid
mom flx ratio 5.00
norm vel across j = 9 plane at t= 1.158E -1
cycle 4008
min= -0.12644E+04 max= 0.28912E+04 l= -0.84887E+03 h= 0.24757E+04 dq= 0.41557E+03

Figure 5-19

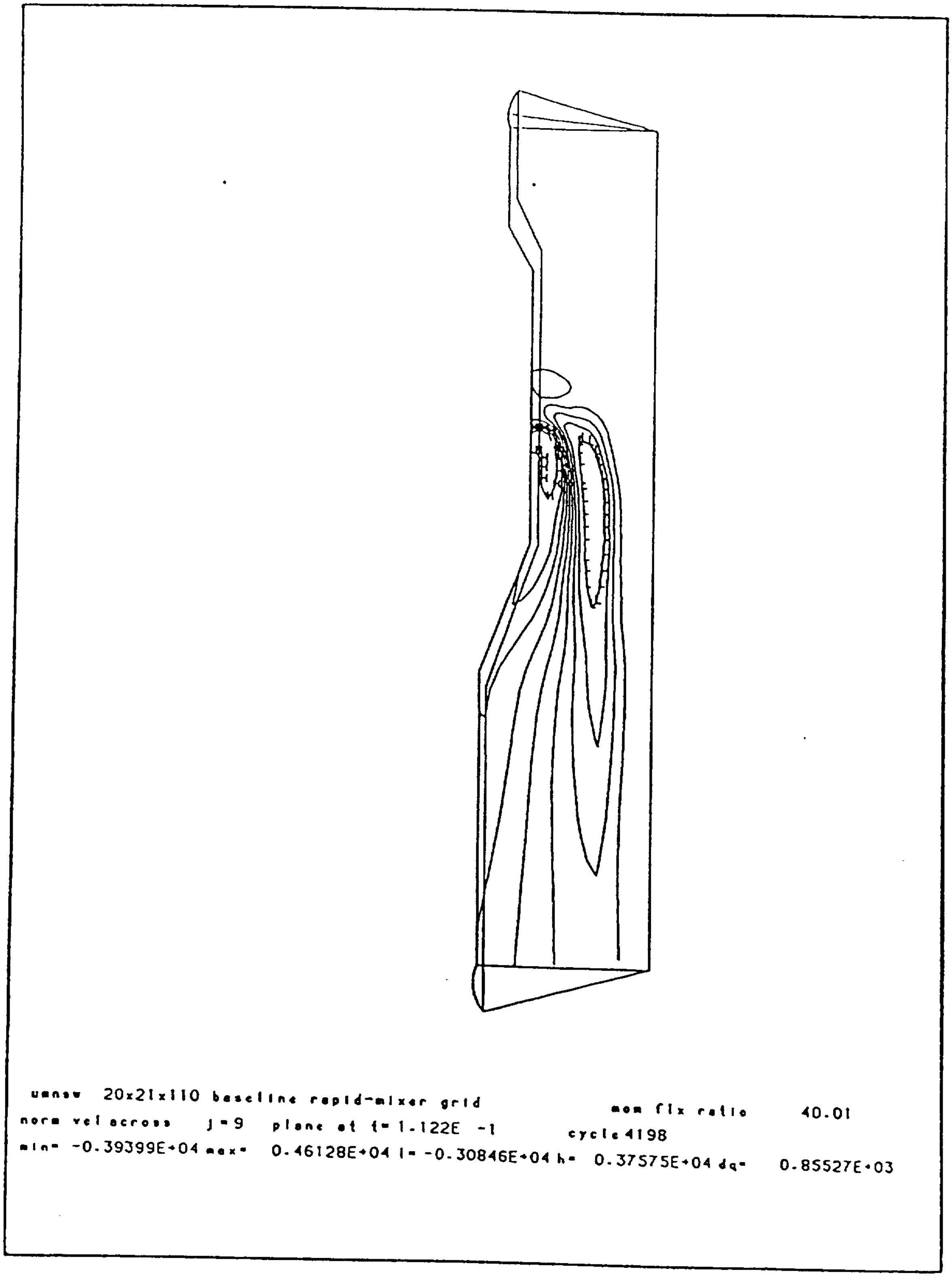

```
umnsw  20x21x110 baseline rapid-mixer grid                mom flx ratio     40.01
norm vel across   j=9  plane at i=1.122E -1        cycle 4198
min= -0.39399E+04 max=  0.46128E+04 l= -0.30846E+04 h= 0.37575E+04 dq=   0.85527E+03
```

Figure 5-20

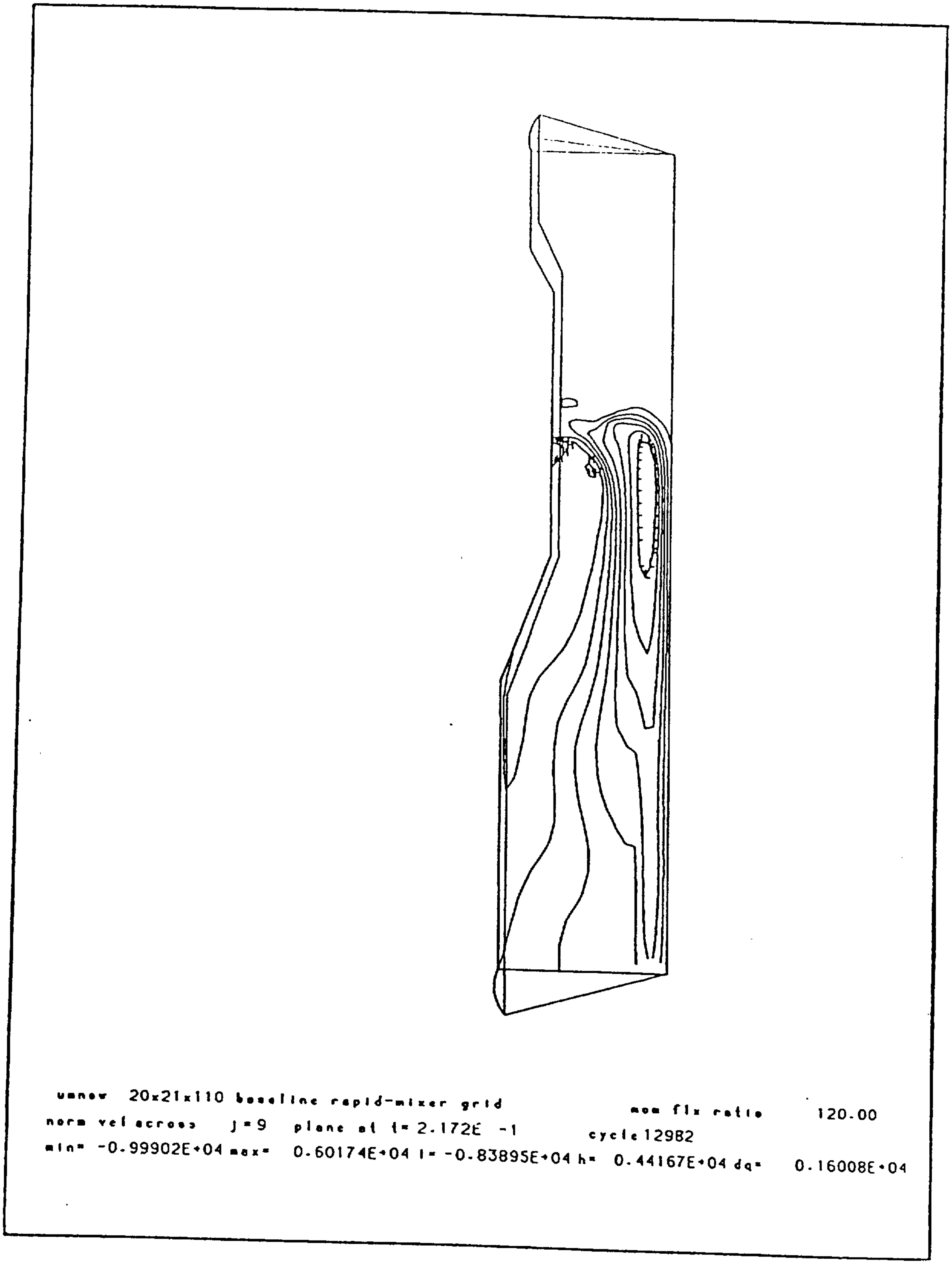
umnew 20x21x110 baseline rapid-mixer grid
mom flx ratio 120.00
norm vel across j=9 plane at i= 2.172E -1
cycle 12982
min= -0.99902E+04 max= 0.60174E+04 l= -0.83895E+04 h= 0.44167E+04 dq= 0.16008E+04

Figure 5-21

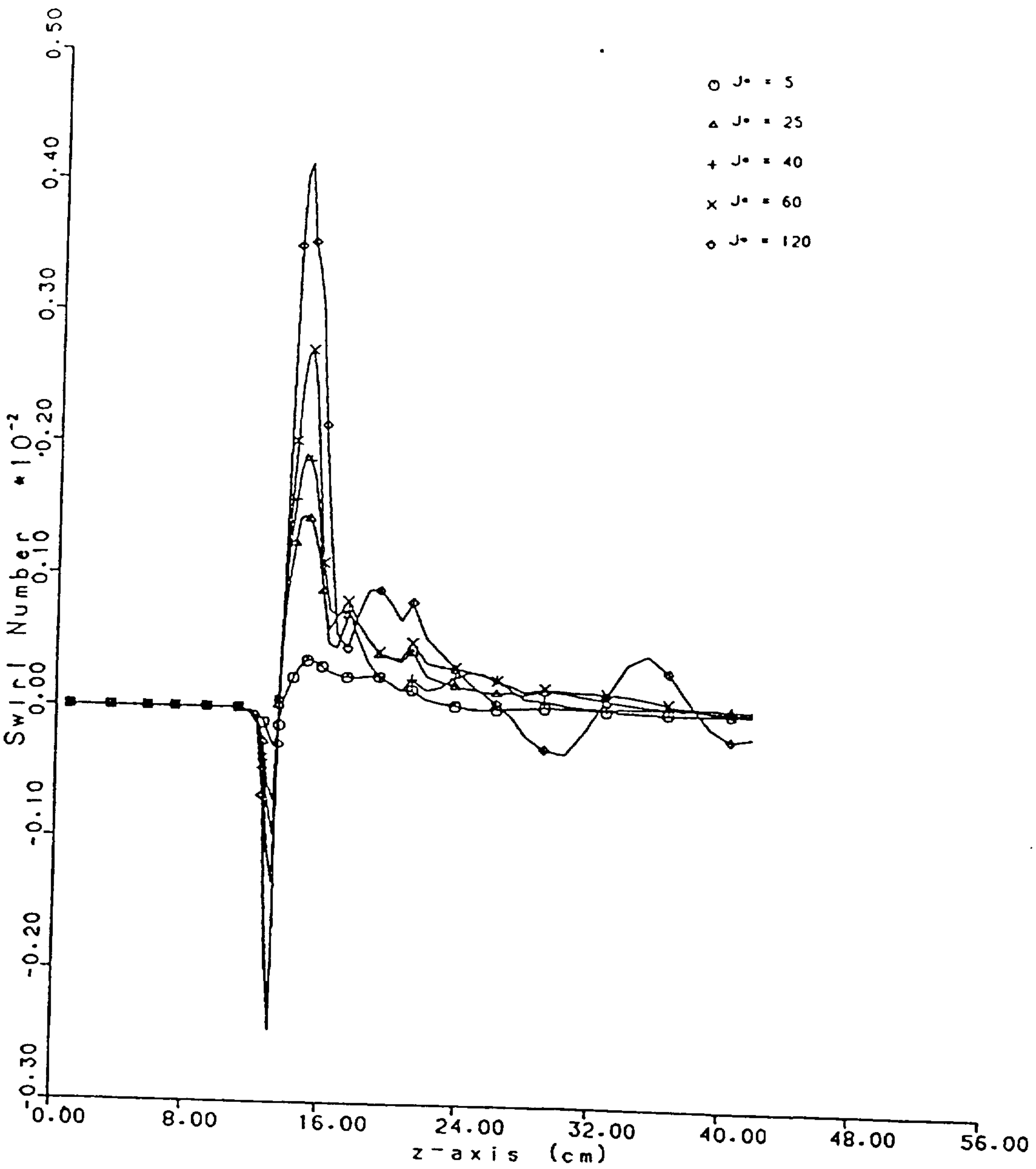

Swirl Number *10^-2
0.50
0.40
0.30
0.20
0.10
0.00
-0.10
-0.20
-0.30
0.00
8.00
16.00
24.00
32.00
40.00
48.00
56.00
z-axis (cm)
○ J* = 5
△ J* = 25
+ J* = 40
× J* = 60
◇ J* = 120

Figure 5-22

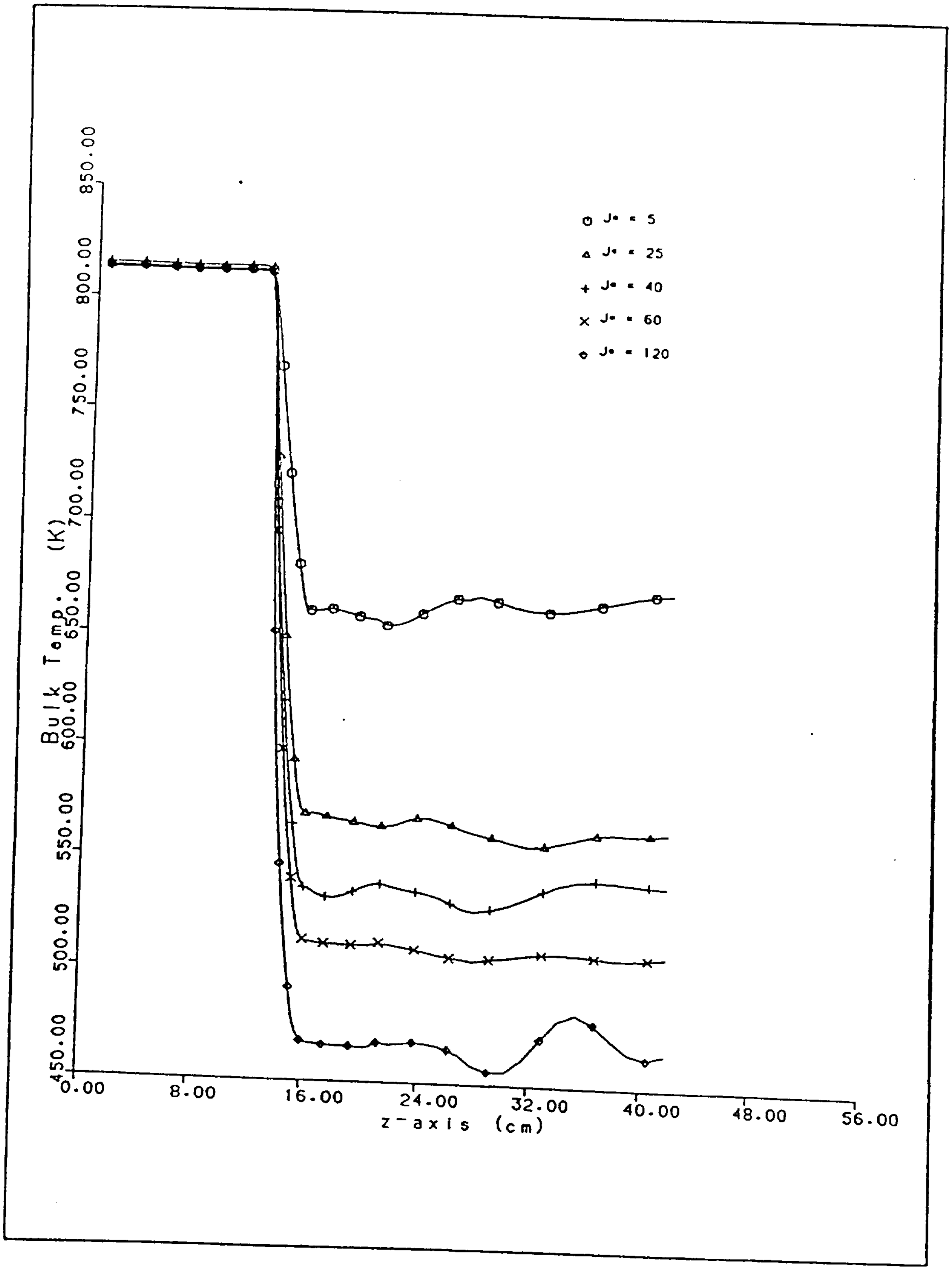

Bulk Temp. (K)
850.00
800.00
750.00
700.00
650.00
600.00
550.00
500.00
450.00
0.00
8.00
16.00
24.00
32.00
40.00
48.00
56.00
z-axis (cm)
J* = 5
J* = 25
J* = 40
J* = 60
J* = 120

Figure 5-23

CHAPTER VI

CONCLUSIONS & RECOMMENDATIONS

VI.1. Conclusions and Flowfield Evaluation

Results presented in chapter 4 and 5 were produced utilizing a tke averaging technique from i=1-4 along the centerline. This method yields the best results with low to mid momentum flux ratios, because the tke values are nearly uniform around the centerline. At high momentum flux ratios (J^*=120) when the jet penetrates near the centerline, this assumption is no longer valid. By superimposing values of turbulence lower than physically realistic, turbulent diffusion is decreased and an unrealistic central channel with excessively high magnitudes of velocity develops along the centerline. This region can be seen on the velocity profiles for the J^* = 120 runs shown in chapter 4 and 5. It is also manifested in the temperature and tke contours. Overall development and trends within the flowfield are characterized below:

1. Jet radial penetration increases with higher momentum flux ratios.
2. The bulk swirling profile extends deeper into the lean zone with higher J^* values.
3. Jet radial penetration increases with decreasing slot angle.
4. Net angular momentum from the inner CW and outer CCW profiles is virtually zero as shown by the dimensionless parameter swirl number. This is consistent with the conservation of angular momentum.

VI.2. Future Work

Small ripples in the bulk temperature profiles from chapter 4 and 5 are related to tke averaging. Bulk temperature profiles generated with runs not using tke averaging along the centerline were found to be much smoother. The disadvantages of tke averaging are more pronounced when investigating temperature difference between high and low contour values as a function of axial location down stream of the point of jet injection. Significant jumps in temperature difference were noted from one axial location to the next. It is clear the tke averaging along the centerline is unacceptable if accurate evaluation of thermal mixing performance is to be conducted.

To eliminate the need to average tke, convergence criteria must be decreased to 1.0e-05 for the pressure solution and to 1.0e-04 for the velocity solution. Runs conducted at lower J^* values show a time step 2 to 3 times higher than the corresponding run utilizing tke averaging. Figures (6-1) to (6-5) present flowfield results from a baseline steady state run with $J^* = 120$ and the reduced convergence criteria. These figures are much improved from the corresponding plots shown in chapters 4 and 5. Two important questions are yet to be answered from this work:

1. Does a slanted slot promote better mixing than a parallel slot.

2. Can the experimental results presented in a URTC report, which state that optimum mixing with the baseline geometry occurs at mid-range J^* values, be validated with the computational model.

Holdeman [10] has concluded that slots with a 45° slant in a rectangular duct produce reduced penetration and poorer thermal mixing than parallel slots. Fox and Gex [13] conducted an experimental investigation of the effect of the angle of injection of a single jet into a large reservoir of fluid, while attempting to minimize induced swirl and vorticity. Oldshue [14] states swirl is detrimental to jet mixing. It is unclear at this point if swirl within the circular axisymmetric baseline geometry is detrimental to mixing performance. If the jet and hot axial mainstream have mixed perfectly at a given z coordinate downstream of the point of jet injection there will be no variation of temperature along the cross section. The profile will be flat and have the numerical value equivalent to bulk temperature at the given z coordinate. Future work will include calculations for various momentum flux values with 45° slot and parallel slot geometries, and a comparison of temperature departure from the bulk mean temperature as a function of axial position. These calculations will take advantage of improved convergence criteria for velocity and pressure solutions to eliminate the need for tke averaging along the centerline.

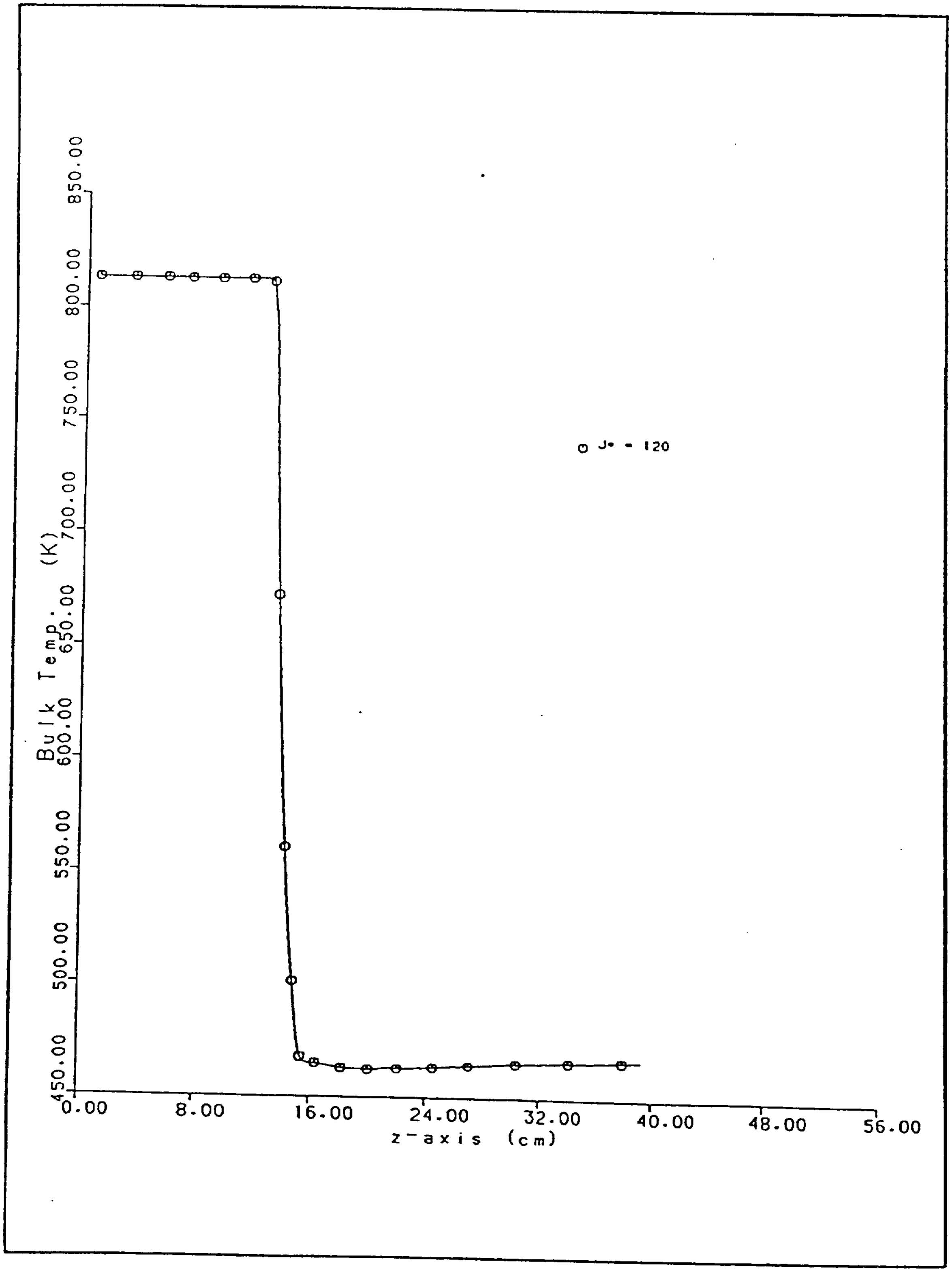
Bulk Temp. (K)
850.00
800.00
750.00
700.00
650.00
600.00
550.00
500.00
450.00
0.00
8.00
16.00
24.00
32.00
40.00
48.00
56.00
z-axis (cm)
○ J* = 120

Figure 6-1

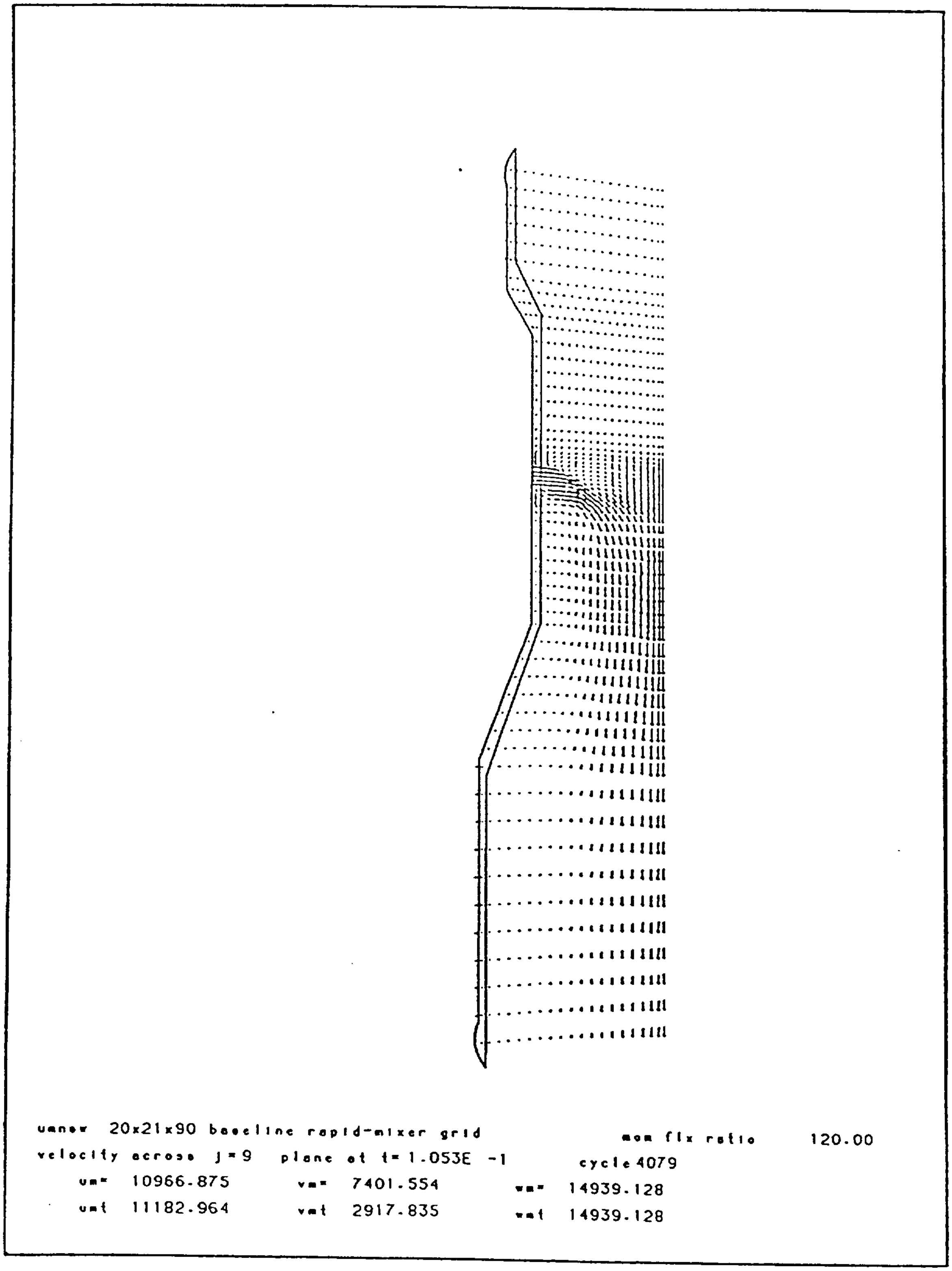

```
umnew  20x21x90 baseline rapid-mixer grid                mom flx ratio     120.00
velocity across  j=9  plane at t= 1.053E -1        cycle 4079
    um=  10966.875       vm=  7401.554       wm=  14939.128
    umt  11182.964       vmt  2917.835       wmt  14939.128
```

Figure 6-2

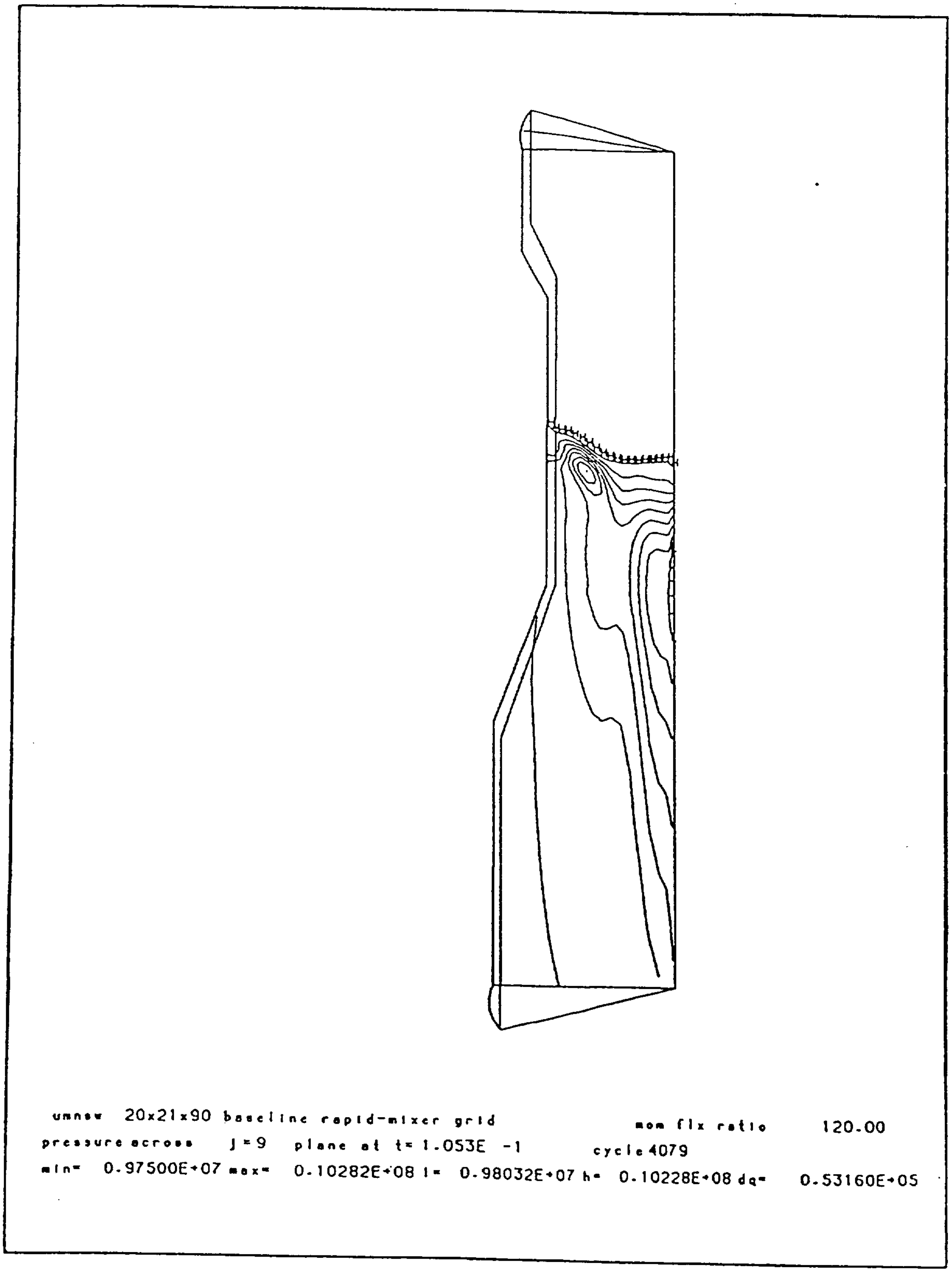
umnew 20x21x90 baseline rapid-mixer grid
mom flx ratio 120.00
pressure across j = 9 plane at t= 1.053E -1
cycle 4079
min= 0.97500E+07 max= 0.10282E+08 l= 0.98032E+07 h= 0.10228E+08 dq= 0.53160E+05

Figure 6-3

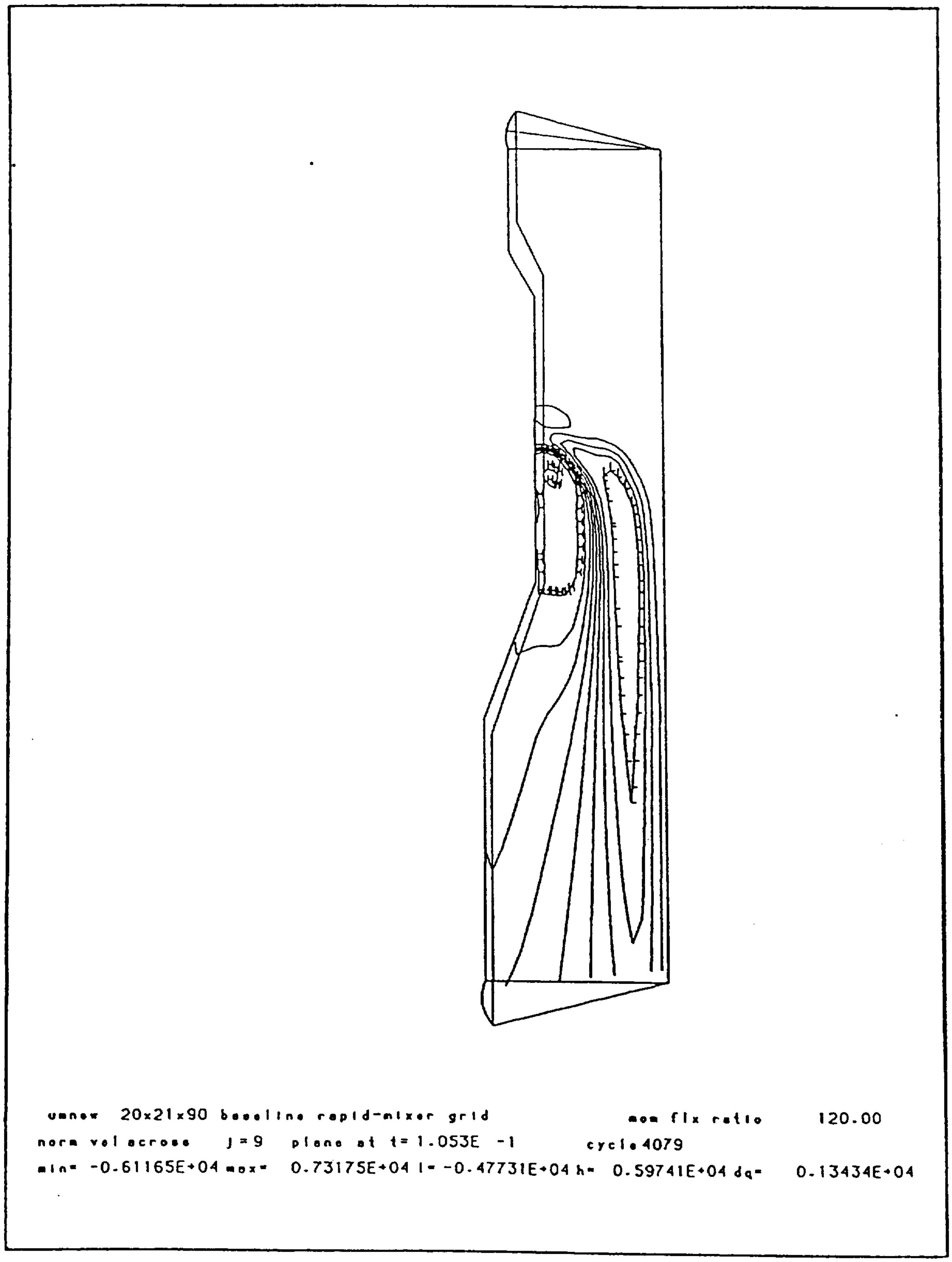
umnew 20x21x90 baseline rapid-mixer grid
mom flx ratio 120.00
norm vel across j = 9 plane at t= 1.053E -1
cycle 4079
min= -0.61165E+04 max= 0.73175E+04 l= -0.47731E+04 h= 0.59741E+04 dq= 0.13434E+04

Figure 6-4

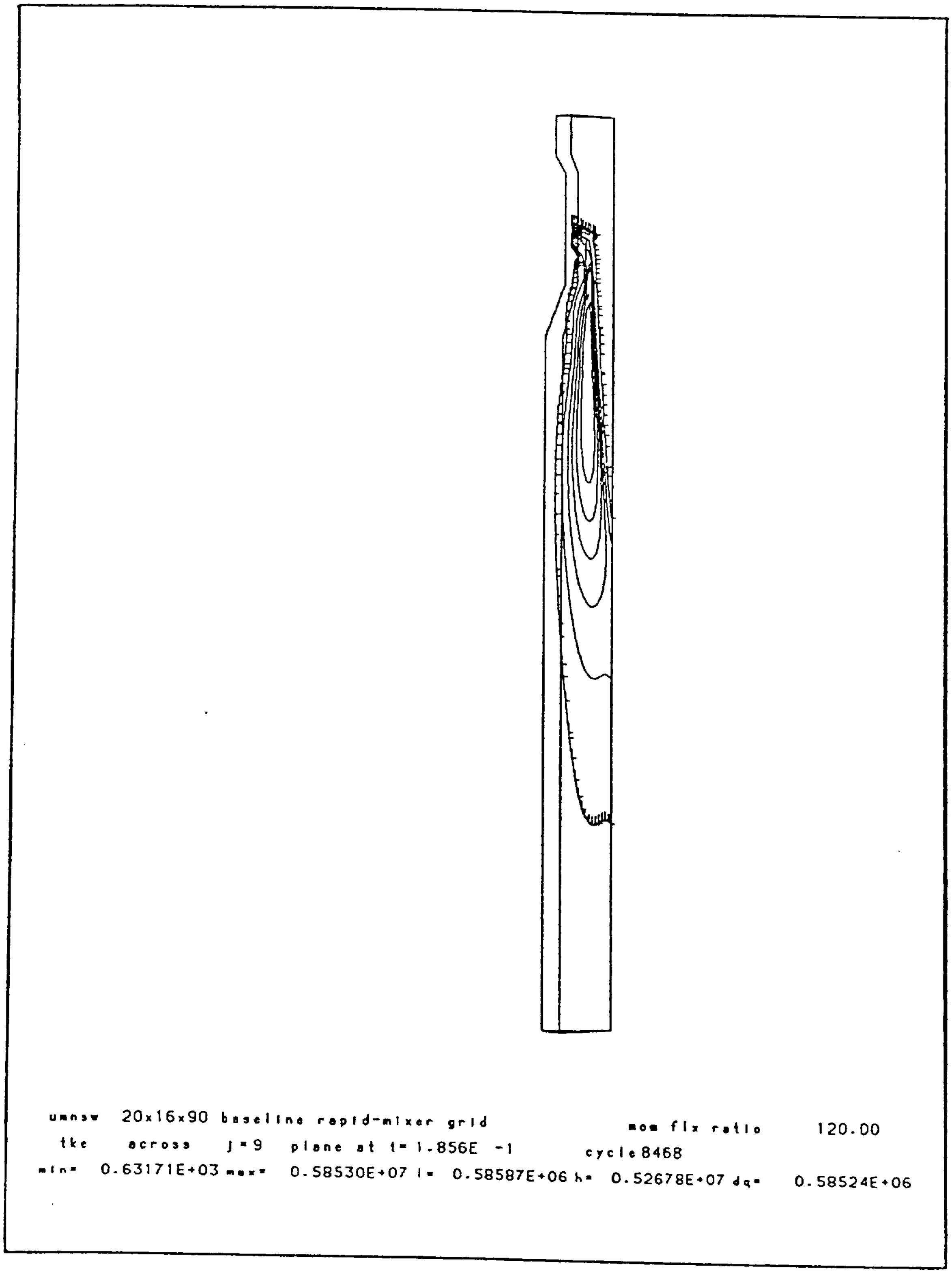
umnsw 20x16x90 baseline rapid-mixer grid
mom flx ratio 120.00
tke across j = 9 plane at t = 1.856E -1
cycle 8468
min= 0.63171E+03 max= 0.58530E+07 l= 0.58587E+06 h= 0.52678E+07 dq= 0.58524E+06

Figure 6-5

REFERENCES

1. Lefebvre, A.H., Gas Turbine Combustion. New York: Hemisphere Publishing Corp., 1983.

2. Keffer, J.F., Baines, W.D., "The Round Turbulent Jet in a Cross-Wind," J. Fluid Mechanics, 1963, 15, Part 4.

3. Ramsey, J.W., Goldstein, R.J., "Interaction of a Heated Jet with a Deflecting Stream," J. Heat Transfer, 1971.

4. Moussa, Z.M., Trischka, J.W., "The Near Field Mixing of a Jet with a Cross Stream," J. Fluid Mechanics, 1977, 80, Part 1.

5. Adler, D., Baron A., "Prediction of a Three-Dimensional Circular Turbulent Jet in Crossflow," AIAA Journal, 1979, 17.

6. Patankar, S.V., Basu, D.K., Alpay, S.A., "Prediction of the Three-Dimensional Velocity Field of a Deflected Jet," J. Fluids Engineering, 1977.

7. Kamotani, Y., Greber, I., "Experiments on Confined Turbulent Jets in a Crossflow," NASA CR-2392, 1974.

8. Holdeman, J.D., Srinivasan, R., Berenfeld, A., "Experiments in Dilution Jet Mixing," AIAA Journal, 1984, Vol. 22.

9. Holdeman, J.D., "Perspectives on the Mixing of a Row of Jets with a confined Crossflow," NASA Tech. Mem. 83457, 1983.

10. Holdeman, J.D., Srinivasan, R., Coleman, E.B., "Experiments in Dilution Jet Mixing - Effects of Multiple Rows & Non-Circular Orifices," AIAA-85-1104, 1985.

11. Sherif, S., Pletcher, R., "Measurements of the Flow & Turbulence Characteristics of Round Jets in Crossflow," Journal of Fluids Enginginee ring, 1989, Vol. III.

12. Beer, J.M., Chigier, N.A., "Combustion Aerodynamics," Applied Science, London, 1972.

13. Fox, E.A., Gex, V.E., A.I. Ch. E. J., 1956, 2(4):539.

14. Oldshue, J.Y., Fluid Mixing Technology. McGraw Hill Pub. Co., New York, 1983.

APPENDIX A

CASE GEOMETRY REVIEW

Definition of Geometric Variables:

ZM - Z coordinate of the point of transition between the 30° contraction and the mixing region.

ZBOC - Z coordinate of the upstream edge of the slanted slot.

ZEOC - Z coordinate of the downstream edge of the slanted slot in.

ZML - Z coordinate of the transition between the mixing region and the 21° expansion.

ZLN - Z coordinate of the transition between the 21° expansion and the lean zone.

45 Degree Slanted Slot 39,627 Cell Mesh:

ZM = 7.28 cm
ZBOC = 13.15 cm
Z(k=25) = 14.03 cm
ZEOC = 15.38 cm
Z(k=40) = 19.44 cm
ZML = 21.25 cm
ZLN = 27.87 cm
Z(k=55) = 32.95 cm
Z(k=60) = 39.30 cm
Z(k=65) = 45.65 cm
Z(k=75) = 58.34 cm
Z(k=85) = 74.05 cm
Z(k=95) = 99.45 cm

j = 9 Corresponds to 14.624°

Lean Zone Length = 44.18" included with this mesh.

Corresponding Figures:

2-1,2-2,2-14,2-15,2-16,2-17,2-18,
4-1 to 4-50,4-57 to 4-62,4-65,4-67,
4-69,4-71,4-72,4-73

30° Slanted Slot 51,282 Cell Mesh:

ZM = 7.179 cm
ZBOC = 12.88 cm
Z(k=25) = 13.99 cm
ZEOC = 15.64 cm
Z(k=40) = 20.62 cm
ZML = 21.25 cm
ZLN = 27.87 cm
Z(k=55) = 35.49 cm
Z(k=60) = 41.84 cm

j = 9 Corresponds to 11.459°

Lean Zone Length = 45.183" included with this mesh.

Corresponding Figures:

5-1 to 5-23

45° Slanted Slot Partially Blocked Off 28,101 Cell Mesh:

ZM = 7.28 cm
ZBOC = 13.15 cm
Z(k=25) = 14.37 cm
ZEOC = 15.38 cm
ZML = 21.25 cm
ZLN = 27.87 cm
Z(k=60) = 39.04 cm

j = 9 Corresponds to 14.624°

Lean Zone Length = 24.15" included with this mesh.

Corresponding Figures:

2-3 to 2-13

45° Slanted Slot 16,660 Cell Mesh:

ZM = 7.28 cm
ZBOC = 13.15 cm
Z(k=28) = 14.87 cm
ZEOC = 15.38 cm
ZML = 21.25 cm
ZLN = 27.87 cm
Z(k=60) = 37.02 cm

j = 9 Corresponds to 14.624°

Lean Zone Length = 29.99" included with this mesh.

Corresponding Figures:

4-51 to 4-56,4-63

45° Slanted Slot Reduced Length 32,487 Cell Mesh:

Lean Zone Length = 33.20" included with this mesh.

a. Results generated with tke averaging along the centerline.

   Corresponding Figures:

   4-64,4-66,4-68,4-70

b. Results generated without tke averaging utilizing increased convergence criteria for the velocity and pressure solution.

   Corresponding Figures:

   6-1 to 6-5

APPENDIX B

History Plots

Steady state determination was facilitated with three sets of history plots for each geometry. Each set included pressure, temperature and velocity. The most upstream location is found to reach steady state first and the furthest downstream location last. If pressure, temperature and velocity are at steady state along the nz plane (the mixer outlet) it can be assumed the flowfield has reached steady state at all other regions of the mesh. To conserve cpu required to reach steady state the entire lean zone was not allowed to reach steady state prior to terminating the run. Instead, history plots from a point slightly downstream the transition point between the 21° expansion and the lean zone were used to determine if the area of interest (the mixing region) had reached steady state. The following are i,j and k coordinates where the history plots were taken:

45° Slanted Slot Mesh: i,j,k = 8,8,60
45° Slanted Slot Coarse Mesh: i,j,k = 7,8,60
30° Slanted Slot Mesh: i,j,k = 11,8,60

These locations correspond to positions at the end of the area of interest and roughly centered with respect to the radial and azimuthal directions within the 30 degree sector mesh. Table B.1 categorizes history plots included with this appendix by mesh type.

TABLE B.1

45° Slanted Slot Mesh

$J^* = 5$	B-1,B-2,B-3
$J^* = 25$	B-4,B-5,B-6
$J^* = 40$	B-7,B-8,B-9
$J^* = 60$	B-10,B-11,B-12
$J^* = 120$	B-13,B-14,B-15

30° Slanted Slot Mesh

$J^* = 5,25,60,120$	B-16,B-17,B-18
$J^* = 40$	B-19,B-20,B-21

45° Slanted Slot Coarse Mesh

$J^* = 25$	B-22,B-23,B-24

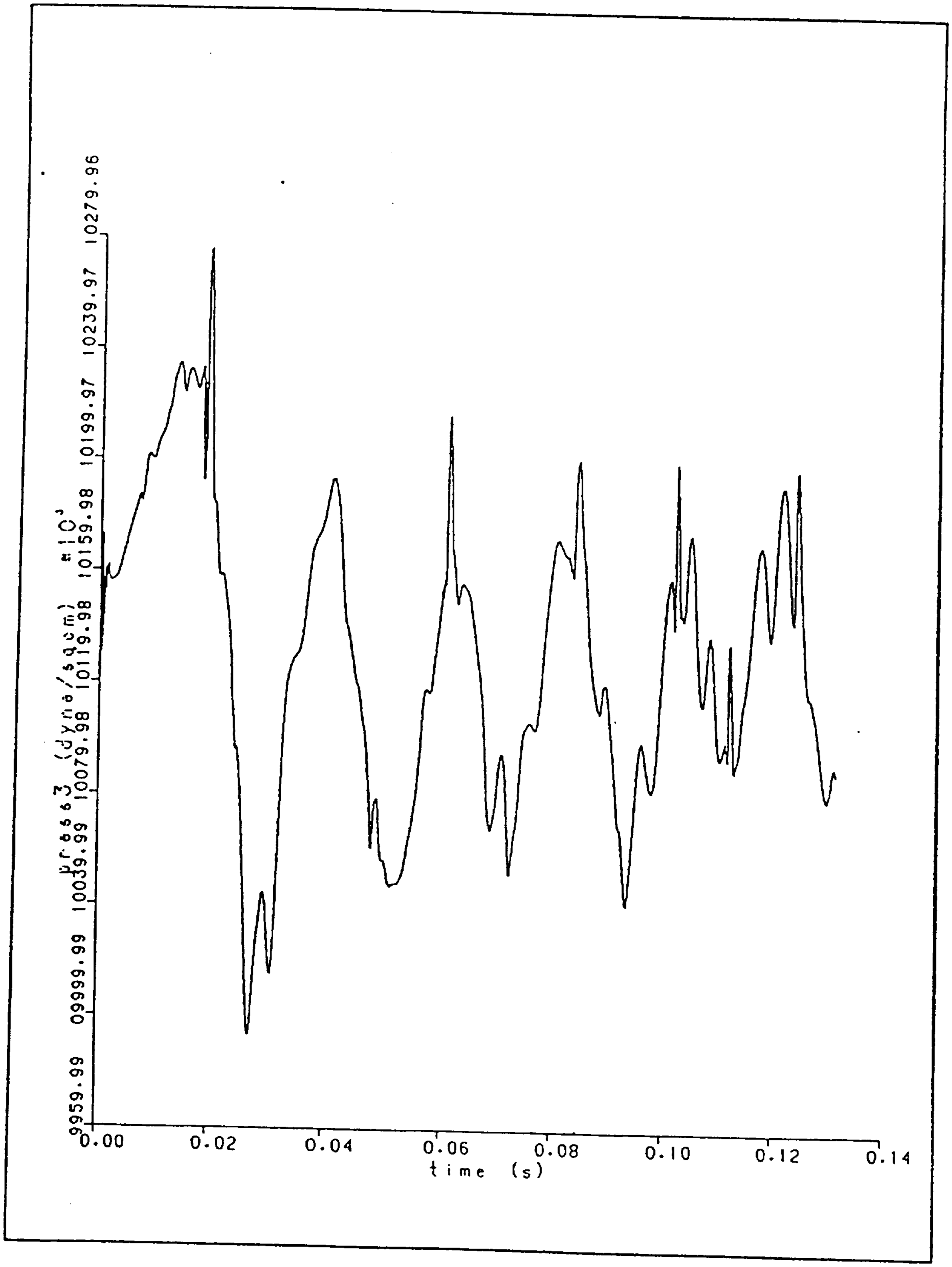
press3 (dyne/sqcm) *10³
9959.99
09999.99
10039.99
10079.98
10119.98
10159.98
10199.97
10239.97
10279.96
0.00
0.02
0.04
0.06
0.08
0.10
0.12
0.14
time (s)

Figure B-1

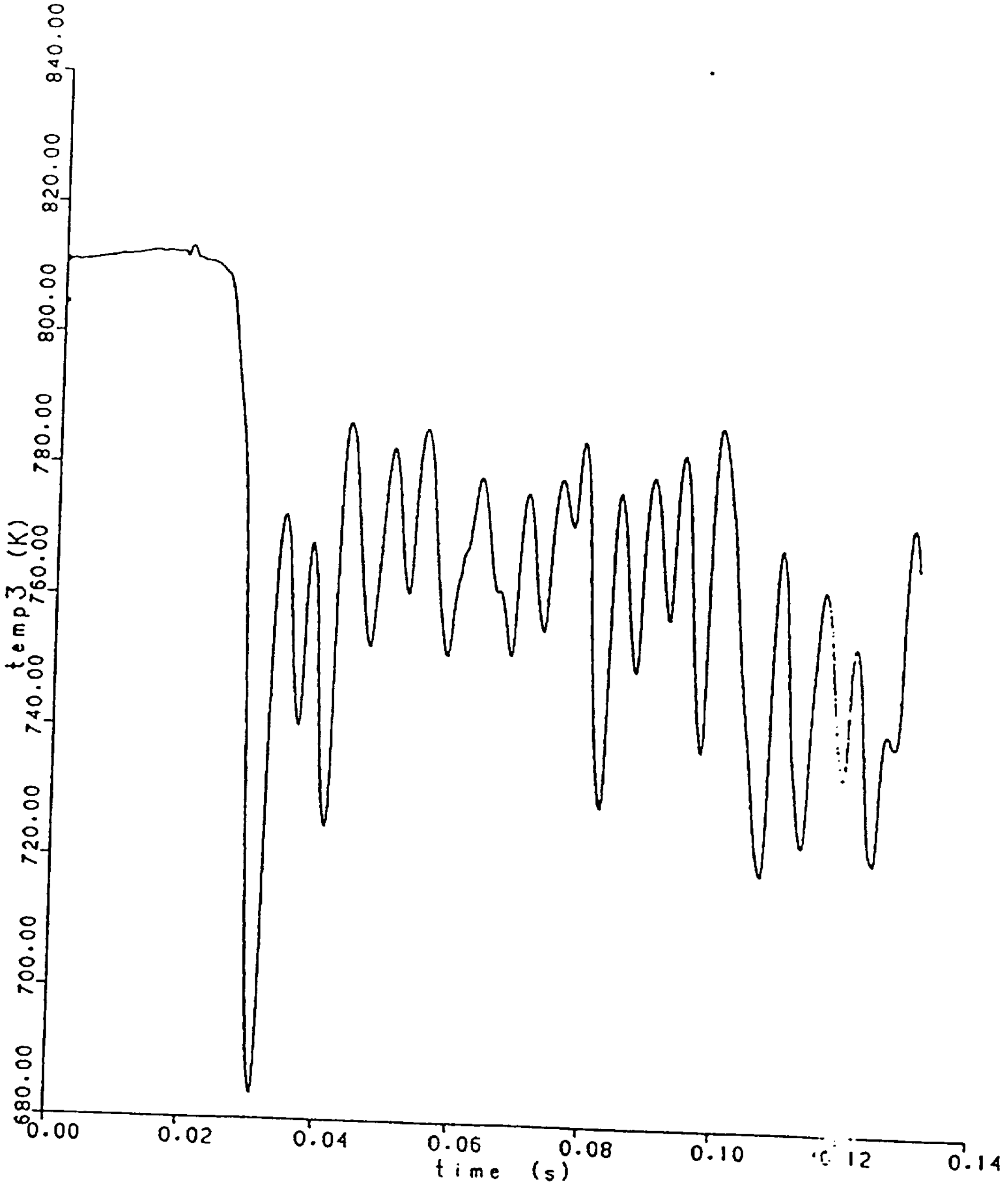
840.00
820.00
800.00
780.00
760.00
740.00
720.00
700.00
680.00
temp3 (K)
0.00
0.02
0.04
0.06
0.08
0.10
0.12
0.14
time (s)

Figure B-2

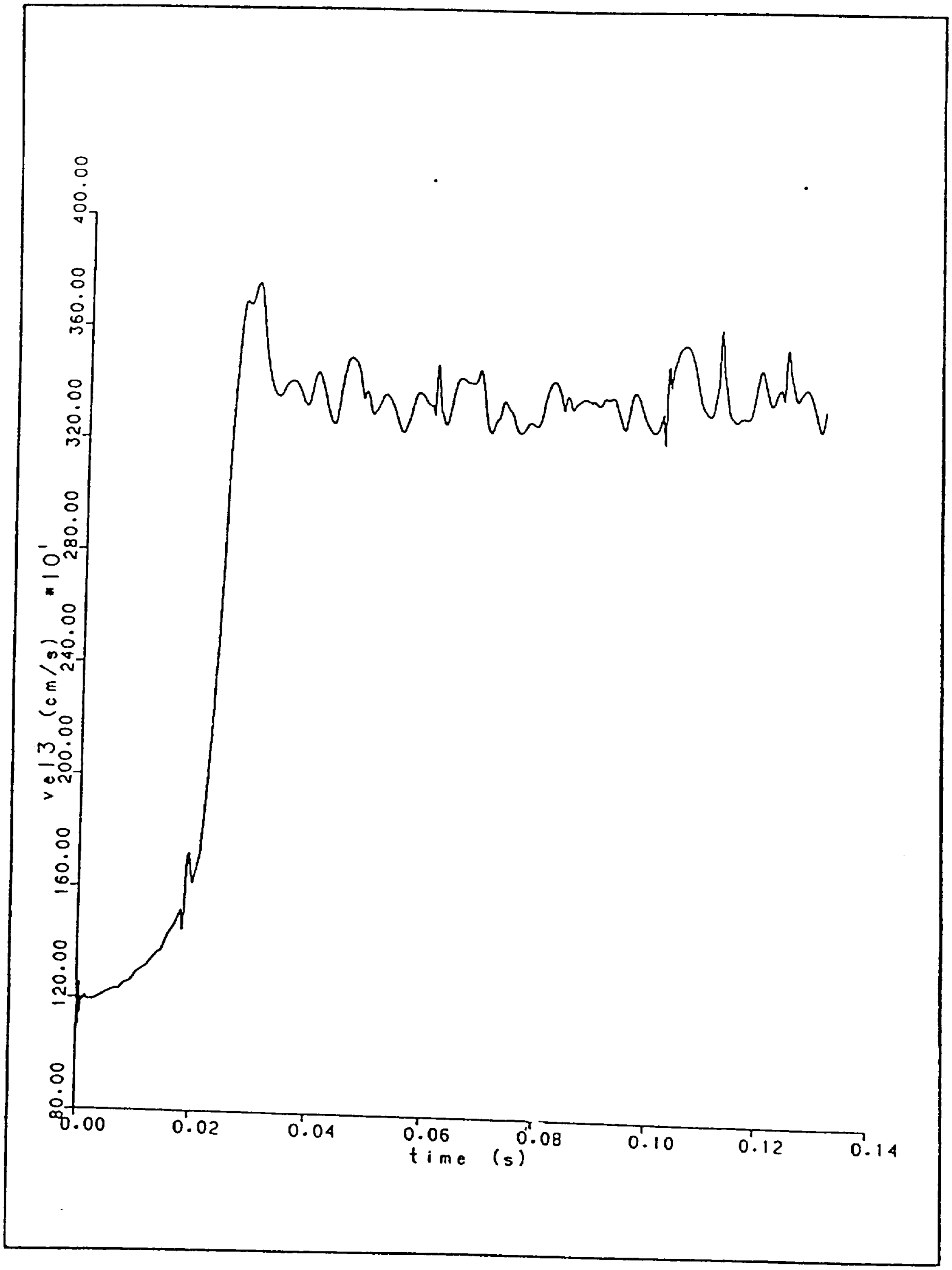
vel3 (cm/s) *10¹
80.00
120.00
160.00
200.00
240.00
280.00
320.00
360.00
400.00
0.00
0.02
0.04
0.06
0.08
0.10
0.12
0.14
time (s)

Figure B-3

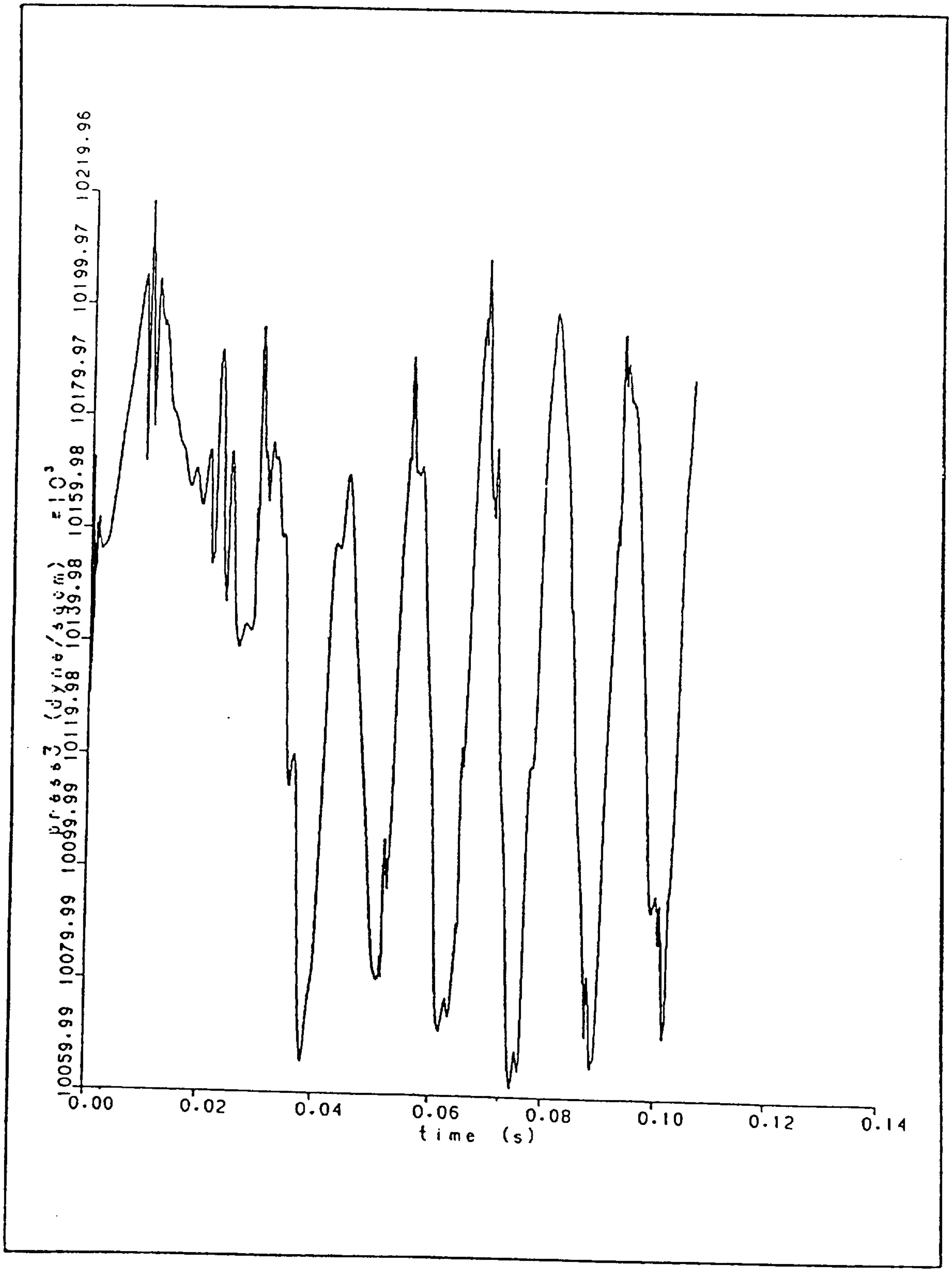
10059.99
10079.99
10099.99
10119.98
10139.98
10159.98
10179.97
10199.97
10219.96
press3 (dyne/sqcm) *10³
0.00
0.02
0.04
0.06
0.08
0.10
0.12
0.14
time (s)

Figure B-4

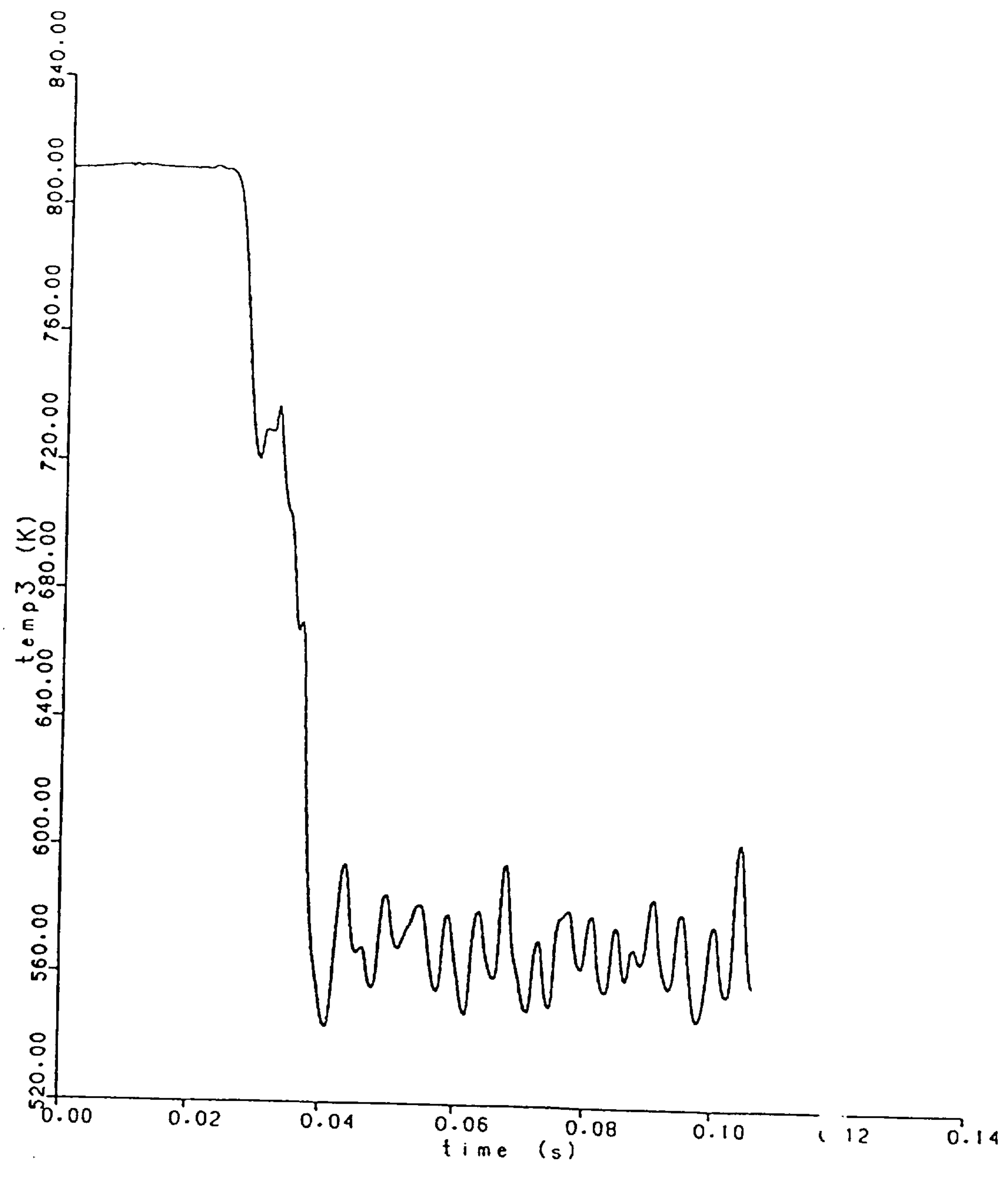
840.00
800.00
760.00
720.00
680.00
640.00
600.00
560.00
520.00
temp3 (K)
0.00
0.02
0.04
0.06
0.08
0.10
12
0.14
time (s)

Figure B-5

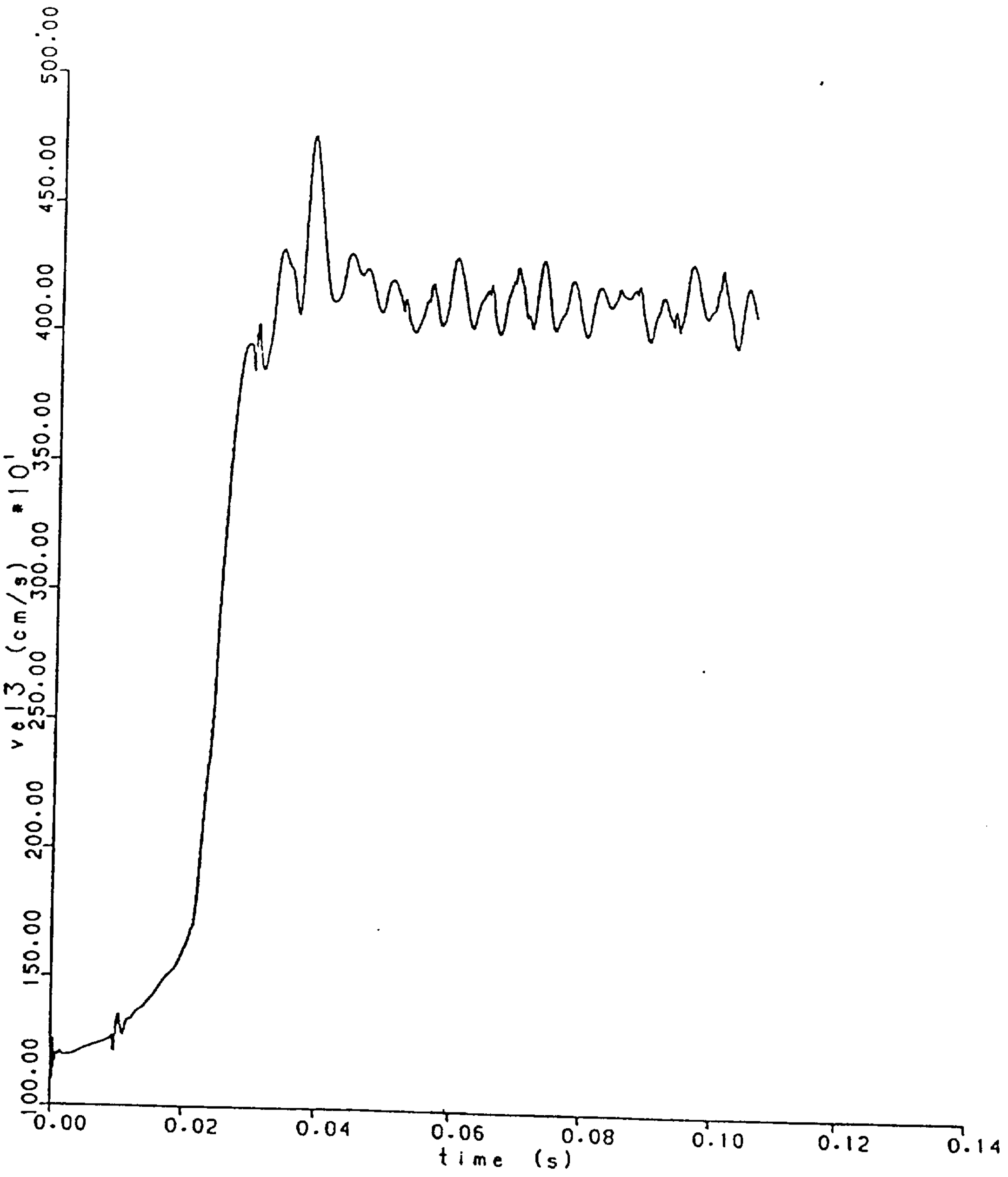

vel3 (cm/s) *10¹
100.00
150.00
200.00
250.00
300.00
350.00
400.00
450.00
500.00
0.00
0.02
0.04
0.06
0.08
0.10
0.12
0.14
time (s)

Figure B-6

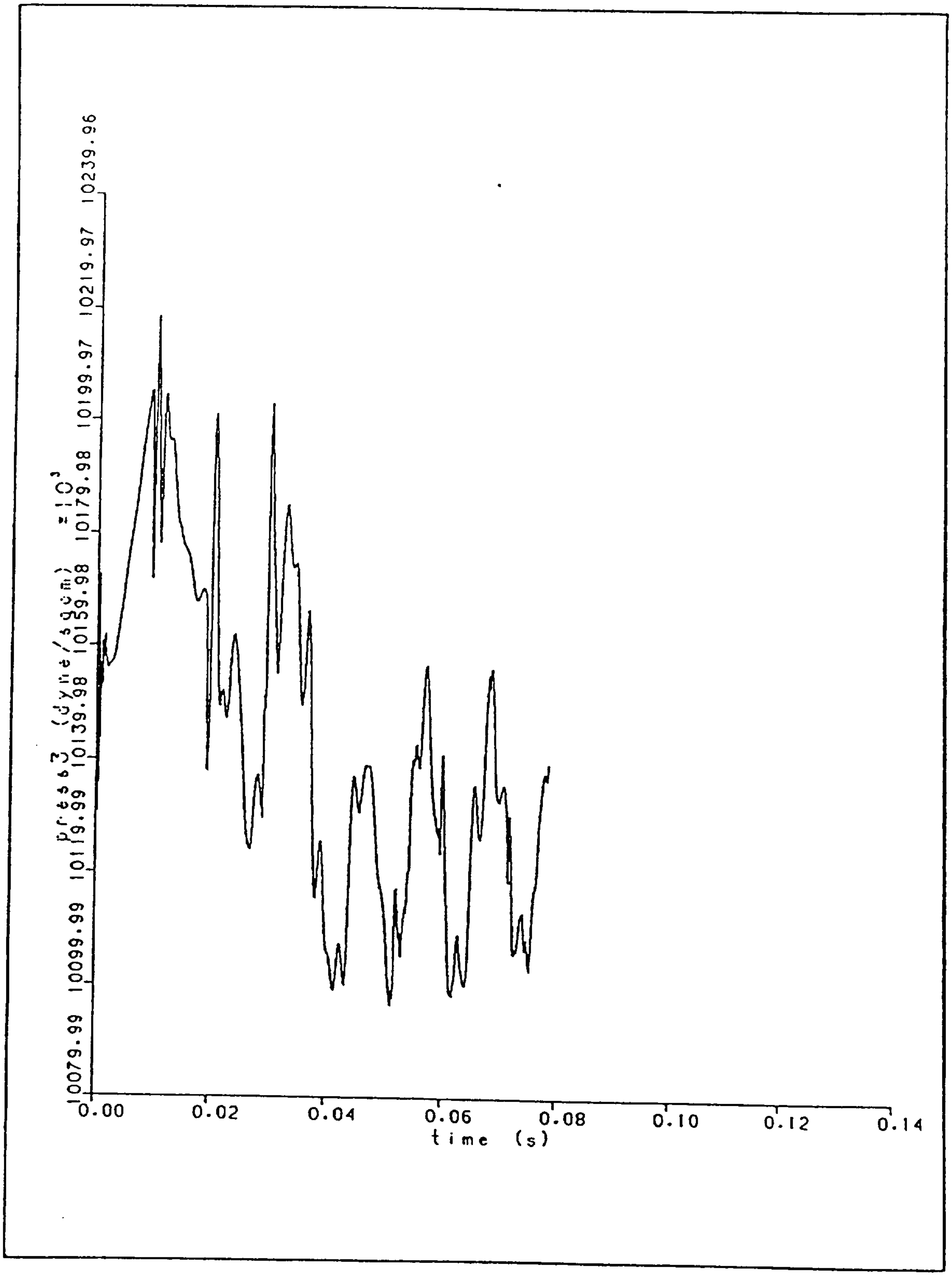
press3 (dyne/sqcm) *10³
10239.96
10219.97
10199.97
10179.98
10159.98
10139.98
10119.99
10099.99
10079.99
0.00
0.02
0.04
0.06
0.08
0.10
0.12
0.14
time (s)

Figure B-7

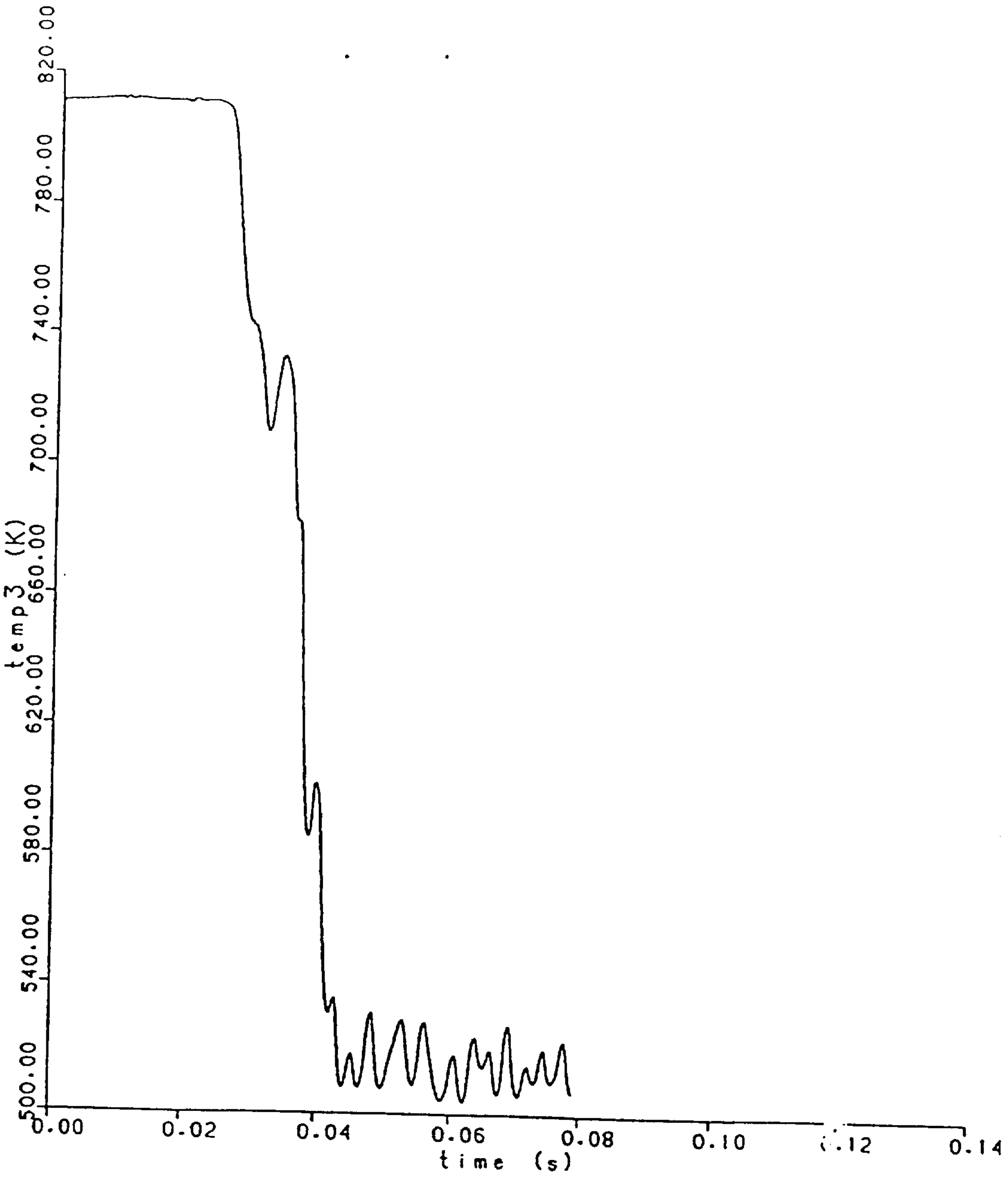

820.00
780.00
740.00
700.00
660.00
620.00
580.00
540.00
500.00
temp3 (K)
0.00
0.02
0.04
0.06
0.08
0.10
0.12
0.14
time (s)

Figure B-8

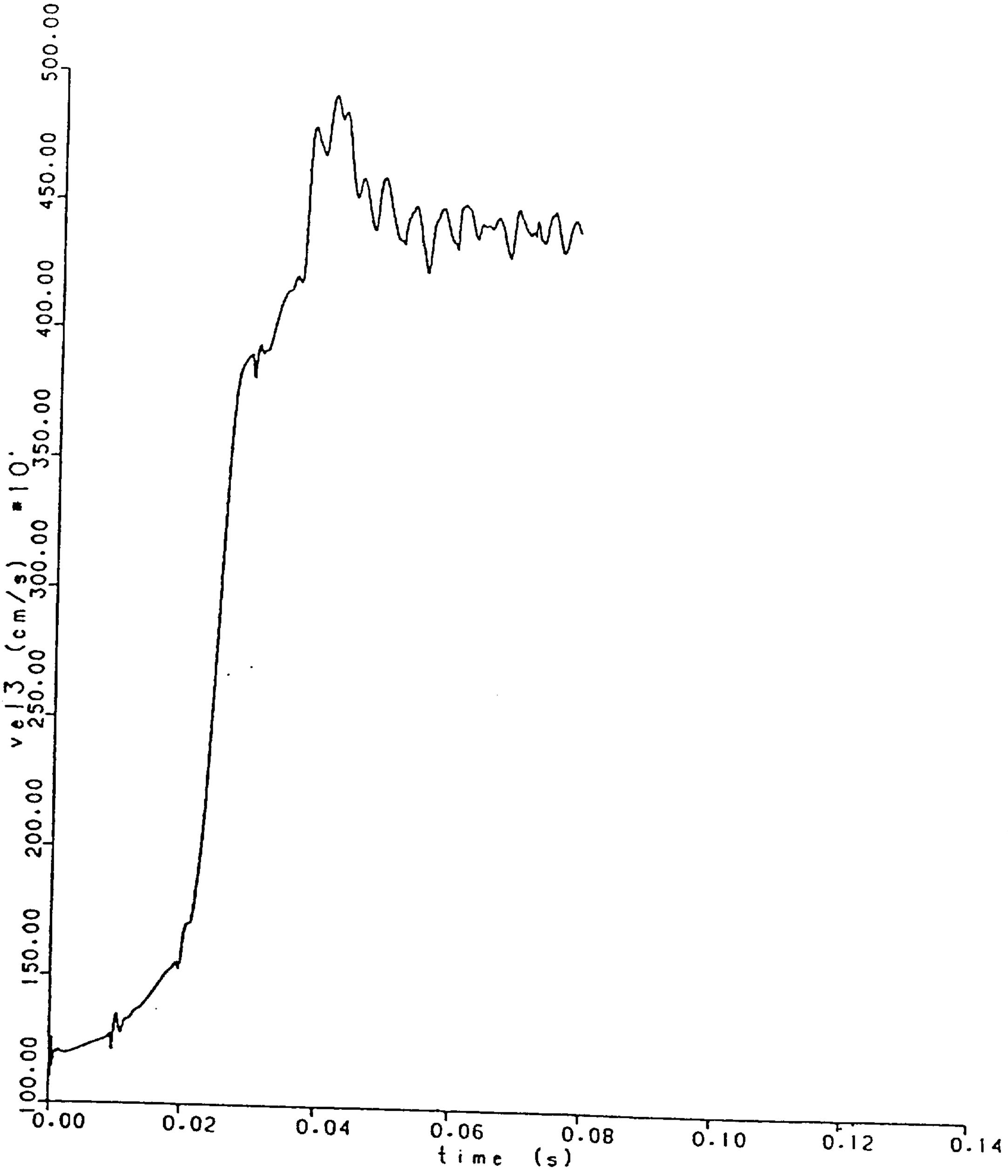
vel3 (cm/s) *10'
100.00
150.00
200.00
250.00
300.00
350.00
400.00
450.00
500.00
0.00
0.02
0.04
0.06
0.08
0.10
0.12
0.14
time (s)

Figure B-9

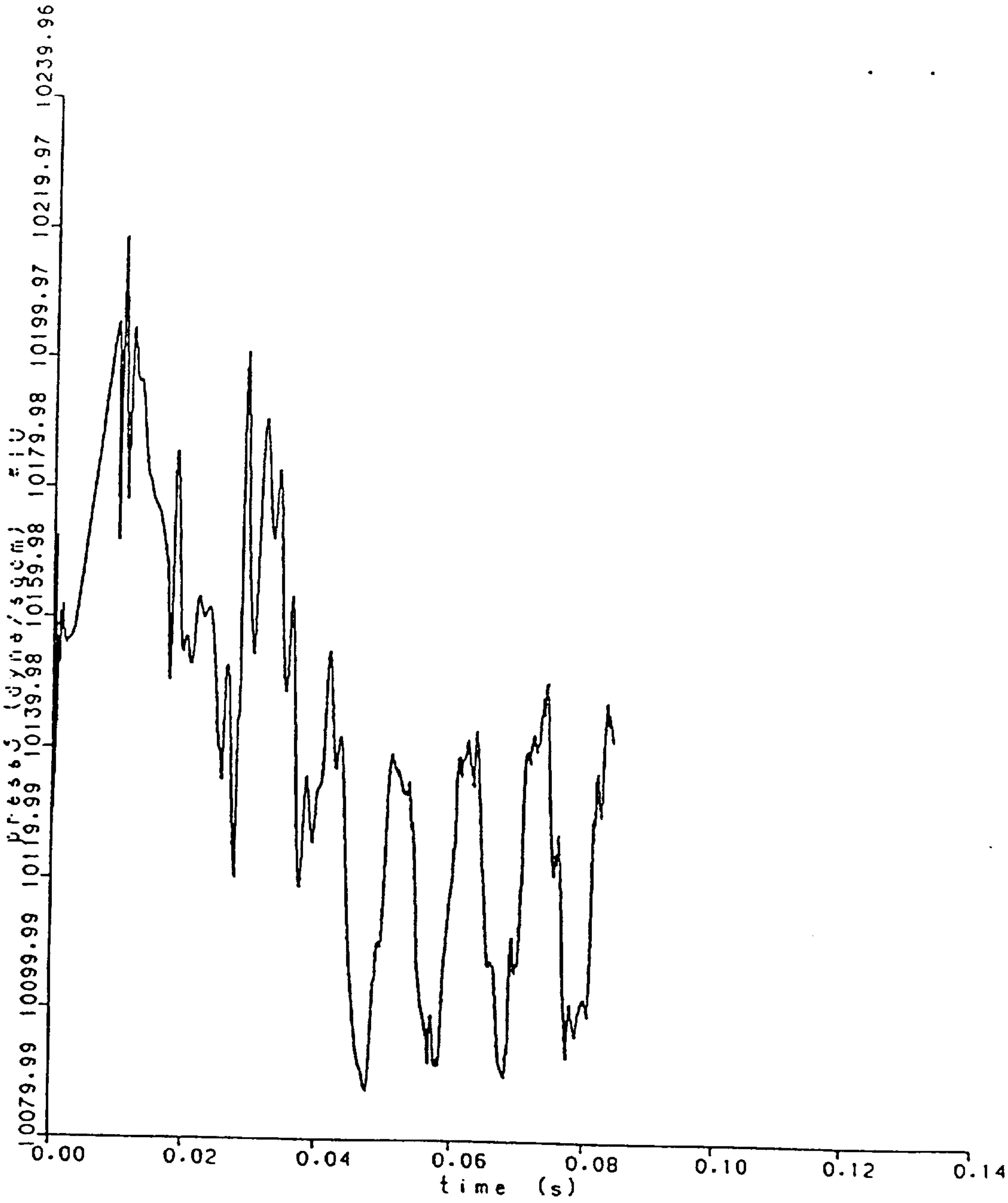
10239.96
10219.97
10199.97
10179.98
10159.98
10139.98
10119.99
10099.99
10079.99
press5 (dyne/sqcm) *10
0.00
0.02
0.04
0.06
0.08
0.10
0.12
0.14
time (s)

Figure B-10

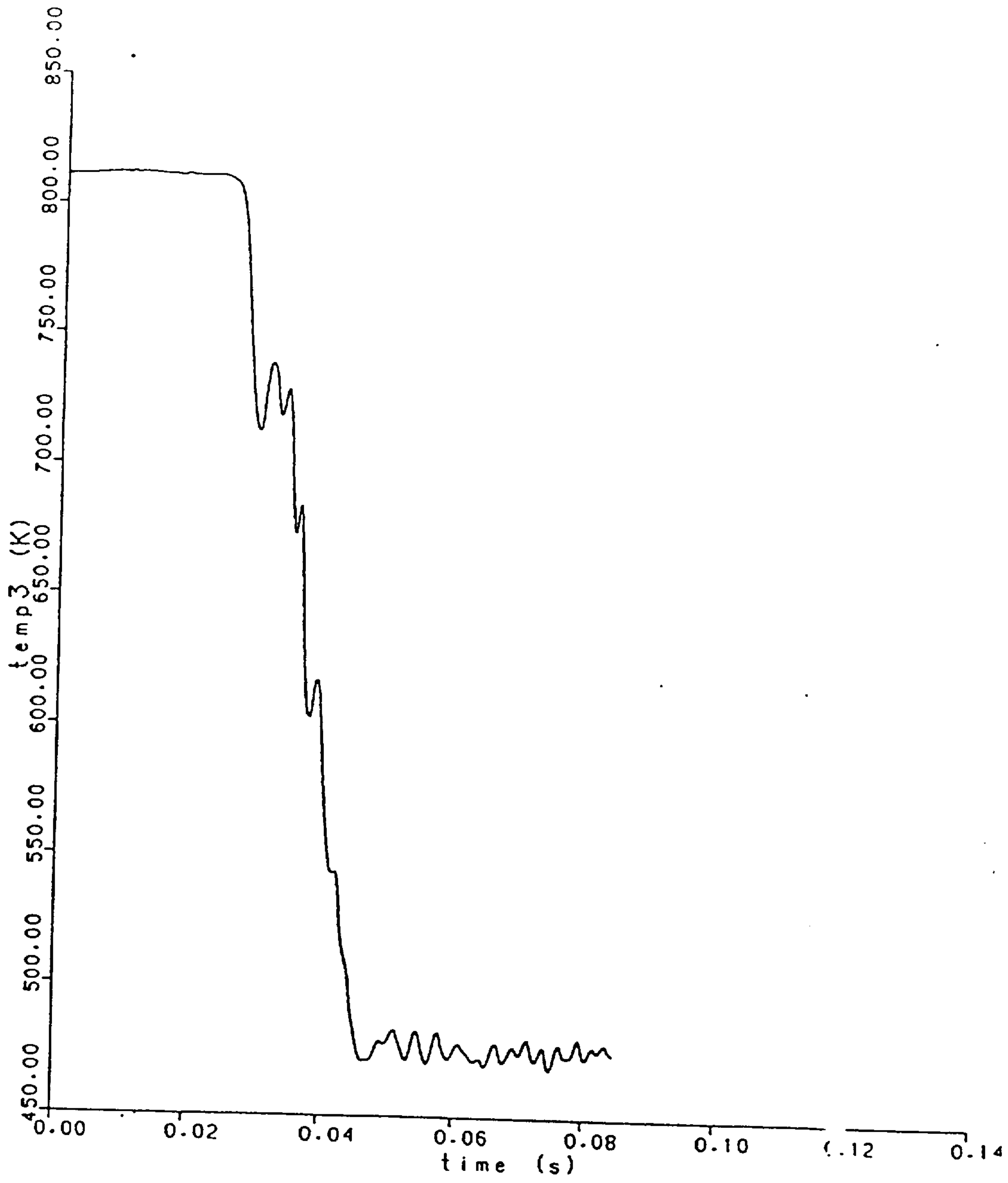
850.00
800.00
750.00
700.00
650.00
600.00
550.00
500.00
450.00
temp3 (K)
0.00
0.02
0.04
0.06
0.08
0.10
0.12
0.14
time (s)

Figure B-11

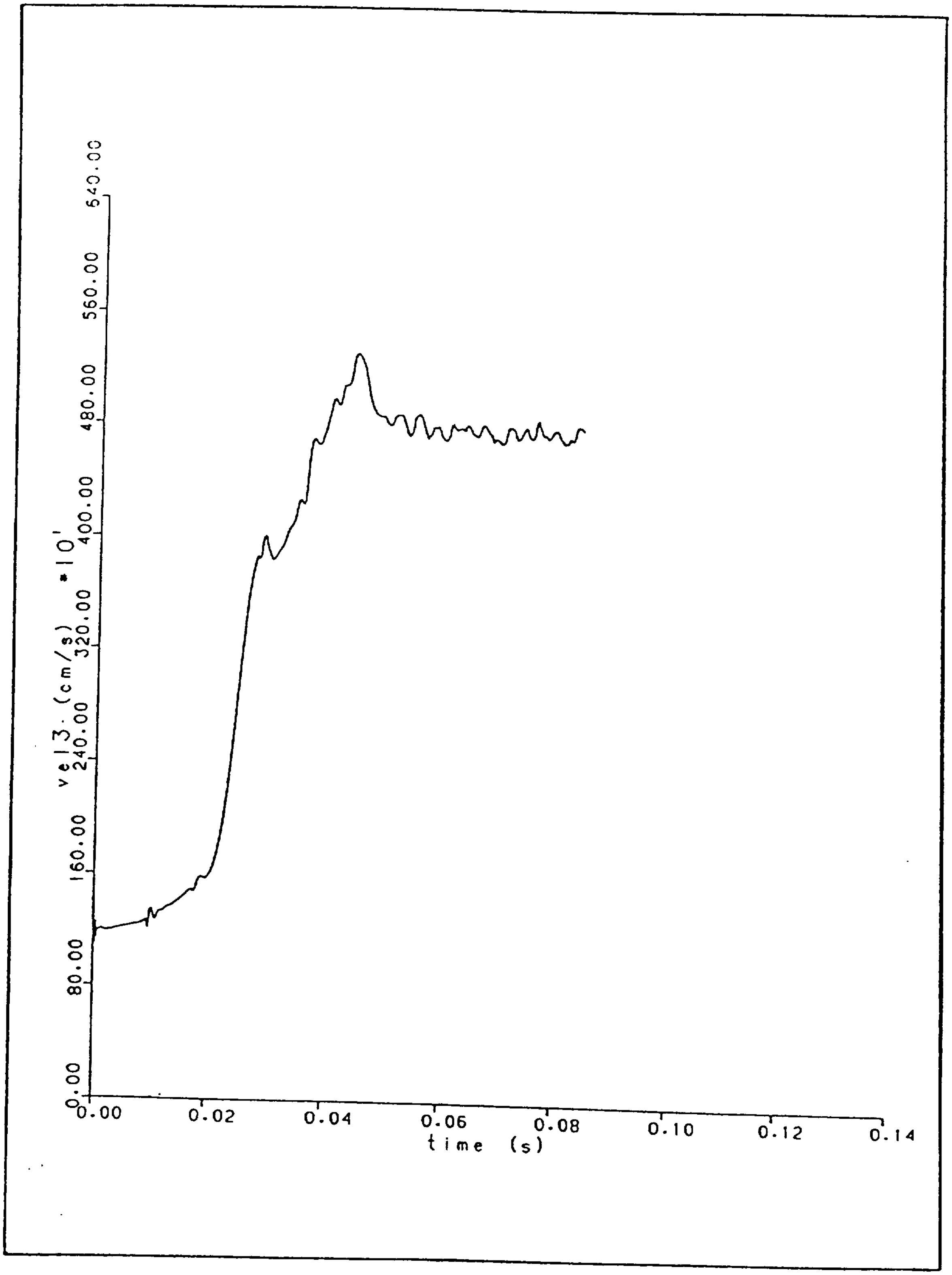

vel3 (cm/s) *10¹
0.00
80.00
160.00
240.00
320.00
400.00
480.00
560.00
640.00
0.00
0.02
0.04
0.06
0.08
0.10
0.12
0.14
time (s)

Figure B-12

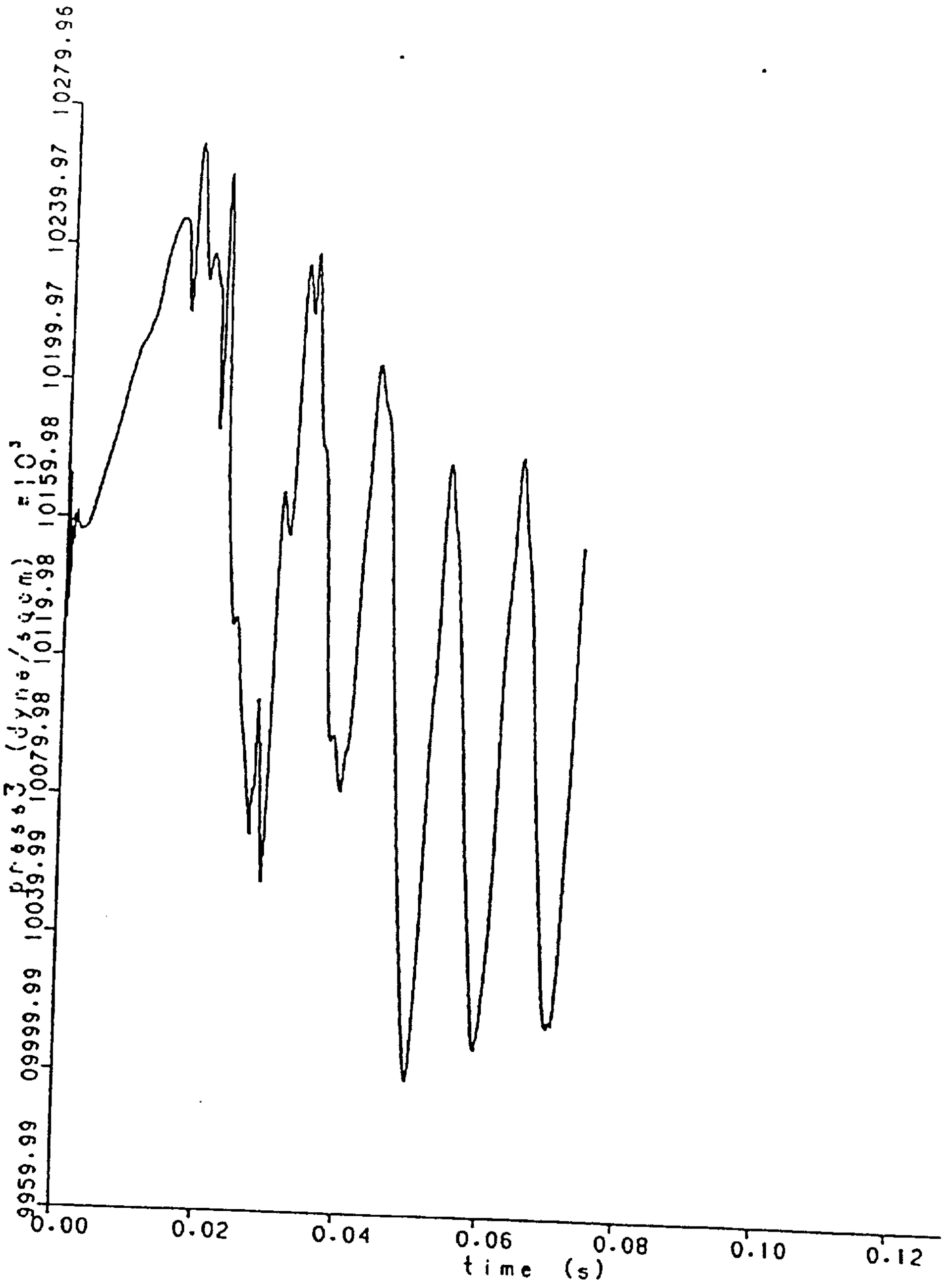
press3 (dyne/sqcm) *10³
9959.99
09999.99
10039.99
10079.98
10119.98
10159.98
10199.97
10239.97
10279.96
0.00
0.02
0.04
0.06
0.08
0.10
0.12
time (s)

Figure B-13

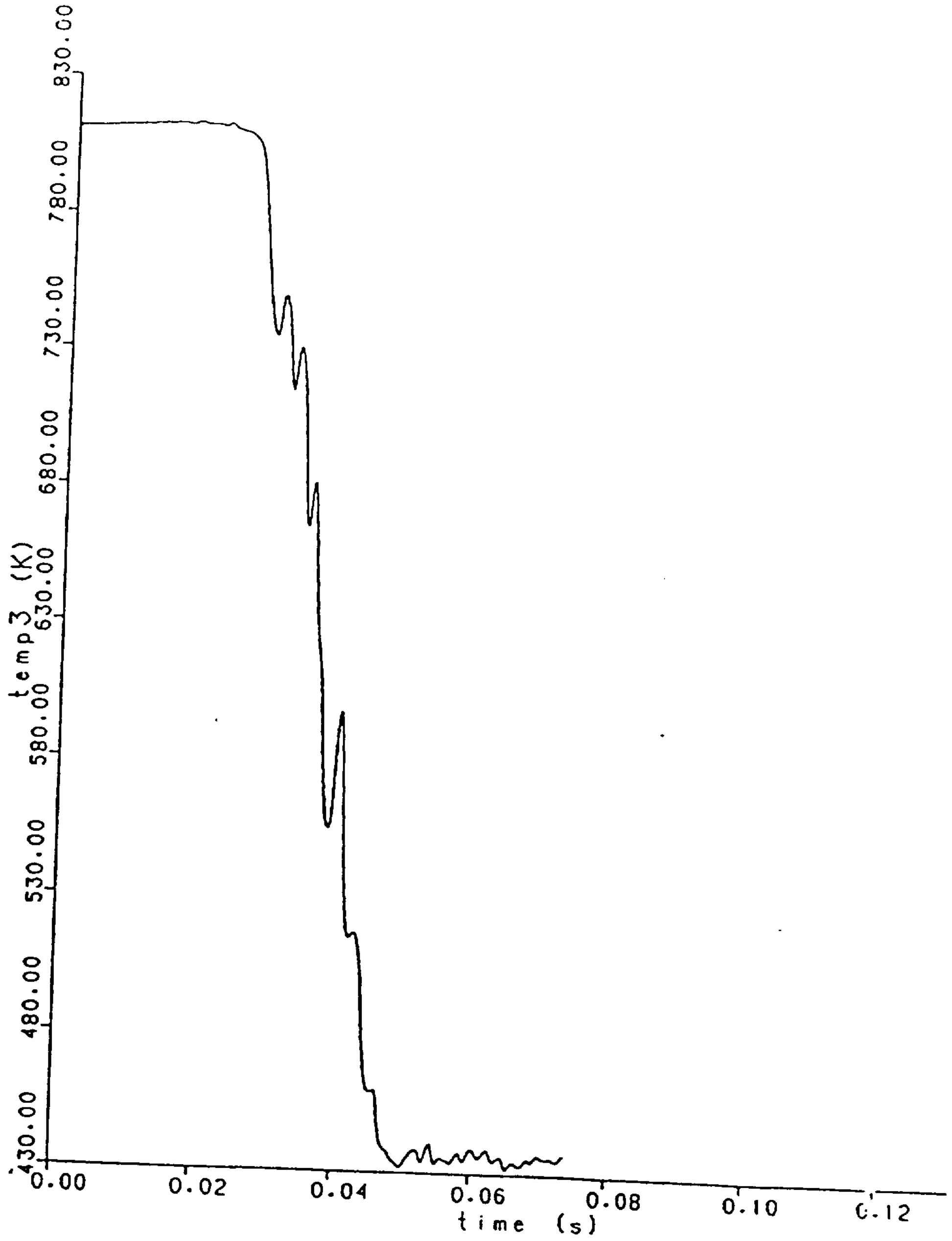
830.00
780.00
730.00
680.00
630.00
580.00
530.00
480.00
430.00
temp3 (K)
0.00
0.02
0.04
0.06
0.08
0.10
0.12
time (s)

Figure B-14

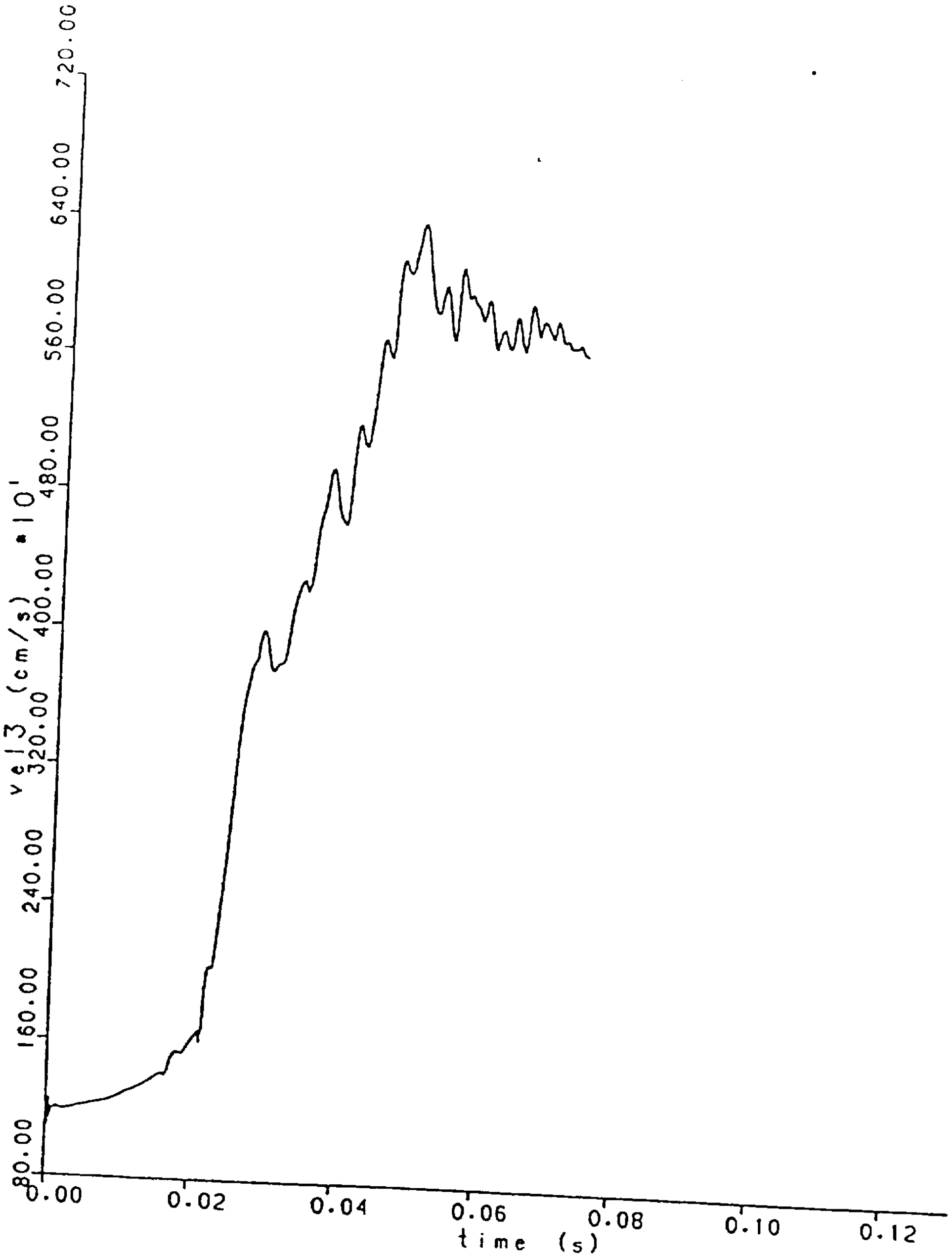
vel3 (cm/s) *10¹
80.00
160.00
240.00
320.00
400.00
480.00
560.00
640.00
720.00
0.00
0.02
0.04
0.06
0.08
0.10
0.12
time (s)

Figure B-15

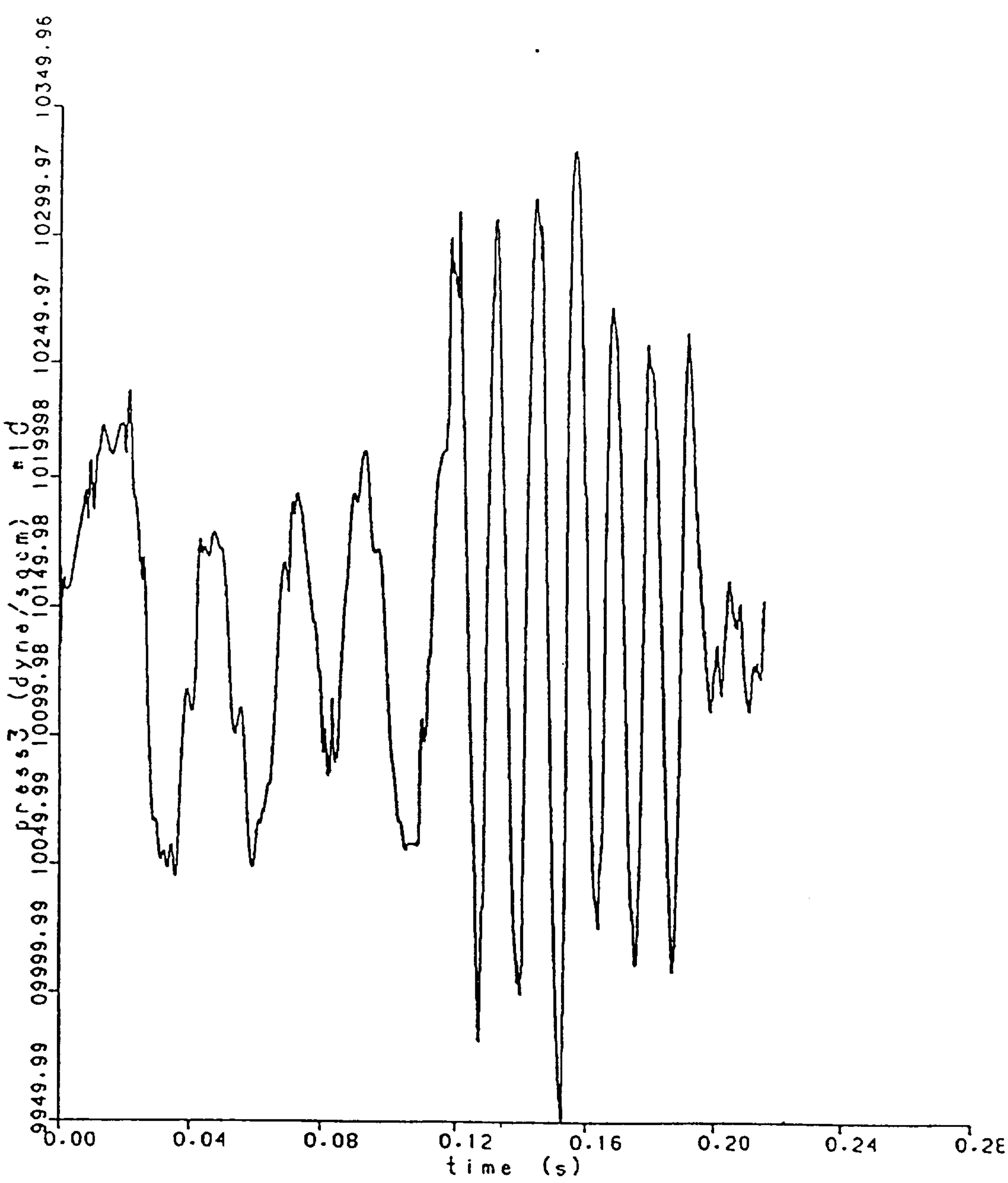
press3 (dyne/sqcm) mid
9949.99
09999.99
10049.99
10099.98
10149.98
1019998
10249.97
10299.97
10349.96
0.00
0.04
0.08
0.12
0.16
0.20
0.24
0.28
time (s)

Figure B-16

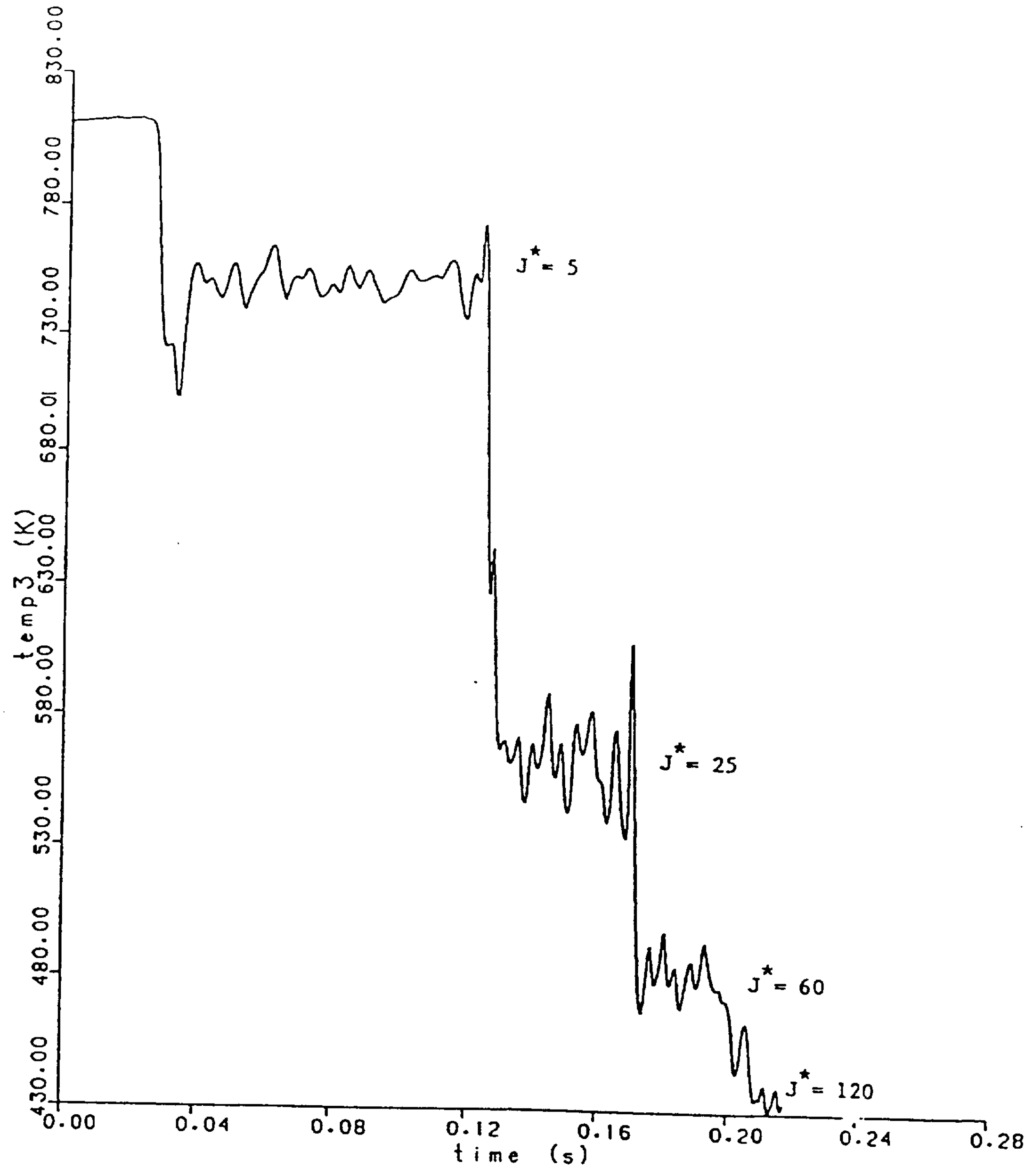

830.00
780.00
730.00
680.01
630.00
580.00
530.00
480.00
430.00
temp3 (K)
0.00
0.04
0.08
0.12
0.16
0.20
0.24
0.28
time (s)
J* = 5
J* = 25
J* = 60
J* = 120

Figure B-17

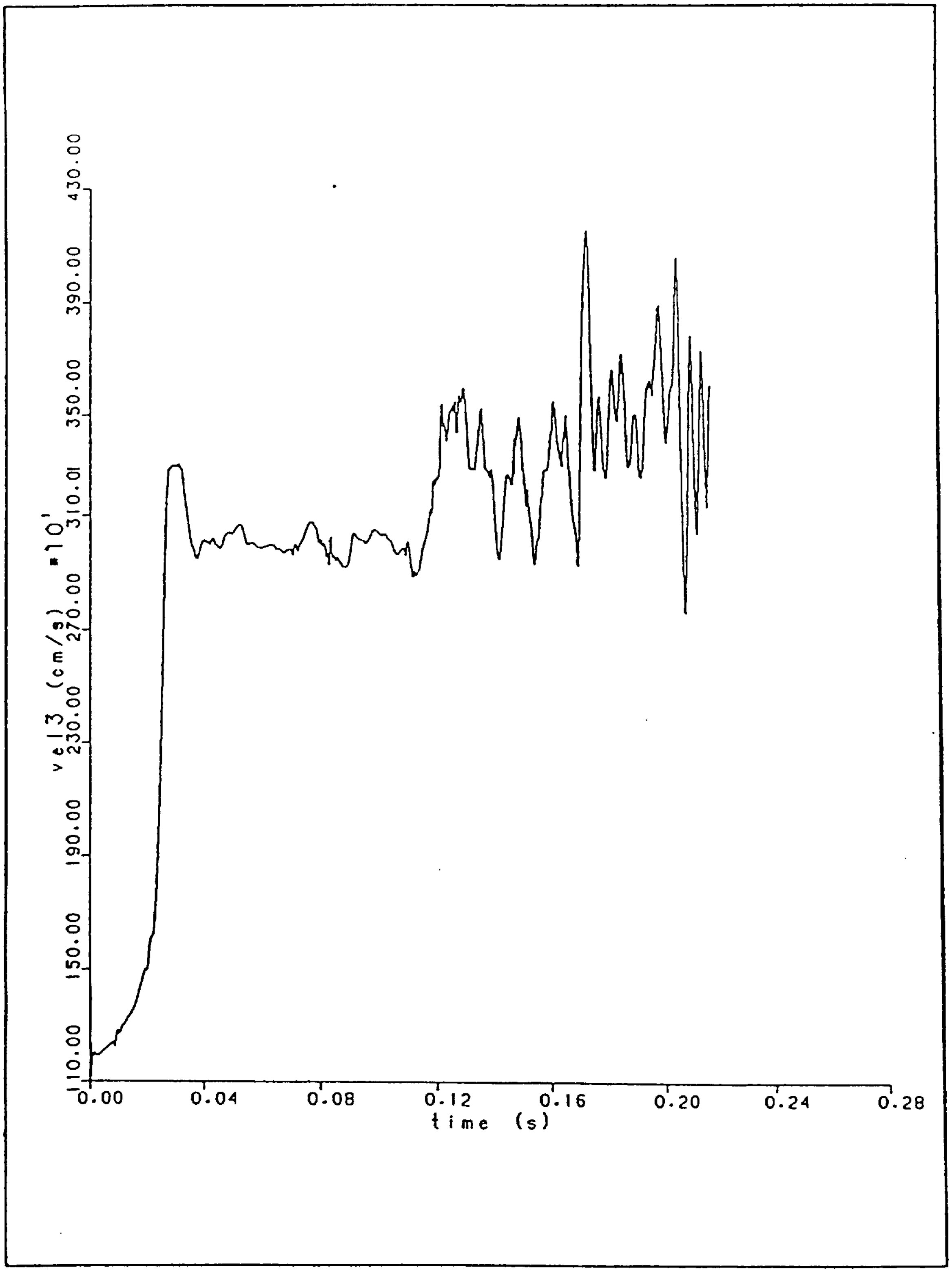
430.00
390.00
350.00
310.01
270.00
230.00
190.00
150.00
110.00
vel3 (cm/s) *10'
0.00
0.04
0.08
0.12
0.16
0.20
0.24
0.28
time (s)

Figure B-18

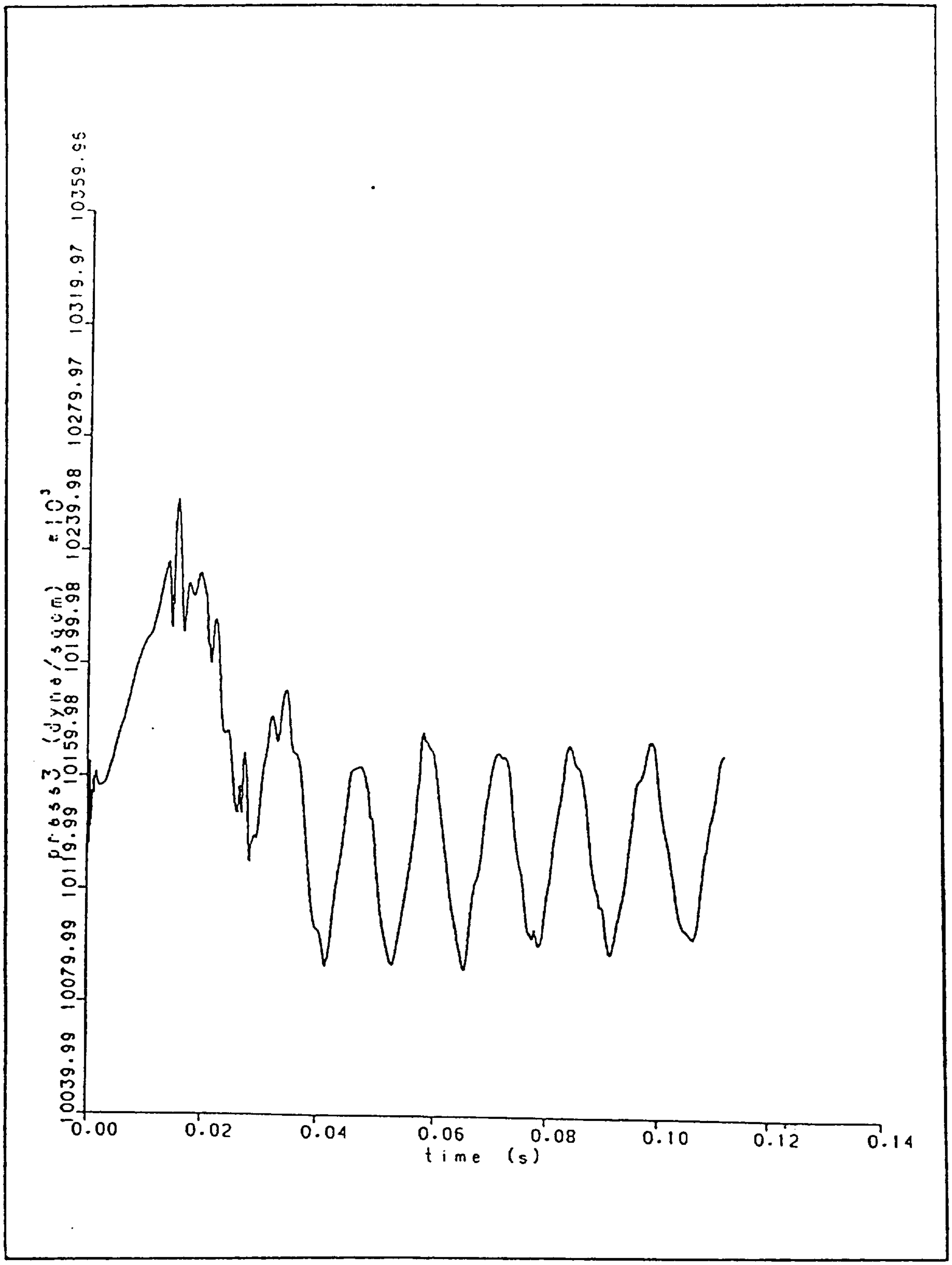
press3 (dyne/sqcm) *10^3
10039.99
10079.99
10119.99
10159.98
10199.98
10239.98
10279.97
10319.97
10359.95
0.00
0.02
0.04
0.06
0.08
0.10
0.12
0.14
time (s)

Figure B-19

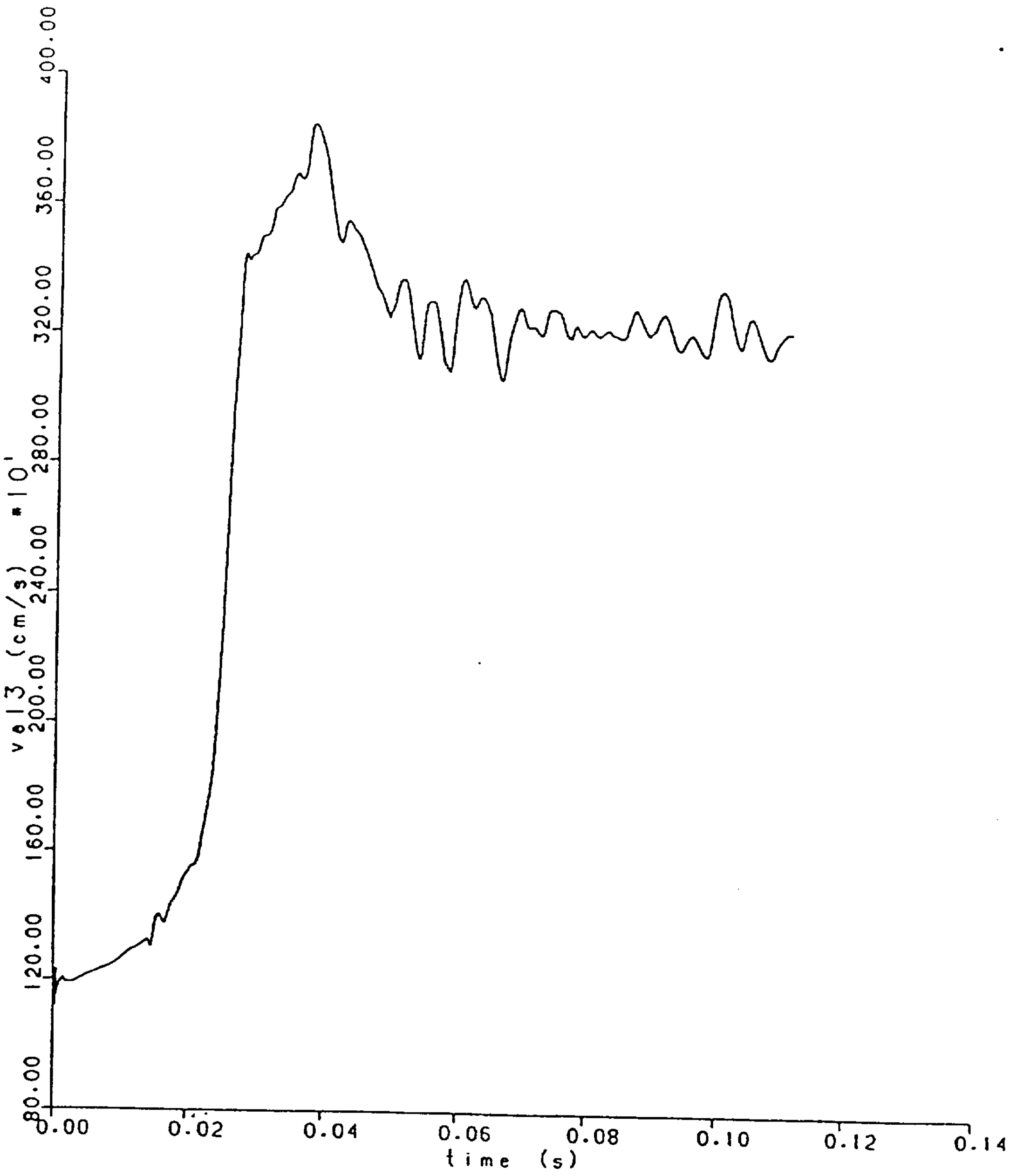
vel3 (cm/s) *10¹
400.00
360.00
320.00
280.00
240.00
200.00
160.00
120.00
80.00
0.00
0.02
0.04
0.06
0.08
0.10
0.12
0.14
time (s)

Figure B-21

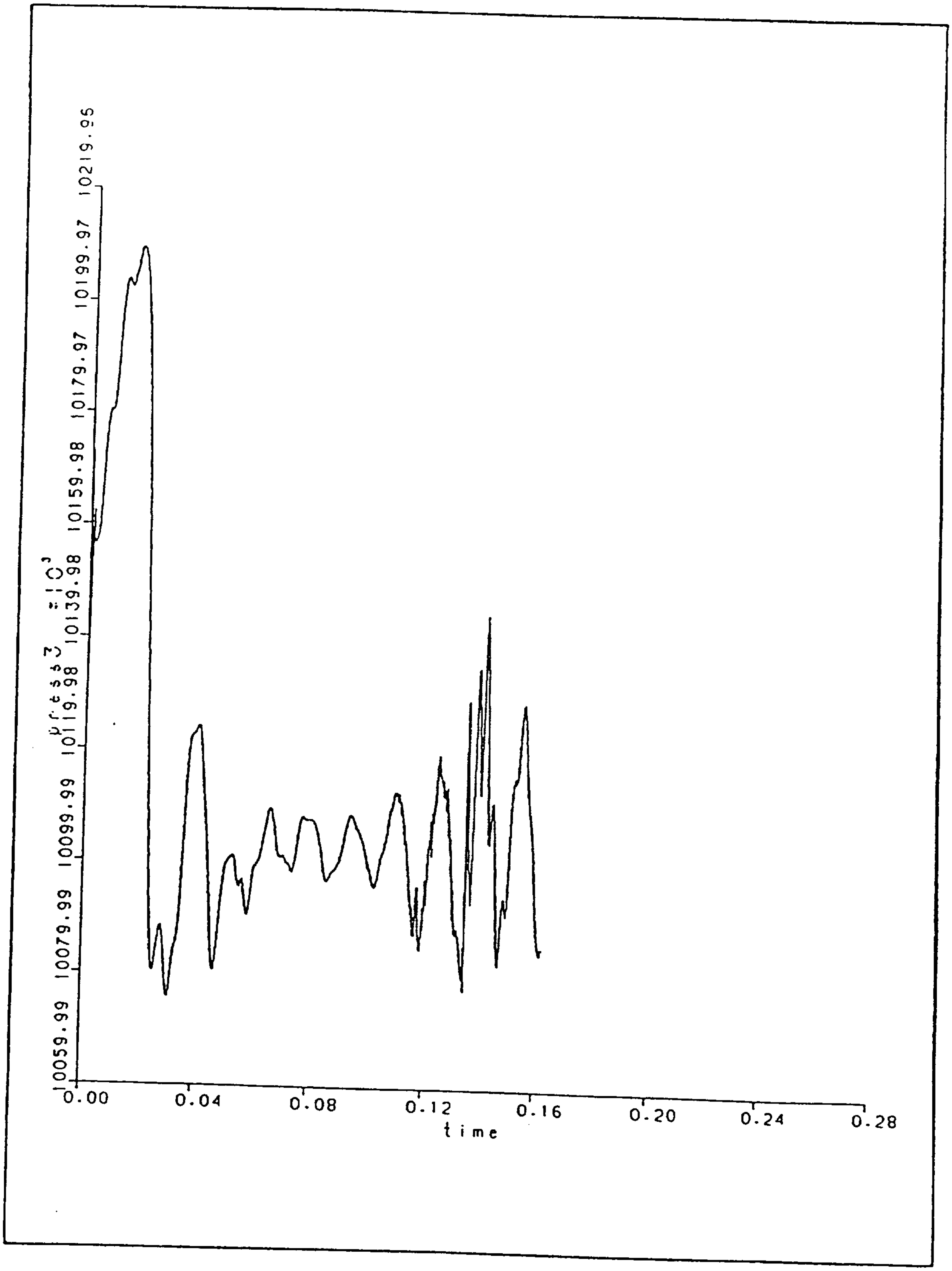
10219.95
10199.97
10179.97
10159.98
10139.98
10119.98
10099.99
10079.99
10059.99
press3 *10³
0.00
0.04
0.08
0.12
0.16
0.20
0.24
0.28
time

Figure B-22

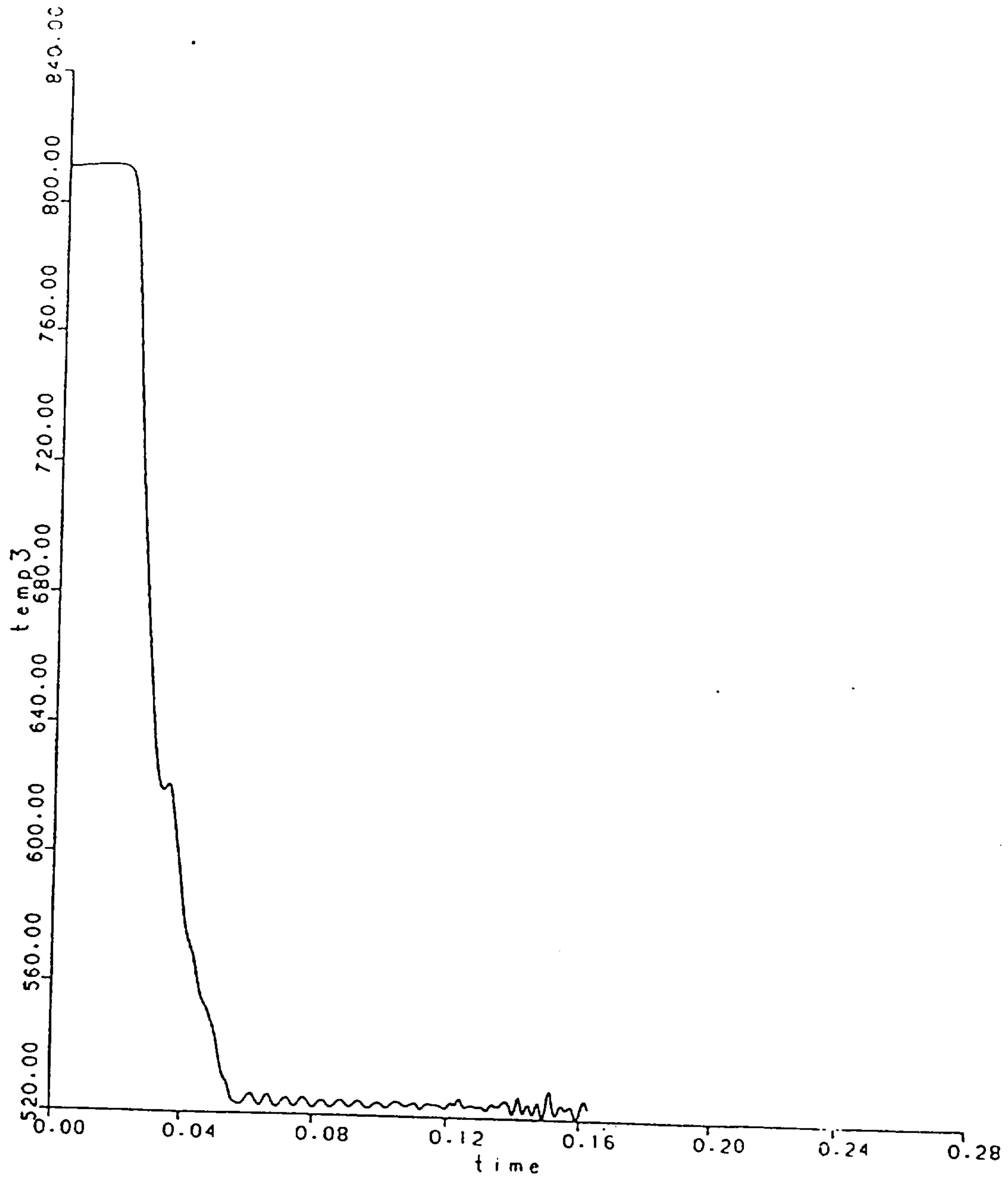

840.00
800.00
760.00
720.00
680.00
640.00
600.00
560.00
520.00
temp3
0.00
0.04
0.08
0.12
0.16
0.20
0.24
0.28
time

Figure B-23

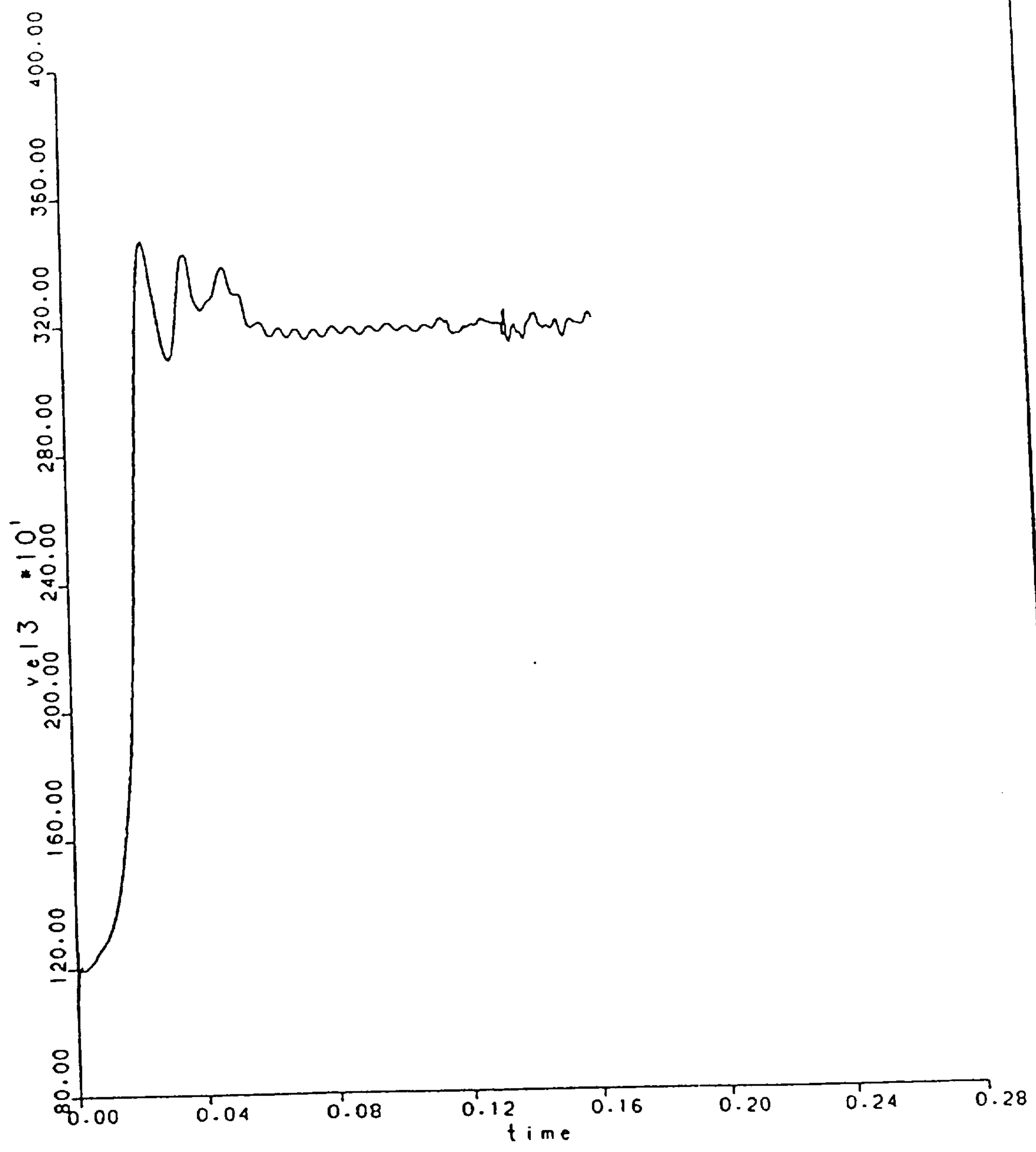
400.00
360.00
320.00
280.00
240.00
200.00
160.00
120.00
80.00
vel3 *10¹
0.00
0.04
0.08
0.12
0.16
0.20
0.24
0.28
time

Figure B-24

APPENDIX C
PUBLICATIONS

AIAA 91-2081

Three-Dimensional Calculation of the Mixing of Radial Jets from Slanted Slots with a Reactive Cylindrical Crossflow

N.S. Winowich and S.A. Moeykens
University of Maine
Orono, ME
H.L. Nguyen
NASA Lewis Research Center
Cleveland, OH

AIAA/SAE/ASME/ASEE
27th Joint Propulsion Conference
June 24-26, 1991 / Sacramento, CA

THREE-DIMENSIONAL CALCULATION OF THE MIXING OF RADIAL JETS FROM SLANTED SLOTS WITH A REACTIVE CYLINDRICAL CROSSFLOW

N. S. Winowich* and S. A. Moeykens**
University of Maine
Orono, Maine

H. L. Nguyen+
NASA Lewis Research Center
Cleveland, Ohio

Abstract

A description is given of a numerical model that calculates the three-dimensional chemically reacting flowfield in an experimental low emission combustor. Of particular interest, is the simulation of radial dilution air jets and to assess their effectiveness in promoting both a uniform and rapid quench of the hot mainstream gases exiting the fuel rich primary stage. The ICEd-ALE finite volume computational method is used in the study. Consistent with experimental observations, radial jets issuing from slanted slots interact with a cylindrical axially flowing mainstream to produce a bulk swirl velocity downstream of the slot region. The swirl pattern at a given axial station is comprised of a clockwise rotating region near the wall and a counterclockwise rotating region extending from the combustor centerline. The jet radial penetration and downstream swirl velocity axial development are found to depend mainly on the jet-to-mainstream momentum flux ratio. Emission index calculations indicate that there was not excessive thermal NO_x production due to local high temperatures in the quick quench region for the case presented. Further work with parameter variations to determine the optimal mixer design and operating conditions, in conjunction with experimental validation, is necessary to firmly establish a practical design base.

1. Introduction

Civil transport aircraft which would fly at higher speeds and cruise at stratospheric altitudes are currently under investigation. The associated propulsion systems for such aircraft must operate with ultra-low emissions (a factor of ten reduction from present levels) in order to meet environment regulations. One possible advanced low emission combustor with potential to meet this criteria is known as the Rich-burn/Quick-quench/Lean-burn (RQL) concept.[1-3] The RQL concept stages the combustion into three zones (Fig. 1). The initial fuel rich burning zone (equivalence ratio greater than unity) is followed by a quick quench zone and then a lean reaction zone for complete combustion. If the quench process is rapid and uniform, the high temperature and subsequent thermal NO_x that would result as the mixture passess relatively slowly through the stoichiometric condition can be avoided. Also the lean zone stoichiometry (temperature) must be controlled, which, with a proper volume (residence time), will complete the consumption of CO, UHC, and smoke without generating excess thermal NO_x that would offset the advantages gained in the rich zone and quick-quench mixer.

The objective of the present study is to establish a three-dimensional numerical model of the RQL combustor with particular emphasis on the quick-quench mixer and lean zone regions. Therefore, the fuel and air supply to the rich zone is assumed to be uniform and completely premixed. This is a limiting operating case for the rich-burn zone. A more detailed model would have to resolve the fuel injection nozzle and primary air injection separately. Rapid mixing of the diluent quench air with the hot combustion gases leaving the rich-burn zone is desired to provide a uniform rapid quench for any continuing chemical reactions and thereby suppress thermal NO_x formation. Stirred reactor calculations have demonstrated that in the limit of instantaneous mixing the RQL combustor can achieve ultra-low emission levels under cruise operating conditions[4]. The quick-quench mixer is a confined mixing problem with as much as seventy-five percent of the total flow entering through the dilution jets.[5] Therefore, the equilibrium temperature of the exiting flow may differ significantly from that of the entering mainstream flow . To control or tailer the combustor exit temperature pattern, it is necessary to be able to characterize the exit distribution in terms of the upstream flow and geometry. This requires a model of the entire combustor.

---

*Asst. Professor, Mech. Engineering
**Graduate Student, Mech. Engineering
+Aerospace Engineer, Propulsion Systems Division

2. Computational Method

A gas turbine combustor is a complex system in which a number of physical processes occur simultaneously. These processes include subsonic fluid flow, turbulent transport of mass, momentum, and energy, wall heat transfer, turbulent flame propagation, formation and quenching, dilution jet mixing, pollutant formation, and perhaps fuel spray dynamics. The overall combustor performance is the net result of a complex interplay among these various effects. Extensive application of the ICEd-ALE finite volume method, primarily to internal combustion engines, have demonstrated it to be a reliable and robust technique for the modeling of chemically reactive fluid dynamics with fuel sprays.[6-7]

The ICEd-ALE technique is a hybrid of the Implicit Continuous-fluid Eulerian (ICE)[8] and Arbitrary Lagrangian-Eulerian (ALE)[9] methods. The former provides flow-speed versatility through an implicit treatment of the pressure calculation while the latter allows for arbitrarily shaped hexahedronal shaped cells which may be used to model curved or moving boundaries. The overall calculation is a result of contributions from separate Eulerian and Lagrangian phases. This tends to result in reduced numerical diffusion in contrast to purely Eulerian difference methods.

An overview of the governing equations solved by the ICEd-ALE finite volume scheme follows.

Conservation Equations

Mass:

$$\frac{\partial \rho_m}{\partial t} + \vec{\nabla}\cdot(\rho_m \vec{u}) = \vec{\nabla}\cdot\vec{J}_m + \dot{\rho}_m^c$$

for the mth species, where ρ_m is the mass density of species m, $\vec{u}$ is the fluid velocity, $\vec{J}_m$ is the diffusive mass flux of species m, and $\dot{\rho}_m^c$ is the rate of change of ρ_m due to chemical reaction. The diffusive mass flux is given by Fick's Law:

$$\vec{J}_m = \rho D \vec{\nabla} Y_m$$

where ρ is the total mass density and Y_m is the species mass fraction. The mass diffusivity D, which is assumed to be the same for all species, is determined using the Schmidt number Sc, (assumed constant):

$$D = \frac{\mu}{\rho Sc}$$

where μ is viscosity.

$$\frac{\partial \rho}{\partial t} + \vec{\nabla}\cdot(\rho\vec{u}) = 0$$

Momentum:

$$\frac{\partial(\rho\vec{u})}{\partial t} + \vec{\nabla}\cdot(\rho\vec{u}\vec{u}) = -\vec{\nabla}p - \vec{\nabla}\rho k + \vec{\nabla}\cdot\underset{\sim}{\sigma}$$

where p is the fluid pressure, and k is the specific turbulent kinetic energy. The viscous stress tensor is Newtonian and is expressed as:

$$\underset{\sim}{\sigma} = \mu[\vec{\nabla}\vec{u} + (\vec{\nabla}\vec{u})^T] + \lambda\vec{\nabla}\cdot\vec{u}\underset{\sim}{U}$$

where μ and λ are the shear and bulk viscosity coefficients, $\underset{\sim}{U}$ is the unit dyadic tensor, and superscript T denotes the transpose. The viscosity coefficients are given by:

$$\mu = \mu_{air} + c_\mu \rho \frac{k^2}{\varepsilon}$$

and

$$\lambda = -\frac{2}{3}\mu$$

where ε is the specific turbulent kinetic energy dissipation rate and c_μ is an empirical turbulence constant equalling 0.09. A Sutherland formula is used for the molecular viscosity of air with A_1 and A_2 constant:

$$\mu_{air} = \frac{A_1 T^{3/2}}{T + A_2}$$

Energy:

$$\frac{\partial(\rho I)}{\partial t} + \vec{\nabla}\cdot(\rho\vec{u}I) = -p\vec{\nabla}\cdot\vec{u} - \vec{\nabla}\cdot\vec{q} + \rho\varepsilon + Q^c$$

where I is the specific internal energy and Q^c is a source term due to chemical heat release. The total heat flux $\vec{q}$, is gained by summing the effects of heat conduction and enthalpy transport by mass diffusion:

$$\vec{q} = \vec{q}_c + \vec{q}_d = -K\vec{\nabla}T - \Sigma h_m \vec{J}_m$$

where K is the thermal conductivity, T is the fluid temperature, and h_m is the species specific enthalpy. The thermal conductivity is determined using the Prandtl number Pr (assumed constant):

$$K = \frac{\mu c_p}{Pr}$$

where c_p is the specific heat at constant pressure.

Turbulence Equations

A two-equation k-ε turbulence model is used. It solves the following pair of equations for k and ε:

$$\frac{\partial \rho k}{\partial t} + \vec{\nabla}\cdot(\rho\vec{u}k) + \frac{2}{3}\rho k\vec{\nabla}\cdot\vec{u} =$$

$$\underset{\sim}{\sigma}:\vec{\nabla}\vec{u} + \vec{\nabla}\cdot[\frac{\mu}{Pr_k}\vec{\nabla}k] - \rho\varepsilon$$

$$\frac{\partial \rho \varepsilon}{\partial t} + \vec{\nabla}\cdot(\rho\vec{u}\varepsilon) + [\frac{2}{3} c_{\varepsilon_1} + c_{\varepsilon_3})]\rho\varepsilon\vec{\nabla}\cdot\vec{u} =$$

$$\vec{\nabla}\cdot[\frac{\mu}{Pr_\varepsilon} \vec{\nabla}\varepsilon] + \frac{\varepsilon}{k} [c_{\varepsilon_1} \underset{\sim}{\sigma}:\vec{\nabla}\vec{u} - c_{\varepsilon_2}\rho\varepsilon]$$

where $c_{\varepsilon 1}$, $c_{\varepsilon 2}$, $c_{\varepsilon 3}$, Pr_k, and Pr_ε are empirical constants having the following values:[10]

$$c_{\varepsilon_1} = 1.44 \quad c_{\varepsilon_2} = 1.92 \quad c_{\varepsilon_3} = -1.0$$

$$Pr_k = 1.0 \quad Pr_\varepsilon = 1.3$$

With values for k and ε, the turbulent length scale L is computed directly from:

$$L = c_{\mu_\varepsilon} \frac{k^{3/2}}{\varepsilon}$$

where

$$c_{\mu_\varepsilon} = [\frac{c_\mu}{Pr_\varepsilon(c_{\varepsilon_2} - c_{\varepsilon_1})}]^{1/2} .$$

State and Chemical Equations

The state relations are assumed to be those of an ideal gas mixture, therefore,

$$p = R_0 T \sum_m (\rho_m/W_m),$$

$$I(T) = \sum_m (\rho_m/\rho) I_m(T)$$

$$c_p(T) = \sum_m (\rho_m/\rho) c_{pm}(T),$$

$$h_m(T) = I_m(T) + R_0 T/W_m ,$$

where R_0 is the universal gas constant; W_m the molecular weight of species m, c_{pm} the specific heat at constant pressure of species m.

Using propane (C_3H_8) as fuel, a two-step global chemical kinetics mechanism is used to model the combustion of the fuel-air mixture:

$$2C_3H_8 + 7O_2 \rightarrow 8H_2O + 6CO$$

$$2CO + O_2 \leftrightarrow 2CO_2$$

Nitric oxide (NO) formation is modeled by the extended Zeldovich mechanism:

$$O + N_2 \leftrightarrow N + NO$$

$$O + NO \leftrightarrow O_2 + N$$

$$N + OH \leftrightarrow H + NO$$

The global reaction rate expression is:

$$\dot{\omega}_{global} = k_{fr} \prod_m (\frac{\rho_n}{W_m})^{b'} - k_{br} \prod_m (\frac{\rho_m}{W_m})^{a'}$$

where a' and b' are not necessarily the stoichiometric coefficients, but may instead be empirical constants determined from experiment or detailed kinetics calculations.[11] The forward and backward reaction rate coefficients k_{fr} and k_{br} are determined from the Arrhenius:

$$k = AT^\zeta \exp(\frac{-E_a}{R_0 T})$$

The temperature exponent ζ, the activation energy E_a, and the pre-exponential term A, are also determined from correlation with experimental results.

Six equilibrium reactions are considered:

$$H_2 \leftrightarrow 2H$$

$$O_2 \leftrightarrow 2O$$

$$N_2 \leftrightarrow 2N$$

$$O_2 + H_2 \leftrightarrow 2OH$$

$$O_2 + 2H_2O \leftrightarrow 4OH$$

$$O_2 + 2CO \leftrightarrow 2CO_2 .$$

The rate of each equilibrium reaction is determined implicitly from:

$$\prod_m (\frac{\rho_m}{W_m})^{\nu'' - \nu'} = K_c(T)$$

where ν' and ν'' are the stoichiometric coefficients of species m on the left and right side, respectively, and $K_c(T)$ is the known equilibrium constant which may be a function of temperature.

3. Computational Model

Computing Mesh

For twelve slanted slots which are equally spaced around the rapid mixer circumference, the flowfield will be periodic every 30 deg. in the azimuthal direction. Hence, a 30 deg. three-dimensional sector mesh composed of 32,320 cells is used for this case. The mesh consists of 20 cells (21 i-planes of vertices) in the radial (r) direction, 16 cells (17 j-planes of vertices) in the azimuthal (θ) direction, and 101 cells (102 k-planes of vertices) in the axial (z) direction (Fig. 2.). The slot region is resolved with local mesh refinement, with 5 cells along the slot width (θ) and 11 cells along the length (z) (Fig. 3).

Boundary Conditions

The mainstream inlet (3) conditions and jet inlet (J) conditions are both assumed to be uniform. Since the j = 1 and j = 17 azimuthal vertex planes are periodic the radial and azimuthal velocity components must be equal at corresponding vertices on these planes. Similarly, convective fluxing is adjusted to ensure equality between efflux and influx of any scalar variable on corresponding cell surfaces. Specified temperatures are set for T_3 and T_J for mainstream and jet inlets. Turbulent law-of-the-wall formulations are used to represent the velocity and thermal boundary layers at solid walls. The inflow turbulent kinetic energy is set as 10% of the mean inflow kinetic energy:

$$k_3 = .1(V_3^2/2) \qquad k_J = .1(V_J^2/2)$$

where V_3 is the mainstream inlet axial velocity and V_J is the jet radial inlet velocity. The inflow turbulent length scales are:

$$L_3 = .1\ R_r \qquad L_J = .1\ W_s$$

where R_r is the rich zone radius and W_s is the slot width.

The slot inflow was specified on square cell surfaces on the i = 21 plane in the slot region (k = 35 - 46). The slot slant was represented by specifying V_J along diagonal rows of vertices (Fig. 3). For cells bisected by the slot edge the mass flow rate was reduced by one half of that for cells lying completely within the slot.

4. Results

Nonreactive Flow

A comparison is made between slots parallel to the combustor centerline with slots slanted at 45 deg. The flow conditions are:

$$P_3 = 10\text{ atm} = 1.013 \times 10^7 \text{dynes/cm}^2,$$

$$T_3 = 811\text{ k},\ V_3 = 1600\text{ cm/s},$$

$$T_J = 298\text{ k}$$

The jet inlet velocity V_J was determined for a given jet-to-mainstream momentum flux ratio:

$$J^* = \frac{\rho_J V_J^2}{\rho_3 V_3^2}$$

Results were determined for values of J* = 40 and 60.

For the parallel slots, the effect of an axial crossflow on a purely radial injection jet produces a pair of counter-rotating vortices with mirror symmetry between the slots when viewed on a given z-plane (Fig. 4). For slanted slots, however only a single vortex develops between slots (Fig. 5). For slots slanted in a clockwise sense, all the vortices will have a clockwise rotation. These twelve vortices near the wall of the quick-quench mixer act in effect as swirlers spaced around the circumference of the mixer. The cumulative effect is to produce a net clockwise swirl velocity incipient at the tailing slot edge and persisting downstream into the lean zone region. The outer clockwise swirl velocity induces an inner counterclockwise swirl velocity region between the centerline axis and the outer swirl region (Fig. 6) The downstream swirl development is shown in Fig. 7. Note that the outer swirl region is clearly distinguished by positive contour lines which terminate at the combustor wall, while the inner swirl region has negative contour lines which tend to form a closed region. This type of swirl velocity pattern has been observed experimentally for slanted slot jet injections into a cylindrical crossflow.

The relative mixing effectiveness between the parallel slot and slanted slot cases was evaluated in terms of deviation from the bulk internal energy at a given axial (z) location. The bulk internal energy passing through a given cross section is:

$$I_B = \frac{\int I d\dot{m}}{\dot{m}}$$

where $\dot{m}$ is the total mass flow rate through the cross section. The mixing effectiveness (η) is then defined as:

$$\eta = \frac{\int |I - I_B| d\dot{m}}{I_B \dot{m}}$$

The variation of η with z is shown in Fig. 8 for both the slanted slots (indicated by (45)) and parallel slot injection.

Reactive Flow

One reactive flow results case is presented which corresponds to equivalence ratios of 1.6 and .5 in the rich and lean zones respectively. The operating conditions are:

$$P_3 = 6.89 \times 10^6 \text{dynes/cm}^2 (100\text{ psia}),$$

$$\dot{m}_f = 63.9\text{ g/s},\ \dot{m}_{ar} = 625.9\text{ g/s},$$

$$T_J = 811\text{ k}$$

where $\dot{m}_f$ and $\dot{m}_{ar}$ are the fuel and rich zone air mass flow rates respectively.

The slanted slots once again produce a swirl velocity development downstream of the slot region (Figs. 9-10). The jet in effect acts as a flameholder. The consumption of propane and fuel mass fraction are shown in Figs. 11-12. Temperature contours are shown in Figs. 13-14. The momentum flux ratio based on the rich zone momentum flux is J* = 28. The average cross sectional temperature along the combustor is shown in Fig. 15. The pattern factor along the combustor is shown in Fig. 16. The pattern factor is defined as:

$$PF = \frac{\overline{T}_{max} - \overline{T}_4}{\overline{T}_4 - \overline{T}_3}$$

where $\overline{T}_3$ is the average inlet temperature, $\overline{T}_4$ is the average temperature of a cross section, and T_{max} is the maximum temperature of a cross section. Emission index variation for CO and NO is shown in Figs. 17-18.

5. Conclusions

The ICEd-ALE method is a versatile and accurate computational method for the modeling of the reactive flowfields inside gas turbine combustors. Radial dilution air jet injection through slanted slots into a mainstream flow in a duct of circular cross sectional area results in a bulk swirl velocity downstream of the slot region. The swirl velocity considerably enhances thermal mixing in comparison to parallel slot injection. A completely premixed fuel/air supply was used to minimize thermal NO_x production in the rich zone and isolate the NO_x contribution from the quick-quench mixer and lean zone regions. Excessive NO_x generation (exit emission index 1.2) was not observed for the case presented. Further analysis, along with experimental validation, is necessary for a more thorough understanding of the RQL combustion processes.

6. Acknowledgements

This work was supported by NASA grant NAG 3 1115.

7. References

1. Clark, D.W. and Wilkes, C., "Low Emission Combustion Technology Program Final Report," U. S. Dept. of Energy, Report No. DOE/MC/20227-1695, 1984.

2. Washam, R.M., "Dry Low NO Combustion System for Utility Gas Turbines," ASME Paper 83-JPGC-GT-13, 1983.

3. Peters, J.E., "Current Gas Turbine Combustion and Fuels Research and Development," Journal of Propulsion and Power, Vol. 4, No. 3, 1988, pp 193-206.

4. Nguyen, H.L., Bittker, D., and Niedzwiecki, R., "Investigation of Low NO_x Staged Combustor Concept in High Speed Civil Transport Engines," AIAA Paper 89-2942, 1989.

5. Holdeman, J.D., Srinivasan, R., and White, C.D., "An Empirical Model of the Effects of Curvature and Convergence on Dilution Jet Mixing," AIAA Paper 88-3180, 1988.

6. Cloutman, L.D., Dukowicz, J.K., Ramshaw, J.D., and Amsden, A.A., "CONCHAS-SPRAY: A Computer Code for Reactive Flows with Fuel Sprays," Los Alamos National Laboratory report LA-9294-MS, May 1982.

7. Amsden, A.A., O'Rourke, P.J., and Butler, T.D., "KIVA-II: A Computer Program for Chemically Reactive Flows with Sprays," Los Alamos National Laboratory report LA-11560-MS, May 1989.

8. Westbrook, C.K., "A Generalized ICE Method for Chemically Reactive Flows in Combustion Systems," Journal of Computational Physics, 29, pp 67-80, 1978.

9. Hirt, C.W., Amsden, A.A., and Cook, J.L., "An Arbitrary Lagrangian-Eulerian Computing Method for All Flow Speeds," Journal of Computational Physics, <u>14</u>, pp 227-253, 1974.

10. Jones, W.P. and Launder, B.E., "The Prediction of Laminarization with a Two-Equation Model of Turbulence," International Journal of Heat and Mass Transfer, Vol. 15, pp 301-314, 1972.

11. Westbrook, C.K. and Dryer, F.L., "Chemical Kinetic Modeling of Hydrocarbon Combustion," Progress in Energy and Combustion Science, Vol. 10, pp 1-57, 1984.

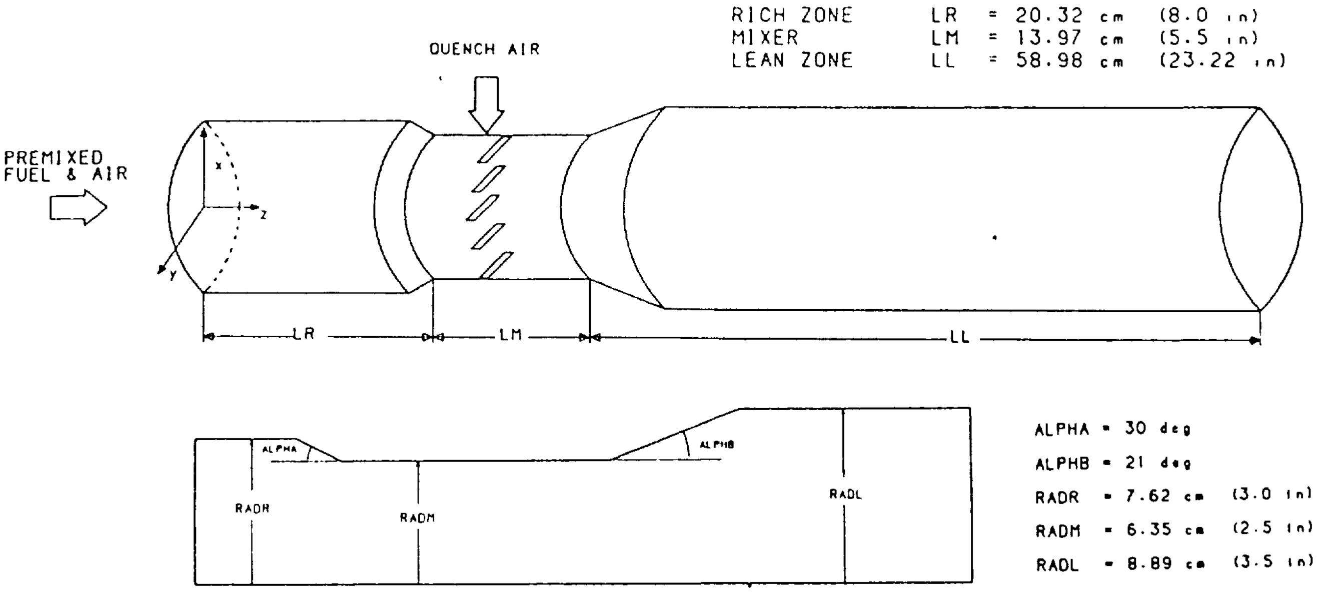

Figure 1. Rich-burn/Quick-quench/Lean-burn Combustor

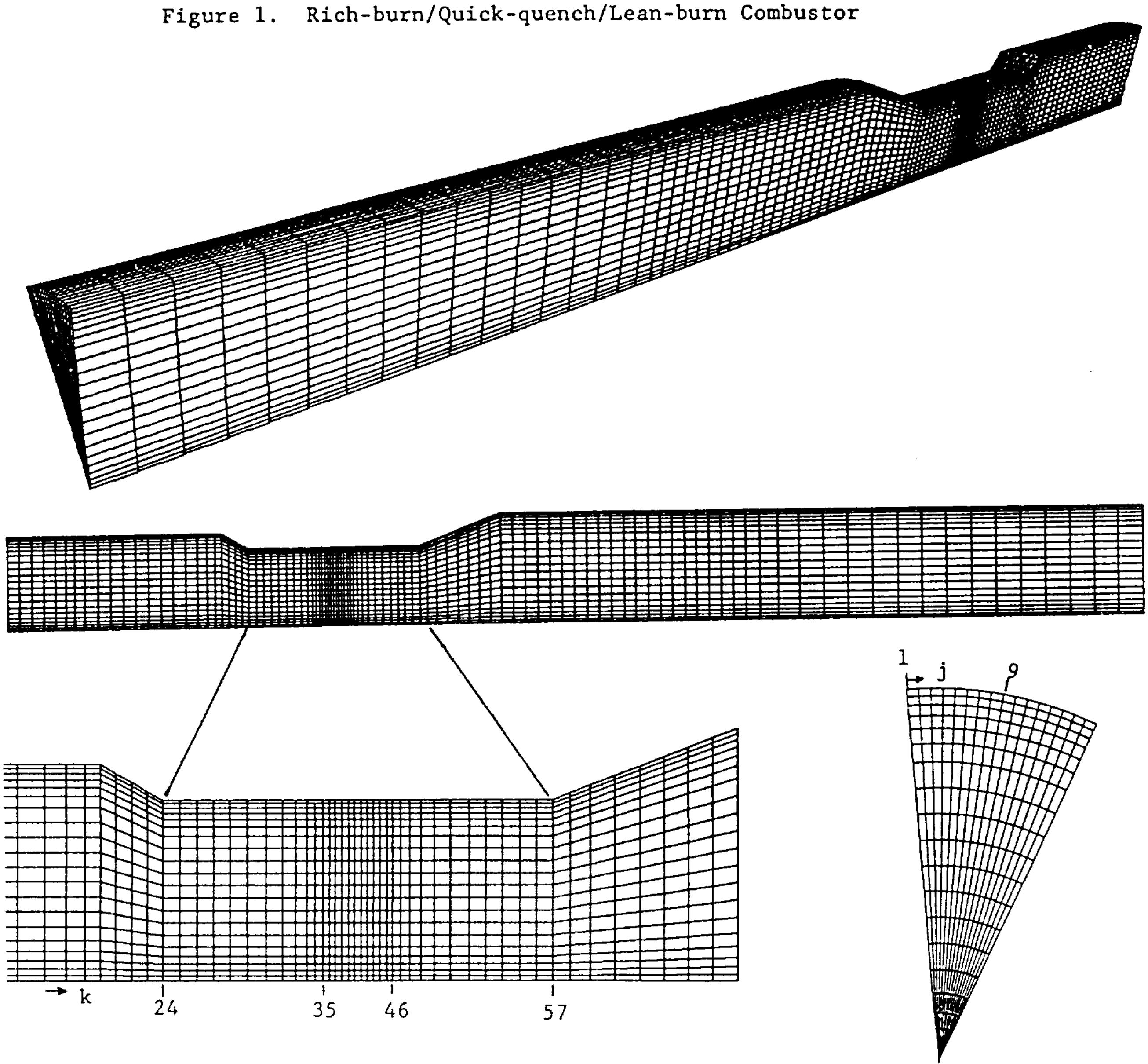

Figure 2. Computational mesh.

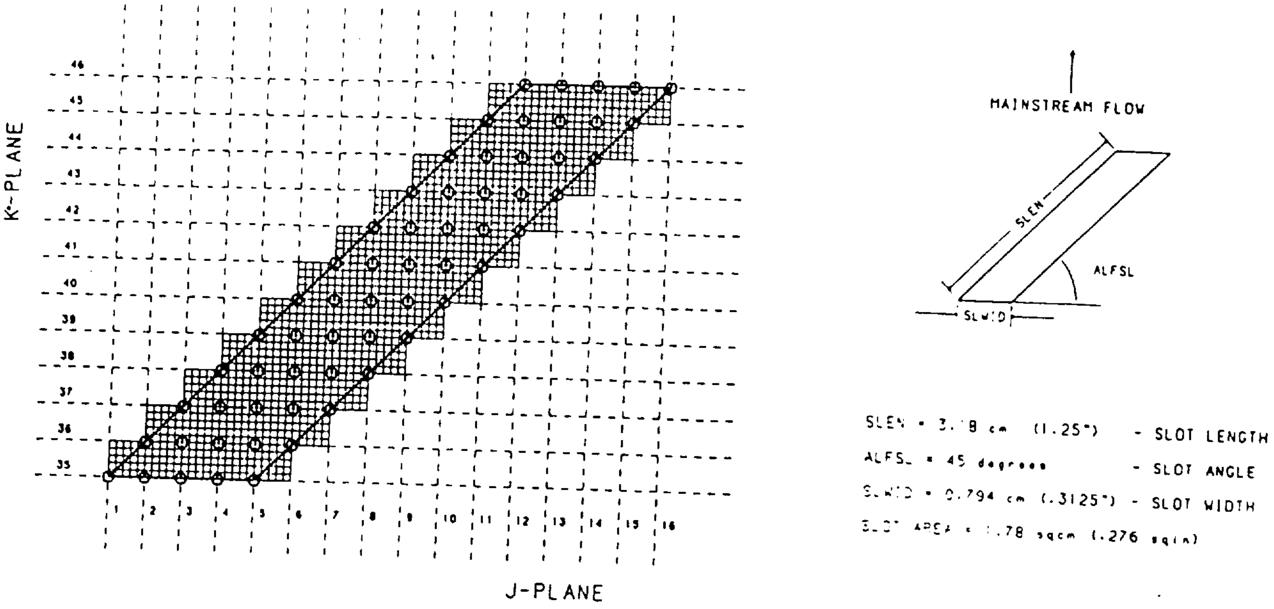

Figure 3. Jet inlet velocity vertices and slot geometry.

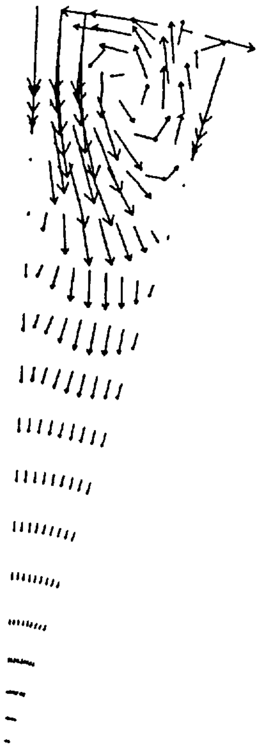

Figure 4. Parallel slot vortex.

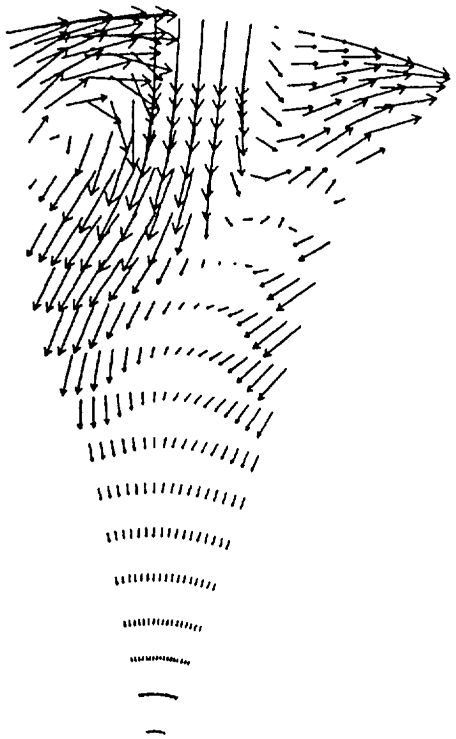

Figure 5. Slanted slot vortex.

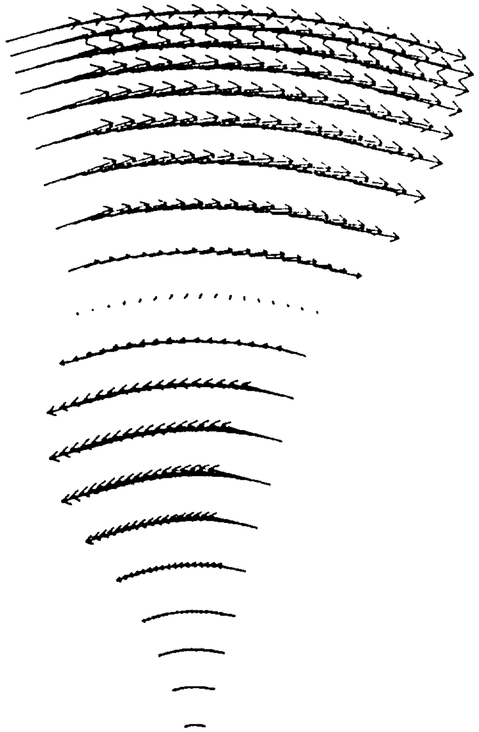

Figure 6. Swirl velocity(k=56,J^*=60).

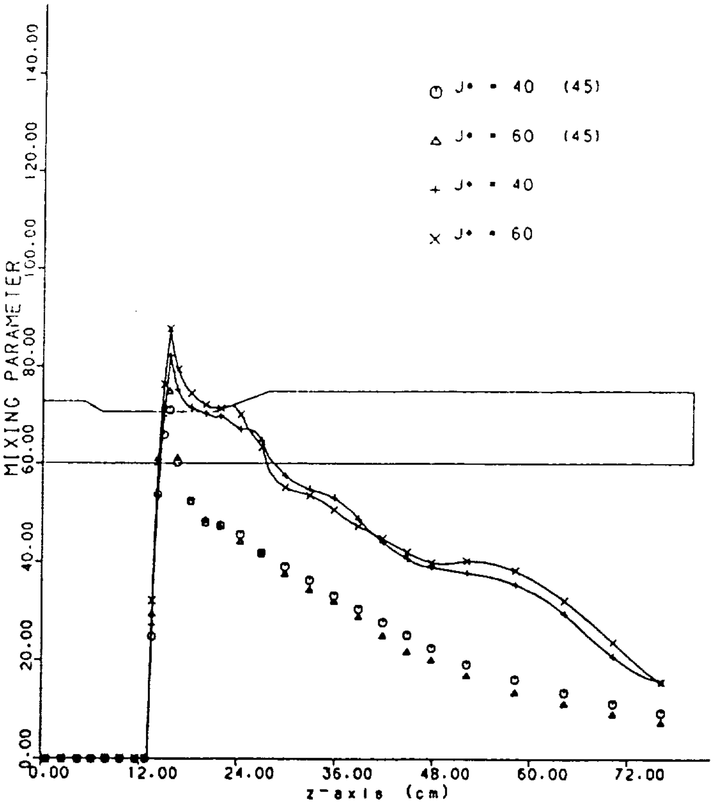

Figure 8. Mixing effectiveness,(45) is slanted slot.

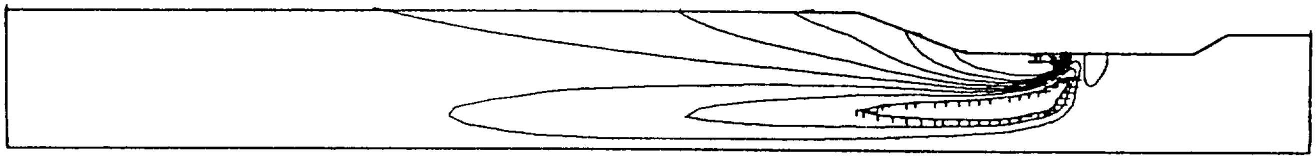

Figure 7. Swirl velocity contours, H=5116 cm/s, L=-2517 cm/s (j=9,J^*=60).

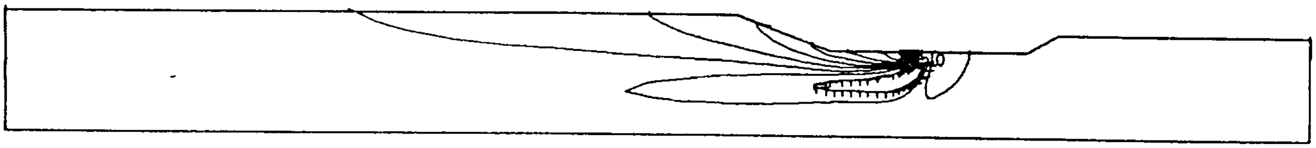

Figure 9. Swirl velocity contours, H=12277 cm/s, L=-3963 cm/s (j=9,J^*=28).

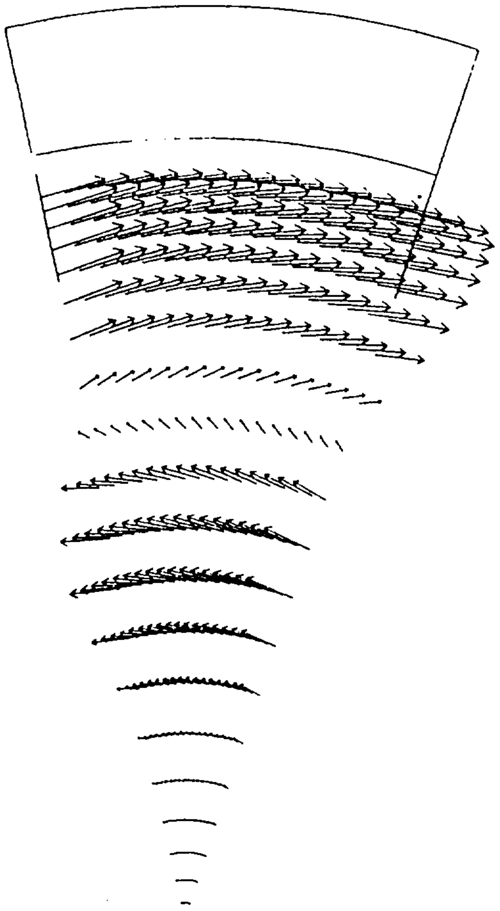

Figure 10. Swirl velocity(k=60,J^*=28).

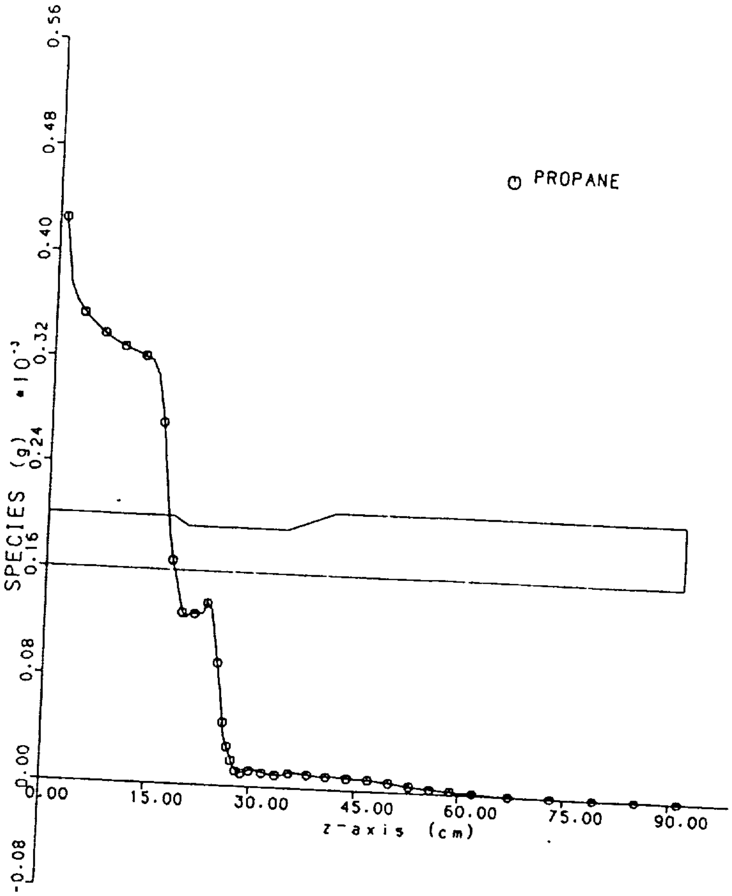

Figure 11. Propane depletion.

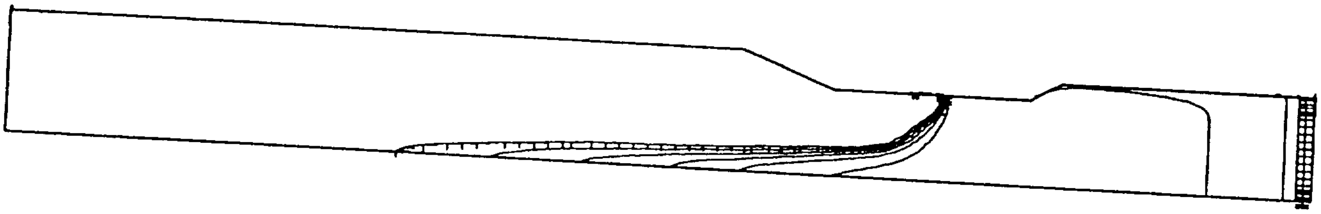

Figure 12. Propane mass fraction, H=.0286, L=.00318,(j=9, J^*=28).

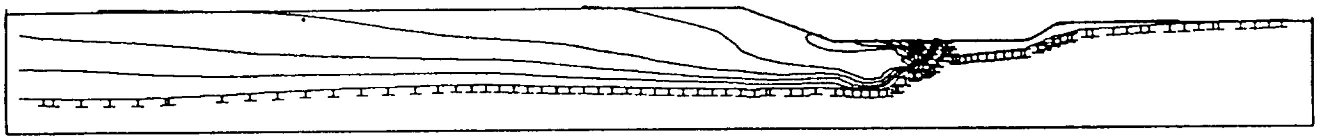

Figure 13. Isotherms, H=2380 K, L=986 K, (j=9, J^{*}=28).

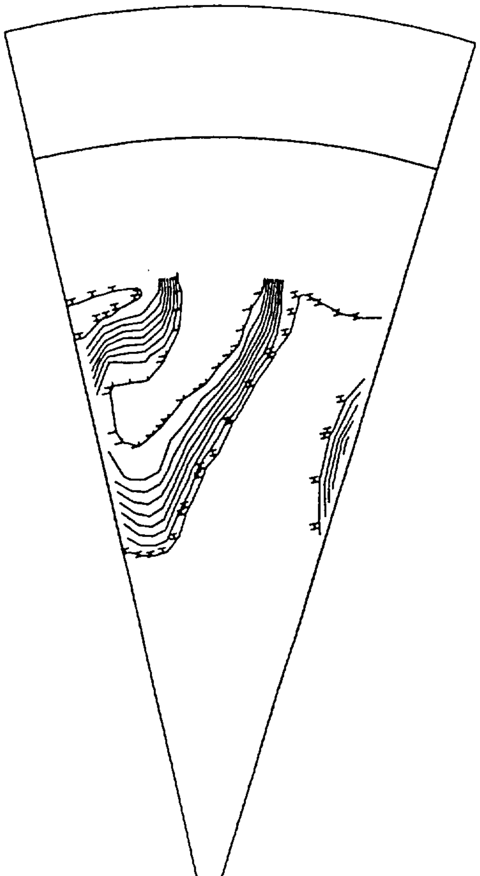

Figure 14. Isotherms, H=2332 K, L=981 K,(k=40, J^{*}=28).

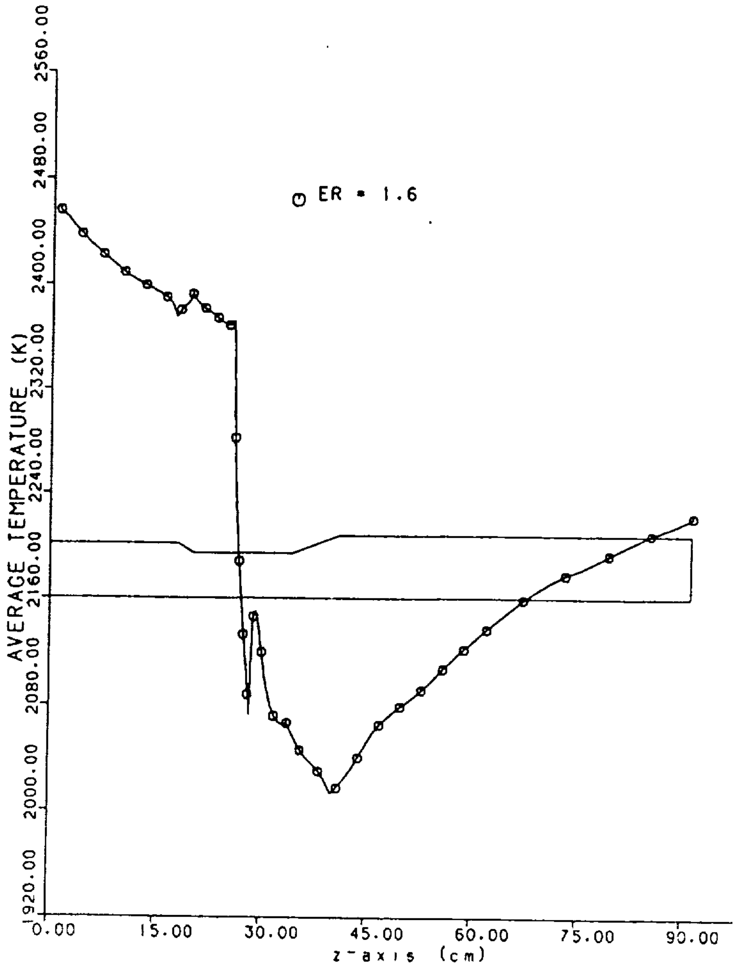

Figure 15. Average cross sectional temperature variation.

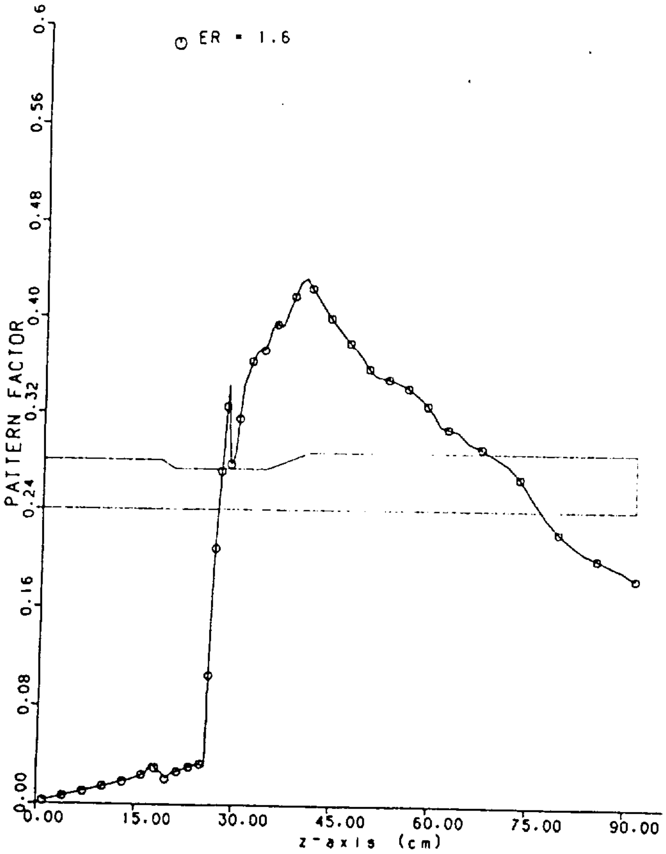

Figure 16. Pattern factor.

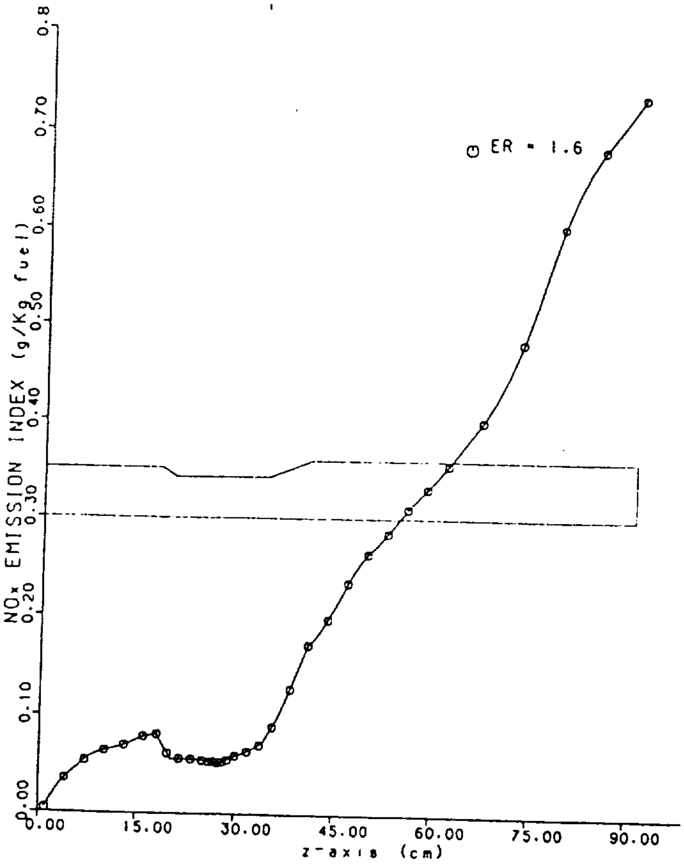

Figure 17. NO emission index.

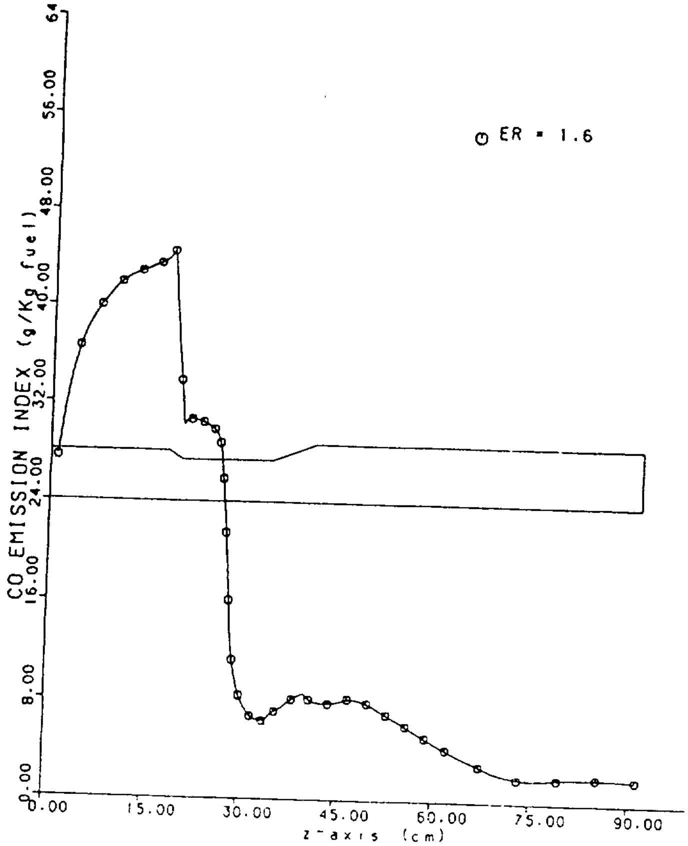

Figure 18. CO emission index.